

**VELOCITY-MAP IMAGING PHOTOELECTRON SPECTROSCOPY OF SMALL  
MOLECULAR ANIONS**

by

Allan Maple de Oliveira

B.S., University of Sao Paulo, 2011

A thesis submitted to the  
Faculty of the Graduate School of the  
University of Colorado in partial fulfillment  
of the requirements for the degree of  
Doctor of Philosophy  
Chemical Physics

2017

This thesis entitled:

Velocity-Map Imaging Photoelectron Spectroscopy of Small Molecular Anions

written by Allan Maple de Oliveira

has been approved for the Committee on Chemical Physics

by

---

W. Carl Lineberger

---

Veronica M. Bierbaum

The final copy of this thesis has been examined by the signatories, and we find that both the content and the form meet acceptable presentation standards of scholarly work in the above mentioned discipline.

DATE: \_\_\_\_\_

Oliveira, Allan Maple (Ph.D. Chemical Physics)

Velocity-Map Imaging Photoelectron Spectroscopy of Small Molecular Anions

Thesis directed by Professor W. Carl Lineberger

Gas phase anion photoelectron spectroscopy presents an opportunity for investigating molecules that are inaccessible by other experimental techniques, by providing data on the structure, reactivity and energetics of short-lived radicals and transition state species. Our recent development of a novel, plasma entrainment source of cold, weakly-bound anions opens a door to new exotic species to be investigated. In this thesis, I explore the capabilities of photoelectron spectroscopy and its application to small exotic molecular anions, while further developing and employing the novel dual-valve ion source.

The thesis begins with a brief history of photoelectron spectroscopy, followed by a description of the experimental apparatus. The first anion studied using the new anion source is the weakly bound methide anion ( $\text{CH}_3^-$ ). This experiment provides the first measurement of the inversion splitting of this simple pyramidal carbanion. The precise measurement of the electron affinity (EA) of the methyl radical provides accurate measurements of the gas phase acidity of methane, which defines the acidity scale of hydrocarbons.

I then explore the spectroscopy of the atmospherically significant HONO molecule, via photoelectron spectroscopy of the open-shelled  $\text{HONO}^-$  radical anion.  $\text{HONO}^-$  is produced in a reaction between  $\text{OH}^-$  and  $\text{NO}$ , a feat accomplished in the cold, collision-rich environment of the novel anion source. This experiment allows for the first measurement of the EA of HONO and the excitation energy to its lowest excited state, the triplet, which is inaccessible by most spectroscopic techniques.

Next, I investigate of the electronic structure of singly substituted alkoxy radicals. The new dual-valve source allowed for controlled synthesis of hydroxymethoxide and aminomethoxide. The selective substitution allows us to probe what effect the substituting group has on the electronic structure of alkoxy radicals, leading to a correlation between the substituent group's electronegativity and the EAs and excited state energies of the radicals.

Finally, I investigate the biologically relevant 7-azaindole and its hydrogen bonded dimer. The photoelectron spectrum of 7-azaindole provides a measurement of the EA of the 7-azaindoyl radical and reveals an unexpected behavior of the spectrum, where most of the observed signal derives from a process other than direct photodetachment.

## DEDICATION

*To the lives of my grandparents Geute and Orencio, and of my cousin Ricardo, who sadly parted  
this world during my time in Boulder.*

*May God bless their souls.*

## ACKNOWLEDGEMENTS

As a naïve young man I had little idea of what I was really getting into, but, as I wrote in my essay for the application process, it was going to be a path full of challenges. It was harder than what I imagined, but, hey, should it be any different? A Ph.D. is the highest attainable degree in one's education! Here I am now, writing my Ph.D. thesis, which pretty much means that I succeeded. It wasn't easy though. It was a long path of difficulties, conflicts with my experiment, with people that I worked with, but mostly with my inner Self, as I in times had to descend into chaos to then reemerge victorious from the ashes – something that is true for anything meaningful in life. The few paragraphs that follow are what I consider the “true introduction” to my thesis, where I acknowledge the difficulties, successes and people that were essential to its completion.

First, I must thank my Ph.D. thesis advisor W. Carl Lineberger. I had the immense opportunity of working with one of the great scientists of the century. A person that not only created a field of research, but also left a legacy of extremely talented scientists, from Hartmut Hotop, his very first postdoc, to Mark Johnson, Dan Neumark and ultimately Julia Lehman, with whom I had the pleasure of working. Julia was responsible for a great amount of my learning on how to succeed in my Ph.D.: from how to work in the lab effectively, to how to write papers and ultimately how to be a hard-ass worker. Despite the occasional conflicts we had, I understand that most of it came from her believing in my potential and wanting me to fully achieve it. It is possible that I learned more from Julia than what I did from Carl himself. I also had the chance of working with Yu-Ju Lu, the senior graduate student who trained me initially. Yu-Ju is an extremely talented experimentalist and it was an honor learning some of his magic lab tricks, if one could say that. In the latter part of my graduate career I had the pleasure of working with

Daniel Nelson, another senior graduate student in the group. Dan is a very smart person, one of the smartest people I know, who became not only a great lab-mate, but also a good friend. Dan not only has a great technical understanding of laboratory instruments and electronics, but has also an amazing ability to explain things clearly. I learned a whole lot from my discussions (sometimes heated arguments) with Dan these past six months. Having conversations with him about science, mathematics, music, politics, philosophy and also videogames, pop-culture and good beer has been extremely gratifying and fun.

Some other academics must be acknowledged here as well. The professors that compose my thesis committee are certainly some of them! I thank Mathias Weber, Heather Lewandowski, Veronica Bierbaum, Barney Ellison for being my thesis committee, and Eric Cornell for being part of the oral examination committee. Starting in my oral exams, these amazing people made me understand science as I do today. Our Tuesday morning ion super-group meetings, composed of essentially the research groups of the professors in my thesis committee, was a great place for sharing ideas and organizing my thoughts as I presented my findings there a number of times. I must also thank other people that believed in me and encouraged me in my endeavors: Margaret Asirvatham for mentoring me in my teaching aspirations and for believing in my passion and potential for teaching, Veronica Bierbaum for her kindness and encouragement and the professors/instructors with whom I worked with as a teaching assistant, Molly Larsen, Niels Damrauer and Joseph Falke.

I also have to acknowledge the amazing JILA staff, specifically the JILA shops (instrument, computing, electronics, etc.). Of the staff, a few people deserve special acknowledgement. The first that comes to mind is Krista Beck, the secretary/assistant of Carl and of other amazing JILA professors. Krista always made JILA events and scheduling things go

superbly well. From the computing group Jim McKown and Corey Keasling were always there to fix bugs and (try to) teach me how to write script for my calculations. Also from the computing group, J.R. Raith III has to be recognized for his support with computer hardware and Windows problems (curse you DaVis!!!). J.R. and I have spent a good amount of time talking about video games, old computers, heavy metal and other cool, essential-to-life stuff, so it was really great having him around for more than just the technical support stuff. From the electronics shop, James Fung-a-Fat and Terry Brown are gratefully acknowledged for all the help with lab electronics problems and for being good people to talk to in the hallways. In the machine shop, I have to particularly acknowledge the sometimes grumpy Todd Asnicar and the always cheerful Hans Green. Not only are these people amazing machinists, but they are also incredible people to have informal (sometimes formal as well) conversations about the most varied topics. From the Supply Office/Building Maintenance, I must acknowledge Brian Lynch for our chats about good beer and Dave Erickson for the morning chats and his candy basket.

I must also thank my family and friends, who supported me throughout this journey. Here in Boulder I didn't make a lot of friendships, but the few that I made were certainly a matter of quality over quantity. Friends like Dan Nelson, whom I mentioned before, Tony Tumminello, Ricardo Carvalho, Curtis Beimborn and Michael Thompson, were essential to my mental sanity as we hung out sharing pints of good beer while taking a break from the science work. From all my Boulder friends, I must thank Andrew Chomas the most, as he has been a true friend for me and I really hope to keep in touch with him for many years to come. My wife's family deserves a big thanks. They really made me part of their family as well and supported us during our time here. Also, whenever we got the chance to visit, they treated me with the love they would give a son. Finally, my own family is the one that deserves most of my gratefulness. Grandpas and

grandmas, uncles, cousins and aunts, and most importantly, Mom, Dad and bro Julian. Thanks for making me who I am today. I love you very much and miss being closer to you.

Finally, the person I have to thank the most of all is my partner for life, my wife Debora. She's the one that has made most of the sacrifice during this journey. She left her job and family to move to the United States with me with just the mere chance that one day she would be working towards a Ph.D. herself. Thankfully, her dedication, hard work and discipline has gotten her the opportunity to study Materials Science at the Colorado School of Mines. I am very grateful and proud of her achievements, as she not only proved she deserves a Ph.D., but also is doing it in record time (less than 4 years!) with stellar performance. Her success only makes me stronger and inspires me to be a better person every day. By supporting me each and every day, she's responsible for a great deal of my achievements, not in graduate school, but in everything in my life. I could not have done it without her. I love you, Debora.

## CONTENTS

CHAPTER I: INTRODUCTION TO THE THESIS .....	1
1.1 Photoelectron Spectroscopy: Fundamentals .....	1
1.2 Photodetachment cross sections and angular distributions .....	16
1.3 Photoelectron versus other spectroscopic techniques .....	22
1.4 Overview of the thesis .....	26
1.5 Chapter 1 references .....	35
CHAPTER II: EXPERIMENTAL AND THEORETICAL METHODS.....	39
2.1 Experimental Methods .....	39
2.1.a Overview of the instrument.....	39
2.1.b Ion Source .....	42
2.1.c Mass Spectrometer .....	50
2.1.d Laser System.....	55
2.1.e Velocity-map Imaging Spectrometer .....	56
2.2 Theoretical Methods .....	60
2.2.a Ab-initio calculations .....	60
2.2.b Photoelectron spectra simulations.....	62
2.3 Data analysis .....	63
2.3.a Image processing.....	63
2.3.b Assignments and uncertainties.....	65
2.4 Chapter 2 references .....	68
CHAPTER III: PHOTOELECTRON SPECTROSCOPY OF THE METHIDE ANION (CH <sub>3</sub> <sup>-</sup> ) .....	71
3.1 Introduction and Motivation .....	71
3.2 Experimental Methods .....	73
3.3 Experimental Results .....	75
3.3.a Introductory remarks .....	75
3.3.b Photoelectron Angular Distributions.....	79
3.3.c Vibrational structure and electron affinities .....	84
3.4 Theoretical Methods and Results.....	89
3.3.a Anion potential energy surface.....	89
3.4.b Photoelectron Spectra and Electron Affinities .....	93
3.5 Discussion .....	94
3.5.a Gas-phase Acidities.....	94

3.5.b Inversion Splitting, Electron Affinity, and Anion Potential Energy Surface .....	97
3.6 Conclusions.....	99
3.7 Chapter 3 references .....	102
CHAPTER IV: PHOTOELECTRON SPECTROSCOPY OF THE NITROUS ACID ANION (HONO <sup>-</sup> )	
.....	105
4.1 Introduction.....	105
4.2 Methods.....	108
4.2.a Experimental .....	108
4.2.b Theoretical Methods .....	109
4.3 Results and Discussion .....	114
4.3.a Introductory remarks .....	114
4.3.b Ground State: cis-HONO $X^1A'$ .....	118
4.3.c Vibrational Analysis.....	125
4.3.d Contribution of the trans-HONO <sup>-</sup> isomer to the photoelectron spectrum.....	130
4.3.e Electronic Structure of HONO <sup>-</sup> .....	137
4.3.f Thermochemistry of HONO .....	145
4.3.g Triplet State: cis-HONO $a^3A''$ .....	147
4.4 Conclusions.....	151
4.5 Chapter 4 references .....	153
CHAPTER V: PHOTOELECTRON SPECTROSCOPY OF THE HYDROXYMETHOXIDE ANION	
(H <sub>2</sub> C(OH)O <sup>-</sup> ) .....	157
5.1 Introduction.....	157
5.2 Methods.....	159
5.2.a Experimental .....	159
5.2.b Theoretical Methods .....	160
5.3 Results.....	168
5.3.a Experimental Photoelectron Spectra and EA(H <sub>2</sub> C(OH)O <sup>•</sup> ) .....	168
5.3.b H <sub>2</sub> C(OH)O <sup>•</sup> $X^2A$ Vibrational Assignments .....	175
5.3.c H <sub>2</sub> C(OH)O <sup>•</sup> $A^2A$ .....	180
5.4 Discussion.....	182
5.4.a H-OCO Torsion.....	182
5.4.b Methanediol Thermochemistry .....	187
5.4.c Photodetachment Producing H <sub>2</sub> C(OH)O <sup>•</sup> $X^2A$ and $A^2A$ Electronic States.....	188
5.5 Conclusions.....	189
5.6 Geometry optimization and frequencies of hydroxymethoxide and hydroxymethoxy .....	192

5.7 Chapter 5 references .....	196
<b>CHAPTER VI: PHOTOELECTRON SPECTROSCOPY OF THE AMINOMETHOXIDE ANION, <math>\text{H}_2\text{C}(\text{NH}_2)\text{O}^-</math></b> .....	
6.1 Introduction.....	199
6.2 Methods.....	201
6.2.a Experimental .....	201
6.2.b Theoretical .....	202
6.3 Results.....	204
6.3.a Initial remarks .....	204
6.3.b Identification of anion with $m/z=46$ .....	205
6.3.c Overview and Electron Affinity of Aminomethoxy.....	207
6.3.d Determination of Aminomethoxy Term Energy, $T_0(A \leftarrow X)$ .....	215
6.3.e Vibrational analysis.....	219
6.3.f Unassigned transitions .....	222
6.4 Discussion.....	222
6.4.a Thermochemistry of aminomethanol .....	222
6.4.b Comparison of aminomethoxy with other singly substituted alkoxy radicals .....	225
6.5 Conclusions.....	228
6.6 General Optimization Results .....	230
6.7 Chapter 6 references .....	235
<b>CHAPTER VII: PHOTOELECTRON SPECTROSCOPY OF 7-AZAINDOLIDE AND 7-AZAINDOLE DIMER ANIONS</b> .....	
7.1 Introduction.....	239
7.2 Methods.....	243
7.2.a Experimental .....	243
7.2.b Theoretical .....	246
7.3 Results and Discussion .....	247
7.3.a Overview spectrum of 7-azaindolidide .....	247
7.3.b High resolution photoelectron spectra of 7-azaindolidide .....	251
7.3.c Comparison between indolyl and 7-azaindolyl .....	268
7.4.d Photoelectron spectrum of $(7\text{-azaindole})_2^-$ .....	270
7.6. Chapter 7 references .....	277
BIBLIOGRAPHY .....	281
APPENDICES .....	300

## LIST OF TABLES

Table 3.1: Experimentally determined electron binding energies of each peak and transition assignments for each peak in the photoelectron spectra of CH <sub>3</sub> <sup>-</sup> and CD <sub>3</sub> <sup>-</sup> .....	78
Table 3.2: Anisotropy parameter ( $\beta$ ) measurements for each peak in the CH <sub>3</sub> <sup>-</sup> photoelectron spectra used. ....	83
Table 3.3: Observed umbrella mode ( $\nu_2$ ) vibrational frequencies and derived spectroscopic constants of neutral <sup>•</sup> CH <sub>3</sub> and <sup>•</sup> CD <sub>3</sub> (cm <sup>-1</sup> ).....	88
Table 3.4: Computational results for the CH <sub>3</sub> <sup>-</sup> /CD <sub>3</sub> <sup>-</sup> 4D transition state barrier height ( $E_B$ ) and <sup>•</sup> CH <sub>3</sub> / <sup>•</sup> CD <sub>3</sub> electronic contribution to the electron affinity ( $\Delta E_{elec}$ ). All values are given in wavenumbers (cm <sup>-1</sup> ). ....	92
Table 3.5: Thermal corrections ( $H_{298K}^0 - H_{0K}^0 = \int_0^{298.15} C_p(T) dT$ ) for the individual species in the methane deprotonation thermochemical cycle.....	96
Table 3.6: Summary of major results of Chapter 3, experimental and theoretical.....	101
Table 4.1: Calculated (MP2/aug-cc-pVTZ) equilibrium geometries of cis-HONO <sup>-</sup> , cis-HONO (S <sub>0</sub> ), and cis-HONO (T <sub>1</sub> ), as well as the difference between geometry parameters of the anion and neutral structures ( $\Delta$ = anion structure – neutral structure). Distances are given in Angstroms and the angles are in degrees. ....	127
Table 4.2: Vibrational transition assignments for the peaks labeled (A–Q) in the photoelectron spectrum reported in Fig. 4.4. ....	128
Table 4.3: Experimental (previous work and this study) and calculated (this study) vibrational frequencies ( $\nu_i$ ) of neutral <i>cis</i> -HONO (S <sub>0</sub> ). All values are given in cm <sup>-1</sup> .....	129
Table 4.4: Comparison of HONO <sup>-</sup> , HONO (S <sub>0</sub> ), and HONO (T <sub>1</sub> ) harmonic frequencies for the <i>trans</i> isomer using different levels of theoretical treatment.....	140
Table 4.5: Comparison of HONO <sup>-</sup> , HONO (S <sub>0</sub> ), and HONO (T <sub>1</sub> ) energies and geometries for the <i>trans</i> isomer using different levels of theoretical treatment.....	141
Table 4.6: Comparison of HONO <sup>-</sup> , HONO (S <sub>0</sub> ), and HONO (T <sub>1</sub> ) energies and geometries for the <i>cis</i> isomer using different levels of theoretical treatment.....	143
Table 4.7: Comparison of HONO <sup>-</sup> , HONO (S <sub>0</sub> ), and HONO (T <sub>1</sub> ) harmonic frequencies for the <i>cis</i> isomer using different levels of theoretical treatment.....	144
Table 4.8: Summary of the experimental results of Chapter 4.....	146
Table 5.1: Calculated torsional potential energy surface scan (CCSD(T)/aug-cc-pVTZ for H <sub>2</sub> C(OH)O <sup>-</sup> $\tilde{X}^1A'$ and H <sub>2</sub> C(OH)O <sup>•</sup> $\tilde{X}^2A$ , and EOM-CCSD/aug-cc-pVTZ for H <sub>2</sub> C(OH)O <sup>•</sup> $\tilde{A}^2A$ ).....	165
Table 5.2: Fit parameters of equation 5.1 for each of the potentials.....	166
Table 5.3: Calculated minimum energy structure of H <sub>2</sub> C(OH)O <sup>-</sup> $\tilde{X}^1A'$ (CCSD(T)/aug-cc-pVTZ), H <sub>2</sub> C(OH)O <sup>•</sup> $\tilde{X}^2A$ (ROCCSD(T)/aug-cc-pVTZ), and H <sub>2</sub> C(OH)O <sup>•</sup> $\tilde{A}^2A$ (CIS/aug-cc-pVTZ)....	177

Table 5.4: Vibrational transition assignments for the peaks labeled a'–e (Fig. 5.5) and B (Fig. 5.4).....	179
Table 5.5: Calculated (ROCCSD(T)/aug-cc-pVTZ) optimized geometries of $\text{H}_2\text{C}(\text{OH})\text{O}^{\bullet} \tilde{X}^2A$ . .....	192
Table 5.6: Calculated (ROCCSD(T)/aug-cc-pVTZ) harmonic vibrational frequencies of $\text{H}_2\text{C}(\text{OH})\text{O}^{\bullet} \tilde{X}^2A$ . .....	193
Table 5.7: Calculated (CIS/aug-cc-pVTZ) harmonic vibrational frequencies of $\text{H}_2\text{C}(\text{OH})\text{O}^{\bullet} \tilde{A}^2A$ . .....	194
Table 5.8: Calculated (CCSD(T)/aug-cc-pVTZ) harmonic vibrational frequencies of $\text{H}_2\text{C}(\text{OH})\text{O}^{\bullet} \tilde{X}^1A$ . .....	195
Table 5.9: Summary of the major results of Chapter 5.....	191
Table 6.1: Optimized structural parameters of $\text{H}_2\text{C}(\text{NH}_2)\text{O}^-$ (CCSD(T)/aug-cc-pVTZ) and $\text{H}_2\text{C}(\text{NH}_2)\text{O}$ in its ground (ROCCSD(T)/aug-cc-pVTZ) and excited (CAS(5,4)/aug-cc-pVTZ) states.....	230
Table 6.2: Calculated (CCSD(T)/aug-cc-pVTZ) harmonic vibrational frequencies ( $\omega_i$ ) of $\text{H}_2\text{C}(\text{NH}_2)\text{O}^- \tilde{X}^1A'$ . .....	231
Table 6.3: Harmonic vibrational frequencies ( $\omega_i$ ) of $\text{H}_2\text{C}(\text{NH}_2)\text{O}^{\bullet}, \tilde{X}^2A'$ (ROCCSD(T)/aug-cc-pVTZ). .....	232
Table 6.4: Harmonic vibrational frequencies ( $\omega_i$ ) of $\text{H}_2\text{C}(\text{NH}_2)\text{O}^{\bullet}, \tilde{A}^2A''$ (CAS(5,4)/aug-cc-pVTZ). .....	233
Table 6.5: Calculated rotational constants for aminomethoxy: Anion $\tilde{X}^1A'$ and neutral ground $\tilde{X}^2A'$ (RCCSD(T)/aug-cc-pVTZ, RO for neutral) and neutral excited $\tilde{A}^2A''$ (CAS(5,4)/aug-cc-pVTZ). .....	234
Table 6.6: Calculated (B3LYP/aug-cc-pVTZ) addition reaction enthalpies ( $\Delta_{\text{rxn}}H_{0\text{K}}^{\circ}$ ) between amide anion ( $\text{NH}_2^-$ ) and formaldehyde ( $\text{H}_2\text{CO}$ ) forming the anionic products shown in Fig. 6.1 and electron affinities of the corresponding neutral species. All values include zero-point energy. .....	209
Table 6.7: Vibrational transition assignments for the peaks in the photoelectron spectra (Figs. 6.3, 6.4 and 6.5). .....	221
Table 6.8: Summary of major results of Chapter 6. ....	224

## LIST OF FIGURES

Figure 1.1: Schematic representation of the photoionization process generating the hydronium cation, $H^+$ .....	3
Figure 1.2: Schematic representation of a photodetachment process of a generic diatomic molecule $M_2$ .....	6
Figure 1.3: Potential energy surfaces of the amide anion ( $NH_2^-$ ) and the ground and first excited states of the amino radical ( $NH_2$ ). .....	13
Figure 1.4: Photoelectron spectrum of the amide anion ( $NH_2^-$ ) obtained with a photon energy of 3.494 eV ( $\lambda = 355$ nm). .....	14
Figure 1.5: Behavior of photoelectron angular distributions for the cases of detachment from several <i>s-p</i> mixed states.....	21
Figure 1.6: Schematic representation of the thermochemical cycle of HA.....	25
Figure 1.7: Potential and spectra representative of the photoelectron spectroscopic investigation of the methide anion. ....	28
Figure 1.8: Summary of the work reported in chapter 4 depicting photodetachment of $HONO^-$ , accessing the singlet and triplet electronic states of $HONO$ and their behavior as they are formed <i>via</i> photodetachment of the $HONO^-$ anion.....	30
Figure 1.9: Intramolecular interaction trend of singly substituted alkoxy radical as described in Chapters 5 and 6. ....	32
Figure 1.10: Chemical structures of deprotonated indole (indolide), deprotonated 7-azaindole (7-azaindolide) and $(7\text{-azaindole})_2^-$ anion.....	34
Figure 2.1: Schematic representation of the photoelectron spectrometer.....	41
Figure 2.2: Specific design and functional details of the dual valve, plasma entrainment ion source. ....	45
Figure 2.3: Photograph of the dual valve plasma entrainment ion source described in this section. The individual components of the source are labeled accordingly.....	48
Figure 2.4: Ozonide argon clusters ( $O_3^-(Ar)_n$ ) optimization and cluster size distribution shifts as a function of valve body temperature. ....	49
Figure 2.5: Detailed schematic representation of the Wiley-McLaren Time-of-Flight mass spectrometer. ....	51
Figure 2.6: Detailed view of the VMI spectrometer with the velocity-mapping of the photoelectrons from $O_2^-$ .....	58
Figure 3.1: Photoelectron spectra of $CH_3^-$ . The experimental spectrum using 1.165 eV (red) or 0.383 eV (black) photon energies are shown in the upper panel.....	76
Figure 3.2: Photoelectron spectra of $CD_3^-$ . Analogous description as Figure 3.1.....	77

Figure 3.3: $\text{CH}_3^-$ photoelectron anisotropy parameter ( $\beta$ ) as a function of electron kinetic energy. ....	82
Figure 3.4: Schematic potential energy curves (not to scale) of $\text{CH}_3^-$ (black) and $\bullet\text{CH}_3$ (green) as a function of the inversion angle ( $\varphi$ ). ....	85
Figure 4.1: 1-D electronic potential energy curves (CBS-QB3) for <i>cis</i> -HONO as functions of the central $r_{\text{ON,c}}$ bond length. ....	111
Figure 4.2: The <i>cis</i> -HONO $^-$ photoelectron spectrum using 355 nm (3.49 eV) photons.....	116
Figure 4.3: Photoelectron spectrum of <i>cis</i> -HONO $^-$ using photon energies of 532 nm (2.33 eV, green), 1064 nm (1.16 eV, purple), and 1613 nm (0.769 eV, orange).....	120
Figure 4.4: Scaled experimental photoelectron spectrum (black trace), Franck-Condon factors (green sticks), and convoluted simulation (red).....	123
Figure 4.5: Comparison of the calculated (ROMP2/aug-cc-pVTZ) photoelectron spectrum of <i>trans</i> -HONO $^-$ and the experimental data. ....	132
Figure 4.6: Comparison of the calculated photoelectron spectrum of HONO $^-$ with both <i>cis</i> (UMP2/aug-cc-pVTZ, green sticks) and <i>trans</i> (ROMP2/aug-cc-pVTZ, blue sticks) isomers, and the experimental data. ....	134
Figure 4.7: Potential energy as a function of the HONO $^-$ dihedral angle calculated at the CBS-QB3 level of theory. ....	136
Figure 4.8: Calculated photoelectron spectrum of <i>trans</i> -HONO $^-$ (red trace) with (a) ROMP2/aug-cc-pVTZ, and (b) CCSD/aug-cc-pVTZ level of theory/basis-set.....	142
Figure 4.9: Detailed T $_1$ excited state photoelectron spectrum of <i>cis</i> -HONO $^-$ using 301 nm (4.12 eV) photon energy. The green sticks are the calculated FCFs by the methods described in the text. ....	148
Figure 5.1: Calculated (CCSD(T)/aug-cc-pVTZ) 1D potential energy curves of the torsional coordinate for the electronic states of hydroxymethoxy accessed in the photodetachment process. ....	162
Figure 5.2: Calculated 1D potential energy curves as functions of the torsional coordinate for the H $_2\text{C}(\text{OH})\text{O}^- \tilde{X}^1A'$ (blue), H $_2\text{C}(\text{OH})\text{O}^* \tilde{X}^2A$ (red), and H $_2\text{C}(\text{OH})\text{O}^* \tilde{A}^2A$ (purple) states.....	167
Figure 5.3: Upper panel: Experimental anisotropy parameters ( $\beta$ ) as a function of electron kinetic energy. Middle panel: Experimental photoelectron spectrum of H $_2\text{C}(\text{OH})\text{O}^-$ , using 3.49 eV (355 nm) photon energy. Lower panel: Convoluted photoelectron simulations of detachment to the ground (green) and excited (blue) electronic states of H $_2\text{C}(\text{OH})\text{O}^*$ , along with their sum (red dots). ....	170
Figure 5.4. Upper panel: Experimental photoelectron spectrum of H $_2\text{C}(\text{OH})\text{O}^-$ using 2.74 eV (453 nm) photon energy. Lower panel: Calculated (CCSD(T)/aug-cc-pVTZ) Franck-Condon factors (sticks) and convoluted simulation (blue trace).....	172

Figure 5.5: Upper panel: Photoelectron spectrum of $\text{H}_2\text{C}(\text{OH})\text{O}^-$ using 2.33 eV (532 nm) photon energy. Lower panel: Calculated (CCSD(T)/aug-cc-pVTZ) Franck-Condon factors (sticks) and convolved simulation (blue trace) with assigned transitions.....	174
Figure 5.6: $\text{H}_2\text{C}(\text{OH})\text{O} \cdot \tilde{X}^2A$ H-OCO calculated (ROCCSD(T)/aug-cc-pVTZ) torsional potential comparison. ....	185
Figure 6.1: Structural isomers of aminomethoxide discussed in the text.....	208
Figure 6.2: Upper panel: Photoelectron anisotropy parameter ( $\beta$ ) of aminomethoxide (black dots) as a function of electron kinetic energy (eKE). Lower panel: VMI photoelectron spectrum of aminomethoxide obtained with a photon energy of 3.494 eV.....	210
Figure 6.3: Upper panel: Measured anisotropy parameter $\beta$ associated with the experimental photoelectron spectrum found in the middle panel. Middle panel: Photoelectron spectrum obtained using a photon energy of 2.172 eV. Lower panel: Calculated photoelectron spectrum for transitions from the ground electronic state of the aminomethoxide.....	212
Figure 6.4: Photoelectron spectrum obtained using a photon energy of 2.038 eV.....	214
Figure 6.5: Lower panel: Photoelectron spectrum obtained using 2.329 eV photon energy (532 nm). Upper panel: Anisotropy parameter $\beta$ as a function of eKE.....	216
Figure 6.6: Experimental photoelectron spectrum obtained with 3.494 eV photon energy (black trace), calculated FCFs for transitions from the ground state of the anion ( $\tilde{X}^1A'(v=0)$ ) to neutral ground (red sticks) and neutral excited (blue sticks) electronic states of aminomethoxy.....	218
Figure 6.7: Upper panel: Photoelectron anisotropy parameter ( $\beta$ ) as a function of electron kinetic energy (eKE) for aminomethoxy (blue dots) and hydroxymethoxy (red dots). Lower panels: Photoelectron spectrum of hydroxymethoxide (red) and aminomethoxide anions (blue) obtained with a photon energy of 3.49 eV (355 nm).....	227
Figure 7.2: Photoelectron spectrum of indolide reproduced from Nelson <i>et al.</i> .....	240
Figure 7.1: Resulting mass spectrum from ion generation procedure described in section 7.2.a. The displayed range of mass units shows the production of 7-azaindolide and (7-azaindole) <sub>2</sub> ..	244
Figure 7.3: Overview photoelectron spectrum of the 7-azaindolide anion obtained with a photon energy 3.494 eV (black trace) accessing the ground electronic state of 7-azaindolyl.....	250
Figure 7.4: Comparison between the experimental low resolution overview spectrum of 7-azaindolide (black trace) and calculated spectrum (red sticks).....	253
Figure 7.5: Photoelectron spectrum of 7-azaindolide acquired with a photon energy of 2.719 eV and calculated FCF stick spectrum (red sticks). The eBE axis spans a range of 0.119 eV, and corresponds to the same magnified region as shown in Figs. 7.3 and 7.4.....	255
Figure 7.6: Compiled photoelectron spectra of 7-azaindolide acquired with various photon energies plotted as a function of electron Binding Energy (eBE).....	261
Figure 7.7: Compiled photoelectron spectra of 7-azaindolide acquired with various photon energies and plotted as a function of eKE.....	262

Figure 7.8: Upper panel: Overview photoelectron spectrum of 7-azaindolidide (black trace) and the Gaussian fit (orange trace) to the apparent underlying baseline (see text for details). Lower panel: Photoelectron spectrum of 7-azaindolidide with a Gaussian continuum (orange trace in the upper panel) subtracted.....267

Figure 7.9: Overview photoelectron spectrum of  $(7\text{-azaindole})_2^-$ , accessing the ground and first excited states of  $(7\text{-azaindole})_2$ . This spectrum is obtained with a photon energy of 3.494 eV..272

Figure 7.10: Photoelectron spectrum of  $(7\text{-azaindole})_2^-$  acquired with a photon energy of 1.165 eV.....273

Figure 7.11: Detailed photoelectron spectrum of  $(7\text{-azaindole})_2^-$  acquired with a photon energy of 3.494 eV. ....274

# CHAPTER I

## INTRODUCTION TO THE THESIS

### 1.1 Photoelectron Spectroscopy: Fundamentals

Photoelectron spectroscopy is a spectroscopic technique based on the photoelectric effect. The modelling of this physical phenomenon by Albert Einstein resulted in the award of the Nobel Prize in Physics 1921<sup>1</sup> and lies at the very core of the development of quantum mechanics. The observed phenomenon, made by the physicist Heinrich Hertz in 1887,<sup>2</sup> was the following: A metallic surface in vacuum exhibited electron emission upon irradiation with light. The curious thing about this phenomenon was that no electron emission was observed above a specific wavelength, and the number of electrons emitted was not dependent on the wavelength. In other words, below certain wavelengths, when emission was observed, the number of electrons emitted did not change when the wavelength was made shorter (larger photon energy). In addition, after electron emission was observed, an increase in photon energy made the kinetic energy of the electron vary linearly with photon energy. The phenomenon was, therefore, modelled as:

$$eKE = h\nu - \phi \quad (1.1)$$

where  $eKE$  is the electron kinetic energy,  $h\nu$  is the photon energy and  $\phi$  is the work function of the metal. In more intuitive terms,  $\phi$  is the threshold potential, *i.e.* the minimum energy required to remove the electron from this metallic surface. If  $h\nu \leq \phi$ , no emission was observed and if  $h\nu > \phi$ , electron emission is observed with a kinetic energy varying linearly with photon energy, thus, satisfactorily modelling the phenomenon observed by Hertz. The act of measuring the kinetic

energy of the emitted electrons in order to determine  $\phi$  was designated “Photoelectron Spectroscopy.”

A similar phenomenon can be observed in gas phase. In isolated atoms,  $\phi$  is analogously the energy required to remove an electron from a neutral atom, generating a cation and an electron. In this case, instead of  $\phi$ , the threshold energy is defined as ionization potential (IP) or ionization energy (IE). The formation of a cation from a neutral atom/molecule upon interaction with a photon is defined as “photoionization” and it is illustrated in its simplest example in Fig. 1.1 for the hydrogen atom. Fig. 1.1 displays the photoionization of H, illustrating the physical representation of the process. If the energy of the photon absorbed by the system is sufficiently high as to bring the electron from its most stable orbit to an orbit in which the radius tends to infinity, the once neutral H atom now becomes a positively charged proton, infinitely separated from the negatively charged electron. The well-known IE of hydrogen atom was later named the Rydberg constant ( $R_H$ ) and is one of the best known physical constants, with an experimentally determined value of 13.6056930090(81) eV.<sup>3</sup> If the photon energy is greater than  $R_H$ , by conservation of energy and momentum and due to the electron’s overwhelmingly smaller mass when compared to the proton, essentially the entire remaining energy of the photons is transferred to the electron increasing its kinetic energy. We then recover the initial observation of electron emission from a metallic surface when irradiated by light in the much simpler system of an isolated neutral atom.

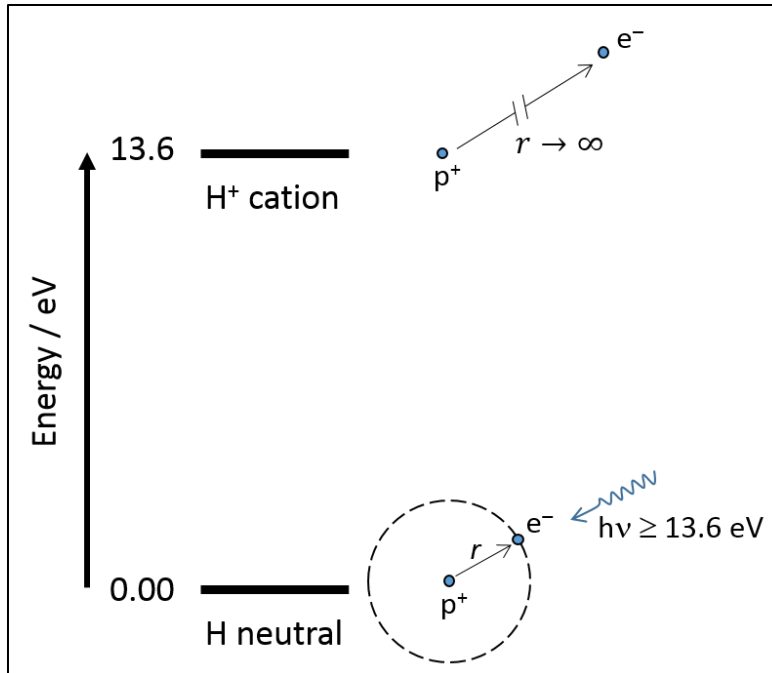


Figure 1.1: Schematic representation of the photoionization process generating the  $H^+$  cation from neutral hydrogen upon interaction with a photon of energy greater than or equal to  $\sim 13.6$  eV. Here, the energy of neutral H is defined as zero.

The analysis of emission of electrons upon interaction with photons can also be applied to anions, which are the focus of this thesis, and can be exemplified in similar terms. Instead of a neutral H atom, we now start with an H atom which possesses an additional electron, forming the hydride anion ( $\text{H}^-$ ). In an analogous manner, the interaction of  $\text{H}^-$  with a photon with enough energy can bring an electron from  $\text{H}^-$  to a state in which the electron is essentially “free”, *i.e.* infinitely separated from the now neutral H atom. The process of forming a neutral atom from the corresponding anion is designated “photodetachment”. For the example above the  $\text{H}^-$  atom will lose an electron, forming H, if  $h\nu > 0.754 \text{ eV}$ .<sup>4</sup> For anions, the analogous quantity to the IE is known to as the electron affinity (EA). The EA represents the minimum amount of energy necessary to remove an electron from an anion generating a neutral atom. By convention, the EA is referred to as belonging to the neutral species (from the example above  $\text{EA}(\text{H}) = 0.754 \text{ eV}$ ), as a positive EA value indicates that energy is gained when the electron is added to the neutral atom. If the EA is negative, the anion is higher in energy than the corresponding neutral and therefore, attaching an electron to this species is an endothermic process. For molecules, which compose the totality of the material described in this thesis, the existence of multiple electronic, vibrational, and rotational states allows equation 1.1 to be more instructively written as:

$$eKE = h\nu - eBE \quad (1.2)$$

where  $eBE$  is the electron binding energy of a specific electronic, vibrational or rotational state, depending on the system in question. The  $eBE$  value that corresponds to the EA is the energy difference between the generalized ground states of anion and neutral species.

Photoelectron spectroscopy is a technique which relies on measurement of the kinetic energy of the photodetached electrons. By measuring the kinetic energy distribution of the electrons that are detached upon interaction with a photon, described here as photodetached

electrons or photoelectrons, a photoelectron spectrum is generated. Once a target molecule is established, the photodetachment process for a generalized molecular anion  $M_2^-$  can be broadly described by:



While the light source of  $h\nu$  will be described in Chapter 2, it is important to state that for accurate measurements of the photoelectron kinetic energy, laser light is utilized as it provides high intensity, narrow linewidths, short pulse duration, etc. A well-defined photon energy is necessary so that the measurement of the kinetic energy and therefore the binding energy can be precise and accurate. Since the energy levels of molecules are quantized, we see that by assigning discrete values for eBE, for a fixed  $h\nu$ , a discrete spectrum of eKE will be obtained. Again, by conservation of energy, if  $h\nu > \text{EA}$  of the target molecule, photoelectrons will be observed with the remainder of the energy being deposited in either the kinetic energy of the electrons or the internal states (degrees of freedom) of the molecule. As will become clear in Chapter 2, our experimental resolution does not allow for the separation of rotational lines, thus, the photoelectron spectra provide a vibrationally resolved spectrum of the electronic states of the corresponding neutral molecule.

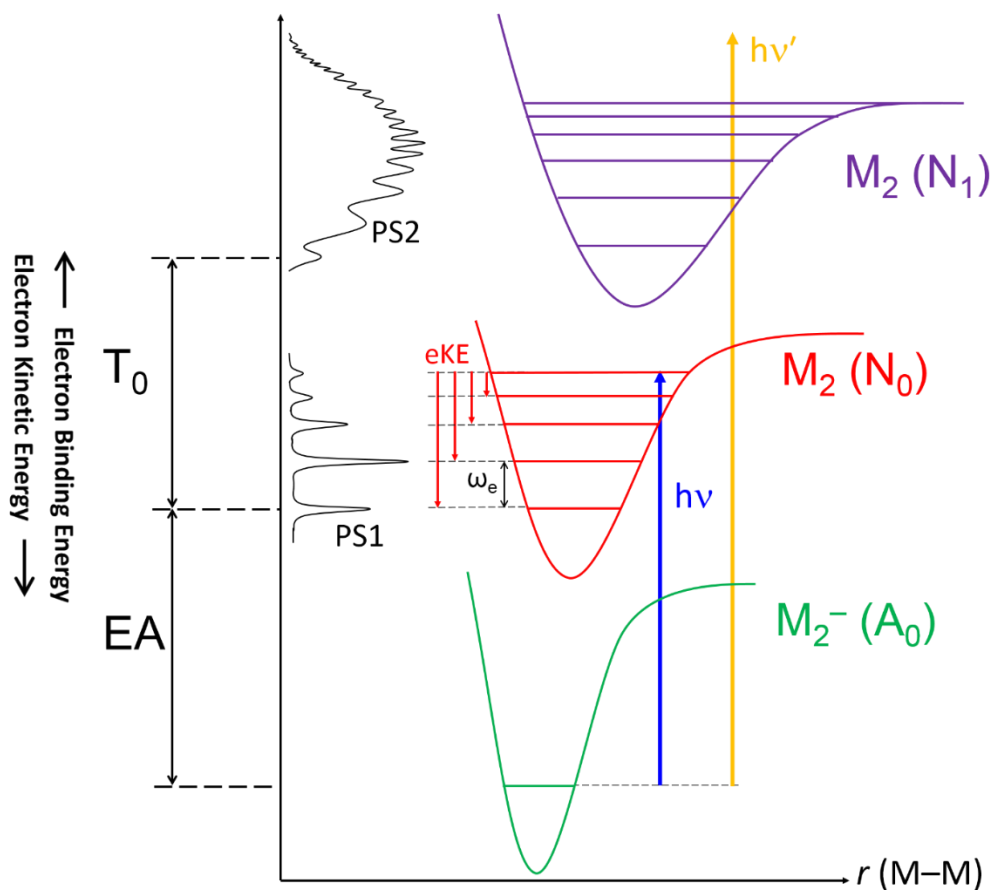


Figure 1.2: Schematic representation of a photodetachment process of a generic diatomic molecule  $M_2$ . The blue upward arrow represents the photon energy used to access the neutral ground state of  $M_2$ . The orange upward arrow represents a higher photon energy that accesses both electronic states, the ground and first excited states of  $M_2$ . The downward red arrow represents the discrete measured electron kinetic energies that generate the peaks represented in the photoelectron spectrum PS1, schematically drawn along the y-axis. The kinetic energies associated with the higher photon energies (orange arrow) were omitted for simplicity.

To explain how photoelectron spectra are generated and interpreted, Fig. 1.2 shows a schematic representation of the process. Fig. 1.2 shows three potential energy curves for the arbitrary diatomic molecule  $M_2$ , the anion ground electronic state ( $A_0$ ), neutral ground state ( $N_0$ ) and one neutral excited state ( $N_1$ ). The curves  $M_2^- (A_0)$ ,  $M_2 (N_0)$  and  $M_2 (N_1)$  show the relative energy of  $M_2$  as a function of the M–M bond length. The blue upward arrow represents a photon energy that accesses the  $N_0$  state. This photon energy generates the photoelectron spectrum PS1. If a higher photon energy (orange upward arrow) is employed, both  $N_0$  and  $N_1$  states are accessed and, as a consequence, both PS1 and PS2 photoelectron spectra are generated. This figure shows some important quantities that can be obtained from photoelectron spectra. The peak with the highest observed eKE (or lowest eBE) represents the transition between ground vibrational states of the anion and neutral and is defined as the EA of  $M_2$ . As was stated above, the existence of discrete energy levels in the molecule results in a photoelectron spectrum with discrete peaks, each positioned in the corresponding eBE of the vibrational levels of  $M_2$ . The spacing between peaks centers, therefore, provides the measurement of the vibrational frequency ( $\omega_e$ ) of the  $M_2$  stretching mode in the  $N_0$  state. In an analogous manner, when the higher photon energy is used and the  $N_1$  state is accessed, the vibrational frequency of the  $N_1$  state can be measured. Moreover, the difference between the eBEs of the origin transitions of the  $N_0$  and  $N_1$  states provides a measurement of the term energy ( $T_0$ ) of  $M_2$ , which is the energy separation between these two electronic states.

The photoelectron spectra related to each one of the electronic states of  $M_2$  (PS1 and PS2) have different extent the vibrational progressions and relative intensities of the transitions. This brings us to question what determines the relative intensities of the peaks in a photoelectron spectrum. Fig. 1.2 shows that the potential energy curves of  $A_0$ ,  $N_0$  and  $N_1$  have different shapes

and equilibrium bond distances. The  $A_0$  state has a shorter equilibrium M–M bond length and a higher bond strength. The  $N_1$  state has an even longer M–M equilibrium bond length and lower bond strength than the  $N_0$  state. In order to understand this, if we imagine that we instantaneously remove an electron from  $M_2^-$ , the  $M_2$  molecule will find itself away from its equilibrium geometry. In brief terms, a larger displacement from equilibrium will result in a larger activation of vibrational modes, *i.e.* longer vibrational progression (such as PS2, Fig. 1.2). In a classical mechanical picture, if we consider that the atoms M are connected by a spring with spring constant  $k$  the potential energy can be described by:

$$V(\mathbf{r}) = -\frac{k(\mathbf{r} - \mathbf{r}_0)^2}{2} = -\frac{\mu\omega_0^2}{2}(\mathbf{r} - \mathbf{r}_0) \quad (1.4)$$

where  $\mathbf{r}$  is the internuclear distance,  $\mathbf{r}_0$  is the equilibrium bond length,  $k$  is the force constant of the M–M bond,  $\mu$  is the reduced mass of  $M_2$  and  $\omega_0$  is the harmonic frequency of the M–M stretching vibration. One can see that a larger displacement from equilibrium will result in a larger force acting on the atoms of  $M_2$  ( $\vec{F} = -\vec{\nabla}V$ ). Thus, a larger vibrational activity will be expected if the geometry change between electronic states is larger, as the atoms will vibrate in order to reach their equilibrium distance in the final state. Although the phenomenology described by the classical mechanical picture is correct, it lacks quantitative information of what the relative intensities of the transitions should be.

In order to provide a quantitative model of the vibration of molecules and of the intensities of the peaks in a photoelectron spectrum, a quantum mechanical approach has to be taken. For that, we initially rely on the Born-Oppenheimer approximation which is to consider that, the electrons, being much lighter than the nuclei, instantly adjust to any nuclear motion.

This assumption allows the total Hamiltonian of the system to be separable into its electronic, nuclear and spin parts:

$$\mathcal{H}_{tot} \approx \mathcal{H}_{nuclear} + \mathcal{H}_{electronic} + \mathcal{H}_{spin} \quad (1.5)$$

which allows the total wavefunction to be written as a product form:

$$\psi_{tot} = \psi_{nuclear} \psi_{electronic} \psi_{spin} = \psi_n \psi_e \psi_s \quad (1.6)$$

In the photodetachment process, again utilizing the Born-Oppenheimer approximation, the removal of the electron places the initial ground state anion rovibrational wavefunction on the potential energy surface of the neutral, with the nuclei in the same configuration as the anion equilibrium structure. For the sake of simplicity, we will proceed with the derivation for the simple case of the molecule  $M_2$  considering only the vibrational component  $\psi_v$  of the nuclear wavefunction and that only the ground vibrational level of the anion is populated (see Eq. 1.12 and associated text). We can therefore express the anion wavefunction as a linear combination of neutral wavefunctions which are eigenfunctions of the neutral state Hamiltonian and therefore form a complete set of orthonormal functions. By doing this, we obtain the following expression:

$$\psi_{anion}(v=0) = \sum_{v=0}^{all\ states} a_v \psi_{neutral}(v) \quad (1.7)$$

where  $a_v$  are the expansion coefficients that can be obtained by:

$$a_v = \int_{-\infty}^{\infty} dr \psi_{anion}^*(v=0) \psi_{neutral}(v) = \langle v_{initial} | v_{final} \rangle \quad (1.8)$$

We define the FC factor of the  $v^{\text{th}}$  transition as the square modulus of  $a_v$ :

$$FCF_{v^{\text{th}}\ transition} \equiv |\langle v_{initial} | v_{final} \rangle|^2 \quad (1.9)$$

The FC factor physically represents the projection of the anionic vibrational wavefunction onto a neutral eigenstate. In other terms, it represents the overlap between the initial and final state vibrational wavefunctions. From this, one can see that, if the geometries of anion and neutral states are similar, or close to similar, the overlap is large, resulting in  $a_0 \approx 1$ . This means that the expansion shown in eq. 1.8 has the  $v = 0$  expansion term as the largest and essentially only relevant term. In other words, the anion wavefunction is also an eigenfunction of the neutral state's Hamiltonian. In the photoelectron spectrum, therefore, a single transition will be observed corresponding to the  $v = 0$  in the anion to the  $v = 0$  transition in the neutral. If, however, the geometries are significantly different between the initial and final states, the overlap of the vibrational wavefunctions  $v = 0$  is small and therefore more terms in the expansion are necessary to satisfactorily describe the anionic wavefunction. This results in a distribution of amplitudes. In the photoelectron spectra, this will be observed by a distribution of peaks corresponding to many quanta of the neutral state vibrations, where the relative intensities of the peaks are directly proportional to the ratios of the expansion coefficients, *i.e.* the FC factors.

Understanding the photoelectron spectrum of  $M_2$  requires predicting the spacing of the peaks in PS1 and PS2, *i.e.* the frequency of the M–M stretching vibration, in addition to the FC factors. For modelling the  $M_2$  vibrational frequency, the quantum harmonic oscillator approximation is a good model, provided we limit ourselves to dealing with small displacements of the M–M bond, *i.e.* sufficiently close to the bottom of the  $M_2$  potential energy well. While the full derivation of this problem is out of the scope of this chapter, it suffices to state that the problem can be solved analytically by utilizing the potential energy operator analogous to Eq. 1.4 (see Ref. 5 for complete derivation). This will result in the following expression for the eigenvalues (energy levels,  $E_v$ ) of the problem:

$$E_v = \omega_e \left( v + \frac{1}{2} \right) \quad (1.10)$$

For polyatomic molecules, as those described in Chapters 3 through the end of this thesis, the single M–M vibrational coordinate is replaced by the  $3N-6$  vibrational normal modes, where  $N$  is the number of atoms in the molecule. Within this same approximation, the  $3N-6$  vibrations are harmonic and independent of each other. When higher vibrational quanta are reached, the potential energy curve deviates from the parabolic harmonic potential, thus requiring anharmonic terms to be included in the aforementioned expression. Although the derivation is beyond the scope of this chapter, for the molecules studied here we often utilize the energy levels of an anharmonic oscillator to model their vibrational frequencies. The anharmonic expression for the vibrational energy levels then becomes:

$$E_{v, n^{th} \text{ mode}} = \omega_n \left( v + \frac{1}{2} \right) + x_{nn} \left( v + \frac{1}{2} \right)^2 + \dots \quad (1.11)$$

where  $x_{nn}$  is the first order anharmonicity constant and, considering the precision of our experiment, will be the only anharmonic term we will be able to measure. Full a thorough description of vibrational normal modes and their application to spectroscopy, see Refs. 6, 7 and references within.

The photodetachment of the amide anion ( $\text{NH}_2^-$ ), performed in our laboratory during the experiments described in Chapter 6, presents an instructive example of how the difference in equilibrium geometries between anion and neutral states affect the photoelectron spectra. Fig. 1.3 below shows the potential energy curves of the  $\text{NH}_2^-$  as a function of the HNH bending angle ( $\angle_{\text{HNH}}$ ). Both anion and neutral ground electronic states have  $\angle_{\text{HNH}} \approx 102^\circ$  and essentially identical curvature of the potential. This means that, if we express the vibrational wavefunctions

of the anion utilizing anion vibrational eigenfunctions (as described above), only the very first function of the expansion, the eigenfunction of the ground vibrational state of the anion, will have a significant expansion coefficient while all the other terms of the expansion will be negligible. In other words, the projection of the anion wavefunction onto the eigenstates of the neutral molecule will only have significant overlap with one state of the neutral, here, the  $\psi_{neutral}(v = 0)$ . The photoelectron spectrum associated with the ground state of  $\text{NH}_2$ , shown in Fig. 1.4 reflects this fact by exhibiting a single transition located at 0.771 eV eBE (EA of  $\text{NH}_2$ )<sup>8</sup> and no further transitions with significant FC factors. On the other hand, the potential energy surface of the excited state of  $\text{NH}_2$  is considerably different than  $\text{NH}_2^-$ , with the equilibrium structure being *quasi*-linear. In contrast with photodetachment to the ground state, the photoelectron spectrum associated with the excited state is therefore characterized by a long progression of peaks, where the spacing between peaks represents the HNH bending vibrational frequency on the excited state of  $\text{NH}_2$ .

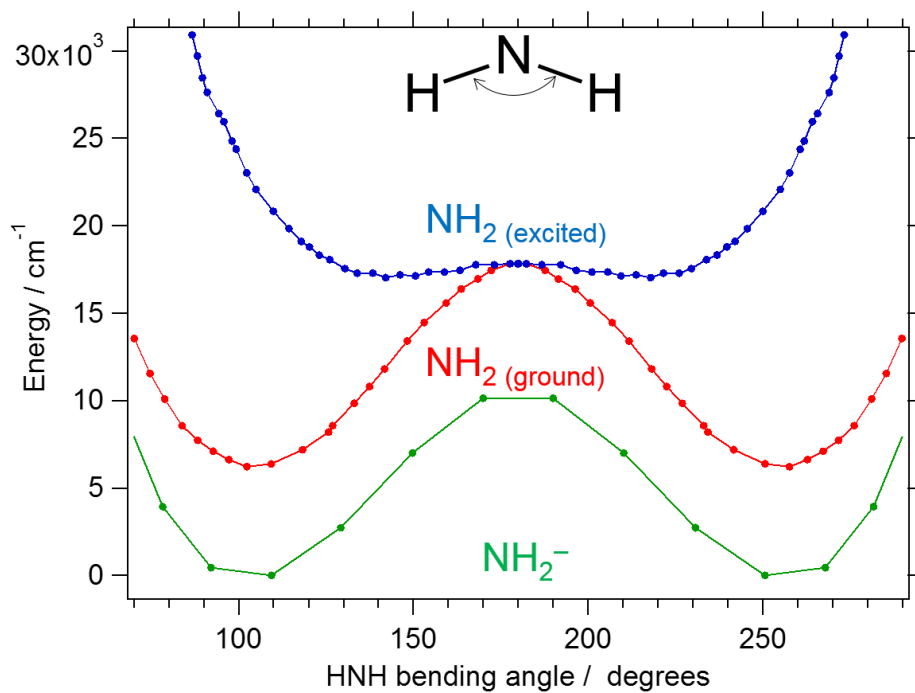


Figure 1.3: Potential energy surfaces of the amide anion (NH<sub>2</sub><sup>-</sup>) and the ground and first excited states of the amino radical (NH<sub>2</sub>). The neutral state surfaces were obtained from Zhou *et al.*<sup>9</sup> and the anion surface was calculated at the B3LYP/aug-cc-pVTZ level of theory for illustrative purposes.

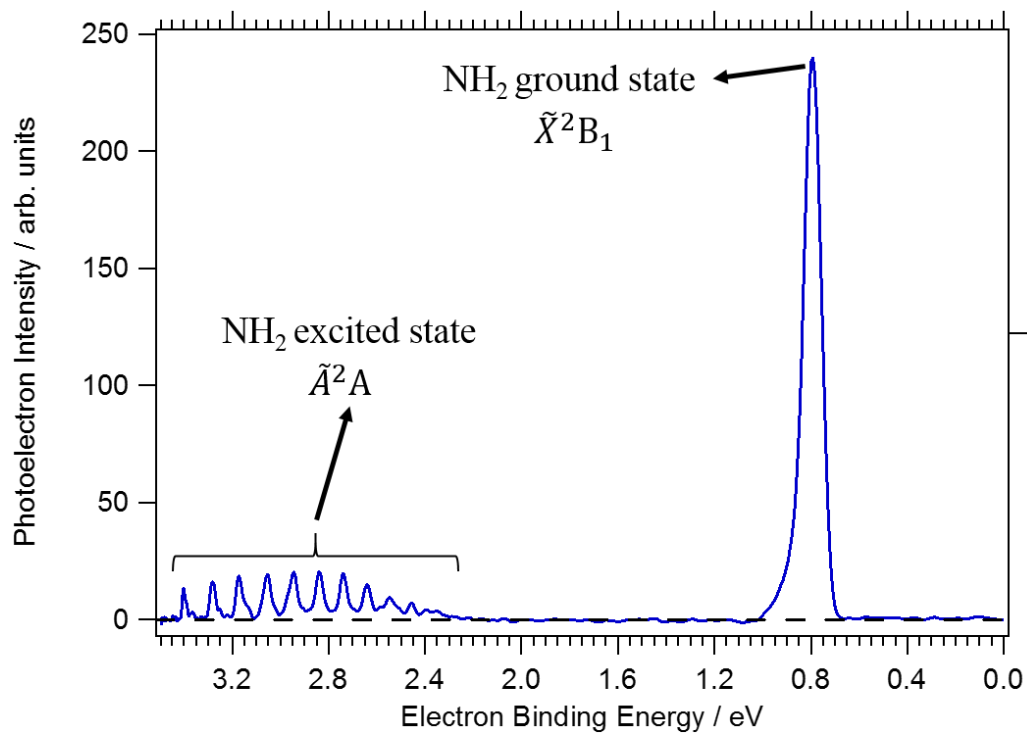


Figure 1.4: Photoelectron spectrum of the amide anion (NH<sub>2</sub><sup>-</sup>) obtained with a photon energy of 3.494 eV ( $\lambda = 355$  nm). These spectra exemplify how the geometry change between anion and neutral states is experimentally observed in the photoelectron spectrum by the different extent of vibrational progressions.

So far, the description of modelling of the intensities of the photoelectron spectra considered that only the anion ground rovibrational level is populated, which is only true for a temperature of 0 K. For higher temperatures, more specifically, vibrational temperatures, the Boltzmann factor (equation 1.12) must be included in the aforementioned formalism.

$$\frac{\mathcal{N}_v}{\mathcal{N}_0} = e^{-\frac{E_v - E_0}{k_B T}} \quad (1.12)$$

resulting in:

$$\text{Intensity}_{v^{\text{th}} \text{ transition}} = \text{FCF}_{v^{\text{th}} \text{ transition}} e^{-\frac{(E_v - E_0)}{k_B T}} \quad (1.13)$$

In this work, since that the anions are generated in a supersonic expansion into vacuum (see Chapter 2), it is not necessarily true that the populations on all internal degrees of freedom obey the Boltzmann distribution and can have significantly different temperatures. Nevertheless, this formalism is utilized for scaling the FC factor of excited vibrational anionic states. The transitions that start in an anion vibrationally excited state are commonly designated vibrational hot bands ( $v_{\text{anion}} = 1, 2, 3 \dots$  to  $v_{\text{neutral}} = 0$ ) and sequence bands ( $v_{\text{anion}} = 1, 2, 3 \dots$  to  $v_{\text{neutral}} = 1, 2, 3 \dots$ ).

Before we continue with this description of photoelectron spectroscopy, it is useful to discuss how the information stated so far relates to the experiments that will be described in this thesis. In regard to the extent of vibrational progressions, although it is possible that the geometries of anion and neutral states are similar, in this thesis, the geometries and bond strengths often change to a significant degree when an electron is added to a neutral molecule. This results in long vibrational progressions, enabling us to measure the vibrational frequencies of the neutral molecules. In regards to the temperature of the anions, effort is made to guarantee

that the anions are internally cold, as will be described in Chapter 2. The presence of vibrational hot bands can considerably complicate the interpretation of photoelectron spectra due to spectral congestion, as well as decrease the resolution. For a thorough discussion of this topic, see Ref 10.

## 1.2 Photodetachment cross sections and angular distributions

The observed intensities in a photoelectron spectrum depend not only on the vibrational wavefunction overlap (FC factors), but also on the electronic portion of the transition probabilities when the anion interacts with the electric field generated by the photons. This electronic part is designated the photodetachment cross section ( $\sigma$ ), and it represents the likelihood of a transition when a photon interacts with the molecule. Physically it can be thought of as the electrical interaction of the light's oscillating electric field and the orbital's electron density in the molecule. This interaction is similar to conventional absorption spectroscopy, however, the final state of the wavefunction also contains the free electron in a continuum of states. Thus, differently from electronic absorption spectroscopy, it is very challenging to calculate the photodetachment cross section theoretically and hence, it will not be attempted in this thesis. The description of photodetachment cross sections in this thesis will be, therefore, qualitative. In order to analyze how  $\sigma$  comes to play in the photoelectron intensity, we utilize a similar formalism as the one employed above. Writing the expression for the transition dipole moment ( $\boldsymbol{\mu} = \boldsymbol{\mu}_{\text{electronic}} + \boldsymbol{\mu}_{\text{nuclear}}$ ) expectation value, we obtain:

$$\begin{aligned}
 P &\equiv \langle \psi_{tot,final} | \boldsymbol{\mu} | \psi_{tot,initial} \rangle \\
 &= \underbrace{\int_{\text{all space}} d\tau \psi_{e,final}^* \boldsymbol{\mu}_e \psi_{e,initial}}_{\equiv \sigma} \underbrace{\int_{\text{all modes}} dq \psi_{v,final}^* \psi_{v,initial}}_{\text{FCF}} \underbrace{\int_{\text{spin states}} ds \psi_{s,final}^* \psi_{s,initial}}_{\text{spin selection rule}}
 \end{aligned}$$

+ vanishing terms (1.14) CHECK

which can be simplified as:

$$P = \sigma \times \text{FCF} \times \delta_{i,i\pm 1/2} \quad (1.15)$$

Here, the overall transition probability is a product of the photodetachment cross section (electronic), the FCF (vibrational) and the spin selection rule, represented as a Kronecker delta function which determines whether or not the transition is allowed. The spin selection rule will be described in the later sections. In this section we focus on photodetachment cross sections and how they vary, and how they play a role in the analysis of photoelectron spectra.

Photodetachment cross sections vary depending on the orbital from which the electron is removed in the photodetachment event. As an example, removing an electron from a larger outer orbital of the molecule will likely have a larger detachment cross section when compared to removing an electron from an inner, smaller orbital. In photoelectron spectroscopy, different electronic states of a neutral molecule are accessed from the anion when the electrons are detached from different orbitals. Hence, different electronic states of the neutral that are produced in this process will have distinct cross sections. Generally, for a specific electronic state, we consider that  $\sigma$  is constant and that the intensity of the transitions observed in the photoelectron spectra are reasonably accounted for with the FC factor. There are, however, a few situations where this approximation breaks down. The first and foremost exception is the behavior of the photodetachment cross section close to detachment threshold ( $h\nu \approx EA$ ), as described in the following paragraphs. There are other less often observed situations where the photodetachment cross sections vary as a function of the photon energy utilized. For those, a description will be provided in the individual chapters that compose this thesis, whenever such description is appropriate.

The behavior of photoelectron cross sections close to detachment threshold was initially described by Eugene Wigner in 1948 for atomic systems and is known as the Wigner threshold law:<sup>11</sup>

$$\sigma \propto (eKE)^{\ell+\frac{1}{2}} \quad (1.16)$$

where  $\ell$  is the orbital angular momentum quantum number of the outgoing electron. To clarify this point, when the photon is absorbed by the electron, the angular momentum the photon ( $\ell=1$ ) is added to that of the electron. The outgoing electron, therefore, possesses  $|\ell_{final}| = |\ell_{initial}| \pm 1$ . As an example, if the initial electron has  $\ell=0$ , *i.e.* is located in an s-orbital, the outgoing electron will have  $\ell=1$ , being detached as a p-orbital, or a p-wave. Equation 1.16 shows that if the  $eKE$  tends to zero, the cross section also tends to zero, at a rate that is proportional to the exponent  $\ell + 1/2$ . The exponent of the expression above being a function of  $\ell$  leads to different electronic states having different behavior close to threshold. This phenomenon can be utilized to probe from what type of orbital the photoelectron originated.

Another way of determining the nature of the electronic states from which the photoelectrons originate is by examining the photoelectron angular distributions. Depending on the orientation of the molecules with respect to the electric field vector of the photons, the oscillation of the electron density in that molecule's orbitals can result in detachment in a preferential direction. This preferred direction with respect to the light's electric field is denoted the angular distribution of the photoelectrons. Experimentally, the angular distributions of the photoelectrons can be detected, once an axis of orientation is defined. This is accomplished by defining a polarization state of the photons. For the example above of an electron at an initial state with  $\ell=0$ , the outgoing p-wave will be detected as a photoelectron angular distribution

perpendicular to the laser polarization vector. If the electron is initially in a p-orbital ( $\ell=1$ ), the outgoing wave can either be an s-wave ( $\ell=0$ ) or a d-wave ( $\ell=2$ ), the photoelectron angular distribution is detected as parallel to the laser polarization vector. The photoelectron angular distribution was modelled by Cooper and Zare in a seminal paper in 1968,<sup>12</sup> and is characterized by the anisotropy parameter  $\beta$ . If we describe the intensity of the photoelectrons (photoelectron counts) as a function of angle relative to the laser polarization, we can express it by the functional form below:

$$I(\theta) = \frac{\sigma}{4\pi} \left( 1 + \frac{\beta}{2} (1 + 3 \cos^2 \theta) \right); -1 \leq \beta \leq 2 \quad (1.17)$$

where  $\sigma$  is the photodetachment cross section and  $\beta$  is the anisotropy parameter. By fitting the above expression to the observed photoelectron angular distribution one can obtain the  $\beta$  value for those photoelectrons. There are three important values of  $\beta$  that deserve attention. When  $\beta = -1$ , the detachment is parallel to the laser polarization vector, when  $\beta = 2$ , the detachment is perpendicular to the polarization vector and when  $\beta = 0$  the detachment is isotropic, *i.e.* equal photoelectron intensity is observed regardless of its orientation with respect to the polarization vector. Besides the limiting values of  $\beta$  described above, the angular distribution varies as a function of the electron's kinetic energy. The modelling of  $\beta$  as a function of eKE is also described for atoms in the paper by Cooper and Zare.<sup>12</sup> For hydrogenic orbitals, the  $\beta(\text{eKE})$  can be derived analytically and its functional form is depicted below in Fig. 1.5, where the  $\beta(\text{eKE})$  for a mixed *s-p* orbital is plotted for several values of a parameter  $Z$ , which describes the ratio between *s* and *p* orbital character (see section 3.3.b. for more detail). For molecules, where the molecular orbital formalism has to be utilized,  $\beta(\text{eKE})$  takes more complicated forms. A great amount of work on modelling angular distributions for molecules was done by Sanov and

coworkers and is extensively discussed in Refs. 13–16 and in Chapter 3. Since electrons originating from different orbitals can have distinct angular distributions, the measurement of  $\beta$  is a powerful tool for identifying electronic states of the neutral molecule and will be extensively utilized throughout this thesis for that purpose.

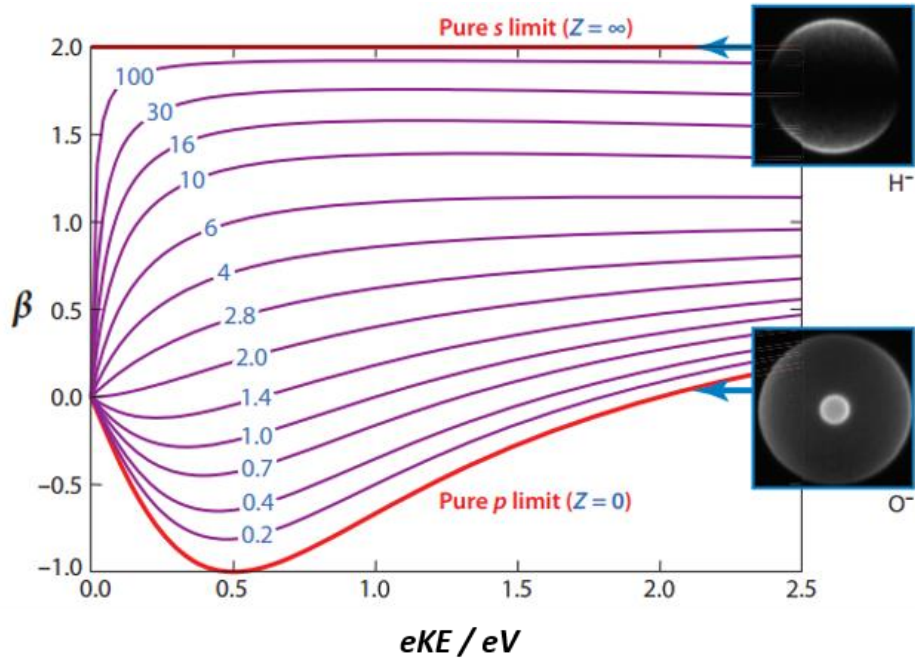


Figure 1.5: Behavior of photoelectron angular distributions for the cases of detachment from several  $s$ - $p$  mixed states, varying as a parameter defined as  $Z$  (see chapter 3), which describes the ratio between  $s$  and  $p$  orbital character. Detachment from pure  $s$ -orbital ( $H^-$ ) and a pure  $p$ -orbital ( $O^-$ ) are exemplified by the red traces. The figure is reproduced from a review by Sanov<sup>14</sup> with some modification.

### 1.3 Photoelectron versus other spectroscopic techniques

Now that the theoretical framework for understanding photoelectron spectroscopy is laid out, we can compare and contrast it to other spectroscopic techniques.

The first aspect of photoelectron spectroscopy that is unique with respect to other techniques is the fact that the use of a single photon energy (or wavelength) can result in the acquisition of a full spectrum. Techniques such as absorption spectroscopy, being performed in the ultraviolet or the infrared, require that the wavelength be scanned so that the light frequency and the molecular vibration are in resonance. Photoelectron spectroscopy, on the other hand, gives a full spectrum of the molecule with a single frequency of light, since the discrete vibrational levels in an electronic state result in discrete values of kinetic energy that the electrons are allowed to have, provided the photon energy is large enough to access these states. Being able to utilize a single color is practically advantageous, since a single frequency laser, rather than a broadband light source, can be utilized to obtain the full spectrum. Thus, one can obtain a full vibrational spectrum of the molecule while still taking advantage of the special properties of laser light, such as high peak power, narrow linewidths and short pulses.

The other major distinction relates to the spin selection rules. While in absorption spectroscopy we have  $\Delta S = 0$  for the spin selection rule, in photoelectron spectroscopy  $\Delta S = \pm 1/2$ . This is easily understood by noticing that, upon photodetachment, a single electron is lost. Since electrons have fractional quanta of spin angular momenta, the loss of an electron requires change of  $\pm 1/2$  in the spin state of the molecule (see Eq. 1.15). This selection rule is of major importance and contrasts to other spectroscopic techniques, since either the anion or the neutral state has to be an open shell radical. This brings us to one of the greatest advantages of

photoelectron spectroscopy when compared to other spectroscopic techniques: The ability to study radicals.

Radicals are chemical species with an unpaired electron which will rapidly react in order to fill the orbital vacancy. With very few exceptions such nitric oxide (NO), these species are extremely reactive and therefore unstable, posing a great difficulty to performing isolated studies on them. This difficulty comes at a significant cost, since radicals play a major role in chemical reactivity, from astrochemical, atmospheric and combustion, to biological and polymer chemistries.<sup>17</sup> Knowing the relative energies of radicals and their reactivity is of utmost importance to the fields of chemical kinetics and dynamics, from gas phase to biological processes. In photoelectron spectroscopy, the fact that a neutral radical is unstable is almost irrelevant to the ease of performing the experiment. Provided the anionic form is stable, a spectrum of the neutral will be obtained regardless of its stability.

Another advantage, also related to the stability of the neutral species, is the ability to acquire spectra of transition state species. Briefly, the transition state of a chemical reaction is a particular configuration of the atoms along that reaction coordinate and is defined as the state corresponding to the highest potential energy along this reaction coordinate.<sup>18-20</sup> If the anion wavefunction, when projected onto the neutral surface upon photodetachment, accesses a region of the potential energy surface that contains a transition state, a spectrum of this transition state can be obtained. Transition states are nearly impossible to probe experimentally due to their extremely short lifetimes, but depending on the structure of the corresponding anion, obtaining spectra of transition states can be relatively straightforward. The group of Neumark has done a considerable amount of investigation of transition state species *via* anion photoelectron spectroscopy.<sup>21,22</sup> As a prototypical example, take the reaction between F and H<sub>2</sub>. This reaction

plays a major role in the detailed understanding of chemical reaction dynamics and gave Y.T. Lee the Nobel Prize in chemistry in 1986, together with Dudley Herschbach and John Polanyi.<sup>23</sup> The transition state of this reaction can be probed by photoelectron spectroscopy, since the equilibrium structure of the F–H–H<sup>-</sup> anion has a similar structure as the transition state [F–H–H]<sup>‡</sup>.<sup>24</sup> This shows how powerful photoelectron spectroscopy can be, allowing unique measurements that are unachievable with other spectroscopic techniques.

Finally, as mentioned in section 1.1, anion photoelectron spectroscopy allows for the determination of the electron affinities (EAs) of neutral atoms and molecules. Our research group has provided a major contribution to the scientific endeavor of determining EAs of atoms and small molecules for the past nearly 50 years.<sup>25–30</sup> The knowledge of the EAs of molecules is crucial for understanding chemical reactivity as, similarly to electronegativity, shows how much an atom or molecule “want” an electron. In fact, the EAs were utilized by Robert Millikan to establish the electronegativity scale for atoms. Contrary to the electronegativity of atoms, which is a theoretical value that depends partly on what type of bond the atom is making, the EA can be directly measured and is a much more fundamental quantity having applications in nearly all fields of chemistry (see Ref. 31 and references within). The EA is also an essential part of the thermochemical cycle that results in the measurement of bond strengths, *i.e.* bond dissociation energies ( $D_0$ ) and/or gas phase acidities, *i.e.* gas phase deprotonation enthalpies ( $\Delta_{\text{acid}}H_{0K}^{\circ}$ ).<sup>32</sup> A schematic representation of this thermochemical cycle is depicted below in Fig. 1.6 for the generic acid HA, and expressed arithmetically in equation 1.18.

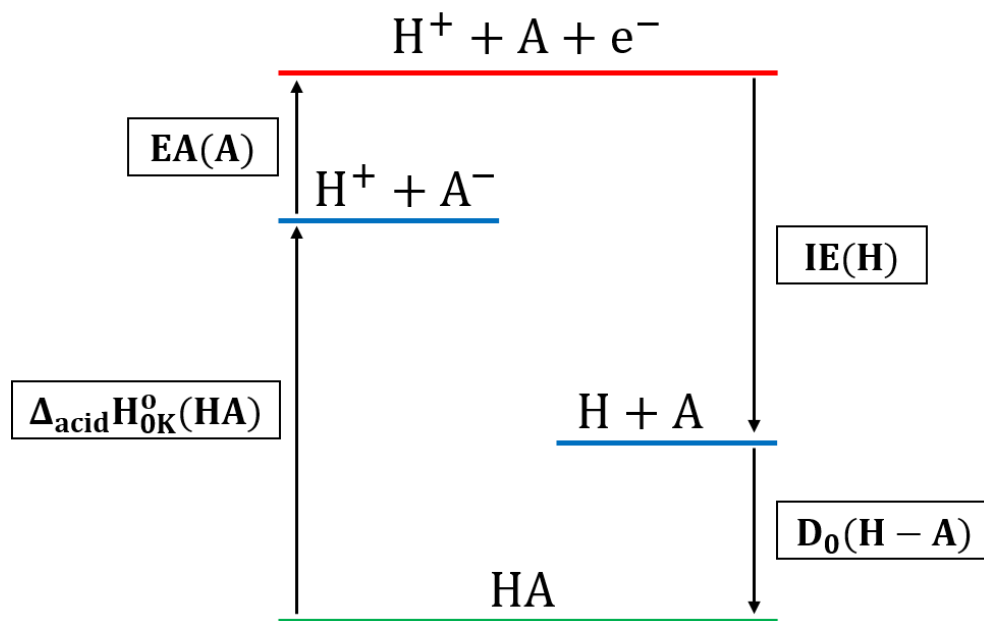


Figure 1.6: Schematic representation of the thermochemical cycle of HA involving the quantities that can be experimentally determined (black boxes), as described in the text.

$$\Delta_{\text{acid}}H_{0\text{K}}^{\circ}(\text{HA}) + \text{EA}(\text{A}) = D_0(\text{H} - \text{A}) + \text{IE}(\text{H}) \quad (1.18)$$

While  $D_0$  can be measured to a high degree of accuracy (often  $< \pm 0.01 \text{ kcal mol}^{-1}$ ),<sup>33</sup> this is not true for gas phase acidities (uncertainties of  $\sim \pm 1 \text{ kcal mol}^{-1}$ ),<sup>34</sup> since its measurement depends on the determination of deprotonation equilibrium constants or acid bracketing with other known acids.<sup>35,36</sup> Hence, a precise determination of the EAs (often  $< \pm 0.1 \text{ kcal mol}^{-1}$ ) can significantly improve the precision and accuracy of measurements of  $\Delta_{\text{acid}}H_{0\text{K}}^{\circ}$ , provided the values for  $D_0$  are known.

Throughout this thesis, we will explore these characteristics of photoelectron spectroscopy in order to study exotic neutral species that are of relevance to fundamental physical chemistry, atmospheric science, combustion chemistry, astrochemistry and biochemistry. The individual chapters are heavily based on peer reviewed published articles with some minor modifications.

## 1.4 Overview of the thesis

In this thesis, we explore the capabilities of photoelectron spectroscopy and its application to small molecular anions. The anions studied here are generated in a dual-valve plasma entrainment pulsed anion source (described in detail in Chapter 2). As a majority, the anions are produced in ion-molecule association reactions in the gas phase, a characteristic that is unique to this source. The thesis then expands upon the experiments described in the Ph.D. thesis of Yu-Ju Lu,<sup>37</sup> a previous graduate student in the group, and Ref. 38, in investigating the capabilities of this source.

A description of the experimental techniques and theoretical methods that were employed throughout this work are presented in Chapter 2. After that, Chapter 3 investigates the

photoelectron spectroscopy of the methide anion ( $\text{CH}_3^-$ ), as illustrated in the graphic displayed in Fig. 1.7. This chapter will show how a precise determination of the EA of  $\text{CH}_3$  can drastically improve the knowledge of the  $\Delta_{\text{acid}}\text{H}_{0\text{K}}^0$  of methane ( $\text{CH}_4$ ), which defines the acidity scale of hydrocarbons in the gas phase.<sup>39</sup> The photoelectron spectrum of  $\text{CH}_3^-$  also enables the first experimental measurement of the umbrella-mode inversion splitting. This project, conducted in collaboration with theorists Professor John F. Stanton, Dr. Joshua H. Baraban and P. Bryan Changala, contributes to the fundamental knowledge of the simplest carbanion employing state-of-the-art high-level theoretical methods.

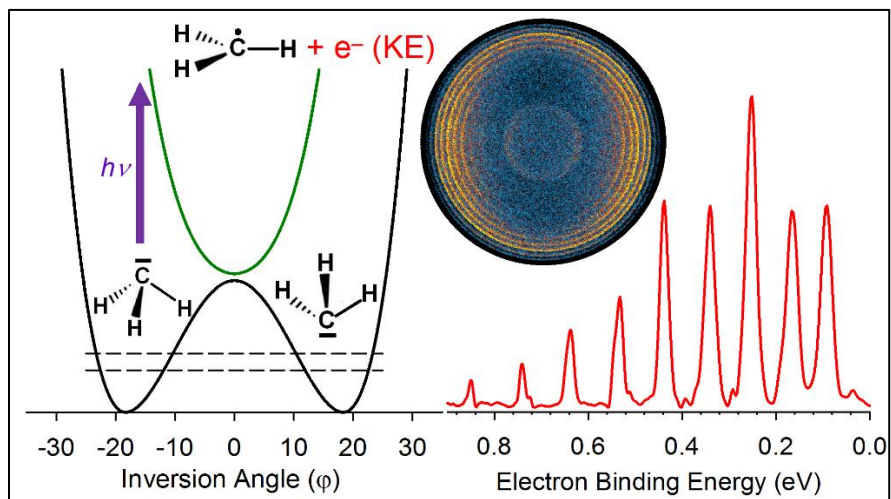


Figure 1.7: Potential and spectra representative of the photoelectron spectroscopic investigation of the methide anion. This figure is reproduced with permission from Oliveira *et al.*<sup>40</sup>

In Chapter 4, we investigate the photoelectron spectroscopy of  $\text{HONO}^-$ , the anion of nitrous acid (HONO), an important atmospheric molecule.<sup>41-47</sup> There, we will employ photoelectron spectroscopy to determine the EA of HONO, which allows for the measurement of the  $\text{HO}^-$ -NO bond dissociation energy through a thermochemical cycle similar to the one described above. The photoelectron spectrum of  $\text{HONO}^-$  takes advantage of the special spin selection rules of photoelectron spectroscopy to access the triplet state of HONO *via* the doublet anion, providing the first experimental measurement of the triplet state term energy. The projection of the anionic wavefunction onto the triplet state surface accesses the transition state of triplet HONO as it dissociates to  $\text{HO} + \text{NO}$ . This shows the advantage of photoelectron spectroscopy in obtaining spectra of transition states. The summary of this work is depicted below in Fig. 1.8, showing the structured singlet ground state ( $S_0$  in red) and the dissociative triplet state ( $T_1$  in blue).

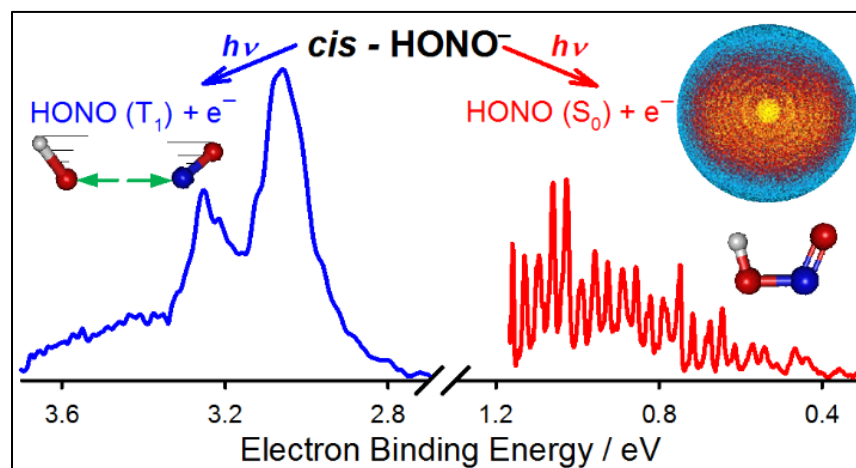


Figure 1.8: Summary of the work reported in Chapter 4 depicting photodetachment of  $\text{HONO}^-$ , accessing the singlet and triplet electronic states of HONO and their behavior as they are formed *via* photodetachment of the  $\text{HONO}^-$  anion. This figure is reproduced with permission from Oliveira *et al.*<sup>48</sup>

In Chapters 5 and 6 we investigate the electronic structure of singly substituted alkoxy radicals ( $\text{H}_2\text{C}(\text{R})\text{O}$ ) *via* the photoelectron spectra of hydroxymethoxide ( $\text{H}_2\text{C}(\text{OH})\text{O}^-$ ) and aminomethoxide ( $\text{H}_2\text{C}(\text{NH}_2)\text{O}^-$ ), respectively. Expanding upon previous studies performed in our group regarding the small alkyl substituted alkoxy radicals,<sup>49</sup> we compare the measured EAs and  $T_0$  of these radicals, associating these values to the intramolecular interactions between the substituting R group and the oxygen atom, as depicted below in Fig. 1.9. The results take advantage of the measurement of the photoelectron angular distributions to identify the electronic states and provide vibrational frequencies of these radicals. The measured EAs are coupled to calculations of the gas phase acidities of the associated acids, methanediol ( $\text{H}_2\text{C}(\text{OH})_2$ ) and aminomethanol ( $\text{H}_2\text{C}(\text{NH}_2)\text{OH}$ ) to provide the O–H bond dissociation energies of these astrochemically and prebiotically relevant species.<sup>50–52</sup>

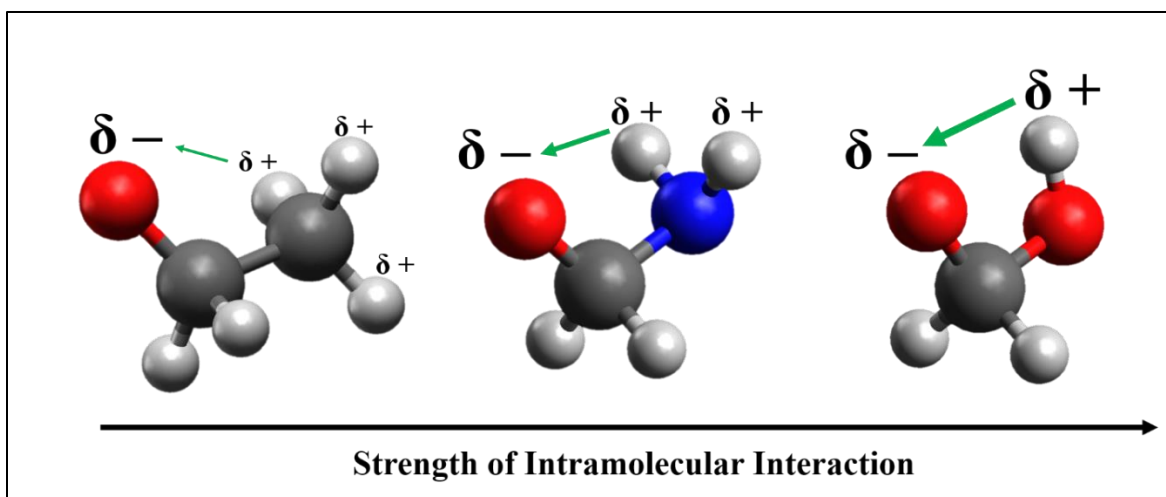
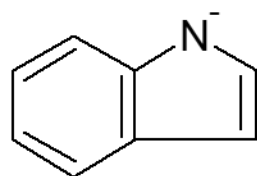
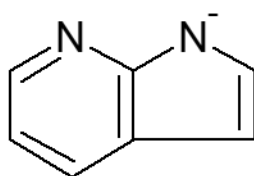


Figure 1.9: Intramolecular interaction trend of singly substituted alkoxy radicals as described in Chapters 5 and 6. This figure shows the increasing strength of the intramolecular interactions in singly substituted alkoxy radicals, from the left: ethoxy, aminomethoxy and hydroxymethoxy.

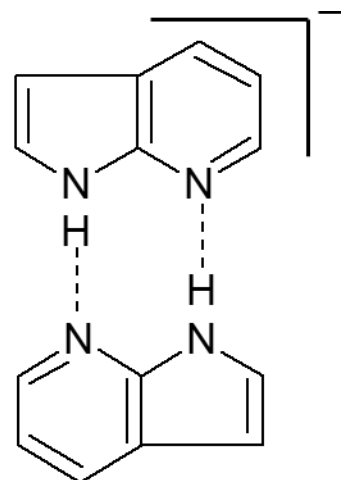
In Chapter 7, we switch gears to investigate a larger polycyclic aromatic molecule: Deprotonated 7-azaindole (7-azaindolate) and the 7-azaindole dimer (Fig. 1.10). 7-azaindole and its dimer are very relevant to the field of biochemistry and biophysics due to its analogous structure and pairing properties to Watson-Crick nucleobases, such as Adenine and Thymine. In our experiment we are able to measure the EA of the corresponding 7-azaindolate radical. Drawing a comparison with the photoelectron spectrum of indolate (also shown in Fig. 1.10), we show how a single isoelectronic substitution can drastically change the behavior of a large rigid molecule by severely affecting its electronic structure. A dramatic increase in dipole moment, from indole ( $\sim 2.5$  Debye) to 7-azaindole ( $\sim 4.6$  Debye) results in electron autodetaching transitions, that are likely accessible through a high density of dipole bound states in 7-azaindolate. This leads to a photoelectron spectrum which behaves in a very unexpected manner, where most of the intensity of the transitions is not due to direct photodetachment, but due to electron autodetachment. This interesting feature led us to seek the collaboration of Professor John Stanton for theoretical calculations and Professor Lai Shen Wang for experiments on autodetaching dipole bound states.



Indolide



7-azaindolide



7-azaindole dimer anion

Figure 1.10: Chemical structures of deprotonated indole (indolide), deprotonated 7-azaindole (7-azaindolide) and (7-azaindole)<sub>2</sub><sup>-</sup> anion.

Although a complete description of 5+ arduous years in the lab is a nearly impossible feat, this thesis hopes to summarize the major contributions I have made to the field of chemistry and let those be accessible to scientists for many years to come.

## 1.5 Chapter 1 references

- <sup>1</sup> A. Einstein, “for His Services to Theoretical Physics, and Especially for His Discovery of the Law of the Photoelectric Effect,” Nobel Prize in Physics, 1921.
- <sup>2</sup> H. Hertz, *Ann. Phys.* **267**, 983 (1887).
- <sup>3</sup> U.D. Jentschura, S. Kotochigova, E.O. LeBigot, P.J. Mohr, and B.N. Taylor, *The Energy Levels of Hydrogen and Deuterium (Version 2.1)*, National Institute of Standards and Technology, Gaithersburg, MD, available online at <http://physics.nist.gov/PhysRefData/HDEL/energies.html>, 2017.
- <sup>4</sup> K.R. Lykke, K.K. Murray, and W.C. Lineberger, *Phys. Rev. A* **43**, 6104 (1991).
- <sup>5</sup> I.N. Levine, *Quantum Chemistry* (Pearson Prentice Hall, 2009).
- <sup>6</sup> E.B. Wilson, J.C. Decius, and P.C. Cross, *Molecular Vibrations : The Theory of Infrared and Raman Vibrational Spectra* (Dover Publications, 1980).
- <sup>7</sup> D.C. Harris and M.D. Bertolucci, *Symmetry and Spectroscopy : An Introduction to Vibrational and Electronic Spectroscopy* (Dover Publications, 1989).
- <sup>8</sup> C.T. Wickhamjones, K.M. Ervin, G.B. Ellison, and W.C. Lineberger, *J. Chem. Phys.* **91**, 2762 (1989).
- <sup>9</sup> S. Zhou, Z. Li, D. Xie, S.Y. Lin, and H. Guo, *J. Chem. Phys.* **130**, 184307 (2009).
- <sup>10</sup> C. Hock, J.B. Kim, M.L. Weichman, T.I. Yacovitch, and D.M. Neumark, *J. Chem. Phys.* **137**, 244201 (2012).
- <sup>11</sup> E.P. Wigner, *Phys. Rev.* **73**, 1002 (1948).
- <sup>12</sup> J. Cooper and R.N. Zare, *J. Chem. Phys.* **48**, 942 (1968).
- <sup>13</sup> E.R. Grumbling and A. Sanov, *J. Chem. Phys.* **135**, 164302 (2011).
- <sup>14</sup> A. Sanov, *Annu. Rev. Phys. Chem.* **65**, 341 (2014).
- <sup>15</sup> R. Mabbs, E.R. Grumbling, K. Pichugin, and A. Sanov, *Chem. Soc. Rev.* **38**, 2169 (2009).
- <sup>16</sup> A. Sanov, E.R. Grumbling, D.J. Goebbert, and L.M. Culberson, *J. Chem. Phys.* **138**, 54311 (2013).
- <sup>17</sup> A.F. Parsons, *An Introduction to Free-Radical Chemistry* (Blackwell Science, 2000).
- <sup>18</sup> K.J. Laidler and M.C. King, *J. Phys. Chem.* **87**, 2657 (1983).

- <sup>19</sup> D.G. Truhlar, *J. Phys. Chem.* **87**, 2664 (1983).
- <sup>20</sup> D.G. Truhlar, B.C. Garrett, and S.J. Klippenstein, *J. Phys. Chem.* **100**, 12771 (1996).
- <sup>21</sup> D.M. Neumark, *Acc. Chem. Res.* **26**, 33 (1993).
- <sup>22</sup> M.L. Weichman, J.A. DeVine, M.C. Babin, J. Li, L. Guo, J. Ma, H. Guo, and D.M. Neumark, *Nat. Chem.* **9**, 950 (2017).
- <sup>23</sup> D.R. Herschbach, Y.T. Lee, and J.C. Polanyi, “for Their Contributions Concerning the Dynamics of Chemical Elementary Processes,” Nobel Prize in Chemistry, 1986.
- <sup>24</sup> J.B. Kim, M.L. Weichman, T.F. Sjolander, D.M. Neumark, J. Klos, M.H. Alexander, and D.E. Manolopoulos, *Science* **349**, 510 (2015).
- <sup>25</sup> T.A. Patterson, H. Hotop, A. Kasdan, D.W. Norcross, and W.C. Lineberger, *Phys. Rev. Lett.* **32**, 189 (1974).
- <sup>26</sup> A. Kasdan and W.C. Lineberger, *Phys. Rev. A* **10**, 1658 (1974).
- <sup>27</sup> W.C. Lineberger and B.W. Woodward, *Phys. Rev. Lett.* **25**, 424 (1970).
- <sup>28</sup> H. Hotop and W.C. Lineberger, *J. Phys. Chem. Ref. Data* **4**, 539 (1975).
- <sup>29</sup> H. Hotop and W.C. Lineberger, *J. Phys. Chem. Ref. Data* **14**, 731 (1985).
- <sup>30</sup> J.H. Lehman and W.C. Lineberger, *J. Chem. Phys.* **147**, 13943 (2017).
- <sup>31</sup> P. Kebarle and S. Chowdhury, *Chem. Rev.* **87**, 513 (1987).
- <sup>32</sup> S.J. Blanksby, T.M. Ramond, G.E. Davico, M.R. Nimlos, S. Kato, V.M. Bierbaum, W.C. Lineberger, G.B. Ellison, and M. Okumura, *J. Am. Chem. Soc.* **123**, 9585 (2001).
- <sup>33</sup> B. Ruscic, *J. Phys. Chem. A* **119**, 7810 (2015).
- <sup>34</sup> K.M. Ervin and V.F. DeTuro, *J. Phys. Chem. A* **106**, 9947 (2002).
- <sup>35</sup> C.H. DePuy and V.M. Bierbaum, *Acc. Chem. Res.* **14**, 146 (1981).
- <sup>36</sup> C.H. DePuy, J.J. Grabowski, and V.M. Bierbaum, *Science* **218**, 955 (1982).
- <sup>37</sup> Y.-J. Lu, Photoelectron Spectroscopy of Small Organic Anions Prepared Using a Novel Cold Ion Source Employing Entrainment of Charged Particles, University of Colorado - Boulder, 2014.
- <sup>38</sup> Y.-J. Lu, J.H. Lehman, and W.C. Lineberger, *J. Chem. Phys.* **142**, 44201 (2015).
- <sup>39</sup> C.H. DePuy, S. Gronert, S.E. Barlow, V.M. Bierbaum, and R. Damrauer, *J. Am. Chem. Soc.* **111**, 1968 (1989).
- <sup>40</sup> A.M. Oliveira, Y.J. Lu, J.H. Lehman, P.B. Changala, J.H. Baraban, J.F. Stanton, and W.C. Lineberger, *J. Am. Chem. Soc.* **137**, 12939 (2015).
- <sup>41</sup> A. Indarto, *Res. Chem. Intermed.* **38**, 1029 (2012).
- <sup>42</sup> D.G. Aubin and J.P.D. Abbatt, *J. Phys. Chem. A* **111**, 6263 (2007).

- <sup>43</sup> V. Bartolomei, M. Sorgel, S. Gligorovski, E.G. Alvarez, A. Gandolfo, R. Strekowski, E. Quivet, A. Held, C. Zetzsch, and H. Wortham, *Environ. Sci. Pollut. Res.* **21**, 9259 (2014).
- <sup>44</sup> R. Kurtenbach, K.H. Becker, J.A.G. Gomes, J. Kleffmann, J.C. Lorzer, M. Spittler, P. Wiesen, R. Ackermann, A. Geyer, and U. Platt, *Atmos. Environ.* **35**, 3385 (2001).
- <sup>45</sup> B. Alicke, U. Platt, and J. Stutz, *J. Geophys. Res.* **107**, 9 (2002).
- <sup>46</sup> J. Kleffmann, T. Gavriloaiei, A. Hofzumahaus, F. Holland, R. Koppmann, L. Rupp, E. Schlosser, M. Siese, and A. Wahner, *Geophys. Res. Lett.* **32**, 5818 (2005).
- <sup>47</sup> B.J. Finlayson-Pitts and J.N. Pitts, *Chemistry of the Upper and Lower Atmosphere : Theory, Experiments, and Applications* (Academic Press, San Diego, 2000).
- <sup>48</sup> A.M. Oliveira, J.H. Lehman, A.B. McCoy, and W.C. Lineberger, *J. Phys. Chem. A* **120**, 1652 (2016).
- <sup>49</sup> T.M. Ramond, G.E. Davico, R.L. Schwartz, and W.C. Lineberger, *J. Chem. Phys.* **112**, 1158 (2000).
- <sup>50</sup> F. Duvernay, A. Rimola, P. Theule, G. Danger, T. Sanchez, and T. Chiavassa, *Phys. Chem. Chem. Phys.* **16**, 24200 (2014).
- <sup>51</sup> B.M. Hays and S.L.W. Weaver, *J. Phys. Chem. A* **117**, 7142 (2013).
- <sup>52</sup> F. Duvernay, G. Danger, P. Theule, T. Chiavassa, and A. Rimola, *Astrophys. J.* **791**, 75 (2014).

*this page is intentionally left blank*

## CHAPTER II

### EXPERIMENTAL AND THEORETICAL METHODS

#### 2.1 Experimental Methods

##### 2.1.a Overview of the instrument

The instrument utilized in the experiments described in this thesis is a Time-of-Flight (TOF) mass spectrometer/Velocity-map Imaging (VMI) anion photoelectron spectrometer. In this section the instrument will be described in detail. For that, a schematic representation of the photoelectron instrument is shown in Fig. 2.1. This figure includes imaginary divisions of this instrument for pedagogical purposes.

Region 1 represents the ion generation region, where the anions of interest will be produced. Practically, the ion source chamber is kept at a pressure of  $\sim 10^{-6}$  Torr, rising to  $\sim 5.0 \times 10^{-5}$  Torr when both valves are operational. The pressure in this chamber is achieved by way of a 12-inch outer diameter oil diffusion pump. Region 2 comprises the Wiley-McLaren time-of-flight mass spectrometer and the ion focusing electrostatic elements. The region that encompasses the ion focusing elements and the acceleration stack (see section 2.1.c) contains two differential pumping apertures, which, by way of two additional oil diffusion pumps, the pressure is brought down from  $\sim 10^{-5}$  Torr in the source region, to  $\sim 10^{-7}$  Torr. Region 3 represents the light source, *i.e.* the laser systems utilized for the photodetachment experiment. Finally, region 4 represents the velocity-map imaging photoelectron spectrometer, where the photoelectrons are detected. This final segment of the instrument, which includes the inline microchannel plate (MCP) detector, is evacuated by two turbomolecular pumps that reduce the

pressure by another order of magnitude, resulting in operating pressures of  $\sim 10^{-8}$  Torr. A cold trap in this region, which can be filled with liquid nitrogen, brings the pressure down to  $\sim 10^{-9}$  Torr. In the following sections each of these regions, and the apparatus that compose them, will be individually described in detail.

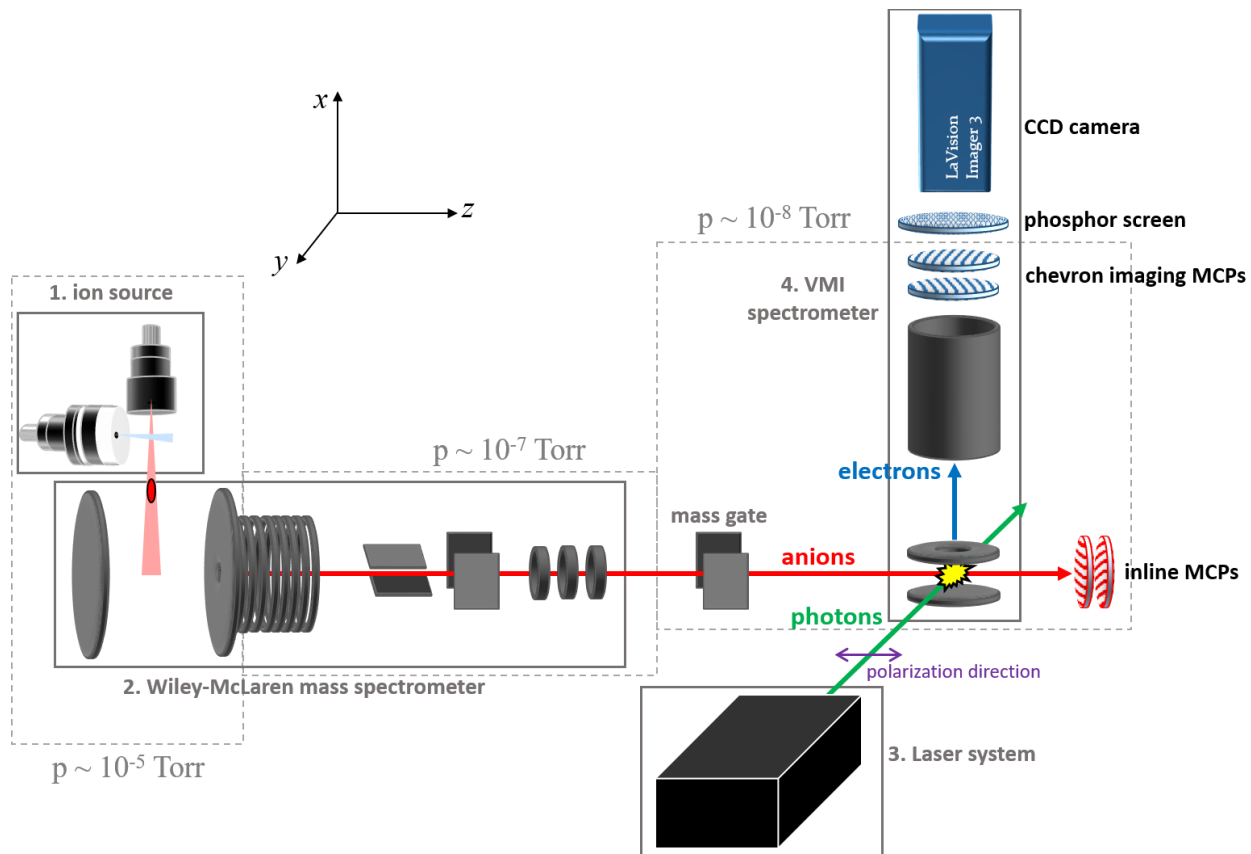


Figure 2.1: Schematic representation of the photoelectron spectrometer. The gray boxed regions numbered 1 through 4 represent imaginary divisions of the instrument created for explanatory purposes, as described in sections 2.1.b through 2.1.e in the text.

### 2.1.b Ion Source

The research reported in this thesis makes use of the dual valve plasma entrainment ion source developed in the group during the past five years. This ion source has been described previously in an original journal article<sup>1</sup> and the Ph.D. dissertation of Yu-Ju Lu,<sup>2</sup> so a similar description will be provided here. In addition, some minor modifications were made and will be reported here.

In Chapter 1, we examined the photoelectron spectroscopic technique and highlighted the advantages it has over other spectroscopies. One of these advantages is the ability to study unstable exotic radicals, provided the corresponding anion is stable and can be produced. The method by which the anions are formed have major implications to the nature of these ions. The choice of a specific ion source puts constraints on what types of anions can be formed, what the temperature of these anions can be, and how practical, experimentally, is the production of these anions. Thus, one of the tasks of the experimentalist is to choose the proper ion source in order to obtain the desired attributes appropriate for the experiment in question. We generate gas phase ions, so that the isolated study of individual molecules *via* photodetachment can be achieved. The temperature of these anions is also a principal attribute with which we are concerned, as a lower temperature facilitates the interpretation of the spectra, a consequence of the reduced intensity of vibrational hot bands (see Chapter 1). A lower temperature also enables the formation of anions that are less stable with respect to electron detachment, as it diminishes the detachment *via* vibrational excitation and/or energetic collisions with other species present in the source region. This is crucial for the formation of weakly bound anions, such as methide ( $\text{CH}_3^-$ ) and  $\text{HONO}^-$ , as described in Chapters 3 and 4, respectively. Finally, for the experiments we

desire to accomplish, the capability of rationally synthesizing anions in the gas phase (in loose terms: “doing chemistry”) is an important feature that the ion source should enable us to perform.

The ion source consists of two orthogonally oriented pulsed General Valves (Parker-Hannifin Series 9), as depicted in Fig. 2.2. Of these valves, we designate the one that is perpendicular to the ion trajectory in the WM-TOF the main valve or main expansion. This main valve produces a supersonic expansion of a buffer gas, which is primarily argon. The supersonic expansion allows for adiabatic cooling that quickly decreases the rotational temperature of the molecules in the expansion. Supersonic expansions, such as this one have been extensively utilized in molecular beam and spectroscopic experiments.<sup>3-6</sup> Perpendicular to this expansion, we place another pulsed valve equipped with a pair of electrodes attached to its faceplate. This valve is designated “side valve” or “side expansion” and it accounts for approximately 10% of the total pressure rise in the vacuum chamber when both valves are operational. By appropriately timing a pulsed negative voltage (see individual chapters for specific voltages) to the front electrode when the gas flow takes place, we create a glow discharge that generates a plasma. The plasma breaks apart the neutral species in the gas expansion into electrons, cations and anions, in addition to neutral species and radicals. Discharge sources have been utilized in the past for the generation of metal anions and exotic species with great success.<sup>7-10</sup> However, the plasma usually forms extremely hot species, which results in substantial spectral congestion due to hot bands.

Here is where the specific operating conditions of this source play a major role. The first condition is that the tension of the springs inside the side valve are set such that the side expansion operates in a choked effusive flow condition. In this way, the charged species that compose the plasma stick together (ambipolar diffusion<sup>11</sup>) while the hot neutral species quickly disperse, avoiding unnecessary heating of the main beam. When this plasma “bullet” is picked up

by – or entrained in – the main supersonic expansion, the high density of buffer gas provides collisional cooling to stabilize the formed ionic products. The orthogonal crossing of the plasma beam and the main expansion also minimizes the interaction between the hot species in the discharge and the cold buffer gas in the main expansion. In this manner, not only the rotational temperature decreases, but the vibrational temperature as well.<sup>1</sup>

One of the consequences of vibrational cooling is that very large clusters can be formed. As an example, we can generate  $\text{OH}^-(\text{Ar})_n$  clusters with  $n = 40$ . At that point, each Ar atom is only bound by  $\sim 0.01$  eV, which, when converted to a vibrational temperature corresponds to approximately 116 K. That is to say that the internal vibrational temperature of  $\text{OH}^-$  has to be  $< 116$  K, or the argon atoms in the cluster would boil off and dissipate the energy. Another feature that is enabled by the efficient vibrational cooling is that, by introducing a small amount (generally  $< 1\%$ ) of a neutral reagent to the main expansion, we can perform chemical reactions between the ions from the side expansion that are entrained into the main expansion and the neutrals there. The crossed expansions provide a dense, buffer gas rich environment, in which sufficient collisions take place to stabilize the ionic reaction products. This dual valve ion source provides a combination of the advantages of a discharge source, where the hard ionization environment of the plasma enables the formation of unusual species, and the flowing afterglow source.<sup>12-14</sup>

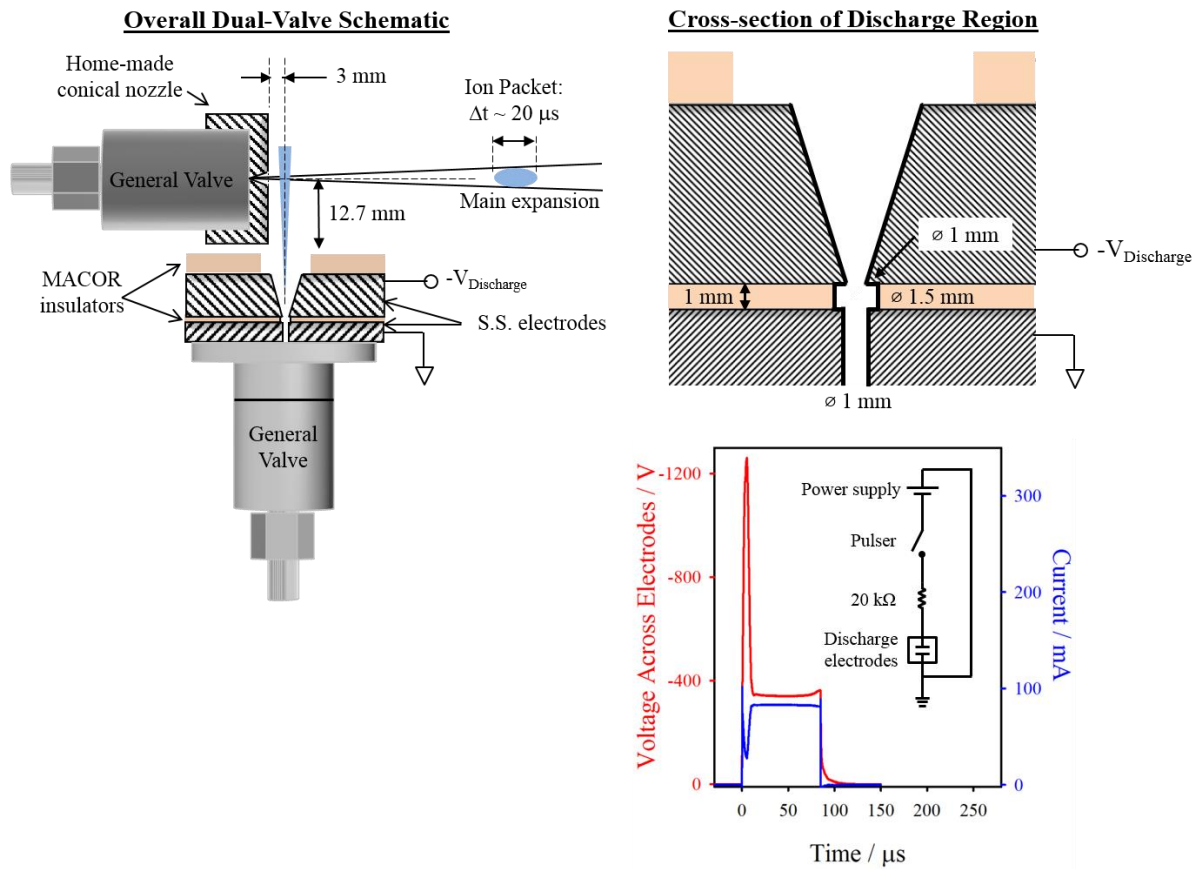


Figure 2.2: Specific design and functional details of the dual valve, plasma entrainment ion source.

This figure is reproduced from Lu *et al.*<sup>1</sup> with some modifications.

During the past 3 years some modifications to the original design were made to expand the capabilities of this ion source. The first one relates to the ability to optimize the formation of large clusters. As mentioned above, the main supersonic expansion is responsible for the cooling and cluster formation that takes place in the source. For that, the conditions of the supersonic expansion are of major importance. By conditions we mean: how dense, collimated and intense is the expansion. In the general valves, these characteristics of the expansion are greatly affected by two factors: The cone angle and aspect ratio on the main faceplate and the tension of the springs inside the valve. A modified faceplate, with a 40° cone angle, 0.5 mm orifice and aspect ratio of 7 was custom made for our applications.<sup>1,2</sup> The second factor, setting the tension on the springs, is easily done by rotating the faceplate, so that the compression on the springs which actuate the main valve solenoid, is changed. While straightforwardly done on a lab bench, this is extremely unpractical when considering that each adjustment requires a breaking of the vacuum in order to access the valve inside the source chamber. To solve this issue, we designed a faceplate holder that enables the adjustment of the tension of the springs from outside the chamber. This adjustment is realized by rotating the valve body, while the faceplate is kept fixed. A picture of this attachment is displayed in Fig. 2.3, which shows a photograph of the dual valve setup as it stands currently.

Cluster size distributions are affected by the temperature of the buffer gas. Therefore, in addition to the above attachment to the main expansion, we also implemented a cooling/heating apparatus to control the temperature of the main valve body. This is fulfilled by an aluminum block that embraces the valve body at a very low clearance. The use of thermally conductive lubricant improves heat transfer between the block and the valve, whose temperature is monitored with a thermocouple. In order to heat the aluminum block, we utilize a polyimide

resistive heater (MINCO). For cooling the block, two procedures can be taken: One is by way of a Peltier device. Another, more efficient strategy that was implemented was that of fluid cooling. For that, the aluminum block was designed in such way that a copper tube can pass through the block in a tight fit. The copper tube extends to the exterior of the chamber where cooling fluid can be flowed through it, which can range from cooled ethylene glycol (down to  $\sim 260$  K,  $-13$  °C), or nitrogen gas at the condensation point ( $\sim 77$  K,  $-196$  °C). This enables a variety of temperatures to be reached, consequently shifting cluster size distributions. An example of this, the formation of ozonide argon clusters ( $\text{O}_3^-(\text{Ar})_n$ ), is depicted below in Fig. 2.4. Controlling the temperature of the main valve also enables the introduction of neutral reagents of low vapor pressure in the main expansion. The ability to heat the main valve body will come to be essential for the introduction of 7-azaindole in the main expansion, as described in Chapter 7.

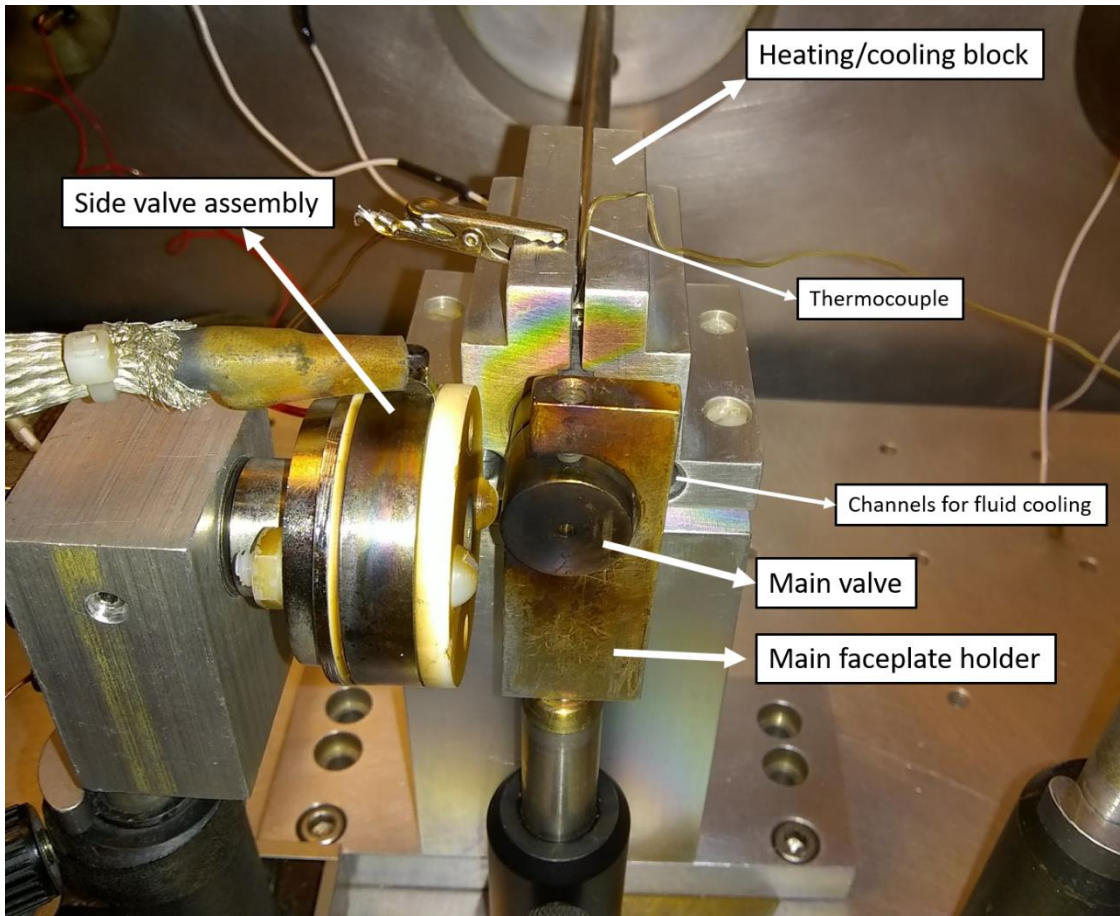


Figure 2.3: Photograph of the dual valve plasma entrainment ion source described in this section. The individual components of the source are labeled accordingly.

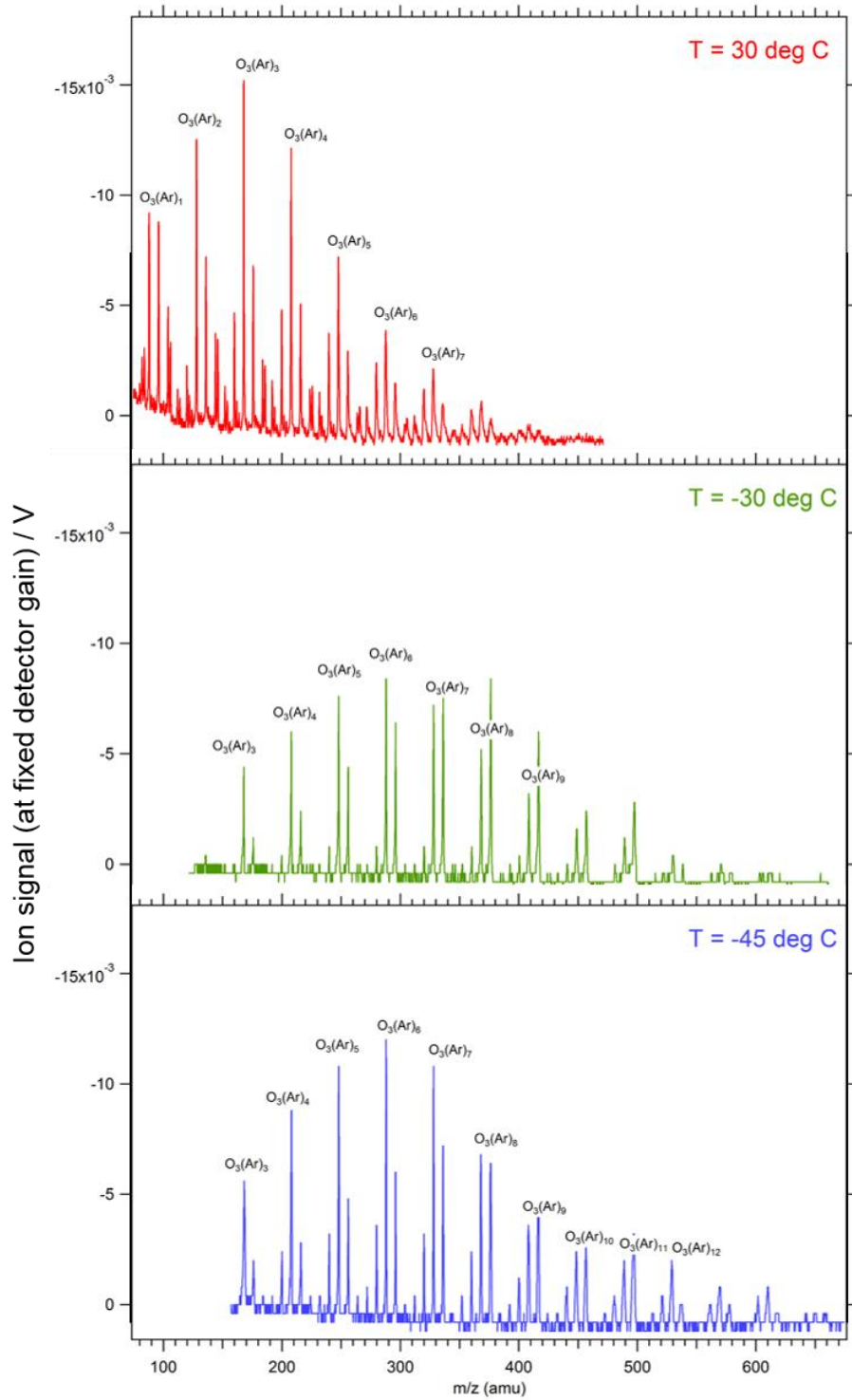


Figure 2.4: Ozonide argon clusters ( $O_3^-(Ar)_n$ ) optimization and cluster size distribution shifts as a function of valve body temperature.

Following their generation, the main expansion carries the formed ions. These ions drift for approximately 20 cm until they reach a set of parallel plates that constitute the first stage of the mass spectrometer. The mass spectrometer is necessary for the separation of the large collection of ions formed in the expansion, so that the photodetachment experiment on individual ions can be performed. The mass spectrometer employed throughout this thesis will be described in the next section.

### *2.1.c Mass Spectrometer*

The dual valve source described in the previous section can generate a large variety of ions. The next stage of the instrument, depicted in Fig. 2.5 represents the Wiley-McLaren time-of-flight (WM-TOF) mass spectrometer<sup>15</sup> that initially removes the neutrals and cations and then separates the anions by their mass-to-charge ratio.

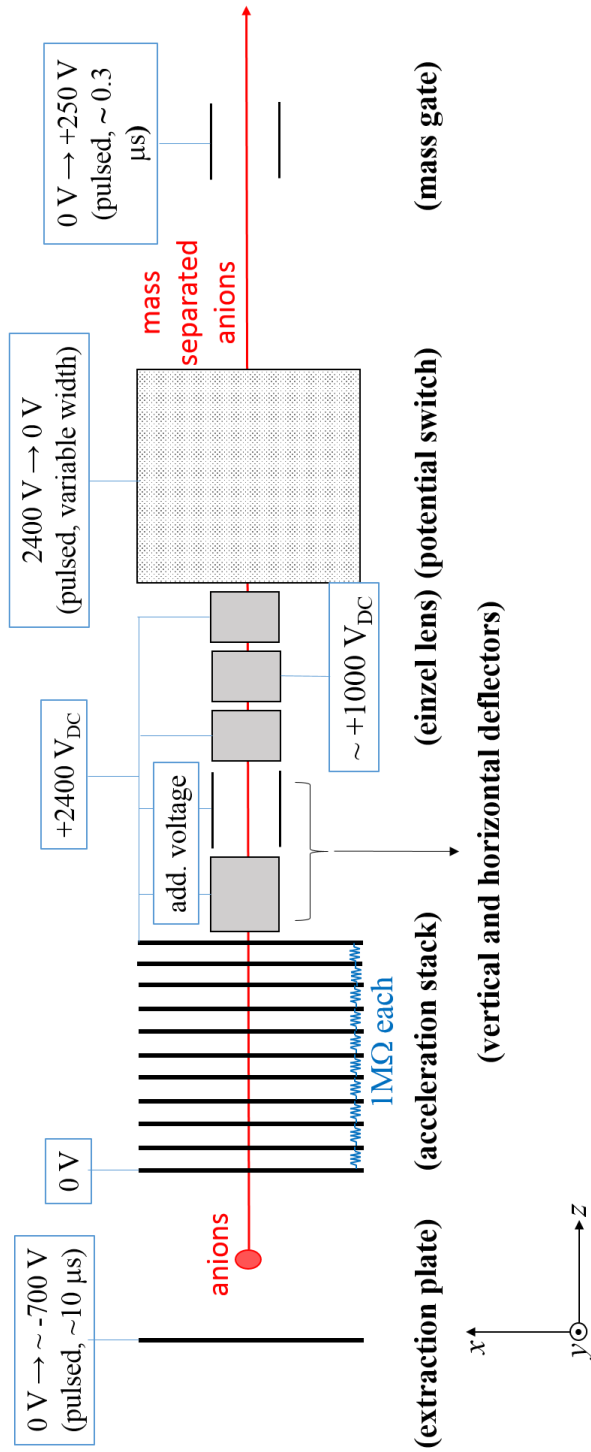


Figure 2.5: Detailed schematic representation of the Wiley-McLaren Time-of-Flight mass spectrometer. The electrostatic elements that compose the flight stack are labeled according to their function in the instrument.

The physical principle of the time-of-flight spectrometer is quite straightforward: By giving all the anions the same kinetic energy ( $E_k$ ), their times of flight (TOF), given a fixed travel distance ( $d$ ), will be different by an amount that is directly proportional to the square root of their mass-to-charge ratio ( $m/z$ ). Starting with the expression for the kinetic energy, we solve for the TOF:

$$E_k = \frac{1}{2}mv^2 \quad (2.1)$$

$$v = \sqrt{\frac{2E_k}{m}} = \frac{d}{TOF} \quad (2.2)$$

$$TOF = d \sqrt{\frac{m}{2E_k}} \quad (2.3)$$

We then utilize the electric potential energy ( $E_{elec}$ ) to which the ions are subject:

$$E_{elec} = E_k = V \times z \quad (2.4)$$

where  $V$  is the electric potential in Volts and  $z$  is the charge of the ion in Coulombs, to obtain:

$$TOF = d \sqrt{\frac{m}{z} \frac{1}{2V}} \quad (2.5)$$

In atomic units, the mass-to-charge ratio ( $m/z$ ) becomes simply the atomic mass of the specific ion, given that the anions are singly charged, ( $z=e$ ). Therefore, we will often refer to the ions  $m/z$  as simply stating the atomic mass of the specific anion in question. As an example, hydroxide anions ( $\text{OH}^-$ ) have  $m/z=17$  atomic mass units (amu).

In our experiment the anions are extracted by a pulsed negative voltage of  $\sim -700$  V and then gradually accelerated by a series of plates up to  $+2300$  V (Fig. 2.5). This gives all anions a kinetic energy of approximately 3000 eV. The Wiley-McLaren (WM) design makes use of the dual stage acceleration in order to provide a greater mass resolution and also control the point where the ions are spatially focused (focused in the  $z$ -direction Fig. 2.1 and 2.5). For a full derivation of the WM focusing conditions see the original work by Wiley and McLaren;<sup>15</sup> however in summary, the ability to control the spatial focus ( $z$ -direction focus) of the ions enables us to choose either the inline ion detector, where the mass spectra are acquired, or the laser interaction region for optimal signal in the VMI spectrometer. Immediately after this acceleration stage, pairs of horizontal and vertical deflectors serve the purpose of steering the ions in a desired direction, by voltages of  $\sim 50$  V above the float potential ( $+2400$  V). Downstream from this point, we utilize an einzel lens to focus the ions in the  $x$ - $y$  plane.

Up to this point, the ions are referenced to their acceleration voltage ( $+2300$  V), *i.e.* they have  $+2300$  V as their ground. In order to avoid floating the remainder of the ion optics and detectors to  $+2300$  V, we utilize a potential switch. This device consists of a long ( $\sim 1$  m) cylindrical metal mesh and takes advantage of the fact that the electric field inside a conducting cylinder is zero. Thus, while the ions are inside the metal mesh, the voltage on that mesh is quickly switched from  $+2300$  V to 0 V, re-referencing the ions to earth ground. Depending on the timing of the switch, a set of atomic mass units – those whose TOF puts them inside the metal cylinder when the switch is triggered – are allowed through the instrument. Appendix I contains a short program written in Mathematica in order to calculate the appropriate times of flights of the anions as a function of their mass-to-charge ratio and their originating position in

the initial stage of the WM-TOF spectrometer, which is the region between the extraction plate and the acceleration stack.

Downstream from the potential switch, the mass separated ions can be mass selected by the use of a mass gate, placed  $\sim 20$  cm before the laser-anion interaction region. The mass gate selects ions of a desired  $m/z$  ratio by pulsing a  $\sim 250$  V voltage on a set of parallel plates. The electric field generated in the mass gate is perpendicular to the ion trajectory and thus reflects the unwanted ions by appropriately timing the voltage pulse. By that point in the WM-TOF spectrometer, the ions are mass separated by  $\sim 250$  ns/amu. Therefore, by applying a voltage pulse of equivalent width, we can mass select ions within a single amu to go through the remainder of the flight tube. Generally, in this experiment, the laser pulse timing is sufficient to detach electrons from anions within a single  $m/z$ , but for experiments such those described in Chapter 4, the use of the mass gate is crucial for reducing photoelectron background as a result of detachment of ions of masses within 1 amu from the target anion.

Following the mass gate, the ions reach the final region of the instrument: the detection region. Here, they pass through first stage of the VMI photoelectron spectrometer (described in section 2.1.e), where they are crossed by the laser beam. Finally, the ions reach an inline microchannel plate (MCP) detector. Here, the ions are accelerated towards the MCP by the same voltage that supplies the gain on the detector, which are in the range of +1000 V to +1500 V. The ion intensities versus TOF as detected by the MCPs are captured by a digital oscilloscope, generating mass spectra.

### *2.1.d Laser System*

In this experiment, the light source utilized for photodetachment is based on a pulsed Nd:YAG laser (Coherent Infinity). Chapter 1 notes that, in photoelectron spectroscopy, a full spectrum can be obtained with a single wavelength. However, due to experimental details that will be outlined in section 2.1.e, a collection of wavelengths is utilized. The specific wavelengths utilized in this experiments are described in each of the individual chapters, but a brief overview of the laser system is provided here.

As any standard Nd:YAG laser, the fundamental lasing line has a wavelength of 1064.4 nm, which gives photons of 1.164 eV of energy. In addition to the fundamental wavelength, we often utilize the second and third harmonics, namely 532.6 nm (2.329 eV) and 354.9 nm (3.495 eV), respectively. This Nd:YAG laser provides pulses of  $\sim 3$  ns, average powers of up to 600 mJ/pulse and linewidths of  $\sim 250$  MHz. The laser can be pulsed at a rate up to 100 Hz, but normally, the laser is operated at a repetition rate of 80 Hz in order to match the repetition rate of the pulsed valves in the ion source, which is limited by the pumping speed of the system.

In order to increase the number of available wavelengths to be utilized for photodetachment, this Nd:YAG laser is also equipped with a commercial UV pumped optical parametric oscillator (OPO). The OPO is pumped by the third harmonic of the Nd:YAG (354.9 nm) and outputs tunable wavelengths ranging from approximately 420 to 650 nm. The principle of operation of OPOs can be found in Ref. 16 or in any laser text book. In addition to the OPO, we utilize a dye laser (Quanta-Ray PDL-1) to extend the available wavelengths. The dye laser can be utilized with a vast collection of commercially available laser dyes and also be equipped with home-built second-harmonic (SHG), sum-frequency (SFG) or difference-frequency (DFG) generation stages.

For the photodetachment experiment and the measurement of the photoelectron anisotropy parameters (see section 1.2), the laser polarization must be set as parallel to the ion trajectory (horizontal, in the laboratory frame), by depicted as a purple double headed arrow in Fig. 2.1. For the wavelengths which don't already have this polarization state at the output of the laser, the polarization is rotated by way of either a half-waveplate or a polarizing periscope. In order to decrease the amount of other polarization states in the beam, we utilize a Brewster window at the laser entry port into the instrument. The Brewster window blocks the vertically polarized light and thus purifies the polarization state of the photons.

Prior to the chamber entrance window, we focus the laser beam with a 500 mm nominal focal length converging lens. This increases the photon density in the laser-ion interaction region and also approximates the originating location of the photoelectrons as a point source, which is extremely important for optimal velocity-mapping (see Ref. 17). The lens is mounted on a translation stage which allows for micrometric adjustment of the focal point in the  $x$ ,  $y$  and  $z$  directions. The adjustment of the position of the photoelectron originating point is crucial for optimal resolution to be reached. The photodetachment events take place in the laser-ion interaction region (yellow spark in Fig. 2.1). Photodetachment is realized by appropriately timing the laser q-switch trigger, so that the laser pulse and the ion packet of a specific  $amu$  are overlapped temporally. At that time and location, the photoelectrons are extracted by a negative voltage pulse into the VMI spectrometer, which is described in the following section.

### *2.1.e Velocity-map Imaging Spectrometer*

As was described in Chapter 1, the photoelectron spectra are generated by measuring the kinetic energy distribution of the photodetached electrons. However, no mention is made as to how the kinetic energy of the electrons is measured. There are a variety of methods with which

one can perform this measurement, such as the hemispherical energy analyzer<sup>18-20</sup> or a magnetic bottle.<sup>21</sup> In the experiments described in this thesis, we make use of the velocity-map imaging (VMI) method.

The VMI spectrometer is an ingenious device that was developed by Eppink and Parker in order to improve the imaging of ions in photodissociation experiments.<sup>17</sup> The VMI is composed of a simple arrangement of a repeller plate, and an acceleration stage (see Fig. 2.6). Eppink and Parker found that, by use of a position sensitive detector, and by appropriately setting the voltage ratio between the repeller and acceleration stages (in this experiment  $V_{\text{repeller}}/V_{\text{accel}} = 0.4$ ), the produced ions could be velocity focused in the directions orthogonal to the flight path. That is, all particles with the same initial velocity vector are mapped onto the same point on the detector.<sup>17</sup> The resulting image will then contain a two-dimensional projection of the initial 3D particle distribution, where particles of the same speed are projected onto a circle of a defined radius, which is directly proportional to their speeds in the detector plane.

In our experiment, we employ the VMI technique to image photoelectrons, as shown in Fig. 2.1 and 2.6. Subsequent to the interaction with the laser, the 3D photoelectron cloud is velocity focused onto a position sensitive microchannel plate (MCP)/phosphor screen detector. The projection on the phosphor screen is then imaged by a CCD camera, which is digitally acquired by a computer. The VMI images contain rings that correspond to specific electron velocities. Fig. 2.6 is a cartoon of the VMI process utilizing a specific example of photodetachment of molecular oxygen anion ( $\text{O}_2^-$ ).

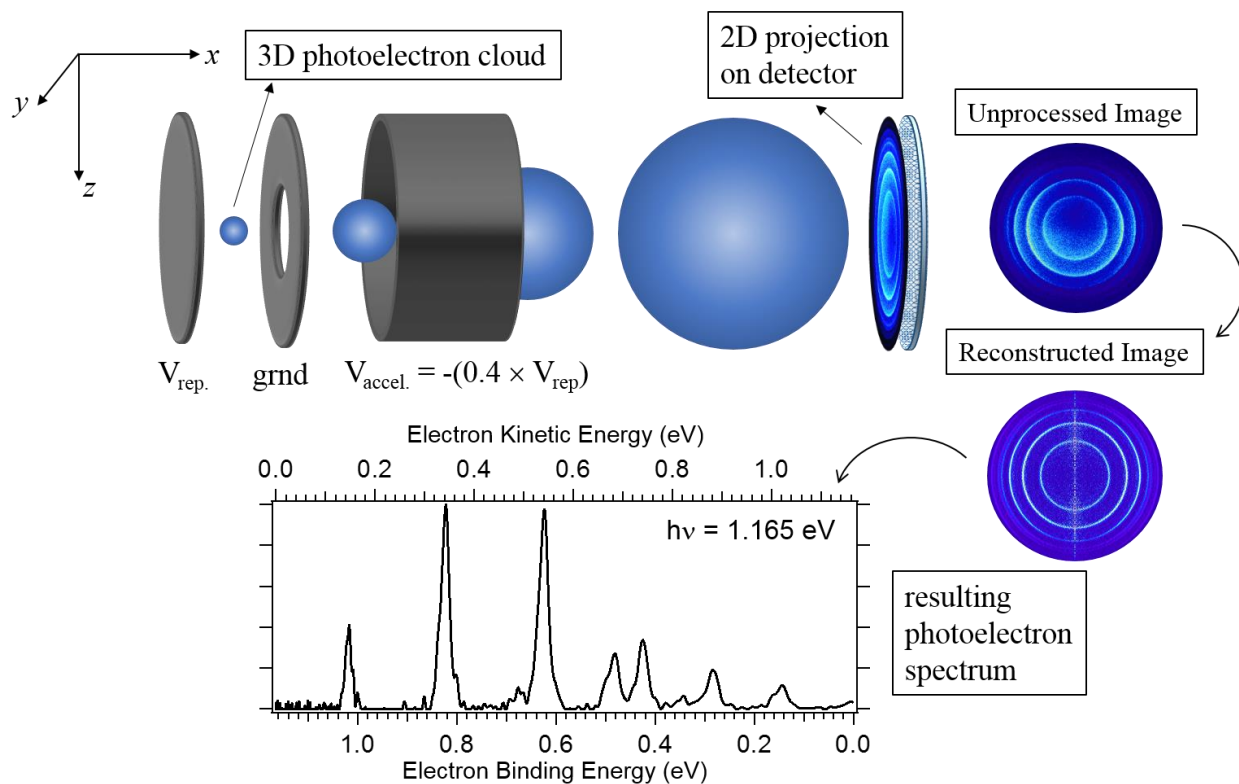


Figure 2.6: Detailed view of the VMI spectrometer with the velocity-mapping of the photoelectrons from  $\text{O}_2^-$ . The expanding sphere represents the photoelectron 3D cloud which is velocity-mapped onto the MCP/Phosphor screen detector. The resulting photoelectron spectrum is processed by the methods described in section 2.3.a.

This detector of course measures the velocity and not the kinetic energy of the photoelectrons. Although the conversion between velocity and kinetic energy is straightforward ( $KE = \frac{1}{2} m\mathbf{v}^2$ ), it results in a major experimental consequence about this type of detection: The energy resolution varies with electron kinetic energy. This fact is easily understood since kinetic energy is quadratic in speed. The initial image can be processed (see section 2.3.a) into an array of equally spaced points, that correspond to photoelectron intensity *versus* electron speed. As we convert speed to kinetic energy through a Jacobian transformation, the spacing of the points in the array consequently gets larger as speed increases. This means that a peak at low eKE will be narrower than that same peak at high eKE. In our instrument, specifically, the full width at half maximum (*fwhm*) of the observed peaks as a function of eKE follows approximately the functional form:

$$fwhm_{\text{individual peak}}(eKE) \approx 0.003 + 0.03 eKE \text{ [eV]} \quad (2.6)$$

where we have a constant offset of  $\sim 3$  meV, which is the limiting resolution when small eKEs are measured, and a linear term that increases with eKE. Thus, in VMI experiments, the resolution is often given as a percent value, corresponding to the ratio  $fwhm/eKE$ . In this experiment, when considering  $eKE \gtrsim 0.3$  eV, the ratio between peak full width at half maximum (*fwhm*) and eKE reaches a constant value of  $\sim 3\%$ .

The changing resolution of the VMI might seem like a disadvantage when compared to other types of detection, such as the hemispherical analyzer which possesses constant resolution of  $\sim 10$  meV. However, this can be utilized to our advantage. By analyzing electrons with low eKE, equation 2.6 shows that the resolution in our instrument reaches a limiting value of  $\sim 3$  meV. The detection of slow electrons in VMI instruments in order to obtain better resolution is often designated Slow Electron Velocity-map Imaging (SEVI). The SEVI technique was

pioneered and extensively explored by Neumark and coworkers in order to obtain high resolution (*fwhm*  $\sim 2 \text{ cm}^{-1}$  or 0.2 meV) photoelectron spectra.<sup>22,23</sup> In some of the experiments described in this thesis, a SEVI-like approach is taken in order to obtain resolutions of  $\sim 3 \text{ meV}$ , which is limiting to our experiment.

## 2.2 Theoretical Methods

### 2.2.a *Ab-initio* calculations

Throughout this thesis, we employ quantum chemical calculations in order to predict and interpret our experimental data. The vast majority of the calculations are performed by the Gaussian suite of programs,<sup>24</sup> and make use of the plethora of methods and basis sets available there. The details of each calculation are described in the individual chapters that compose this thesis. For the majority of the chapters, we utilize single reference methods that vary in accuracy and computational cost. Gaussian is utilized for calculations using density functional theory methods, often employing the popular B3LYP (Becke-3 Lee-Yang-Parr) hybrid functional.<sup>25</sup> For the smaller molecules studied, we often employ the high level CCSD(T) (Coupled Cluster Singles and Doubles with non-iterative Triples) method.<sup>26-28</sup> While the basis sets may vary, we frequently utilize the Dunning-type augmented correlation consistent basis sets (aug-cc-pVnZ)<sup>29,30</sup> which have proven to give accurate results for the calculations performed here. Gaussian calculations are not only a very useful resource for predicting relative energies of molecules, EAs,  $T_0$  and vibrational frequencies of the molecules studied here, but also extremely practical and straightforward to set up and analyze.

Other types of calculations that were applied, particularly in Chapter 6, are the so called multireference-type calculations.<sup>31</sup> Different from the theoretical methods described above,

multireference methods are required when the wavefunction of the system cannot be well described by a single Slater determinant. The use of multiple Slater determinants to generate the reference wavefunctions is what defines a multireference calculation. Multireference calculations encompass methods such as Complete Active Space Self-Consistent Field (CASSCF), Multi Reference Configuration Interaction (MRCI), among others.<sup>31,32</sup> As opposed to the single reference calculations performed in Gaussian, these calculations are less of “black-boxes”. That is to say that a more careful analysis of the calculation details must be done. In the CAS calculations, one of the most important steps is the choice of the active space. This consists of choosing the particular orbitals and electrons that are involved in the desired calculation of the target molecule, so that the excitations of the electrons in these orbitals are physically meaningful. A proper choice can be difficult to do *a priori* without a great amount of intuition and previous experience from the user. Nevertheless, there are some strategies that the beginner, such as myself, can follow in order to choose the correct active spaces for these types of calculations. Refs. 33 and 34 provide such guidance and Appendix II contains a brief description of the choice of the active space in multireference calculations, as the ones described in Chapter 6. All multireference calculations in this thesis are performed utilizing the Molpro 2012 quantum chemical software package.<sup>32</sup>

The calculations described above consist of initial geometry optimizations, providing numerical values for the energies of the molecules and anions in their equilibrium structure, thus resulting in the prediction of adiabatic EAs and  $T_0$ s. In addition, based on a harmonic model, we also calculate the vibrational normal modes and their corresponding frequencies based on the optimized equilibrium geometries. These frequencies are paramount for the simulation of the

photoelectron spectra, which aid the interpretation of the experiments and are described in the subsequent section.

### 2.2.b Photoelectron spectra simulations

The experimental photoelectron spectra can be theoretically predicted in order to aid the interpretation of the experimental data. The spectra are simulated utilizing the equilibrium geometries, harmonic frequencies and normal mode displacement vectors of the anions and corresponding neutrals obtained from the *ab initio* calculations described above in order to calculate the appropriate Franck–Condon (FC) factors (see Chapter 1). In the simulation, the FC factors are calculated within the harmonic oscillator approximation and by employing the Sharp-Rosenstock-Chen method with Duschinsky rotations.<sup>35,36</sup> These calculations can be carried out at a range of vibrational temperatures (Eqs. 1.12 and 1.13), and thus, can include vibrational hot bands when appropriate. This procedure generates a discrete spectrum of sticks, where the intensities correspond to the calculated FC factor and the positions correspond to the calculated vibrational frequency relative to the EA, the transition between the ground vibrational and electronic level in the anion to ground vibrational level in the neutral electronic states. For the vibrational hot bands, as described in section 1.1, the intensity of the sticks corresponds to the calculated FC factor times the Boltzmann factor at a specific temperature (see individual Chapters 3 through 7). For carrying out the above-mentioned simulations, we utilize the PESCAL<sup>37</sup> program, for calculations performed by Gaussian,<sup>24</sup> or the ezSpectrum<sup>38</sup> program for calculations performed by Molpro.<sup>32</sup>

In order to provide a direct comparison between calculation and experiment, the stick spectrum is convolved with Gaussian functions whose integral is normalized to be equal to the

calculated transition intensity, and whose *fwhm* is consistent with the varying instrumental resolution of the VMI spectrometer, as described in section 2.1.e.

## 2.3 Data analysis

### 2.3.a Image processing

Once the velocity-map images are acquired, they must be processed into a 1D photoelectron spectrum. Physically speaking, the acquired images represent a 2D projection of a 3D photoelectron velocity distribution, which must be reconstructed so that all the information contained in the original 3D distribution is recovered. The photoelectron signal in the reconstructed array is then integrated around the polar angle, resulting in a 1D speed distribution. In order to do that, the image must be cylindrically symmetric, which is guaranteed provided the polarization of the photons that generate the photoelectrons is orthogonal to the electron flight path and then, the original 3D distribution can be recovered by a series of methods.<sup>39</sup>

The foremost method for recovering the original 3D photoelectron distribution is by way of an inverse Abel transformation. Abel transformations have been generally utilized in image processing for this purpose as it projects an axially symmetric emission function onto a plane, while the inverse Abel transform is used to calculate the emission function given a projection (*i.e.* a scan or a photograph) of that emission function.<sup>40</sup> The methods by which the inverse Abel transform is carried are plenty, each with their own advantages and disadvantages, and can be found elsewhere.<sup>39</sup> The main effects that the algorithm has on the reconstructions is the introduction of unphysical artifacts such as addition of peaks and/or noise that are not intrinsic to the data, artificial broadening of the peaks and generation of rising baselines. Ref. 39 contains a thorough description of the specifics of each image reconstruction algorithm that is based on the

inverse Abel transform. Through this thesis, we frequently make use of the basis-set expansion method (BASEX), which was implemented by Dribinski *et al.*<sup>41</sup> BASEX has proven to be a fast and reliable method for image processing with minimal creation of aberrations.

In more recent years other types of reconstruction methods were developed by Dick,<sup>42</sup> namely the Maximum Entropy Velocity Image Reconstruction (MEVIR) and Maximum Entropy Velocity Legendre Reconstruction (MEVELER). These methods reconstruct the images without the use of an inverse Abel transform. Details of the methods and their implementation can be found in Ref. 42, but briefly, quoting Dick, in contrast to other methods, these methods never apply an inversion or smoothing to the data. Instead, the program iteratively finds the map which is the most likely cause for the observed data, while the entropy criterion implemented minimizes the information content in this map.<sup>42</sup> This results in a map that contains no information for which there is no evidence in the data, thus minimizing reconstruction aberrations. We thus frequently utilize this method of image processing. The specific method by which the spectra reported in this thesis is reconstructed is described in the individual chapters, but MEVELER has been the method of choice for the aforementioned features and for its remarkably accurate image centering algorithm. The issue with centering images is described in the following paragraph.

Another point worth mentioning is that in order to perform a proper reconstruction, the center point of the image must be chosen so that the integration about the cylindrical axis is appropriate. Even a minor error in the choice of the center can significantly alter the position of the observed peaks in the reconstructed speed distribution since the center represents the point of zero electron velocity, thus introducing a systematic error to the measurement of the position of that peak. In addition, a wrong center can result in reconstruction aberrations. There are several

methods by which the center of an image can be chosen, but they often require some amount of judgement by the person performing the procedure. The best way to find the correct center is to pick an initial center “by eye”, divide the image in four quadrants based on that center point, symmetrize each of the quadrants into a full image, perform a reconstruction of each of these four images, and, finally, compare the reconstructed images. If a target peak in the reconstructions of each of the four quadrants is invariantly in the same position in the 1D distribution, the center was appropriately chosen. If not, a different center must be chosen and the procedure repeated. One can see how tedious and impractical is this procedure (see Appendix III for a painful example of the procedure). The centering algorithm (F2QC) developed by Dick<sup>42</sup> and part of the MEVIR/MEVELER package has proven to be remarkably accurate at finding the correct center of images, even when compared to the rigorous procedure described above. In addition to that, the program certainly is not subject to human personal biases, and thus the F2QC/MEVELER package became our preferred method of analyzing and processing the VMI images.

### *2.3.b Assignments and uncertainties*

Once the photoelectron spectra are obtained, we must analyze them to extract the important information, such as the EAs, vibrational frequencies and  $T_0$ s. As mentioned in section 1.1, the photoelectron spectra of anions provide a vibrational spectrum of the corresponding neutral electronic state. The vibrational frequencies of the neutral state are obtained by measuring the difference in peak centers between the origin transition of the vibrational progression, which is the EA of that particular neutral, and a particular peak. However, in order to know to what type of vibration (*i.e.* molecular motion) a peak corresponds, we rely on a combination of physical intuition and comparison with calculation. The physical intuition is

based on what type of geometry change occurs upon photodetachment. This indicates which type of vibration will be expected to be active (*i.e.* have a significant FC factor) in the photoelectron spectrum. The calculated spectrum provides vibrational assignments of individual peaks by a comparison of the positions of the experimental and calculated peaks. The peak that most closely matches the position of the predicted transition and has a vibrational normal mode that is expected to be active, is likely the vibration responsible for the intensity of the peak. The uncertainties in these measurements derive from a combination of the uncertainties associated with the statistical error in fitting the peaks to Gaussian functions, the absolute energy scale calibration and the number of independent measurements of the individual peaks. These uncertainties are considered to be independent of one another and therefore are added in quadrature and result, on average, in uncertainties of 1 to 2 meV. However, it is important to note that the error associated with the measurement of the transitions is likely greater than the above value, due to the presence of unresolved transitions, as described below.

The assignment of peaks that correspond to a single FC active transition are straightforward. However, when multiple calculated transitions are responsible for the intensity of a single peak, firm assignments become more complicated and therefore are subject to larger uncertainties. Often, the width of a peak is indicative of whether it is composed of a single or multiple transitions. By acquiring a calibration spectrum with a previously investigated atomic anion, we can know what the limiting width at a specific eKE should be, since atoms are certainly not subject to rotational broadening. The inability of knowing precisely what transition is responsible for a peak's intensity consequently increases the uncertainty in our measurements and are primarily due to two factors. First, since our experimental resolution does not allow for separation of the rotational structure, the peak center does not necessarily correspond to the band

origin of a transition. In order to address this, the procedure described by Engelking<sup>43,44</sup> for rotational band shifts is employed. The procedure was described correctly in Ref. 43, but there was an error in the band shift equation reported in that paper which was recognized in Ref. 44. This Engelking model accounts for the fact that rigid-rotor rotational selection rules appropriate for a bound-free transition are more complicated than for a bound-bound transition; however, the analysis is limited to a selection rule of no change in the J, K populations ( $\Delta J = \Delta K = 0$ ). The offset between the peak center and the band-origin ( $\Delta E_{\text{rot}}$ ) for an asymmetric top, as a function of rotational temperature, is given by:

$$\Delta E_{\text{rot}} \approx -k_{\text{B}}T \left[ \frac{A'}{2A''} + \frac{B'}{2B''} + \frac{C'}{2C''} - \frac{3}{2} \right] + \frac{B'' - B'}{3} \quad (2.7)$$

where  $A$ ,  $B$  and  $C$  are the rotational constants of the target molecules, which are obtained by either calculation or a previous measurement. The primed quantities refer to the upper state (neutral) and the double-primed quantities refer to the lower state (anion). Second, many of the peaks in the experiments are not resolution limited and, therefore, are subject to further broadening. Specifically, more than one vibrational transition can account for the width of the peaks, and hence when assigning a transition to a non-resolution limited peak, the actual band origin of that transition may reasonably be located within a wide range comprising the *fwhm* of that peak. Therefore, for these cases, we utilize the peak *fwhm* ( $\pm fwhm/2$ ) to provide the uncertainties for the assigned transitions. All of these uncertainties have to be accounted for in the measurements of the vibrational frequencies and quantities such as the EA and  $T_0$ . Procedures that are specific to each species studied in this thesis will be described in the respective individual chapters.

## 2.4 Chapter 2 references

- <sup>1</sup> Y.-J. Lu, J.H. Lehman, and W.C. Lineberger, *J. Chem. Phys.* **142**, 44201 (2015).
- <sup>2</sup> Y.-J. Lu, *Photoelectron Spectroscopy of Small Organic Anions Prepared Using a Novel Cold Ion Source Employing Entrainment of Charged Particles*, University of Colorado - Boulder, 2014.
- <sup>3</sup> R. Campargue, *J. Phys. Chem.* **88**, 4466 (1984).
- <sup>4</sup> R.E. Smalley, L. Wharton, and D.H. Levy, *Acc. Chem. Res.* **10**, 139 (1977).
- <sup>5</sup> A.T. Droege and P.C. Engelking, *Chem. Phys. Lett.* **96**, 316 (1983).
- <sup>6</sup> O.F. Hagena and W. Obert, *J. Chem. Phys.* **56**, 1793 (1972).
- <sup>7</sup> D.L. Osborn, D.J. Leahy, D.R. Cyr, and D.M. Neumark, *J. Chem. Phys.* **104**, 5026 (1996).
- <sup>8</sup> D.W. Boo, Y. Ozaki, L.H. Andersen, and W.C. Lineberger, *J. Phys. Chem.* **101**, 6688 (1997).
- <sup>9</sup> X. Li, A. Grubisic, S.T. Stokes, J. Cordes, G.F. Gantefor, K.H. Bowen, B. Kiran, M. Willis, P. Jena, R. Burgert, and H. Schnockel, *Science*, **315**, 356 (2007).
- <sup>10</sup> E. Garand, T.I. Yacovitch, and D.M. Neumark, *J. Chem. Phys.* **130**, 64304 (2009).
- <sup>11</sup> F.F. Chen, *Introduction to Plasma Physics* (Springer US, 1995).
- <sup>12</sup> V.M. Bierbaum, *Int. J. Mass Spectrom.* **377**, 456 (2015).
- <sup>13</sup> E.E. Ferguson, *J. Am. Soc. Mass Spectrom.* **3**, 479 (1992).
- <sup>14</sup> F.C. Fehsenfeld and A.L. Schmeltekopf, *Adv. Chem.* **80**, 83 (1969).
- <sup>15</sup> W.C. Wiley and I.H. McLaren, *Rev. Sci. Instrum.* **26**, 1150 (1955).
- <sup>16</sup> S. Hooker and C.E. Webb, *Laser Physics* (Oxford University Press, 2010).
- <sup>17</sup> A.T.J.B. Eppink and D.H. Parker, *Rev. Sci. Instrum.* **68**, 3477 (1997).
- <sup>18</sup> C.E. Kuyatt and J.A. Simpson, *Rev. Sci. Instrum.* **38**, 103 (1967).
- <sup>19</sup> A. Kasdan and W.C. Lineberger, *Phys. Rev. A* **10**, 1658 (1974).
- <sup>20</sup> R.J. Celotta, R.A. Bennett, J.L. Hall, M.W. Siegel, and J. Levine, *Phys. Rev. A* **6**, 631 (1972).
- <sup>21</sup> H. Handschuh, G. Ganteför, and W. Eberhardt, *Rev. Sci. Instrum.* **66**, 3838 (1995).
- <sup>22</sup> M.L. Weichman, J.A. DeVine, D.S. Levine, J.B. Kim, and D.M. Neumark, *Proc. Natl. Acad. Sci.* **113**, 1698 (2016).
- <sup>23</sup> D.M. Neumark, *J. Phys. Chem. A* **112**, 13287 (2008).
- <sup>24</sup> M.J. Frisch, G.W. Trucks, H.B. Schlegel, G.E. Scuseria, M.A. Robb, J.R. Cheeseman, G. Scalmani, V. Barone, B. Mennucci, G.A. Petersson, H. Nakatsuji, M. Caricato, X. Li, H.P. Hratchian, A.F. Izmaylov, J. Bloino, G. Zheng, J.L. Sonnenberg, M. Hada, M. Ehara, K. Toyota, R. Fukuda, J. Hasegawa, M. Ishida, T. Nakajima, Y. Honda, O. Kitao, H. Nakai, T. Vreven, J.A.

Montgomery Jr., J.E. Peralta, F. Ogliaro, M.J. Bearpark, J. Heyd, E.N. Brothers, K.N. Kudin, V.N. Staroverov, R. Kobayashi, J. Normand, K. Raghavachari, A.P. Rendell, J.C. Burant, S.S. Iyengar, J. Tomasi, M. Cossi, N. Rega, N.J. Millam, M. Klene, J.E. Knox, J.B. Cross, V. Bakken, C. Adamo, J. Jaramillo, R. Gomperts, R.E. Stratmann, O. Yazyev, A.J. Austin, R. Cammi, C. Pomelli, J.W. Ochterski, R.L. Martin, K. Morokuma, V.G. Zakrzewski, G.A. Voth, P. Salvador, J.J. Dannenberg, S. Dapprich, A.D. Daniels, Ö. Farkas, J.B. Foresman, J. V. Ortiz, J. Cioslowski, and D.J. Fox, Gaussian 09 Revision B.01, Gaussian Inc. Wallingford, CT (2009).

- <sup>25</sup> A.D. Becke, *J. Chem. Phys.* **98**, 5648 (1993).
- <sup>26</sup> J.F. Stanton, *Chem. Phys. Lett.* **281**, 130 (1997).
- <sup>27</sup> G.W. Trucks, J.A. Pople, and M. Head-Gordon, *Chem. Phys. Lett.* **157**, 479 (1989).
- <sup>28</sup> R.J. Bartlett, J.D. Watts, S.A. Kucharski, and J. Noga, *Chem. Phys. Lett.* **165**, 513 (1990).
- <sup>29</sup> R.A. Kendall, T.H. Dunning, and R.J. Harrison, *J. Chem. Phys.* **96**, 6796 (1992).
- <sup>30</sup> T.H. Dunning, *J. Chem. Phys.* **90**, 1007 (1989).
- <sup>31</sup> C.J. Cramer, *Essentials of Computational Chemistry : Theories and Models* (Wiley, 2004).
- <sup>32</sup> H.J. Werner, P.J. Knowles, G. Knizia, F.R. Manby, and M. Schutz, *WIREs Comput. Mol. Sci.* **2**, 242 (2012).
- <sup>33</sup> M.W. Schmidt and M.S. Gordon, *Annu. Rev. Phys. Chem.* **49**, 233 (1998).
- <sup>34</sup> A.C. Borin and A.V.S. de Araújo, *Quim. Nova* **38**, 738 (2015).
- <sup>35</sup> T.E. Sharp and H.M. Rosenstock, *J. Chem. Phys.* **41**, 3453 (1964).
- <sup>36</sup> K.M. Ervin, J. Ho, and W.C. Lineberger, *J. Phys. Chem.* **92**, 5405 (1988).
- <sup>37</sup> K.M. Ervin, PESCAL, available online at [wolfweb.unr.edu/~ervin/pes/](http://wolfweb.unr.edu/~ervin/pes/) (2010).
- <sup>38</sup> V.A. Mozhayskiy and A.I. Krylov, ezSpectrum, available online at [iopshell.usc.edu/downloads/](http://iopshell.usc.edu/downloads/) (2016).
- <sup>39</sup> B.J. Whitaker, *Imaging in Molecular Dynamics: Technology and Applications : A User's Guide* (Cambridge University Press, 2004).
- <sup>40</sup> A.D. Poularikas, *The Transforms and Applications Handbook* (CRC Press, 2000).
- <sup>41</sup> V. Dribinski, A. Ossadtchi, V.A. Mandelshtam, and H. Reisler, *Rev. Sci. Instrum.* **73**, 2634 (2002).
- <sup>42</sup> B. Dick, *Phys. Chem. Chem. Phys.* **16**, 570 (2014).
- <sup>43</sup> P.C. Engelking, *J. Phys. Chem.* **90**, 4544 (1986).
- <sup>44</sup> M.J. Travers, D.C. Cowles, E.P. Clifford, G.B. Ellison, and P.C. Engelking, *J. Chem. Phys.* **111**, 5349 (1999).

*this page is intentionally left blank*

## CHAPTER III

### PHOTOELECTRON SPECTROSCOPY OF THE METHIDE ANION ( $\text{CH}_3^-$ )

This chapter is partially reproduced from: *Oliveira, A.M., Lu, Y.-J., Lehman, J.H., Changala, P.B., Baraban, J.H., Stanton, J.F., Lineberger, W.C., Journal of the American Chemical Society, vol. 137, p. 12939 – 12945 (2015)* with permission of the authors.

#### 3.1 Introduction and Motivation

There is great scientific interest in investigating the methide anion ( $\text{CH}_3^-$ ) and the related species  $\text{CH}_3$  (methyl radical) and  $\text{CH}_4$  (methane).  $\text{CH}_4$  and  $\text{CH}_3$  were studied extensively due to their fundamental importance in combustion and many other chemical processes.<sup>1-13</sup>  $\text{CH}_3^-$ , has been less studied, but draws significant interest from both applied and a fundamental points of view.

In the applied science perspective,  $\text{CH}_3^-$  is the simplest carbanion, which are anions with a formal negative charge located at a carbon center and ubiquitous in many areas of chemistry.<sup>14</sup> Second  $\text{CH}_3^-$  is of interest to the astrochemical community as it is present in the atmosphere of Saturn's moon Titan, a model system for prebiotic Earth.<sup>15-18</sup>

On the fundamental science side,  $\text{CH}_3^-$  is isoelectronic with  $\text{NH}_3$  and  $\text{H}_3\text{O}^+$ , and has a similar pyramidal structure ( $C_{3v}$  point group). This structure results in a double-well electronic potential energy surface along the umbrella inversion coordinate, which leads to a splitting of vibrational levels below the barrier to inversion. Because of the numerous experimental and

theoretical studies available for  $\text{NH}_3$  and  $\text{H}_3\text{O}^+$ , both have become prototypes in studying inversion/tunneling splittings, as well as tests for the validity of new theoretical treatments. In  $\text{NH}_3$ ,<sup>19–21</sup> the inversion splitting of the ground vibrational state was the transition employed in the first MASER,<sup>22</sup> and has been experimentally determined as  $0.793\text{ cm}^{-1}$  (24 GHz).<sup>19,23</sup> For hydronium,  $\text{H}_3\text{O}^+$ , a smaller inversion barrier leads to a much larger splitting of  $55.35\text{ cm}^{-1}$ .<sup>24–26</sup> Isotopic substitution, *i.e.*  $\text{ND}_3$  and  $\text{D}_3\text{O}^+$ , lowers the inversion splitting to  $0.053$  and  $15.36\text{ cm}^{-1}$ , respectively.<sup>21,26</sup> The inversion splittings of  $\text{CH}_3^-$  and its isotopologue,  $\text{CD}_3^-$ , however, have not been experimentally determined.

A photoelectron spectrum of  $\text{CH}_3^-$  was initially obtained in 1978 by Ellison *et al.*<sup>27</sup> in our group, resulting in the determination of the EA of  $\text{CH}_3$  as  $0.08 \pm 0.03\text{ eV}$ . From this measurement, the gas phase acidity ( $\Delta_{\text{acid}}\text{H}_{0\text{K}}^0$ ) was derived for  $\text{CH}_4$  as  $415.2(7)\text{ kcal/mol}$  and is one of the highest known gas phase acidities,<sup>28,29</sup> second only to  $\text{LiOH}$ .<sup>30</sup> DePuy *et al.* used the  $\text{CH}_4$  gas-phase acidity as a reference point to determine other alkane acidities.<sup>29</sup> This makes a precise determination of the acidity very important.

The challenge in producing the anion is the principal reason for the lack of experimental studies on methide.<sup>31,32</sup> In Ellison *et al.*'s<sup>27</sup> study, they claimed that  $\text{CH}_3^-$  was produced in a surface catalyzed decomposition of ketene ( $\text{H}_2\text{C}=\text{C}=\text{O}$ ). Although the ion produced was undoubtedly  $\text{CH}_3^-$ , the formation route was at least mysterious and, according to private communication with the authors, not easily reproduced. This difficulty can be explained by the small EA of  $\text{CH}_3$ , which makes it prone to electron autodetachment, or the large gas phase acidity of  $\text{CH}_4$ , deeming the deprotonation of methane essentially impossible. The novel ion source described in Chapter 2 enabled us to produce stable intense beams of anions with weakly bound electron such as  $\text{CH}_3^-$ . The straightforward generation of  $\text{CH}_3^-$  through the discharge of

pure methane and the fact that the VMI detection allows us to obtain much better resolution than the initially reported spectrum by Ellison, motivated us to revisit the experiment, particularly hoping that we could determine the inversion splitting in  $\text{CH}_3^-$  experimentally.

Besides the experimental work, this project draws attention from theoretical collaborators as previous computational investigations<sup>9,33,34</sup> have failed in reproducing the experimental spectrum and energetics concomitantly.<sup>6,33</sup> The strong anharmonicity of the anion electronic potential surface complicates the calculation of both the vibrational zero-point energy (ZPE) and the effective inversion barrier size. The ZPE in combination with the barrier shape has a large effect on the magnitude of the inversion splitting and therefore, a very high quality surface is required for reliable calculations. By comparison with experiment, calculations can possibly provide very useful information that cannot be measured experimentally, such as the inversion barrier height and the anion-neutral electronic potential energy surface crossing points.

In this chapter, we report high-resolution photoelectron spectra of  $\text{CH}_3^-$  and its isotopologue  $\text{CD}_3^-$ . The experimental results provide a point of reference for building an accurate potential energy surface for the methide anion. New high-level electronic structure and vibrational calculations of the  $\text{CH}_3^-$  and  $\text{CD}_3^-$  anions show excellent agreement with experimental findings.

### **3.2 Experimental Methods**

This experiment employs the negative ion photoelectron velocity-map imaging (VMI) spectrometer described in Chapter 2. For this study, the ions are generated in our dual valve pulsed plasma-entrainment anion source using 40 psig argon in the main valve and 20 psig  $\text{CH}_4$

99.99% purity or CD<sub>4</sub> 99% atom D in the side valve pulsed discharge assembly operating at -900 V and 40~100  $\mu$ s.

We use the following wavelengths for photodetachment: 1064 nm (1.165 eV, 3.5 mJ/pulse) and 3239 nm (0.383 eV, 50~100  $\mu$ J/pulse). This mid-IR wavelength comes from difference frequency generation (DFG) of 1064 nm with 801 nm (532 nm pumped LDS 798 dye laser) in a  $1 \times 1 \times 3$  cm<sup>3</sup> magnesium oxide doped lithium niobate crystal (MgO:LiNbO<sub>3</sub>). These wavelengths are focused into the interaction region using a 0.5 m nominal focal length CaF<sub>2</sub> lens (Thorlabs, Inc.).

The kinetic energy scale is defined primarily by using an internal calibration of the umbrella mode frequency of neutral  $\bullet$ CH<sub>3</sub>. In order to verify the accuracy of the photoelectron kinetic energy measurements, we calibrate our energy scale by comparing the  $\nu_2$  ( $\nu = 0 \rightarrow \nu = 4$ ) umbrella mode frequency (2791(4) cm<sup>-1</sup>) in neutral  $\bullet$ CH<sub>3</sub> from Yamada *et al.*<sup>5</sup> and Hermann *et al.*<sup>8</sup> using an energy scale calibration from the O<sub>2</sub> spacing from ( $\nu = 0 \rightarrow \nu = 4$ ) transition (4598.84 (3) cm<sup>-1</sup>)<sup>5</sup> and *vice-versa*. The vibrational level spacings are consistent within 0.0001 eV (1 cm<sup>-1</sup>) in O<sub>2</sub> and 0.0005 eV (4 cm<sup>-1</sup>) in  $\bullet$ CH<sub>3</sub>, which confirms that the energy scale uncertainty does not significantly affect the electron kinetic energy measurements. The values and error bars reported herein are weighted averages of all measurements, which include the uncertainty in the energy scale calibration, statistical error in peak center given by a least squares Gaussian fit to the experimental peaks, and error associated with a displacement from peak center due to a rotational band-origin shift (see Chapter 2).

While the mid-IR, 3239 nm wavelength can give us the best resolution (see Chapter 2), the much higher laser flux available with 1064 nm radiation allows for much less noisy data and

also better adjustment of the conditions necessary for a high resolution experiment. As mentioned in Chapter 2, the point of interaction between the laser and ion beam is what ultimately limits the resolution in the experiment, for these reasons both spectra are close to equivalent in overall quality. The mid-IR data, however, provides us the most accurate position of the  $\nu\text{CH}_3$  ( $\nu = 3$ ) peak, and therefore the best calibration of the spacing  $\nu\text{CH}_3$  ( $\nu = 1 - 3$ ). This is taken into account when we weigh the experimental data to obtain the inversion splitting.

### 3.3 Experimental Results

#### 3.3.a Introductory remarks

The dual valve plasma entrainment anion source<sup>35</sup> enables efficient synthesis and cooling of  $\text{CH}_3^-$ . The experimental photoelectron spectra of  $\text{CH}_3^-$  and  $\text{CD}_3^-$ , depicted in the top panels of Figures 3.1 and 3.2 respectively, show an extended vibrational progression indicative of a large geometry change upon electron photodetachment. The overall  $\text{CH}_3^-$  spectrum is consistent with the lower resolution one reported by Ellison *et al.*<sup>27</sup> The  $\text{CD}_3^-$  photoelectron spectrum reported here is the only experimental result obtained for this isotopic species. The binding energies corresponding to the center of each labelled peak are shown in Table 3.1 below. The small features between peaks C through E are not reproducible and are artifacts from the inverse Abel transformation when converting the photoelectron images to the 1D spectra.

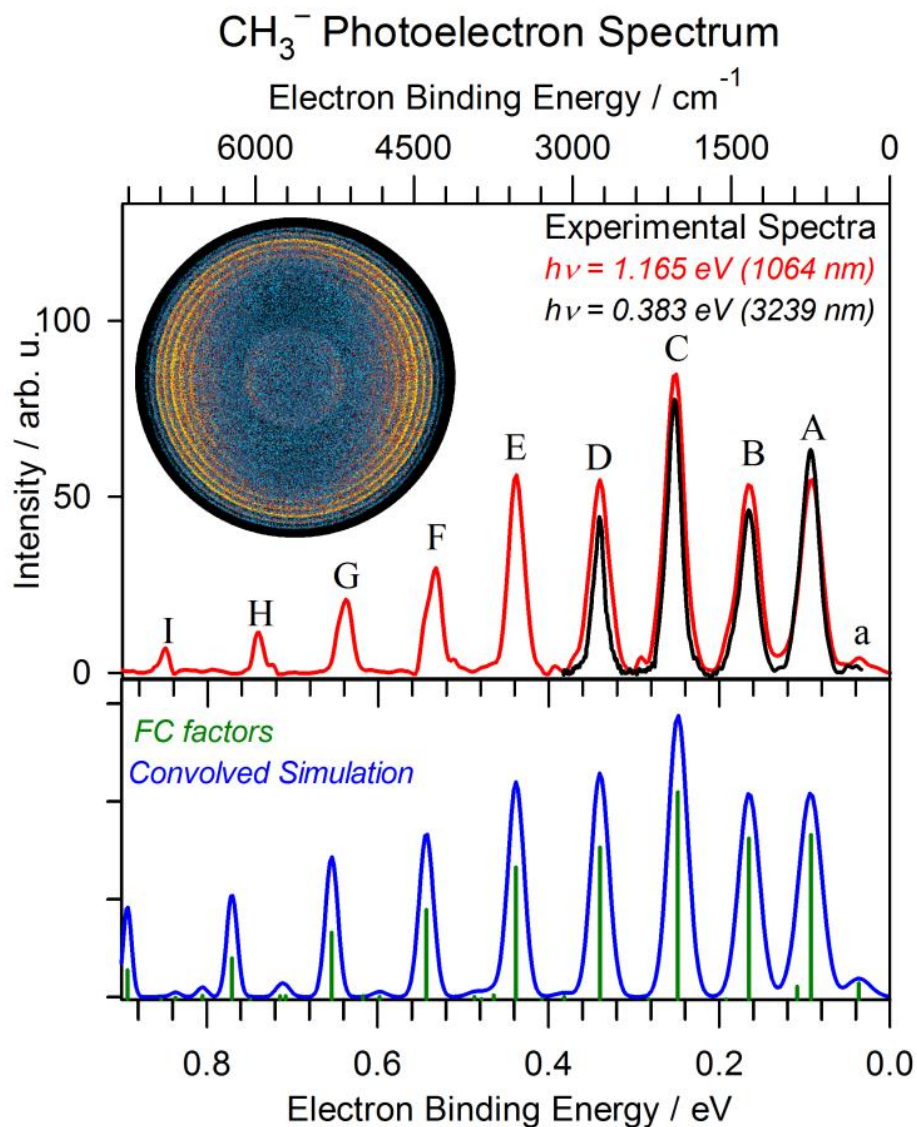


Figure 3.1: Photoelectron spectra of CH<sub>3</sub><sup>-</sup>. The experimental spectrum using 1.165 eV (red) or 0.383 eV (black) photon energies are shown in the upper panel. The peak assignments (upper and lowercase letters) and positions are provided in Table 3.1. The inset shows a raw velocity mapped photoelectron image using 1.165 eV photon energy, with the direction of the laser polarization parallel to the y-axis of the graph. Note that the center ring in the image is a contaminant due to detachment from CH<sub>2</sub><sup>-</sup>. The lower panel shows the spectrum calculated by methods described in section 3.4.

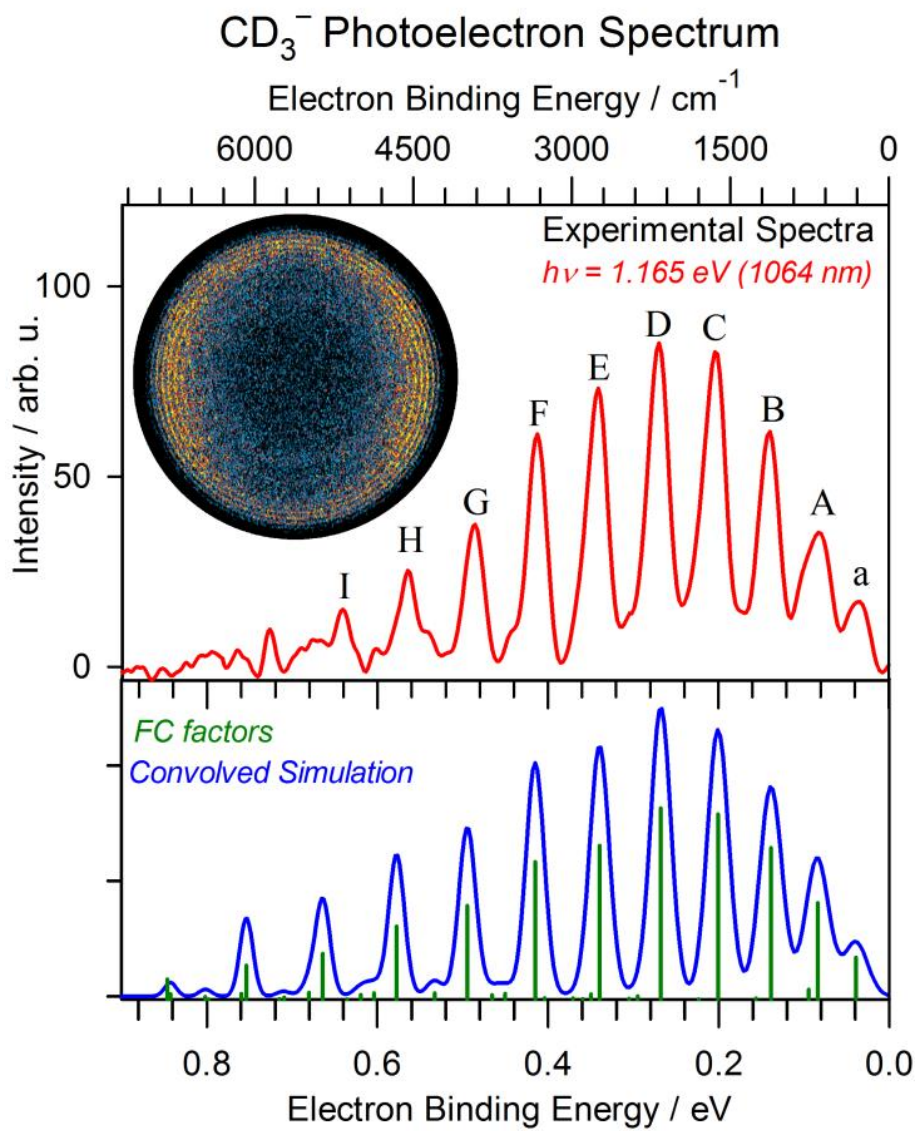


Figure 3.2: Photoelectron spectra of CD<sub>3</sub><sup>-</sup>. Analogous description as Figure 3.1.

Table 3.1: Experimentally determined electron binding energies of each peak and transition assignments for each peak in the photoelectron spectra of  $\text{CH}_3^-$  and  $\text{CD}_3^-$ . Each eBE value corresponds to the center of each individual transition, as determined by fitting the peak to a Gaussian form. The values in parentheses are the uncertainties described in the text.

$\bullet\text{CH}_3 + e^- \leftarrow \text{CH}_3^-$			$\bullet\text{CD}_3 + e^- \leftarrow \text{CD}_3^-$		
Peak <sup>a</sup>	eBE / $\text{cm}^{-1}$	Assign. $\nu_2' \leftarrow \nu_2''$	Peak <sup>a</sup>	eBE / $\text{cm}^{-1}$	Assign. $\nu_2' \leftarrow \nu_2''$
a	303(10)	$0 \leftarrow 1^+$	a	294(8)	$0 \leftarrow 1^+$
A	757(9)	$0 \leftarrow 0^+$	A	674(8)	$0 \leftarrow 0^+$
B	1340(5)	$1 \leftarrow 0^-$	B	1128(7)	$1 \leftarrow 0^-$
C	2045(5)	$2 \leftarrow 0^+$	C	1640(7)	$2 \leftarrow 0^+$
D	2755(4)	$3 \leftarrow 0^-$	D	2175(7)	$3 \leftarrow 0^-$
E	3542(6)	$4 \leftarrow 0^+$	E	2748(7)	$4 \leftarrow 0^+$
F	4308(6)	$5 \leftarrow 0^-$	F	3325(5)	$5 \leftarrow 0^-$
G	5157(5)	$6 \leftarrow 0^+$	G	3917(3)	$6 \leftarrow 0^+$
H	5977(4)	$7 \leftarrow 0^-$	H	4545(4)	$7 \leftarrow 0^-$
I	6860(3)	$8 \leftarrow 0^+$	I	5170(3)	$8 \leftarrow 0^+$

<sup>a</sup>Peak labels shown in Figures 3.1 and 3.2.

### 3.4.b Photoelectron Angular Distributions

The eKE dependence of  $\beta$  yields direct information about the hybrid orbital composition of the methide anion HOMO (see Chapter 2). The photoelectron anisotropy parameter is derived for each peak in the vibrational progressions shown in Figures 3.1 and 3.2. The intensity (number of electron counts) as a function of the angle ( $I(\theta)$ ) with respect to the laser polarization at the radius corresponding to each peak is fit to the form<sup>36</sup>,  $I(\theta) \propto (1 + \frac{\beta}{2}(1 + 3 \cos^2 \theta))$ . The error in the resulting  $\beta$  values, shown in Figure 3.3, comes from the scatter of the measured  $\beta$  values across each peak *fwhm*.

The  $\beta$  values as a function of photodetached electron kinetic energy (eKE) are fit to the modified Wigner-Bethe-Cooper-Zare equation in the work by Sanov *et al.*<sup>37</sup> that describes the angular anisotropy of electron photodetachment from a mixed *sp* hybrid orbital as a function of electron kinetic energy (eKE):

$$\beta(\text{eKE}) = \frac{2 Z \text{ eKE} + 2A \text{ eKE}^2 - 4 \text{ eKE} \cos(\delta_2 - \delta_0)}{\frac{1}{A} + 2A \text{ eKE}^2 + Z \text{ eKE}} \quad (3.1)$$

where

$$Z = \frac{1-f}{f} \frac{B}{A}$$

Here,  $Z$  and  $A$  and  $B$  are parameters whose physical significance is described below, and  $\cos(\delta_2 - \delta_0)$  is the relative phase-shift between the outgoing waves of  $\Delta\ell = \pm 1$ . The  $A$  and  $B$  parameters describe the scaling of the radial dipole integrals corresponding to the  $l \rightarrow l \pm 1$  ( $A$ ) and  $l \leftrightarrow l - 1$  ( $B$ ) photodetachment channels. While there are initially four fitting parameters, Sanov shows that

for mixing  $2s$  and  $2p$  hydrogenic orbitals, the ratio  $B/A$  becomes  $8/3$ , and  $\cos(\delta_2 - \delta_0) \cong 1$ , *i.e.*, no phase-shift between the outgoing electron waves, which reduces the number of fitting parameters to two. The parameter  $f$  is associated with the relative  $p$ -character of the initial orbital, where the limiting cases of  $f = 0$  and  $1$  describe pure  $s$  and  $p$  orbitals, respectively, according to the following expression for the HOMO of the anion:

$$|\psi\rangle_{HOMO} = \sqrt{1-f}|s\rangle + \sqrt{f}|p\rangle \quad (3.2)$$

The ratio of the  $A$  and  $B$  photodetachment channels (now assumed to be  $8/3$ ) is included in the fitting equation through the  $Z$  parameter, and weighted by the coefficient  $(1-f)/f$  for the relative contributions of the  $s$  and  $p$  orbitals. More detailed information can be found in papers by Sanov.<sup>37-40</sup>

The  $\beta$  parameters obtained from the experimental data are shown in Figure 3.3 for the  $\text{CH}_3^-$  photoelectron spectra using  $1.165$  eV and  $0.383$  eV photon energies. In addition, we include here photoelectron spectra taken with  $2.33$  eV and  $1.63$  eV photon energies (not shown in this thesis). The solid green line in Figure 3.3 is the best fit of Eq. 3.1 to the experimental data, resulting in  $f = 0.80$  and  $A = 1.15$  eV<sup>-1</sup>. The grey shaded area depicts the sensitivity of the experimental fit as  $f$  is varied from  $0.7$  to  $0.9$ , while  $A$  is held constant. The dashed horizontal line at  $\beta = 0$  corresponding to an isotropic photoelectron angular distribution at all eKE is shown for clarity. The image inset in Figure 3.3 shows the calculated HOMO of  $\text{CH}_3^-$ , which results in  $f = 0.89$  (dashed blue curve), consistent with the experimental value. The measurements included in Figure 3.3 are summarized in Table 3.2.

The anisotropy data show experimental evidence of the  $sp^3$  hybridization of the pyramidal  $\text{CH}_3^-$  anion. The  $f$  factor of  $0.80$  indicates that the electron is detached from an orbital

whose wavefunction has approximately 80%  $p_z$ -character and 20%  $s$ -character. This is very similar to the expected  $f$  factor of 0.75 for an  $sp^3$  hybrid orbital. Interestingly, this  $f$  factor decreases to 0.74 if the  $B/A$  ratio is allowed to vary away from the assumed  $8/3$  (2.67). The resulting  $B/A$  ratio is then closer to 2, which is similar to the ratio derived for mixing the larger  $3s$  and  $3p$  hydrogenic orbitals.<sup>39</sup>

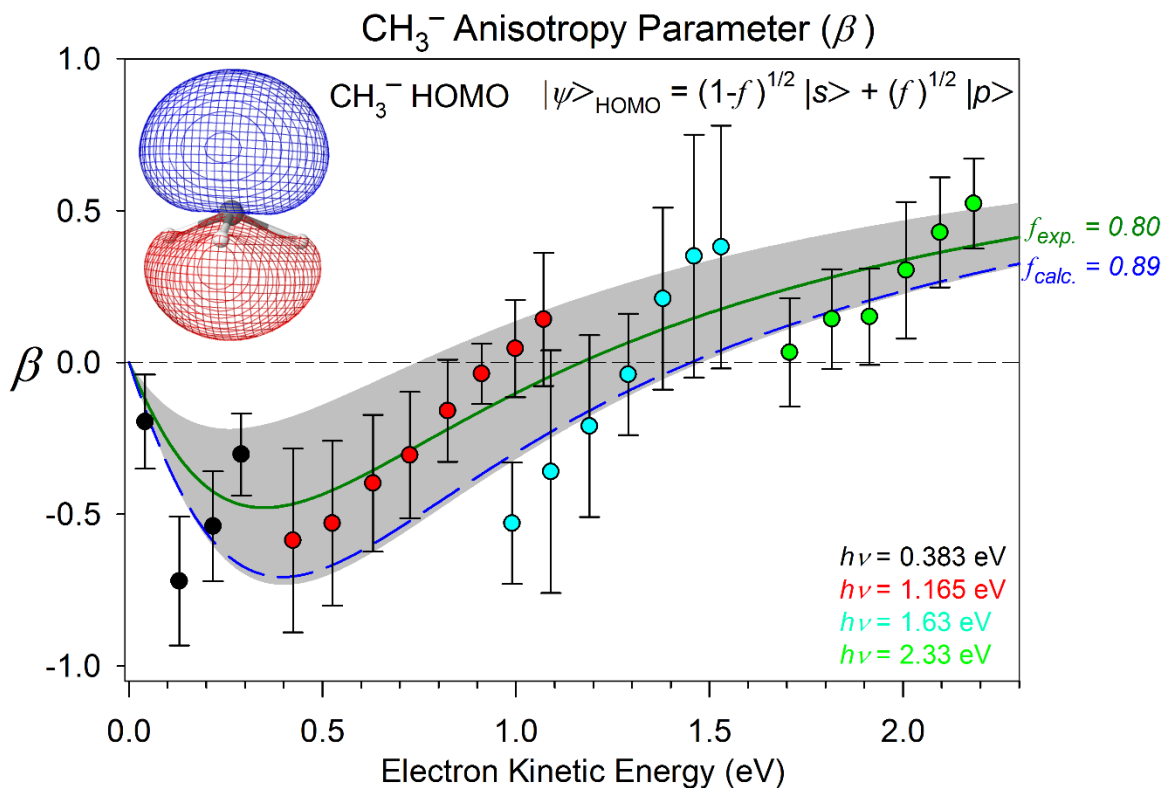


Figure 3.3: CH<sub>3</sub><sup>-</sup> photoelectron anisotropy parameter ( $\beta$ ) as a function of electron kinetic energy. The  $\beta$  values (circles) are from the peaks observed in the photoelectron spectra using 0.383 eV (black), 1.165 eV (red), 1.63 eV (blue), and 2.33 eV (green) photon energies. The best fit of Eq. (1) to the experimental data ( $f = 0.80$ ,  $A = 1.15$ ) is shown as the solid green curve and the calculated value from the CH<sub>3</sub><sup>-</sup> HOMO ( $f = 0.89$ ) is shown as the blue dashed curve. The grey shaded area shows the sensitivity of the  $f$  factor to the fit to the experimental values. Here, the  $f$  factor was varied by  $\pm 0.1$  while keeping  $A$  constant.

Table 3.2: Anisotropy parameter ( $\beta$ ) measurements for each peak in the  $\text{CH}_3^-$  photoelectron spectra used. The values are color coded to match Figure 3.3.

$\text{CH}_3 + e^- \leftarrow \text{CH}_3^-$		
eKE (eV)	$\beta$	$\nu_2' \leftarrow \nu_2''$
2.18	0.5(2)	1 $\leftarrow$ 0 <sup>+</sup>
2.10	0.4(2)	2 $\leftarrow$ 0 <sup>-</sup>
2.01	0.3(2)	3 $\leftarrow$ 0 <sup>+</sup>
1.91	0.2(3)	4 $\leftarrow$ 0 <sup>-</sup>
1.82	0.1(2)	5 $\leftarrow$ 0 <sup>+</sup>
1.71	0.0(1)	6 $\leftarrow$ 0 <sup>-</sup>
1.53	0.4(2)	0 $\leftarrow$ 0 <sup>+</sup>
1.46	0.4(4)	1 $\leftarrow$ 0 <sup>-</sup>
1.38	0.2(3)	2 $\leftarrow$ 0 <sup>+</sup>
1.29	0.0(2)	3 $\leftarrow$ 0 <sup>-</sup>
1.19	-0.2(3)	4 $\leftarrow$ 0 <sup>+</sup>
1.09	-0.4(4)	5 $\leftarrow$ 0 <sup>-</sup>
1.07	0.1(2)	0 $\leftarrow$ 0 <sup>+</sup>
1.00	0.0(2)	1 $\leftarrow$ 0 <sup>-</sup>
0.99	-0.5(4)	6 $\leftarrow$ 0 <sup>+</sup>
0.91	0.0(1)	2 $\leftarrow$ 0 <sup>+</sup>
0.82	-0.2(2)	3 $\leftarrow$ 0 <sup>-</sup>
0.73	-0.3(2)	4 $\leftarrow$ 0 <sup>+</sup>
0.63	-0.4(2)	5 $\leftarrow$ 0 <sup>-</sup>
0.53	-0.5(3)	6 $\leftarrow$ 0 <sup>+</sup>
0.42	-0.6(3)	7 $\leftarrow$ 0 <sup>-</sup>
0.29	-0.3(2)	0 $\leftarrow$ 0 <sup>+</sup>
0.22	-0.5(2)	1 $\leftarrow$ 0 <sup>-</sup>
0.13	-0.7(2)	2 $\leftarrow$ 0 <sup>+</sup>
0.04	-0.2(1)	3 $\leftarrow$ 0 <sup>-</sup>

### 3.3.c Vibrational structure and electron affinities

Because of the anion double well potential energy surface along the umbrella inversion coordinate (see Figure 3.4), the ground vibrational state is split into two levels of opposite parity with respect to the umbrella inversion. These inversion levels are labelled as  $0^+$ , the lower, even parity inversion level and  $0^-$ , the upper, odd parity inversion level. Figure 3.4 shows a schematic 1D representation (not to scale) of the potential energy surfaces of  $\text{CH}_3^-$  (black) and  $\bullet\text{CH}_3$  (green) as a function of umbrella inversion angle ( $\varphi$ ), where  $\varphi = 0^\circ$  represents the  $D_{3h}$  symmetry planar structure.

The anion and neutral potential energy curves were calculated by the methods described in section 3.4 and are the relaxed inversion potential for the anion, where at each value of  $\varphi$ , the C–H bond lengths are optimized. The wavefunctions shown in Figure 3.4 were calculated numerically using the Numerov method. The symmetries of the wavefunctions of these levels determine the selection rules in the photoelectron spectrum. The only allowed transitions (i.e. non-vanishing Franck-Condon factors) are from the anion  $v_2 (v'' = 0^+)$  to neutral  $v_2 (v' = 0, 2, 4 \dots)$ , and anion  $v_2 (v'' = 0^-)$  to neutral  $v_2 (v' = 1, 3, 5 \dots)$ . Note that the  $1^+$  level refers to the lower inversion  $v_2 (v'' = 1)$  level of the anions.

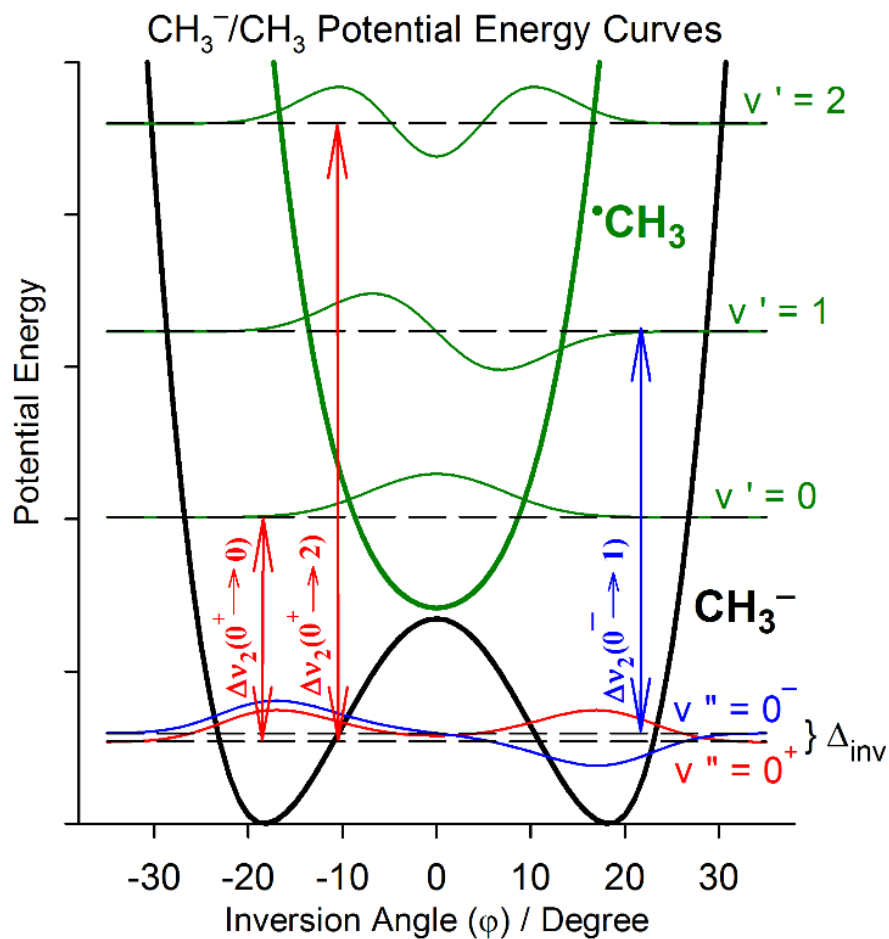


Figure 3.4: Schematic potential energy curves (not to scale) of  $\text{CH}_3^-$  (black) and  $\bullet\text{CH}_3$  (green) as a function of the inversion angle ( $\phi$ ). The red and blue arrows indicate the non-zero Franck-Condon factors from  $v'' = 0^+$  (even wavefunction in red) and  $v'' = 0^-$  (odd wavefunction in blue) in the anion ground state to even and odd quanta of the neutral state, respectively. The inversion splitting in the anion state is labelled  $\Delta_{\text{inv}}$ . See text for details.

The peaks labeled “A” in both spectra correspond to the  $\nu_2(\nu'' = 0^+ \rightarrow \nu' = 0)$  transition, with centers at 0.094(2) eV and 0.083(3) eV, respectively. After a small shift due to the unresolved rotational envelope<sup>41</sup> this results in adiabatic EAs of 0.093(3) eV and 0.082(4) eV for  $\bullet\text{CH}_3$  and  $\bullet\text{CD}_3$ , respectively. The uncertainties include a contribution due to the estimated  $150 \pm 50$  K anion rotational temperature. This EA( $\bullet\text{CH}_3$ ) is consistent with that of Ellison *et al.* of 0.08(3) eV,<sup>27</sup> but with an order of magnitude improvement in precision.

The first peak in the each progression, labelled as “a”, corresponds to a vibrational hot-band transition. The vibrational frequency of the  $\nu_2(\nu'' = 0^+ \rightarrow 1^+)$  umbrella mode in the anion is 444(13)  $\text{cm}^{-1}$  in  $\text{CH}_3^-$  and 373(12)  $\text{cm}^{-1}$  in  $\text{CD}_3^-$ . The spacing between adjacent peaks in the photoelectron spectra shown in Figure 3.1 and 3.2 gives the vibrational frequencies of  $\bullet\text{CH}_3$  or  $\bullet\text{CD}_3$ , respectively. The vibrational frequencies in the neutral state have been measured to very high precision by Yamada *et al.*<sup>5</sup> ( $\bullet\text{CH}_3$ ) and by Sears *et al.*<sup>7</sup> ( $\bullet\text{CD}_3$ ) using diode-laser IR absorption spectroscopy. Because of the aforementioned vibrational selection rules, however, the peaks in the photoelectron spectra are irregularly spaced compared to the neutral umbrella mode frequencies. Specifically, the transitions to the odd vibrational quanta in the neutral are red-shifted (to lower electron binding energy) by  $\Delta_{\text{inv}}$ , as Figure 3.4 shows. Thus, our measured relative peak-center positions and the high-resolution IR data will not be consistent unless  $\Delta_{\text{inv}}$  is taken into account. The equation below is a sample procedure to obtain the inversion splitting from the experimental data:

$$\Delta_{\text{inv}}(\text{CH}_3^-, 0^+ \rightarrow 0^-) = \nu_2(\bullet\text{CH}_3, 0 \rightarrow 3) + \text{eBE}[\text{A}(\nu'' = 0^+ \rightarrow \nu' = 0)] - \text{eBE}[\text{D}(\nu'' = 0^- \rightarrow \nu' = 3)] \quad (3.3)$$

This equation utilizes the high resolution measurement<sup>5</sup> of  $\bullet\text{CH}_3$   $\nu_2$  (0–3) levels and our determination of the eBE corresponding to the centers of peaks A and D; the primes and double primes represent  $\nu_2$  levels in the neutral and anion states, respectively. The equation is also generalized to the other observed peaks. A weighted least-squares minimization of the difference between the relative peak spacing and the high-resolution data, where  $\Delta_{\text{inv}}$  is the optimization parameter, is used to determine  $\Delta_{\text{inv}}$ . With this procedure, all measured frequencies are utilized in the determination of  $\Delta_{\text{inv}}$ . This procedure results in  $\Delta_{\text{inv}}$  of 21(5)  $\text{cm}^{-1}$  in  $\text{CH}_3^-$  and of 6(4)  $\text{cm}^{-1}$  in  $\text{CD}_3^-$ . The largest contribution to the reported uncertainties in the inversion splittings is due to the relative shift in the rotational band origin with increasing vibrational quanta, which is on the order of 4  $\text{cm}^{-1}$ .

The neutral  $\bullet\text{CH}_3/\bullet\text{CD}_3$  vibrational frequencies are shown in Table 3.3. These new data provide seven additional vibrational levels of the methyl radical, namely  $\nu_2$  (6-8) in  $\bullet\text{CH}_3$  and  $\nu_2$  (5-8) in  $\bullet\text{CD}_3$ . A quadratic fit of the vibrational level spacings as a function of vibrational quantum number results in vibrational constants  $\omega_2(\bullet\text{CH}_3) \sim 627 \text{ cm}^{-1}$ ,  $x_{22}(\bullet\text{CH}_3) \sim 18 \text{ cm}^{-1}$ ,  $\omega_2(\bullet\text{CD}_3) \sim 474 \text{ cm}^{-1}$ , and  $x_{22}(\bullet\text{CD}_3) \sim 11 \text{ cm}^{-1}$ , with deviations that fall within the error bars. The measured vibrational frequencies and spectroscopic constants are shown in Table 3.3. Experimentally determined properties of the anion and neutral, together with the theoretical results are summarized in Table 3.6.

Table 3.3: Observed umbrella mode ( $\nu_2$ ) vibrational frequencies and derived spectroscopic constants of neutral  $\cdot\text{CH}_3$  and  $\cdot\text{CD}_3$  ( $\text{cm}^{-1}$ ).

$\nu_2' \leftarrow \nu_2''$	$\cdot\text{CH}_3$		$\cdot\text{CD}_3$	
	Previous work	This work <sup>d</sup>	Previous work <sup>c</sup>	This work <sup>d</sup>
1 $\leftarrow$ 0	606.4531 <sup>a</sup>	606(10)	457.8136	460(10)
2 $\leftarrow$ 1	681.6369 <sup>a</sup>	688(8)	507.9297	510(10)
3 $\leftarrow$ 2	731.0757 <sup>a</sup>	734(7)	542.2841	542(10)
4 $\leftarrow$ 3	772(4) <sup>b</sup>	769(8)	568.6322	570(10)
5 $\leftarrow$ 4	811(4) <sup>b</sup>	790(9)		584(8)
6 $\leftarrow$ 5		830(8)		588(6)
7 $\leftarrow$ 6		845(6)		635(6)
8 $\leftarrow$ 7		864(4)		622(6)
Derived Spectroscopic Constants				
$\omega_2$		627(1) <sup>e</sup>		474(2) <sup>e</sup>
$x_{22}$		18(1) <sup>e</sup>		11(1) <sup>e</sup>
<sup>a</sup> Ref. 5, <sup>b</sup> Ref. 8, <sup>c</sup> Ref. 7				
<sup>d</sup> Values corrected by the inversion splitting. Uncertainties are described in the main text.				
<sup>e</sup> The reported uncertainty is the $1\sigma$ statistical error in a quadratic fit of the inversion corrected peak positions as a function of vibrational quantum number.				

### 3.4 Theoretical Methods and Results

#### 3.3.a Anion potential energy surface

The calculation of the anion potential energy surface uses a reduced dimension approximation instead of a full dimensional treatment. All HCH bond angles are constrained to be equal, thereby enforcing threefold symmetry. This leaves the three C–H bond lengths and the umbrella inversion angle  $\phi$  as the four unconstrained degrees of freedom. The constrained 4D potential energy surface calculation is justified through the use of test calculations on  $\text{NH}_3$  where there is only a few-percent error, which is adequate to meet the goals of these calculations.

The 4D potential energy surface was calculated using the CFOUR quantum chemistry package.<sup>42</sup> The  $J = 0$  nuclear motion calculations were performed using discrete variable representation (DVR) bases for the four active vibrational degrees of freedom and numerical evaluation of the kinetic energy operator, as implemented in the program NITROGEN.<sup>43</sup> The initial 4D potential energy surface was calculated at the CCSD(T)/d-aug-pVTZ level of theory using the CFOUR quantum chemistry package.<sup>42</sup> On this surface, the energy of the barrier height between the planar transition state and the pyramidal equilibrium geometry minima ( $E_B$ ) is  $555 \text{ cm}^{-1}$ . The  $E_B$  value is strongly dependent on the use of diffuse basis functions, as might be expected for this system since the extra electron is more weakly bound at the transition state. The effect of diffuse basis functions is shown in the first three rows of Table 3.4.

Initial vibrational calculations (see below) on the CCSD(T)/d-aug-pVTZ surface yielded ground state inversion splittings approximately one-half the measured values, indicating that the CCSD(T)/d-aug-pVTZ barrier height is probably too high. This reference value was then corrected for the following effects: 1) triple augmentation, 2) core correlation, 3) higher order

excitation terms in the correlation treatment (triples and non-iterative quadruples), and finally 4) extrapolation to the complete basis-set limit (leading to the “Total method/basis-set corrections”).

Additional contributions to the inversion barrier height include: 1) the diagonal Born-Oppenheimer correction (DBOC), 2) scalar relativistic effects including one- and two-electron Darwin and mass-velocity terms, and 3) zero point energy associated with degrees of freedom not explicitly included in the 4D model, namely the degenerate bending mode. All corrections described above are shown in Table 3.4, along with corrections to the electronic contribution to the electron affinity ( $\Delta E_{\text{elec}}$ ).

The diagonal Born-Oppenheimer correction (DBOC) arises from the non-separability of the nuclear and electronic degrees of freedom, and tends to be particularly large for molecules containing light nuclei. The DBOCs for  $\text{CH}_3^-/\text{CH}_3^-(\text{TS})/\text{CH}_3$  and  $\text{CD}_3^-/\text{CD}_3^-(\text{TS})/\text{CD}_3$  are:  $553/542/540 \text{ cm}^{-1}$  and  $456/450/450 \text{ cm}^{-1}$ , respectively, but largely cancel when we calculate  $E_{\text{B}}$  and  $\Delta E_{\text{elec}}$ .

Since the degenerate bending mode ( $\nu_4$ ) is not explicitly included in the 4D electronic potential energy surface calculation, we approximately account for this orthogonal mode by including the change in ZPE of  $\nu_4$  between the anion minima and the transition-state. At the CCSD(T)/d-aug-pVTZ level of theory, the harmonic frequency of the degenerate bending mode  $\nu_4$  ( $\omega_{\text{bend}}$ ) at the transition state ( $1379 \text{ cm}^{-1}$ ) is reduced by  $38 \text{ cm}^{-1}$  relative to its value at the equilibrium geometry ( $1417 \text{ cm}^{-1}$ ).

Taking these corrections to be independent, the reported calculated  $E_{\text{B}}$  and  $\Delta E_{\text{elec}}$  are obtained by adding all the corrections (which do not include the first line of Table 3.4) to the

initial CCSD(T)/d-aug-pVTZ result (shown in bold). This results in a calculated best estimate for the barrier height of 386 cm<sup>-1</sup>, a nearly 25% reduction of the original CCSD(T)/d-aug-pVTZ value of 555 cm<sup>-1</sup>. Given that the best estimate barrier height is significantly lower than the CCSD(T)/d-aug-pVTZ value (386 cm<sup>-1</sup>), we construct a scaled potential surface,  $V_s$ , in terms of the raw CCSD(T)/d-aug-pVTZ potential energy surface,  $V_0$ , as follows:

$$V_s(\vec{q}) = [V_0(\vec{q}) - V_0(\vec{r}, \vec{\varphi}_{eq})] \times \left( 1 - \frac{\Delta_{TS} \theta(|\varphi_{eq}| - |\varphi|)}{V_0(\vec{q}_{TS}) - V_0(\vec{r}_{TS}, \varphi_{eq})} \right) + V_0(\vec{r}, \varphi_{eq}) \quad (3.4)$$

where  $\vec{q} = (\vec{r}, \varphi) = (r_1, r_2, r_3, \varphi)$ ,  $\Delta_{TS}$  is the total transition state energy correction (defined as positive when the corrections lower the barrier height), and  $\theta(x)$  is the Heaviside step function. The form of this scaling is such that  $V_s(\vec{q}_{TS}) = V_0(\vec{q}_{TS}) - \Delta_{TS}$ , as desired. The step function ensures that only points with geometries closer to planarity than the equilibrium geometry ( $|\varphi| < |\varphi_{eq}|$ ) are scaled, while the continuity of the surface is maintained. This procedure is validated by the agreement between our calculated and measured values for the inversion splitting, as described below. This scaled surface is used to calculate the anion umbrella vibrational frequency and inversion splitting. The calculated ground state inversion splittings for CH<sub>3</sub><sup>-</sup> and CD<sub>3</sub><sup>-</sup> are 25.0 and 7.9 cm<sup>-1</sup>, respectively. This is in excellent agreement with our measured values of 21(5) and 6(4) cm<sup>-1</sup>. The anion  $\nu_2$  ( $v'' = 0^+ \rightarrow 1^+$ ) calculated frequencies are 412.3 and 335.9 cm<sup>-1</sup> for CH<sub>3</sub><sup>-</sup> and CD<sub>3</sub><sup>-</sup>, respectively, which are also in reasonably good agreement with the experimental values of 444(13) and 373(12) cm<sup>-1</sup>.

Table 3.4: Computational results for the  $\text{CH}_3^-/\text{CD}_3^-$  4D transition state barrier height ( $E_B$ ) and  ${}^*\text{CH}_3/{}^*\text{CD}_3$  electronic contribution to the electron affinity ( $\Delta E_{\text{elec}}$ ). The initial reference calculation at the CCSD(T)/d-aug-pVTZ level of theory, to which the corrections are applied, is shown in bold. All values are given in wavenumbers ( $\text{cm}^{-1}$ ).

<i>Method/basis-set</i>	$E_B^a$	$\Delta(E_B)^b$	$\Delta E_{\text{elec}}^c$	$\Delta(\Delta E_{\text{elec}})^d$
CCSD(T)/aug-pVTZ	972 $\text{cm}^{-1}$	+417 $\text{cm}^{-1}$	-76 $\text{cm}^{-1}$	-255 $\text{cm}^{-1}$
<b>CCSD(T)/d-aug-pVTZ (ref. calc.)</b>	<b>555</b>	<b>0</b>	<b>179</b>	<b>0</b>
CCSD(T)/t-aug-pVTZ	503 <sup>e</sup>	-52	184	5
AE-CCSD(T)/d-aug-cc-pCVTZ	537	-18	158	-21
CCSDT(Q)/d-aug-pVTZ	518	-37	253	74
CCSD(T) basis-set extrapolation <sup>f</sup>	545	-10	375	196
<i>Total method/basis-set corrections</i>	<i>438</i>	<i>-117</i>	<i>433</i>	<i>254</i>
<i>Further corrections</i>				
DBOC <sup>g</sup>	---	1.833	---	1.857
Darwin correction <sup>h</sup>	---	3	---	-4
$\omega_{\text{bend}}(\text{TS}) - \omega_{\text{bend}}(\text{min})$	---	1.9	---	---
<i>Final Reported Calculation</i>	<i>386/410</i>	<i>---</i>	<i>415/421</i>	<i>---</i>
<sup>a</sup> Planar anion transition state 4D barrier height <sup>b</sup> Difference between $E_B$ at CCSD(T)/d-aug-pVTZ and $E_B$ at this level of calculation. <sup>c</sup> Difference between anion minimum and neutral minimum ( <i>i.e.</i> without zero-point energy corrections) <sup>d</sup> Difference between $\Delta E_{\text{elec}}$ at CCSD(T)/d-aug-pVTZ and $\Delta E_{\text{elec}}$ at this level of calculation. <sup>e</sup> For the anion transition state CCSD(T)/t-aug-pVTZ calculation only, d-aug orbitals were used on the hydrogens, and the energy was calculated at the CCSD(T)/d-aug-pVTZ transition state geometry. <sup>f</sup> Extrapolation of CCSD(T)/d-aug-pVXZ (X=T,Q,5) values. <sup>g</sup> Diagonal Born-Oppenheimer correction calculated at SCF/d-aug-pVTZ plus CCSD corrections calculated with an aug-pVTZ basis. The values refer to the $\text{CH}_3/\text{CD}_3$ systems respectively. <sup>h</sup> Calculated with MP2/d-aug-pCVTZ .				

### 3.4.b Photoelectron Spectra and Electron Affinities

In order to calculate photoelectron spectra, we determine Franck-Condon factors (FCFs) by direct computation of vibrational overlap integrals between the anion and neutral DVR wavefunctions. The simulated spectra for  $\text{CH}_3^-$  and  $\text{CD}_3^-$  are shown, respectively, in the lower panels of Figures 3.1 and 3.2. The Franck-Condon factors (green sticks) were convolved with Gaussians of varying FWHM that match the experimental resolution (blue trace), where the calculated FCFs are directly proportional to the area of each peak. The calculated spectrum was shifted such that the origin transition coincides with the origin of the experimental spectra. Despite their approximate nature, the simulated spectra match the experimental spectra quite well, with the main Franck-Condon envelope clearly reproduced.

The calculated values of the electronic contribution to the electron affinity,  $\Delta E_{\text{elec}}$ , at the same levels of theory as those used to determine the barrier height correction  $\Delta\text{TS}$  are given in Table 3.4.  $\Delta E_{\text{elec}}$  is the energy difference between the anion and the neutral potential energy minima; comparison with the experimentally measured adiabatic EA requires a determination of the anion and neutral ZPEs, since  $\text{EA} = \Delta E_{\text{elec}} + \Delta(\text{ZPE})$ . Here, we estimate a total  $\Delta E_{\text{elec}}$  of  $415 \text{ cm}^{-1}$ , or  $0.051 \text{ eV}$ , around half the measured EA values. This yields calculated EAs for  $\bullet\text{CH}_3$  and  $\bullet\text{CD}_3$  of  $0.094$  and  $0.084 \text{ eV}$ , respectively. We conservatively estimate that the ZPE and electronic contributions to the calculated EA have a total uncertainty of  $100 \text{ cm}^{-1}$  (ca.  $0.010 \text{ eV}$ ), to which the electronic part is the main contributor. These results, together with the experimental findings are reported in Table 3.6.

## 3.5 Discussion

### 3.5.a Gas-phase Acidities

With the more accurately experimentally determined value for EA( $\bullet$ CH<sub>3</sub>) and the new experimental measurement of EA( $\bullet$ CD<sub>3</sub>), we can obtain the gas-phase acidity at 0 K of CH<sub>4</sub> and CD<sub>4</sub>. The below equation shows how the gas-phase acidity of CH<sub>4</sub> is obtained through the thermochemical cycle (see Chapter 2) using D<sub>0</sub>(CH<sub>3</sub>-H) is the bond dissociation energy of the C-H bond in methane (103.340(16) kcal/mol),<sup>44</sup> IE(H) and the EA( $\bullet$ CH<sub>3</sub>) of 2.14(6) kcal/mol as reported here.

$$\Delta_{\text{acid}}H_{0\text{K}}^{\circ}(\text{CH}_4) = D_0(\text{CH}_3\text{-H}) + \text{IE}(\text{H}) - \text{EA}(\text{CH}_3) \quad (3.5)$$

An analogous procedure is followed to obtain the  $\Delta_{\text{acid}}H_{0\text{K}}^{\circ}$  of CD<sub>4</sub> using the corresponding D<sub>0</sub>( $\bullet$ CD<sub>3</sub>-D) = 105.80(3) kcal/mol,<sup>45</sup> IE(D) = 313.67 kcal/mol,<sup>46</sup> and EA( $\bullet$ CD<sub>3</sub>) = 1.90(8) kcal/mol. We obtain gas-phase acidities  $\Delta_{\text{acid}}H_{0\text{K}}^{\circ}(\text{CH}_4) = 414.79(6)$  kcal/mol and  $\Delta_{\text{acid}}H_{0\text{K}}^{\circ}(\bullet\text{CD}_4) = 417.57(8)$  kcal/mol. Compared to the previously determined value for CH<sub>4</sub> of 415.2(7) kcal/mol, this new value is consistent but with an order of magnitude improvement in precision, a consequence of the better determined electron affinities. In order to obtain the gas-phase acidities at 298 K, we use the thermal correction  $H_{298\text{K}}^{\circ} - H_{0\text{K}}^{\circ} = \int_0^{298.15} C_p(T) dT$  where  $C_p(T)$  is the heat-capacity at constant pressure of the individual species.<sup>47</sup> Here, the thermal corrections for CH<sub>4</sub>, H<sup>+</sup> and D<sup>+</sup> are obtained from the Active Thermochemical Tables<sup>44</sup> and are non rigid-rotor/anharmonic oscillator (NRRAO) values. For CD<sub>4</sub>, the thermal correction was obtained from Pamidimukkala *et al.*<sup>48</sup> For CH<sub>3</sub><sup>-</sup> and CD<sub>3</sub><sup>-</sup>, the heat capacities are calculated from the partition functions of the isolated molecules. Here, the rotational contributions to the partition function are calculated in a rigid-rotor approximation using the calculated rotational constants,

while the vibrational contributions are calculated from an explicit sum over the vibrational energy levels of the normal modes. We rely on the measured vibrational frequencies (when available) in conjunction with the calculated frequencies. The thermal corrections are summarized in Table 3.5. This leads to  $\Delta_{\text{acid}}H_{298\text{K}}^{\circ}(\text{CH}_4) = 416.4(2)$  kcal/mol, also in agreement with Ervin's value of 416.8(7) kcal/mol, and  $\Delta_{\text{acid}}H_{298\text{K}}^{\circ}(\text{CD}_4) = 419.2(2)$  kcal/mol.

Table 3.5: Thermal corrections ( $H_{298\text{K}}^{\circ} - H_{0\text{K}}^{\circ} = \int_0^{298.15} C_p(T) dT$ ) for the individual species in the methane deprotonation thermochemical cycle.

Species	$H_{298\text{K}}^{\circ} - H_{0\text{K}}^{\circ}$ (kcal/mol)
$\text{CH}_3^-$	2.554
$\text{H}^+$	1.481
$\text{CH}_4$	2.396
$\text{CD}_3^-$	2.572
$\text{D}^+$	1.481
$\text{CD}_4$	2.473

### 3.5.b Inversion Splitting, Electron Affinity, and Anion Potential Energy Surface

The inversion splittings of isoelectronic species  $\text{NH}_3$  and  $\text{H}_3\text{O}^+$  and their isotopologues have been determined previously to very high precision. The corresponding experimental values are  $0.793\text{ cm}^{-1}$  and  $0.053\text{ cm}^{-1}$  for  $\text{NH}_3$  and  $\text{ND}_3$ , and  $55.35\text{ cm}^{-1}$  and  $15.36\text{ cm}^{-1}$  for  $\text{H}_3\text{O}^+$  and  $\text{D}_3\text{O}^+$  respectively.<sup>19–21,24,25</sup> One of the most valuable results theoretical calculations can give us is the barrier to inversion, since it is not an experimentally measurable quantity. In previous work, Rajamäki *et al.*<sup>49,50</sup> conducted high level 6D potential energy surface calculations of  $\text{NH}_3$ ,  $\text{H}_3\text{O}^+$  and their isotopologues, comparing the calculated vibrational frequencies of the umbrella mode and inversion splittings with experimental data. They achieve sub-wavenumber accuracy for the inversion splittings and report the associated calculated barrier height as are  $650\text{ cm}^{-1}$  for  $\text{H}_3\text{O}^+$  and  $1782\text{ cm}^{-1}$  for  $\text{NH}_3$ . However, the  $\text{CH}_3^-$  system presents a larger challenge for accurate theoretical treatment of the potential energy curve compared to  $\text{NH}_3$  or  $\text{H}_3\text{O}^+$  since neither of these simpler species present the possibility of electron autodetachment at planarity.

With this measurement of  $\Delta_{\text{inv}}$  and the fundamental anion  $\nu_2$  frequency, some of the most important parameters are now known in order to accurately map out the potential energy surface of the anion. The calculations reported herein reproduce the experimental spectra very well, but most importantly, reproduce the  $\Delta_{\text{inv}}$  and the fundamental  $\nu_2$  frequency ( $\nu'' = 0^+ \rightarrow 1^+$ ) of the anion umbrella mode. This gives us confidence in our effective barrier to inversion. Note that in section 3.4 we report a 4D inversion barrier of circa  $400\text{ cm}^{-1}$  which includes the ZPE of the degenerate bending mode. The effective 1D barrier height ( $E_{\text{B}}^{\text{eff}}$ ), on the other hand, includes the zero-point contributions from the remaining stretching vibrational modes, (which differs substantially between the pyramidal and planar geometries, indicating a strong cross-anharmonicity between the inversion motion and the CH stretches) resulting in an effective 1D

barrier of  $661\text{ cm}^{-1}$ . Our effective 1D barrier is reasonably close to that found by Kraemer *et al.*<sup>33</sup> (*ca.*  $833\text{ cm}^{-1}$ ), and the tunneling splittings calculated in their work are similar to ours ( $25.0$  and  $7.9$  for  $\text{CH}_3^-$  and  $\text{CD}_3^-$ , respectively, from the present calculations *versus*  $19$  and  $4\text{ cm}^{-1}$  in Ref.47). However, it should be emphasized here that our tunneling calculations are based on a multidimensional model, and a focus on 1D barriers and their dynamics can be misleading. For example, work by Rajamäki *et al.*,<sup>49,50</sup> indicates that the 1D effective barrier for the hydronium ion inversion is comparable to that calculated here for methide, but the magnitude of the tunneling splitting is significantly greater in the former ( $55\text{ cm}^{-1}$  *versus*  $21\text{ cm}^{-1}$ ). While this is surprising at first, the anharmonicities associated with inversion are greater in methide than in hydronium, which is ultimately responsible for the quite different tunneling splittings, underscoring the sensitivity of this quantity to details of the multidimensional potential surface.

The most recent theoretical work by Dixon *et al.*,<sup>34</sup> at the CCSD(T) level of theory with aug-cc-pVxZ ( $x = \text{D, T, Q}$ ) basis sets, found that the stability of the anion increases with the size of the basis set used. From a complete basis set extrapolation, they predicted a best-estimate adiabatic EA of  $0.07(1)\text{ eV}$ , which is in relatively good agreement with the experimentally determined value. They report that 63% of the EA comes from  $\Delta\text{ZPE}$  contributions between the anion and neutral species and that most of their uncertainty comes from the calculation of the anion ZPE. However, the calculated fundamental vibrational frequencies of the  $\nu_2$  mode were reported as  $783.8\text{ cm}^{-1}$  for  $\text{CH}_3^-$  and  $496.6\text{ cm}^{-1}$  for  $\bullet\text{CH}_3$ , considerably different from the experimental values of  $444(13)\text{ cm}^{-1}$  (this work) and  $606.4531\text{ cm}^{-1}$  (Ref. 5), respectively. Also, the calculations show an inversion barrier of  $720.5\text{ cm}^{-1}$  and suggest that the electron is not bound at planarity, i.e. the electronic potential energy surfaces cross before the  $D_{3h}$  geometry is attained. Considering their calculated anion fundamental  $\nu_2$  ( $784\text{ cm}^{-1}$ ), the  $\nu_2$  ( $\nu'' = 1^+$ )

vibrational level would be considerably higher than the neutral ZPE (by  $420\text{ cm}^{-1}$ ), and therefore the  $\nu_2$  ( $v'' = 1^+$ ) anion would be unstable with respect to electron autodetachment, a finding that contradicts our observation of this level persisting for at least several milliseconds.

Unfortunately, there is no reported calculation of the  $\Delta_{\text{inv}}$  in the most recent work from Dixon *et al.* to compare with our experimental and calculated values. With the large basis sets including diffuse functions and the high level treatment of correlation effects used here, we did not experience the issue of electron autodetachment at planarity. Accordingly, our quantum mechanical treatment is entirely adiabatic, an assumption that seems to be borne out by the agreement with experiment. The intersection between the anion and neutral potential energy surfaces remains an open question. The anion is electronically stable at the anion planar transition state, but unstable at the neutral equilibrium geometry. However, we predict that the uncertainty in the calculated value of  $\Delta E_{\text{elec}}$  is around  $100\text{ cm}^{-1}$ , which is enough to move the seam of intersection between anion and neutral surfaces. Indeed, the close energy spacing of the anion and neutral adiabatic surfaces over such a large range of geometries suggests that it is inappropriate to consider anion autodetachment by examining the bare adiabatic surfaces without explicitly including the effects of vibrational motion.

### 3.6 Conclusions

In this chapter, we report high-resolution gas-phase photoelectron spectra of  $\text{CH}_3^-$  and  $\text{CD}_3^-$ , the simplest carbanions. This experiment was possible due to the generation of a stable intense beam of  $\text{CH}_3^-$  anion using the dual valve plasma entrainment source. We determine a much more accurate value of  $0.093(3)\text{ eV}$  for the  $\bullet\text{CH}_3$  electron affinity, as well as that of  $\bullet\text{CD}_3$ ,  $0.082(4)\text{ eV}$ . With these measured EAs, we determine improved values for 0 K gas-phase acidities of  $\text{CH}_4$  and  $\text{CD}_4$  as  $414.79(6)\text{ kcal/mol}$  and  $417.58(8)\text{ kcal/mol}$ , respectively. With the

available high-resolution vibrational spectroscopy data, we are able to report the first experimental determination of the inversion splitting in  $\text{CH}_3^-$  and  $\text{CD}_3^-$  as  $21(5) \text{ cm}^{-1}$  and  $6(4) \text{ cm}^{-1}$ . We also measure the  $\nu_2 (\nu'' = 0^+ \rightarrow 1^+)$  frequency in  $\text{CH}_3^-$  and  $\text{CD}_3^-$  as  $444(13)$  and  $373(12) \text{ cm}^{-1}$ , respectively and add a collection of overtone frequencies of the umbrella mode of methyl radical. The calculations reported herein are consistent with the experimental findings to a high degree of accuracy. With this in mind, we report a calculated barrier to inversion  $E_B$  of  $386/480 \text{ cm}^{-1}$  for  $\text{CH}_3^-/\text{CD}_3^-$ . The dependence of photoelectron angular distributions anisotropy on photoelectron kinetic energy affirms that the methide anion HOMO arises primarily from  $sp^3$  hybridization. These results provide a benchmark for further theoretical studies of the methide anion. The major results of this work are summarized below in Table 3.6. Questions that remain unanswered and require further theoretical treatment of this system include issues associated with a possible anion/neutral electronic potential energy surface crossing in the vicinity of the planar geometry

Table 3.6: Summary of major results, experimental and theoretical.

	Experiment	Calculation
EA( $\bullet\text{CH}_3$ )	0.093(3) eV	0.094 eV
$\Delta_{\text{Inv}}(\text{CH}_3^-, \nu_2 0^+ \rightarrow 0^-)$	21(5) $\text{cm}^{-1}$	25.0 $\text{cm}^{-1}$
$\text{CH}_3^-, \nu_2(0^+ \rightarrow 1^+)$	444(13) $\text{cm}^{-1}$	412.3 $\text{cm}^{-1}$
$\Delta_{\text{acid}}\text{H}_{0\text{K}}^0(\text{CH}_4)$	414.79(6) kcal/mol	-
$\Delta_{\text{acid}}\text{H}_{298\text{K}}^0(\text{CH}_4)$	416.4(2) kcal/mol	-
EA( $\bullet\text{CD}_3$ )	0.082(4) eV	0.084 eV
$\Delta_{\text{Inv}}(\text{CD}_3^-, \nu_2 0^+ \rightarrow 0^-)$	6(4) $\text{cm}^{-1}$	7.9 $\text{cm}^{-1}$
$\text{CD}_3^-, \nu_2(0^+ \rightarrow 1^+)$	373(12) $\text{cm}^{-1}$	335.9 $\text{cm}^{-1}$
$\Delta_{\text{acid}}\text{H}_{0\text{K}}^0(\text{CD}_4)$	417.58(8) kcal/mol	-
$\Delta_{\text{acid}}\text{H}_{298\text{K}}^0(\text{CD}_4)$	419.2(2) kcal/mol	-

### 3.7 Chapter 3 references

- <sup>1</sup> G. Herzberg and J. Shoosmith, *Can. J. Phys.* **34**, 523 (1956).
- <sup>2</sup> G. Herzberg, *Proc. R. Soc. London Ser. A - Math. Phys. Sci.* **262**, 291 (1961).
- <sup>3</sup> M.E. Jacox, *J. Mol. Spectrosc.* **66**, 272 (1977).
- <sup>4</sup> J. Dyke, E. Lee, and A. Morris, *J. Chem. Soc. Trans. II* **72**, 1385 (1976).
- <sup>5</sup> C. Yamada, E. Hirota, and K. Kawaguchi, *J. Chem. Phys.* **75**, 5256 (1981).
- <sup>6</sup> J.M. Frye, T.J. Sears, and D. Leitner, *J. Chem. Phys.* **88**, 5300 (1988).
- <sup>7</sup> T.J. Sears, J.M. Frye, V. Spirko, and W.P. Kraemer, *J. Chem. Phys.* **90**, 2125 (1989).
- <sup>8</sup> H.W. Hermann and S.R. Leone, *J. Chem. Phys.* **76**, 4759 (1982).
- <sup>9</sup> D.W. Schwenke, *Spectrochim. Acta Part A - Mol. Biomol. Spectrosc.* **55**, 731 (1999).
- <sup>10</sup> M. Zahedi, J.A. Harrison, and J.W. Nibler, *J. Chem. Phys.* **100**, 4043 (1994).
- <sup>11</sup> S. Davis, D.T. Anderson, G. Duxbury, and D.J. Nesbitt, *J. Chem. Phys.* **107**, 5661 (1997).
- <sup>12</sup> W.M. Fawzy, T.J. Sears, and P.B. Davies, *J. Chem. Phys.* **92**, 7021 (1990).
- <sup>13</sup> J.T. Miller, K.A. Burton, R.B. Weisman, W.X. Wu, and P.S. Engel, *Chem. Phys. Lett.* **158**, 179 (1989).
- <sup>14</sup> P.R. Peoples and J.B. Grutzner, *J. Am. Chem. Soc.* **102**, 4709 (1980).
- <sup>15</sup> V. Vuitton, P. Lavvas, R. V Yelle, M. Galand, A. Wellbrock, G.R. Lewis, A.J. Coates, and J.E. Wahlund, *Planet. Space Sci.* **57**, 1558 (2009).
- <sup>16</sup> L.A. Capone, R.C. Whitten, J. Dubach, S.S. Prasad, and W.T. Huntress, *Icarus* **28**, 367 (1976).
- <sup>17</sup> W.J. Borucki, Z. Levin, R.C. Whitten, R.G. Keesee, L.A. Capone, A.L. Summers, O.B. Toon, and J. Dubach, *Icarus* **72**, 604 (1987).
- <sup>18</sup> A.J. Coates, F.J. Crary, G.R. Lewis, D.T. Young, J.H. Waite, and E.C. Sittler, *Geophys. Res. Lett.* **34**, L22103 (2007).
- <sup>19</sup> C.E. Cleeton and N.H. Williams, *Phys. Rev.* **45**, 234 (1934).
- <sup>20</sup> L.H. Jones, *J. Mol. Spectrosc.* **74**, 409 (1979).
- <sup>21</sup> S.N. Murzin and O.N. Stepanov, *Opt. i Spektrosk.* **69**, 497 (1990).
- <sup>22</sup> J.P. Gordon, T.C. Wang, H.J. Zeiger, and C.H. Townes, *Science* **120**, 780 (1954).
- <sup>23</sup> J.P. Gordon, H.J. Zeiger, and C.H. Townes, *Phys. Rev.* **95**, 282 (1954).
- <sup>24</sup> D.J. Liu and T. Oka, *Phys. Rev. Lett.* **54**, 1787 (1985).
- <sup>25</sup> T.J. Sears, P.R. Bunker, P.B. Davies, S.A. Johnson, and V. Spirko, *J. Chem. Phys.* **83**, 2676 (1985).
- <sup>26</sup> M. Araki, H. Ozeki, and S. Saito, *J. Chem. Phys.* **109**, 5707 (1998).

- <sup>27</sup> G.B. Ellison, P.C. Engelking, and W.C. Lineberger, *J. Am. Chem. Soc.* **100**, 2556 (1978).
- <sup>28</sup> N. Tyminska, M. Wloch, and A.T. Royappa, *Int. J. Quantum Chem.* **115**, 42 (2015).
- <sup>29</sup> C.H. DePuy, S. Gronert, S.E. Barlow, V.M. Bierbaum, and R. Damrauer, *J. Am. Chem. Soc.* **111**, 1968 (1989).
- <sup>30</sup> Z.X. Tian, B. Chan, M.B. Sullivan, L. Radom, and S.R. Kass, *Proc. Natl. Acad. Sci. U. S. A.* **105**, 7647 (2008).
- <sup>31</sup> S.T. Graul and R.R. Squires, *J. Am. Chem. Soc.* **111**, 892 (1989).
- <sup>32</sup> S.E. Mitchell, P.M. Conklin, and J.W. Farley, *J. Chem. Phys.* **118**, 11017 (2003).
- <sup>33</sup> W.P. Kraemer, V. Špirko, P.-A. Malmqvist, and B.O. Roos, *J. Mol. Spectrosc.* **147**, 526 (1991).
- <sup>34</sup> D.A. Dixon, D. Feller, and K.A. Peterson, *J. Phys. Chem. A* **101**, 9405 (1997).
- <sup>35</sup> Y.-J. Lu, J.H. Lehman, and W.C. Lineberger, *J. Chem. Phys.* **142**, 44201 (2015).
- <sup>36</sup> J. Cooper and R.N. Zare, *J. Chem. Phys.* **48**, 942 (1968).
- <sup>37</sup> A. Sanov, E.R. Grumbling, D.J. Goebbert, and L.M. Culberson, *J. Chem. Phys.* **138**, 54311 (2013).
- <sup>38</sup> E.R. Grumbling and A. Sanov, *J. Chem. Phys.* **135**, 164302 (2011).
- <sup>39</sup> A. Sanov, *Annu. Rev. Phys. Chem.* **65**, 341 (2014).
- <sup>40</sup> R. Mabbs, E.R. Grumbling, K. Pichugin, and A. Sanov, *Chem. Soc. Rev.* **38**, 2169 (2009).
- <sup>41</sup> P.C. Engelking, *J. Phys. Chem.* **90**, 4544 (1986).
- <sup>42</sup> J. Gauss, M.E. Harding, and P.G. Szalay, CFOUR Coupled-Cluster Techniques for Computational Chemistry, with contributions from A.A. Auer, R.J. Bartlett, U. Benedikt, C. Berger, D.E. Bernholdt, Y.J. Bomble, available online at [www.cfour.de](http://www.cfour.de), 2015.
- <sup>43</sup> P.B. Changala, NITROGEN Numerical and Iterative Techniques for Rovibronic Energies with General Internal Coordinates, a program written by P. B. Changala, available online at [colorado.edu/nitrogen](http://colorado.edu/nitrogen), 2015.
- <sup>44</sup> B. Ruscic, *J. Phys. Chem. A* **119**, 7810 (2015).
- <sup>45</sup> Y. Song, X.M. Qian, K.C. Lau, and C.Y. Ng, *Chem. Phys. Lett.* **347**, 51 (2001).
- <sup>46</sup> U.D. Jentschura, S. Kotochigova, E.O. LeBigot, P.J. Mohr, and B.N. Taylor, The Energy Levels of Hydrogen and Deuterium (Version 2.1), National Institute of Standards and Technology, Gaithersburg, MD, available online at [physics.nist.gov/PhysRefData/HDEL/energies.html](http://physics.nist.gov/PhysRefData/HDEL/energies.html), 2017.
- <sup>47</sup> K.M. Ervin and V.F. DeTuro, *J. Phys. Chem. A* **106**, 9947 (2002).
- <sup>48</sup> K.M. Pamidimukkala, D. Rogers, and G.B. Skinner, *J. Phys. Chem. Ref. Data* **11**, 83 (1982).
- <sup>49</sup> T. Rajamaki, A. Miani, and L. Halonen, *J. Chem. Phys.* **118**, 10929 (2003).
- <sup>50</sup> T. Rajamaki, A. Miani, and L. Halonen, *J. Chem. Phys.* **118**, 6358 (2003).

*this page is intentionally left blank*

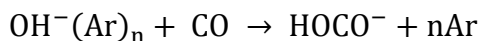
## CHAPTER IV

### PHOTOELECTRON SPECTROSCOPY OF THE NITROUS ACID ANION (HONO<sup>-</sup>)

This chapter is partially reproduced from: *Oliveira, A.M, Lehman, J.H., McCoy, A.B., Lineberger, W.C., Journal of the Physical Chemistry A, vol. 120, p. 1652 – 1660 (2016)* with permission of the authors.

#### 4.1 Introduction

In the previous chapter, where we reported the photoelectron spectroscopy of CH<sub>3</sub><sup>-</sup>, we explored the ion source capability of generating exotic species in the glow discharge, taking advantage of the crossed argon expansion to cool and stabilize the plasma. In this next project we desire to explore the synthetic capabilities of this source. As mentioned in Chapter 2, a discharge source of ions is usually faced as a “black magic” source, where it is hard to predict all the generated species. While this might provide the opportunity of generating exotic species, a more rational approach to generating ions is of great interest, since it allows us to synthesize gas phase anions to our needs. While the synthetic capability of this ions source via ion molecule reactions was demonstrated in Ref. 1, through:



HONO<sup>-</sup> is the first time where an anion with unreported photoelectron spectra was studied with this ion source. The practical reasons choosing HONO<sup>-</sup> are that we are able to generate very large quantities of OH<sup>-</sup>(Ar)<sub>n</sub> clusters, and NO is available from gas suppliers and is one of the few radicals one can obtain directly from a gas cylinder.

Scientifically, HONO is a major source of OH radicals in the troposphere.<sup>2-5</sup> HONO is predicted to be formed at night by heterogeneous conversion<sup>3</sup> and disproportionation of nitrogen dioxide (NO<sub>2</sub>) through reactions with water or hydrocarbons, as well as by direct emissions in polluted urban areas.<sup>3</sup> The central O–N bond is broken following irradiation by sunlight between 300 and 400 nm, giving rise to OH radicals in the atmosphere.<sup>6</sup> Because of its atmospheric importance, HONO has been the subject of many investigations, both theoretical<sup>7-9</sup> and experimental.<sup>10-21</sup> Microwave<sup>19,22</sup> and Fourier transform infrared spectroscopic studies<sup>14,15</sup> of HONO in its ground electronic state determined the structure, rotational constants, and six fundamental frequencies of both *cis* and *trans* isomers. In addition, the weakest bond in HONO was determined to be the central O–N bond, with a ground state bond dissociation energy of 2.079 eV for the lower energy *trans* isomer.<sup>17,23</sup>

The electronic states of HONO have also been investigated, with experimental studies using photon energies spanning UV to deep UV wavelengths to access high-lying electronic states, giving rise to the production of either OH + NO or H + NO<sub>2</sub> in the atmosphere. Using UV absorption spectroscopy, the  $\tilde{A}^1A''$  (S<sub>1</sub>) state of *cis*-HONO was observed to be 3.26 eV higher in energy than the  $\tilde{X}^1A'$  (S<sub>0</sub>) ground state.<sup>24,25</sup> Vertical excitation from the ground electronic state to the S<sub>1</sub> surface, which is repulsive along the HO–NO bond dissociation coordinate, results in breaking the central O–N bond. This is likely to be the atmospheric pathway for OH radical formation.<sup>26</sup> Yu *et al.*<sup>8</sup> performed complete active space (CAS) calculations on the *trans* isomer of HONO, investigating the four lowest energy singlet and triplet excited electronic states and their stabilities with respect to the HO–NO bond dissociation. The lowest energy excited state, the  $\tilde{a}^3A''$  (T<sub>1</sub>) state, was calculated to be approximately 2.3 eV higher in energy than the S<sub>0</sub> ground state and dissociates to OH + NO, but with a small (0.19 eV) barrier along the

dissociation coordinate.<sup>8</sup> While this electronic state is energetically accessible with visible light irradiation, spin selection rules prevent observation of the T<sub>1</sub> state by direct absorption methods.<sup>9</sup> The T<sub>1</sub> state can be accessed, however, via an intersystem crossing transition from the excited  $\tilde{B}^1A'$  (S<sub>2</sub>) state of HONO.<sup>8,27,28</sup> Thus, experimental studies on the T<sub>1</sub> state would be useful in understanding how this electronic state contributes to atmospheric OH production.

Beyond studying the electronic structure of HONO, there has also been interest in the proposed mechanisms for HONO formation in the atmosphere.<sup>2</sup> In addition to the previously mentioned pathways, an alternate proposed mechanism for HONO generation is through its negative ion.<sup>18</sup> Negative-ion chemistry of molecules containing H, O and N is relevant in the atmosphere.<sup>29</sup> The hydroxide anion (OH<sup>-</sup>) is known to be formed through hydrogen atom abstraction from hydrocarbons by O<sup>-</sup>.<sup>29</sup> Van Doren *et al.*<sup>18</sup> have explored the associative detachment reaction: OH<sup>-</sup> + NO → HONO + e<sup>-</sup>. The associative detachment process is believed to arise primarily from autodetachment from HONO<sup>-</sup> vibrational continuum states, making it an inefficient process compared to dissociation back to reactants.<sup>18</sup> However, no experimental data are available either for the dissociation of HONO<sup>-</sup> to OH<sup>-</sup> + NO or the electron affinity (EA) of HONO. Calculations predict this anion's dissociation energy to be 0.49 eV<sup>18</sup> or 0.86 eV,<sup>9</sup> with a predicted EA(HONO) of either 0.15 eV<sup>18</sup> or 0.66 eV,<sup>9</sup> depending on the level of theory employed. Experimental data on HONO<sup>-</sup> are necessary before a conclusion can be drawn concerning the importance of the anion in the atmosphere or its possible role in the production of neutral HONO.

In this work, we report photoelectron spectra of *cis*-HONO<sup>-</sup>, yielding spectroscopic information on *cis*-HONO (S<sub>0</sub>), EA(*cis*-HONO), and the dissociation energy of *cis*-HONO<sup>-</sup> to form OH<sup>-</sup> + NO. Electron detachment from *cis*-HONO<sup>-</sup> using higher photon energies produces

*cis*-HONO ( $T_1$ ) in a configuration near a transition state along the central O–N bond dissociation coordinate. Possible contributions from higher excited states of *cis*-HONO and contributions from the *trans*-isomer are also considered, and are found to provide at most small contributions to the measured signal. Quantum-chemical calculations provide additional insights into the resulting photoelectron spectrum.

## 4.2 Methods

### 4.2.a Experimental

We employ a velocity map imaging (VMI) anion photoelectron spectrometer, described in detail in Chapter 2. Here we produce  $\text{HONO}^-$  by reacting hydroxide ( $\text{OH}^-$ ) with nitric oxide (NO) in the dual-valve pulsed plasma entrainment anion source<sup>1</sup> using 40 psig, 0.5% NO in argon in the main supersonic expansion and an effusive flow of 55 psig, 1%  $\text{O}_2$ , 30%  $\text{H}_2$ , balance Ar in the side valve with pulsed electrical discharge of -2000 V, 40~100  $\mu\text{s}$ . The presence of  $\text{NO}_2$  in the 0.5% NO/Ar gas mixture for the main pulsed expansion poses a potential complication in this experiment.  $\text{NO}_2^-$  can be formed in large quantities in the anion source which is in part due to its high electron affinity ( $\text{EA} = 2.273 \text{ eV}$ ).<sup>30</sup> This results in a large photoelectron imaging background since  $\text{NO}_2^-$  is only one mass unit different from  $\text{HONO}^-$  and can be several orders of magnitude larger in ion intensity compared to  $\text{HONO}^-$ . We use two methods to reduce the amount of photoelectron background due to  $\text{NO}_2^-$ . First, we remove the  $\text{NO}_2$  initially present in the 0.5% NO/Ar gas mixture prior to the gas expansion by flowing the already dilute mixture of 0.5% NO/Ar through a molecular sieve filled copper coil, which is immersed in a methanol/dry-ice bath (~193 K) followed by an Ascarite (NaOH coated Silica) trap. This is analogous to the procedure followed by Van Doren *et al.*<sup>18</sup> While this greatly reduces the amount of  $\text{NO}_2$  initially present, and therefore reduces the  $\text{NO}_2^-$  ion intensity, there is

still a substantial amount of  $\text{NO}_2^-$  (approximately 10 times larger ion intensity compared to  $\text{HONO}^-$ ). To further reduce the photoelectron background, we use a pulsed mass gate (see Chapter 2), which deflects the majority of  $\text{NO}_2^-$  away from the laser interaction region without affecting the absolute  $\text{HONO}^-$  ion intensity.

We use different photon energies to obtain well-resolved photoelectron spectra of *cis*- $\text{HONO}^-$  over the full spectral range of interest. To obtain the full photoelectron spectrum accessing the lowest state, *cis*- $\text{HONO}$  ( $S_0$ ), we utilize the second harmonic of a Nd:YAG laser (532 nm). For higher resolution ground state spectra, we employ 1064 nm (Nd:YAG fundamental) and 1613 nm radiation (difference frequency mixing of 1064 nm and dye-laser generated 640 nm radiation (DCM Exciton Dyes)). The  $T_1$  state of *cis*- $\text{HONO}$  is investigated using both the third harmonic of the Nd:YAG laser (355 nm) and 301 nm photons from frequency doubling the dye-laser generated 602 nm radiation (Rhodamine 640 Exciton Dyes).

The energy scale in the photoelectron spectra accessing *cis*- $\text{HONO}$  ( $S_0$ ) is calibrated using the  $\text{O}_2^-$  photoelectron spectrum.<sup>31</sup> To calibrate the photoelectron spectra of detachment to form *cis*- $\text{HONO}$  ( $T_1$ ), we use the photoelectron spectrum of  $\text{I}^-$ .<sup>32</sup>

#### 4.2.b Theoretical Methods

One-dimensional cuts through the potential energy surfaces (CBS-QB3 composite method) as functions of the central O–N bond distance (labeled as  $r_{\text{ON,c}}$  for the remainder of this manuscript) with all other coordinates optimized, are plotted in Fig. 4.1. As is seen, in cases of electron photodetachment to form the  $S_0$  state of *cis*- $\text{HONO}$ , the shift in the equilibrium value of  $r_{\text{ON,c}}$  between the anion surface (plotted in green) and the  $S_0$  surface for *cis*- $\text{HONO}$  (plotted in black) leads us to expect that there will be evidence of a vibrational progression in at least the

central O–N stretching mode in the photoelectron spectrum. In contrast, the  $T_1$  state of *cis*-HONO at the anion equilibrium geometry is near a transition state along the HO–NO bond dissociation coordinate. In this case, a broad, unresolved photoelectron spectrum is expected. The difference in the nature of the potential surfaces in the vertical detachment region for the  $S_0$  (bound) and  $T_1$  (dissociative) states of *cis*-HONO requires different approaches to model the photoelectron spectra.

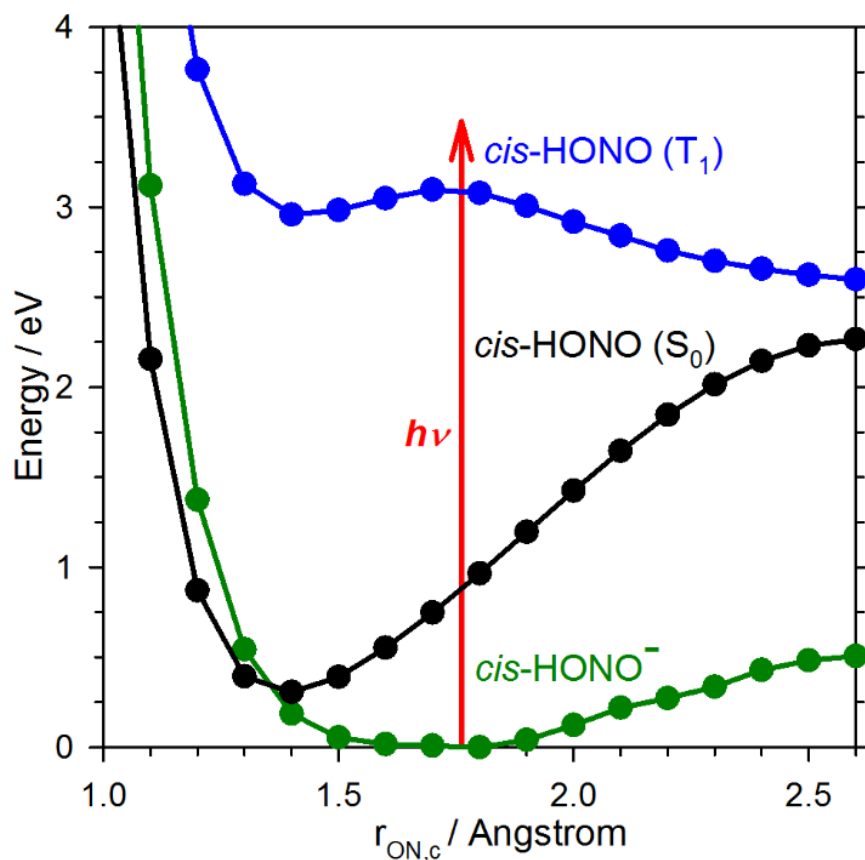


Figure 4.1: 1-D electronic potential energy curves (CBS-QB3) for *cis*-HONO as functions of the central  $r_{\text{ON,c}}$  bond length. The red arrow represents a vertical transition from the anion equilibrium geometry to the ground  $S_0$  and excited  $T_1$  states of neutral HONO. Note: *cis*-HONO ( $T_1$ ) is unstable with respect to isomerization to *trans*-HONO ( $T_1$ ), so what appears to be a minimum on the  $T_1$  potential surface near 1.4 Å in this coordinate is actually a saddle point.

To aid the interpretation of the photoelectron spectrum following electron detachment to form *cis*-HONO ( $S_0$ ), *ab initio* calculations for both *cis*-HONO<sup>-</sup> and *cis*-HONO ( $S_0$ ) were performed at the MP2/aug-cc-pVTZ (UMP2 for the anion) and CCSD(T)/aug-cc-pVTZ level of theory/basis-set for geometry optimization and relative energies. This choice of level of electronic structure was made based on the consistency between the results of the MP2 and CCSD(T) calculations. The electronic structure of HONO<sup>-</sup> will be discussed in section 4.3.e, as it has proven to a rather pathological case for calculations. Using the geometry, harmonic frequencies, and first-order anharmonicity constants from the MP2/aug-cc-pVTZ calculations, Franck-Condon factors (FCFs) were calculated for transitions from *cis*-HONO<sup>-</sup> to *cis*-HONO ( $S_0$ ) using the PESCAL program.<sup>30,33</sup> When available, experimentally determined harmonic frequencies<sup>15,34,35</sup> and first-order anharmonicity constants<sup>15</sup> of *cis*-HONO ( $S_0$ ) were used to determine the transition energies in the PESCAL simulation. When such information was not available, anharmonicity constants derived from the current experimental work or calculated here (MP2/aug-cc-pVTZ) were used (see Table 4.3 for a summary of the values used in the PESCAL simulation). It is important that anharmonic corrections for the vibrational energies of *cis*-HONO ( $S_0$ ) were used in this analysis because of the extended vibrational progression anticipated following electron photodetachment from *cis*-HONO<sup>-</sup>. We do not expect significant population in excited vibrational levels of the anion because of the unique cooling capability of the ion source used in this experiment, and indeed, did not see evidence of this (as discussed below). Thus, the harmonic frequencies for the anion from the UMP2/aug-cc-pVTZ calculations were used in the FCF calculation. For comparison of the PESCAL calculated FCF stick spectrum with the experimental data, we convolute the FCFs with Gaussian functions. For each FCF, the

Gaussian function is characterized by an area equal to the intensity of the calculated FCF and a FWHM dictated by its position (in eKE).

To model electron photodetachment forming *cis*-HONO ( $T_1$ ), calculations proceeded in two steps. First, a two-dimensional scan of the potential energy surface for *cis*-HONO<sup>-</sup> as a function of  $r_{\text{ON,c}}$  and the terminal N=O bond length (labeled as  $r_{\text{NO,t}}$  for the remainder of this manuscript) was performed using the CBS-QB3 composite method, as implemented in Gaussian 09.<sup>36</sup> For each point in the scan, HONO<sup>-</sup> was constrained to a planar *cis* configuration, and the energy was minimized with respect to the remaining three coordinates (OH bond length and HON and ONO angles). The potential was calculated for a grid ranging from 1.0 to 2.2 Å in  $r_{\text{NO,t}}$  and 1.2 to 3.0 Å in  $r_{\text{ON,c}}$  in increments of 0.1 Å. Single-point energies for *cis*-HONO ( $T_1$ ) were calculated at the *cis*-HONO<sup>-</sup> geometries from the *cis*-HONO<sup>-</sup> two-dimensional potential energy surface scan. The choice to evaluate the  $T_1$  surface at the anion optimized geometries provided a better representation of the vertical transition region. It should be noted that at large values of  $r_{\text{ON,c}}$  and  $r_{\text{NO,t}}$ , which correspond to high energy structures on the anion surface, the lowest energy geometry of HONO<sup>-</sup> does not correspond to the *cis* isomer. In these cases, the values of the HON and ONO angles, as well as the OH bond length, were constrained to their optimized values at the largest values of  $r_{\text{ON,c}}$  and  $r_{\text{NO,t}}$  for which *cis*-HONO<sup>-</sup> did not isomerize.

The anion and  $T_1$  potential energy surfaces are used in the calculation of the photoelectron spectrum based on a two-dimensional model Hamiltonian:

$$H = \frac{1}{2\mu_{\text{NO}}} (p_{\text{ON,c}}^2 + p_{\text{NO,t}}^2) + \frac{1}{2} \left( p_{\text{ON,c}} \frac{\cos \theta_{\text{ONO}}}{m_{\text{N}}} p_{\text{NO,t}} + p_{\text{NO,t}} \frac{\cos \theta_{\text{ONO}}}{m_{\text{N}}} p_{\text{ON,c}} \right) + V(r_{\text{ON,c}}, r_{\text{NO,t}})$$

(Eq. 4.1)

where the value of the ONO angle depends on the two NO bond lengths. The calculation was performed using a discrete variable representation (DVR) for the two NO bond lengths.<sup>37</sup> For  $r_{\text{NO,t}}$ , 100 DVR points were used in the range of 1.0 to 2.2 Å, while 750 DVR points spanning 1.2 to 6.3 Å were used for  $r_{\text{ON,c}}$ . The calculated values of the *cis*-HONO ( $T_1$ ) potential surface were extrapolated to values of  $r_{\text{ON,c}}$  that extend beyond the range of calculated electronic energies by assuming an asymptotic form for the potential of

$$V_{\text{asy}} = V_{\infty} - \frac{C_6}{r_{\text{ON,c}}^6} \quad (\text{Eq. 4.2})$$

and fitting the  $V_{\infty}$  and  $C_6$  variables to the calculated values of the potential energy at  $r_{\text{ON,c}} = 2.0$  and 2.1 Å.

The calculation of the photoelectron spectrum was performed in two steps. In the first, for every value of  $r_{\text{ON,c}}$ , a one-dimensional calculation of the energies and wavefunctions for the  $\nu = 0-3$  levels in  $r_{\text{NO,t}}$  was performed, yielding terminal N=O stretch eigenfunctions. Then the two-dimensional Hamiltonian in Eq. 1 was solved in the product basis of sinc-DVR functions<sup>37</sup> in the central O–N stretch and these terminal N=O stretch eigenfunctions. The treatment of the kinetic coupling follows earlier work of Gardiner *et al.* on  $\text{H}_4\text{O}_2^+$ .<sup>38,39</sup> The resulting energies and wavefunctions were used to construct a photoelectron spectrum within the Franck-Condon approximation. This is shown and discussed further in Section 4.3 B.

## 4.3 Results and Discussion

### 4.3.a Introductory remarks

An overview photoelectron spectrum of *cis*-HONO<sup>-</sup> resulting from electron photodetachment using 3.49 eV photon energy is shown in Fig. 4.2. Two broad bands of peaks

are clearly discernable in the raw image, as well as in the reconstructed photoelectron spectrum: a band at low eBE (high velocity, outer ring of the image), and another at high eBE (low velocity, inner rings of the image). The two bands arise from electron photodetachment forming different electronic states of *cis*-HONO. Other photodetachment wavelengths will permit investigation of these bands with much higher photoelectron energy resolution.

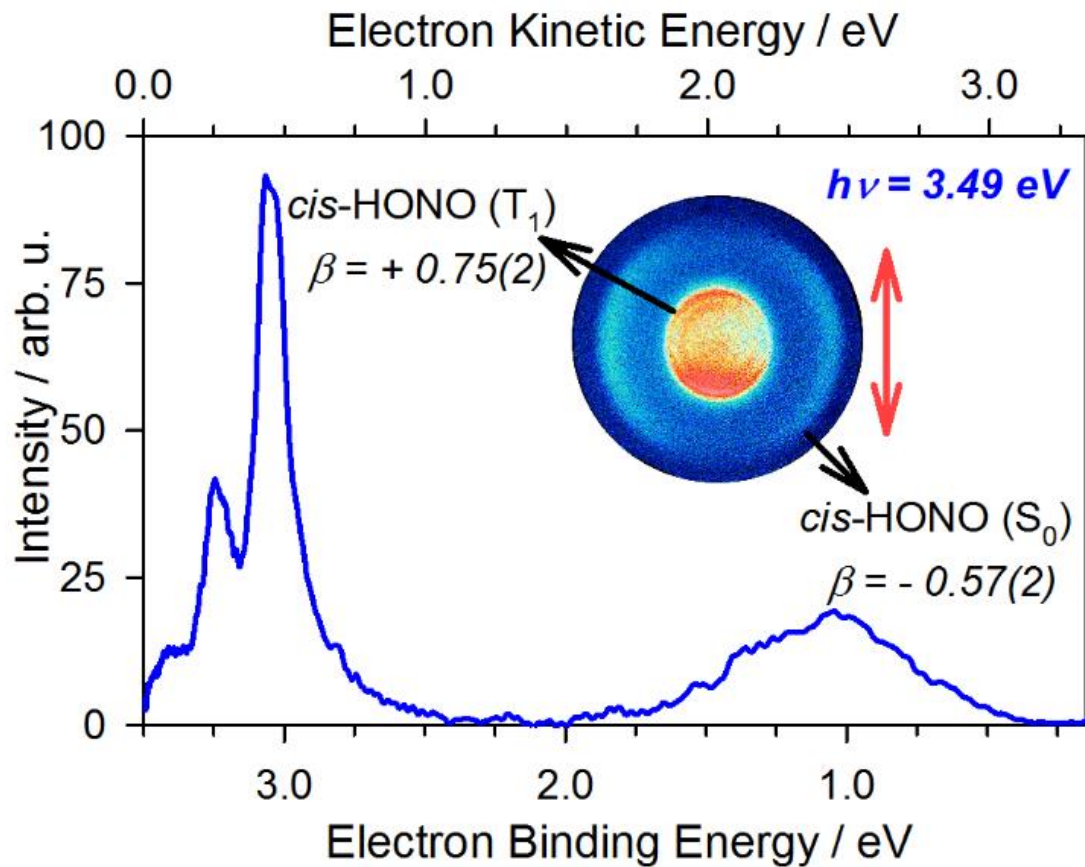


Figure 4.2: The cis-HONO– photoelectron spectrum using 355 nm (3.49 eV) photons. The inset is the unprocessed velocity-mapped image of the photodetached electrons, illustrating the difference in electron angular distribution relative to the laser polarization (red double-headed arrow) following electron photodetachment forming the ground  $S_0$  and excited  $T_1$  states of cis-HONO.

Neutral *cis*-HONO is a closed-shell singlet in its ground state ( $S_0$ ) configuration.<sup>8</sup> The extra electron in *cis*-HONO<sup>-</sup> is added to the  $\pi^*$  antibonding orbital ( $3a''$ ), which is localized along the central O–N bond. This electron may be removed in electron photodetachment, producing the  $S_0$  state of *cis*-HONO. Alternatively, an electron could be removed from the next highest energy doubly occupied orbital,  $10a'$ .<sup>8</sup> Removal of one of these electrons will result in either a singlet ( $S_1$ ) or triplet ( $T_1$ ) electronically excited state of *cis*-HONO. The electronic configurations corresponding to the observed experimental peaks in the photoelectron spectrum are identified through their relative energies and the photodetached electron angular anisotropy.

In Fig. 4.2, the low eBE band (outer ring of image) extends from  $\sim 0.3$  eV to  $\sim 2$  eV electron binding energy, peaking near 1.1 eV. The photoelectron angular distribution of the low eBE band has a negative anisotropy parameter, with  $\beta = -0.57(2)$ , indicating photodetachment from a  $\pi$ -like molecular orbital. This result is consistent with the primarily  $\pi$ -like character of the calculated highest (singly) occupied molecular orbital of *cis*-HONO<sup>-</sup>. The eBE and anisotropy of this band leads us to assign it to electron photodetachment of *cis*-HONO<sup>-</sup> forming the ground  $S_0$  state of neutral *cis*-HONO.

The other band in the spectrum in Fig. 4.2 starts near an eBE of 2.6 eV, approximately 2.3 eV higher in energy than the estimated origin of the low eBE band assigned to *cis*-HONO ( $S_0$ ). The first excited singlet state ( $S_1$ ) is experimentally known to be 3.26 eV higher in energy<sup>24,25</sup> than HONO ( $S_0$ ) for the *cis* isomer. This would correspond to an eBE of over 3.5 eV, which is significantly higher in energy than the experimentally observed peaks starting near an eBE of 2.6 eV, and is inconsistent with this band corresponding to  $S_1$ . While there is no previous experimental information regarding the  $T_1$  state of *cis*-HONO, calculations performed here (CBS-QB3 composite method) show an adiabatic excitation energy from  $S_0$  to  $T_1$  of

approximately 2.58 eV for the *cis*-HONO isomer, in agreement with the observed approximate energy separation between the estimated origins of these two bands. Higher-level CASSCF/CASPT2 calculations were performed previously, but only for *trans*-HONO.<sup>8</sup> In addition, the dominant peak in this band has a photoelectron angular distribution with  $\beta = +0.75(2)$ . The positive value of  $\beta$  indicates electron photodetachment from an orbital with more  $\sigma$ -like character than the lower eBE peak, consistent with detachment from the 10a' second highest doubly occupied molecular orbital in *cis*-HONO<sup>-</sup>. From the combination of the above attributes, we conclude that the band near an eBE = 2.6 eV is likely from photodetachment to produce *cis*-HONO (T<sub>1</sub>). These electronic state assignments will be validated with higher resolution spectra, vibrational analyses, and photoelectron spectrum simulations in the following two sections.

#### 4.3.b Ground State: *cis*-HONO $\tilde{X}^1A'$

In this study, we take advantage of the changing resolution of the VMI detection with electron kinetic energy in order to obtain a better-resolved photoelectron spectrum by using lower energy photons to detach the electron from *cis*-HONO<sup>-</sup>. The results of this process are illustrated in Fig. 4.3. The 1.16 eV and 0.769 eV spectra, purple and orange traces of Fig. 4.3, respectively, show well-resolved peaks and an improved signal-to-noise ratio. In contrast, the photoelectron spectrum using 2.33 eV photon energy mimics the band shown in Fig. 4.2, showing a broad envelope with no discernable structure. Clearly, the broad photoelectron envelope observed when using photon energies well above the photodetachment threshold implies that the anion and neutral states involved have substantial structural differences, and that both vibrational congestion and reduced electron energy resolution at these higher electron kinetic energies conspire to eliminate structure in the photoelectron spectrum. Such spectral

congestion could be anticipated, since there is a large change in geometry between the anion and neutral ( $S_0$ ) *cis*-HONO structures based on quantum-chemical calculations performed here at the MP2/aug-cc-pVTZ level of theory/basis. There is a  $\sim 0.3$  Å ( $\sim 20\%$ ) decrease in  $r_{\text{ON,c}}$  from the anion (1.657 Å) to the ground state neutral (1.387 Å) forms of *cis*-HONO. With the exception of the OH bond length (which decreases by 0.01 Å, or less than 0.5%), all of the other geometric parameters show  $\sim 4$ -10% increase in the bond lengths/decrease in the angles between the anion and neutral states. A common photoelectron signature of molecules with large changes in the geometry between the anion and neutral species is an almost uninterpretable photoelectron spectrum because of the spectral congestion. In some cases,<sup>40,41</sup> an experimental determination of the EA is very difficult since a large geometry change can result in an extremely weak origin transition compared to the most intense portions of the photoelectron spectrum.

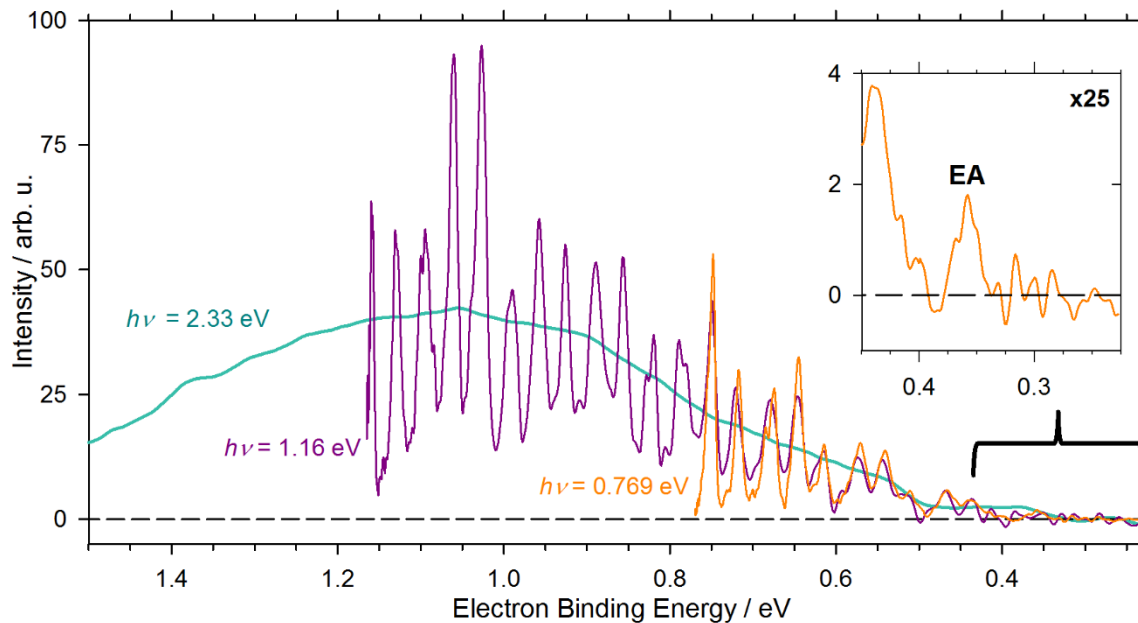


Figure 4.3: Photoelectron spectrum of *cis*-HONO<sup>-</sup> using photon energies of 532 nm (2.33 eV, green), 1064 nm (1.16 eV, purple), and 1613 nm (0.769 eV, orange). The change in resolution as a function of photon energy is characteristic of the VMI detection. The inset graphic shows a magnified view of the peak assigned as the EA.

The peak of the photoelectron spectrum reflects the photodetachment transition with the largest FCF, or the energy difference between the anion and neutral ( $S_0$ ) electronic states of *cis*-HONO at the anion equilibrium geometry. This is referred to as the vertical detachment energy (VDE), and is  $\sim 1.1$  eV for electron photodetachment to form *cis*-HONO ( $S_0$ ). However, despite the nearly 0.8 eV energy difference between the VDE and the origin of the photoelectron spectrum, the lowest eBE peak at 0.358 eV is clearly visible above the signal-to-noise level when lower photon energies are used, as seen in the inset in Fig. 4.3. There are no other peaks observed at lower eBE. This peak is labeled as peak A in Fig. 4.4. In this figure, the concatenated photoelectron spectrum of *cis*-HONO<sup>-</sup> is plotted using the 1.16 eV spectrum for detachment energies above  $\sim 0.76$  eV and the 0.769 eV spectrum is plotted for smaller detachment energies. The resulting spectrum is shown as the black trace in Fig. 4.4, where the major peaks in the experimental spectrum are alphabetically labeled. This concatenated spectrum has been corrected for the change in photodetachment cross section with electron kinetic energy, commonly referred to as the threshold effect.<sup>42</sup> Peak A appears to be a single peak with, again, no observable peaks to lower eBE, while peaks B-C, D-F, and G-I show the start of a repeating pattern in the peak progression. We thus assign peak A as the origin transition, *i.e.* the eBE for peak A is the EA(*cis*-HONO). This assignment is further supported by the photoelectron simulation, discussed below. It is important to recognize that the centers of these peaks will not necessarily correspond to the band origins of the transitions due to an asymmetry of the rotational band contour, as discussed in Chapter 2. Applying a small correction for this rotational shift,<sup>43,44</sup> the resulting EA(*cis*-HONO) = 0.356(8) eV. The calculated EA for *cis*-HONO is 0.324 eV, evaluated at the CCSD(T)/aug-cc-pVTZ level of theory, based on the optimized structures obtained using MP2/aug-cc-pVTZ (UMP2 for the anion) shown in Table 4.1 below. This value agrees very well

with the experimental EA(*cis*-HONO). It is also consistent with the calculation performed here at a higher level of theory (CCSD(T)/aug-cc-pVTZ), resulting in EA(*cis*-HONO) = 0.352 eV. The convolved and stick representations of the simulated spectrum (red trace and green sticks, respectively, in Fig. 4) are used as an aid to assign the observed vibrational transitions of the dominant peaks in the experimental spectrum, the results of which are compiled in Table 4.2.

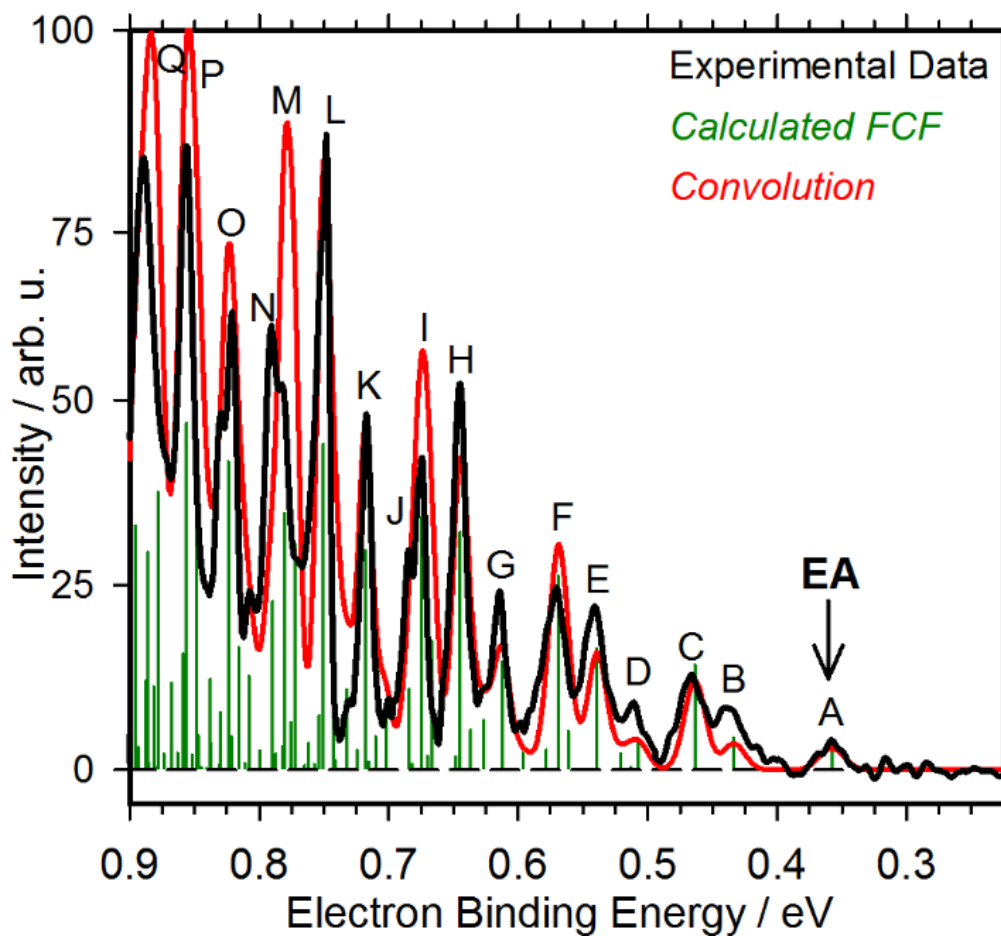


Figure 4.4: Scaled experimental photoelectron spectrum (black trace), Franck-Condon factors (green sticks), and convoluted simulation (red). The peak labels (upper case letters) refer to the *cis*-HONO  $\tilde{X}^1A'$  (S<sub>0</sub>) vibrational assignments compiled in Table 4.2. For electron binding energies below  $\sim 0.76$  eV, the black trace is identical to the 0.769 eV spectrum in Fig. 4.3, while for large electron binding energies, the black trace reproduces the 1.16 eV spectrum shown in Fig. 4.3.

The overall convolved photoelectron spectrum simulation shows excellent agreement with the experimental spectrum, despite the large degree of spectral congestion, particularly for  $eBE \geq 0.7$  eV. The peaks in the photoelectron spectrum are readily assigned, primarily to transitions to states involving excitation of overtones and combination bands of the central O–N stretch ( $\nu_4$ ) and the ONO bend ( $\nu_5$ ) along with states that have one quantum of excitation in the terminal N=O stretch ( $\nu_2$ ) and two fewer quanta of excitation in the central O–N stretch. This last set of states is attributed to the 2:1 Fermi resonance between  $\nu_2$  and  $2\nu_4$ . This progression in  $\nu_4$  is expected based on the geometry change between the anion and neutral forms of *cis*-HONO, discussed above.

The excellent agreement of the simulation with the experimental photoelectron spectrum provides support for the above peak assignments, particularly the EA, and the two assumptions that were made regarding the initially prepared *cis*-HONO<sup>-</sup>: (1) the anion is vibrationally cold; and (2) *cis*-HONO<sup>-</sup> is the dominant isomer present. First, there is no evidence for significant population in excited vibrational levels of *cis*-HONO<sup>-</sup>, which would lead to vibrational hot bands in the photoelectron spectrum. The addition of hot bands into the photoelectron simulation greatly reduces its agreement with the experimental data. The absence of vibrational hot-bands indicates that the anions are vibrationally cold, with vibrational temperatures below 150 K, typical of this ion source.<sup>1</sup> Second, the level of agreement between the experiment and simulation indicates that the *cis* isomer of HONO<sup>-</sup> is the dominant isomer formed in this experiment. We however, investigated the effect that including *trans*-HONO in the photoelectron simulations, as it is discussed in Section 4.3.d below.

### 4.3.c Vibrational Analysis

The calculated spectrum enables the assignment of vibrational transitions attributed to the ground state of *cis*-HONO. The (MP2/aug-cc-pVTZ) equilibrium geometries of HONO<sup>-</sup>, HONO (S<sub>0</sub>), and HONO (T<sub>1</sub>) are reported in Table 4.1. In addition, the changes in geometry parameters between the anion and neutral structures are listed. As shown in Table 4.1, the most significant geometry change between the anion and both neutral equilibrium structures is  $r_{\text{ON,c}}$ .

The labeled peaks in the photoelectron spectrum accessing the S<sub>0</sub> state of HONO shown in Fig. 4.4 are assigned to the vibrational transitions listed in Table 4.2 based on the agreement with the FCFs calculated in PESCAL.<sup>30,33</sup> As discussed in the above, the assignments are primarily to vibrational overtones and combination bands involving  $\nu_4$  (central O-N stretch) and  $\nu_5$  (ONO bend). Because of their long vibrational progressions, we can derive harmonic frequencies and first-order anharmonicity constants for  $\nu_4$  and  $\nu_5$  from the experimental data. To do so, the energy of the vibrational transition relative to the EA (third column in Table 4.2) is plotted as a function of the vibrational quantum number and fit to a quadratic function. For the O-N stretching vibration, this fit results in a harmonic frequency of  $\omega_4 = 856(12) \text{ cm}^{-1}$  with an anharmonicity constant of  $0(3) \text{ cm}^{-1}$ . This corresponds to an experimental fundamental frequency of  $\nu_4 = 856(13) \text{ cm}^{-1}$ , which is in good agreement with  $\nu_4 = 851.94 \text{ cm}^{-1}$  obtained from the previous high-resolution work.<sup>15</sup> This is less anharmonic than our calculated (MP2/aug-cc-pVTZ)  $x_{44} = -11 \text{ cm}^{-1}$ . The inclusion of an  $x_{44}$  anharmonicity constant of  $-11 \text{ cm}^{-1}$  in the Franck-Condon simulation of the photoelectron spectrum significantly decreases the level of agreement between theory and experiment compared to the reported simulation shown in Fig. 4.4 (which uses  $x_{44} = 0$ ), giving us confidence in our experimentally derived first-order anharmonicity constant. The ONO bend was found to be more anharmonic than the O-N stretch, with a harmonic frequency

of  $\omega_5 = 630(5) \text{ cm}^{-1}$  and first order anharmonicity constant of  $x_{55} = -10(2) \text{ cm}^{-1}$ . This results in a fundamental frequency of  $610(6) \text{ cm}^{-1}$ , which is in good agreement with the previously observed fundamental frequency ( $609.0 \text{ cm}^{-1}$ ),<sup>34</sup> as well as the calculated  $x_{55} = -7 \text{ cm}^{-1}$  (MP2/aug-cc-pVTZ).

Since we can only definitively assign overtone transitions to these two vibrational modes, we are unable to obtain vibrational frequencies for all modes of *cis*-HONO. Nevertheless, the frequencies derived from the photoelectron spectrum are in good agreement with previous experimental data, and new experimental anharmonicity constants have also been derived. Table 4.3 shows the spectroscopic constants for neutral *cis*-HONO experimentally determined in this work, as well as a comparison with current literature data and our calculations.

Table 4.1: Calculated (MP2/aug-cc-pVTZ) equilibrium geometries of *cis*-HONO<sup>-</sup>, *cis*-HONO (S<sub>0</sub>), and *cis*-HONO (T<sub>1</sub>), as well as the difference between geometry parameters of the anion and neutral structures ( $\Delta$  = anion structure – neutral structure). Values in parentheses for the *cis*-HONO (S<sub>0</sub>) geometry parameters are based on microwave spectroscopic experiments<sup>22</sup> for comparison. Distances are given in Angstroms and the angles are in degrees.

<b>Parameter</b>	<i>cis</i> -HONO <sup>-</sup>	<i>cis</i> -HONO (S <sub>0</sub> )	$\Delta$	<i>cis</i> -HONO (T <sub>1</sub> )	$\Delta$
$r_{\text{HO}}$ (Å)	0.971	0.980 (0.979)	-0.01	0.974	0.00
$r_{\text{ON}, c}$ (Å)	1.657	1.387 (1.395)	0.27	1.404	-0.25
$r_{\text{NO}, t}$ (Å)	1.238	1.192 (1.188)	0.05	1.199	-0.04
$\angle\text{HON}$ (°)	95.5	104.6 (104.2)	-9.1	101.3	-5.8
$\angle\text{ONO}$ (°)	108.4	113.3 (113.6)	-4.9	129.7	-21.3

Table 4.2: Vibrational transition assignments for the peaks labeled (A–Q) in the photoelectron spectrum reported in Fig. 4.4. Both the absolute peak position (eBE, reported in eV) and the energy relative to the EA (reported in  $\text{cm}^{-1}$ ) are given. The *cis*-HONO ( $S_0$ ) ( $\nu_1'\nu_2' \dots$ )  $\leftarrow$  *cis*-HONO $^-$  ( $\nu_1''\nu_2'' \dots$ ) transitions are labeled using the standard shorthand notation ( $1_{\nu_1'}^{\nu_1'} 2_{\nu_2''}^{\nu_2''} \dots$ ) for vibrational transitions. The assignments are based on the results of the photoelectron simulation in PESCAL and refer to the vibrational modes with the largest FCFs for the labeled peaks in the photoelectron spectrum (Fig. 4.4). The electron binding energy (eV) of each transition is given in parentheses.

Peak	Peak Position (eV)	Energy Relative to EA ( $\text{cm}^{-1}$ )	Assignment (Position, eV)
A	0.358	0	$0_0^0$ (0.358)
B	0.438	641	$5_0^1$ (0.434)
C	0.468	887	$4_0^1$ (0.464)
D	0.514	1258	$5_0^2$ (0.507) $3_0^1$ (0.521)
E	0.542	1479	$4_0^1 5_0^1$ (0.539)
F	0.572	1728	$4_0^2$ (0.569)
G	0.614	2067	$4_0^1 5_0^2$ (0.613)
H	0.646	2321	$4_0^2 5_0^1$ (0.645)
I	0.675	2554	$4_0^3$ (0.675) $2_0^1 4_0^1$ (0.667)
J	0.687	2649	$4_0^1 5_0^3$ (0.684)
K	0.718	2899	$4_0^2 5_0^2$ (0.718)
L	0.749	3152	$4_0^3 5_0^1$ (0.750) $2_0^1 4_0^1 5_0^1$ (0.743)
M	0.781	3407	$4_0^4$ (0.781) $2_0^1 4_0^2$ (0.773)
N	0.792	3496	$4_0^2 5_0^3$ (0.790)
O	0.824	3756	$4_0^3 5_0^2$ (0.824)
P	0.855	4006	$4_0^4 5_0^1$ (0.856) $2_0^1 4_0^2 5_0^1$ (0.848)
Q	0.889	4280	$4_0^5$ (0.886) $2_0^1 4_0^3$ (0.878) $4_0^3 5_0^3$ (0.895)

Table 4.3: Experimental (previous work and this study) and calculated (this study) vibrational frequencies ( $\nu_i$ ) of neutral *cis*-HONO ( $S_0$ ). All values are given in  $\text{cm}^{-1}$ . The frequencies and anharmonicity constants ( $x_{ii}$ ) used in the PESCAL simulation<sup>30,33</sup> are in bold print.

Mode Number (i)	Description	Experimental $\nu_i$ (Previous Work)	Experimental $\nu_i$ (This Study) <sup>a</sup>	Calculated $\nu_i$ (This Study) <sup>b</sup>
1	O–H stretch	3426.196 <sup>c</sup>	-	3416
2	N=O stretch	1640.519 <sup>c</sup>	-	1591
3	HON bend	1315.2 <sup>d</sup>	-	1303
4	O–N stretch	851.9431 <sup>c</sup>	856(13)	862
5	ONO bend	609.0 <sup>e</sup>	610(6)	620
6	Torsion	638.5 <sup>e</sup>	-	664
<sup>a</sup> The reported uncertainty is the statistical error in a quadratic fit of the peak positions as a function of vibrational quantum number. Anharmonicity constants obtained from the fitting procedure are: $x_{44} = \mathbf{0(3)}$ , $x_{55} = \mathbf{-10(2)}$				
<sup>b</sup> Calculation at the MP2/aug-cc-pVTZ level of theory/basis set; anharmonicity constants: $x_{11} = -88$ , $x_{22} = -10$ , $x_{33} = \mathbf{-9}$ , $x_{44} = -11$ , $x_{55} = -7$ , $x_{66} = \mathbf{-15}$				
<sup>c</sup> From Fourier transform spectroscopy; <sup>15</sup> anharmonicity constants: $x_{11} = \mathbf{-94.00}$ , $x_{22} = \mathbf{-11.53}$				
<sup>d</sup> From Kr matrix isolation study <sup>35</sup>				
<sup>e</sup> From Fourier transform spectroscopy <sup>34</sup>				

#### 4.3.d Contribution of the *trans*-HONO<sup>-</sup> isomer to the photoelectron spectrum

In order to investigate the presence of *trans*-HONO in the photoelectron spectrum, we include the calculated spectrum of *trans*-HONO<sup>-</sup> in the overall simulation. Because of the difficulties with calculating the photoelectron spectrum of HONO<sup>-</sup>, as it will be discussed later, we focus on the low eBE region ( $< 0.7$  eV,  $\sim 3000$  cm<sup>-1</sup>), since the relative peak spacings will correspond to well-known vibrational frequencies of the neutral molecule with little contribution of anharmonicities. The results of this analysis, which parallels the calculation of the photoelectron spectrum for *cis*-HONO, are shown in Fig. 4.5. As such, previously determined vibrational frequencies of neutral *trans*-HONO were used,<sup>14</sup> together with the experimentally known anharmonicities, when available. Where anharmonicities have not been reported, the calculated MP2/aug-cc-pVTZ values are employed. In order to directly compare the calculated and experimental spectra, the FCFs were convoluted with Gaussian functions of varying FWHM, as described in section 4.2 above. In addition, the origin of the *trans*-HONO vibrational progression is placed at the measured origin (Peak A) of the spectrum at 0.358 eV, which assumes that *trans*-HONO<sup>-</sup> is the dominant isomer present. While it is expected that the origin of the *trans*-HONO spectrum will be at slightly lower electron binding energies than the dominant *cis* isomer, the calculated difference between the binding energies is comparable to or slightly smaller than the width of the Gaussian functions used in the convolution of the calculated FCFs at an electron binding energy of 0.358 eV. While the transition frequencies for the calculated photoelectron spectrum can be adjusted to match known values, there is not an analogous constraint for the intensities. Given the surprisingly large sensitivity of these intensities to the level of electronic structure theory used to obtain the optimized structures and normal modes, the relative peak intensities are at best qualitative. As such, the level of agreement between

calculation and experiment should be based on peak positions and not necessarily relative intensities. The relative FCF intensities also vary with the level of theory used, again indicating the challenges in determining the electronic structure of the anion. Peaks 2 and 3, which correspond to the transitions  $5_0^1$  and  $4_0^1$  of *trans*-HONO, respectively, are on average  $\sim 0.010$  eV (or  $\sim 80$   $\text{cm}^{-1}$ ) shifted from the experimentally observed peaks B and C. This is beyond the experimental uncertainty of determining the centers of these peaks ( $\leq 40$   $\text{cm}^{-1}$ ). The calculated progression continues to be shifted to lower electron binding energies compared to the experimentally observed peaks as the electron binding energy increases. In addition, the simulation predicts peaks (such as peaks 4 and 7) where no peaks are observed experimentally, while experimentally observed peaks E and G are not anticipated by the calculation. Overall the calculated spectrum for photodetachment from *trans*-HONO<sup>-</sup>, when assuming *trans*-HONO<sup>-</sup> is the dominant isomer, does not reproduce the experiment.

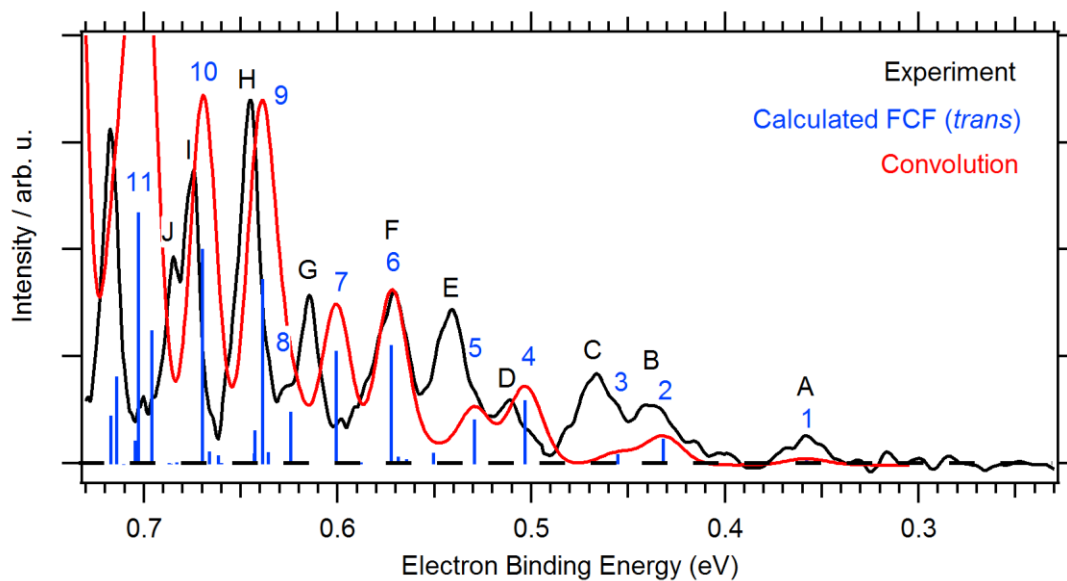


Figure 4.5: Comparison of the calculated (ROMP2/aug-cc-pVTZ) photoelectron spectrum of *trans*-HONO<sup>-</sup> and the experimental data. The blue numbers refer to the calculated transitions and the black letters refer to the experimentally observed peaks, as labeled in Fig. 4.4. The calculated spectrum was scaled to match the intensity of peak H.

Now suppose the peak located at 0.358 eV (Peak A) is the EA of *cis*-HONO, as determined in this chapter, and the *cis*-HONO<sup>-</sup> isomer is dominant. The calculated  $\Delta(\text{EA})_{\text{cis-trans}} \sim 0.06$  eV (CCSD(T)/aug-cc-pVTZ) was used to shift the simulated *trans*-HONO<sup>-</sup> photoelectron spectrum to lower binding energy relative to EA(*cis*-HONO), specifically EA(*trans*-HONO) = 0.295 eV. In addition, the *trans*-HONO<sup>-</sup> calculated spectrum was scaled such that the origin peak is approximately at the baseline noise level at low eBE ( $\sigma_{\text{noise}} \sim 0.6$ ), since no peaks below 0.358 eV were observed experimentally. The origin of the *cis*-HONO<sup>-</sup> calculated spectrum was scaled to be 6.5 times larger than this to match the intensity of peak A, reproducing the stick spectrum in Fig. 4.4. The overall spectrum containing contributions from the *cis* and *trans* isomers was convoluted according to the procedure used for Fig. 4.4. The main points of disagreement are the appearance of a shoulder on peak A and the widths of peaks higher than 0.5 eV. As mentioned in section 4.3.b, the addition of the *trans* isomer in the calculated photoelectron spectrum decreases the agreement between the calculated and the experimental spectrum. Fig. 4.6 can be compared to Fig. 4.4, which contains only the contribution of the *cis* isomer. This result indicates that *cis*-HONO<sup>-</sup> is the dominant isomer. Unfortunately, we are unable to quantify the possible relative amount of *trans*-HONO<sup>-</sup> present because of the reliance on the theoretically predicted photoelectron spectrum. To quantify the amount of *trans*-HONO<sup>-</sup> relative to *cis*-HONO<sup>-</sup>, the full photoelectron spectrum simulations, including the poorly determined high-eBE range, must be used to integrate the total photoelectron signal and compare this with *cis*-HONO<sup>-</sup>. As already stated, the poor determination and large variation of the anion geometry and frequencies with level of theory indicates the challenge this anionic species presents to electronic structure. However, there is no experimental evidence that demands the inclusion of *trans*-HONO<sup>-</sup>.

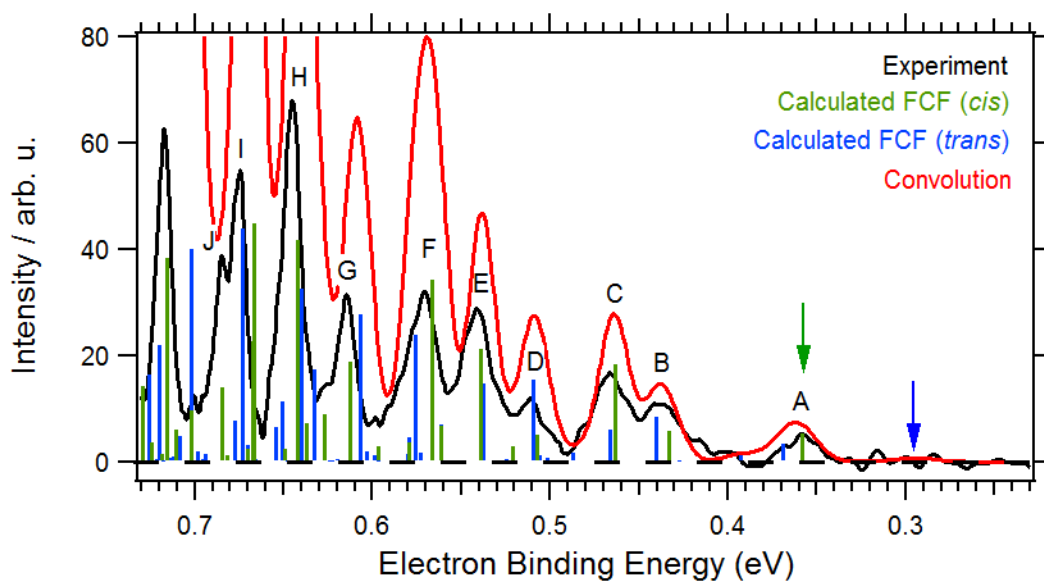


Figure 4.6: Comparison of the calculated photoelectron spectrum of  $\text{HONO}^-$  with both *cis* (UMP2/aug-cc-pVTZ, green sticks) and *trans* (ROMP2/aug-cc-pVTZ, blue sticks) isomers, and the experimental data. The origin of the *trans*-HONO progression (0.295 eV) was scaled down to the noise level.

One way to qualitatively estimate the relative amount that *trans*-HONO<sup>-</sup> could contribute to the spectrum is to investigate the relative energies of both isomers. For this purpose, the isomerization coordinate of HONO<sup>-</sup> was calculated and plotted in Fig. 4.7 where the potential energy of HONO<sup>-</sup> is reported as a function of the dihedral angle. This curve was calculated at the CBS-QB3 level of theory and constructed by varying the HONO<sup>-</sup> dihedral angle and allowing the other coordinates to relax so that the total energy of the system is minimized. As noted in here, *trans*-HONO<sup>-</sup> has a calculated (CBS-QB3) barrier to isomerization of ~0.017 eV, or ~139 cm<sup>-1</sup>, which is smaller than the harmonic frequency of the torsion vibration,  $\omega_6$  (161 cm<sup>-1</sup>, CBS-QB3) for *trans*-HONO<sup>-</sup>. Based on this, we expect that there can likely be only one and at most two torsion levels localized in the *trans*-HONO<sup>-</sup> minimum on the torsion potential. Including harmonic zero-point energy in the six vibrational degrees of freedom, the ground state of *trans*-HONO<sup>-</sup> is ~0.016 eV, or ~130 cm<sup>-1</sup> higher in energy than *cis*-HONO<sup>-</sup>. Using the estimated rotational temperature of 75±25 K, and using a simple Boltzmann distribution under equilibrium conditions, a relative population of 2% (50 K) to 13% (100 K) *trans*-HONO<sup>-</sup> was obtained.

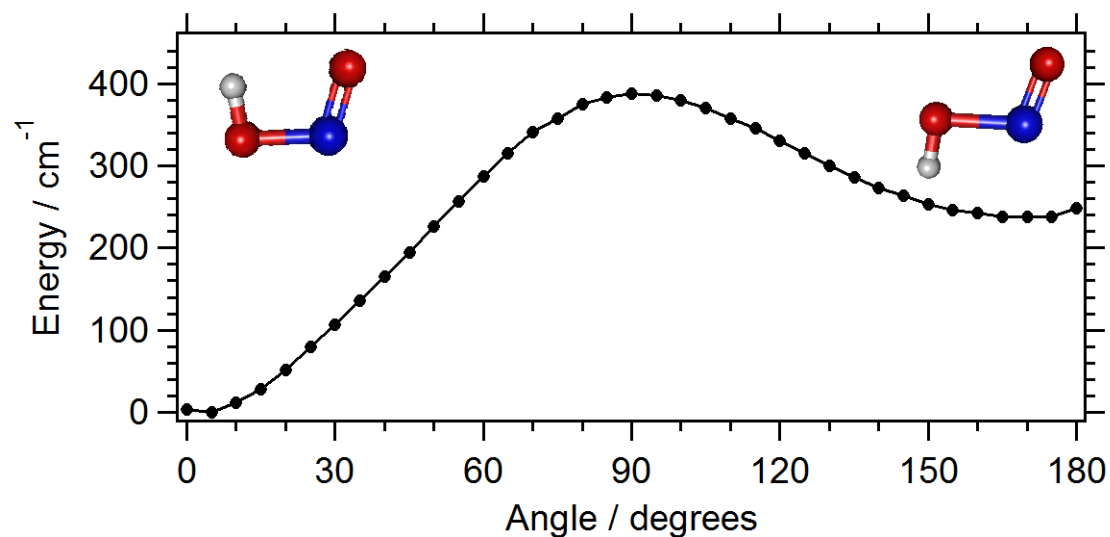


Figure 4.7: Potential energy as a function of the HONO<sup>-</sup> dihedral angle calculated at the CBS-QB3 level of theory. The curve is a relaxed potential energy scan, *i.e.* it was constructed by varying the dihedral angle while the other coordinates were allowed to optimize so that the total energy of the system was minimized.

#### 4.3.e Electronic Structure of $\text{HONO}^-$

$\text{HONO}^-$  presents a surprisingly challenging molecular ion for electronic structure calculation. While a detailed exploration of the electronic structure of this anion is beyond the scope of the present study, challenges are anticipated based on the analysis of the photoelectron spectrum obtained for detachment of an electron to access the  $S_0$  state of *cis*-HONO. Analysis of the results of this part of the study provide a  $D_0(\text{HO}^--\text{NO})$  for *cis*- $\text{HONO}^-$  of only 0.594(9) eV (See section 4.4.f. Thermochemistry of HONO). This energy is small compared to typical covalent bonds and is in line with the expected strength of ion-dipole interactions. Further, the stabilizing interaction between the terminal atoms in *cis*- $\text{HONO}^-$  leads to an increase in its stability relative to the *trans* isomer. We expect that the delicate balance between weak covalent and longer-range ion-dipole interactions in  $\text{HONO}^-$  are responsible for challenges in describing this ion with electronic structure calculations.

To better characterize the structure and frequencies of both isomers of  $\text{HONO}^-$  and the lowest energy singlet ( $S_0$ ) and triplet ( $T_1$ ) states of HONO, we performed electronic structure calculations at several levels of theory: the CBS-QB3 composite method, UMP2/aug-cc-pVTZ, ROMP2/aug-cc-pVTZ, CCSD/aug-cc-pVTZ and CCSD(T)/aug-cc-pVTZ. As is illustrated in the results reported in Tables 4.4 - 4.7, there is considerable variability among these levels of theory, particularly for the central O–N bond length,  $r_{\text{ON,c}}$ , and the frequency associated with the central NO stretch. Both isomers show unusually long central O–N distances and the associated frequencies are unusually low. These trends are more pronounced for the *trans* isomer, for which the binding energy is slightly lower. Comparing the values of  $r_{\text{ON,c}}$ , evaluated at these levels of theory, we find that it covers a range of 0.2 Å for both isomers! In the cases of the shorter central NO bond distances, the excess charge is delocalized across ONO, while at longer

distances, the excess charge localizes on OH. The situation is further complicated in *cis*-HONO<sup>-</sup> as the description of the normal modes is depends strongly on the level of electronic structure theory used. These differences lead to large variations in the intensity patterns for the calculated photoelectron spectrum.

In the case of the *cis* isomer, the UMP2 calculation provides both geometries and normal modes for HONO<sup>-</sup> that are close to the CCSD(T) results. In contrast, the UMP2 calculation for *trans*-HONO<sup>-</sup> provides the longest central NO bond distance and anticipates a vertical detachment energy that is roughly 2 eV larger than any other level of theory. Clearly the UMP2 calculations are failing to capture the extent of covalency in the *trans*-HONO<sup>-</sup> isomer. In this case, the ROMP2 calculation appears to provide a better description, and is in generally good agreement with the results of the CCSD(T) calculations. For this reason, in the discussion that follows, and the discussion in the text, we focus primarily on the results of the UMP2 calculations for the *cis*-HONO<sup>-</sup> and ROMP2 for *trans*-HONO<sup>-</sup>. The neutral species are both described at the MP2 level of theory.

An implication of the large variability in the calculated structure is that the calculated Franck-Condon progression is unexpectedly sensitive to the level of theory used. As an example, Fig. 4.8(b) shows the calculated photoelectron spectrum based on the CCSD/aug-cc-pVTZ calculation. It is not clear if the apparent sensitivity reflects solely challenges in properly describing the electronic structure of HONO<sup>-</sup>, or the calculation of the photoelectron spectrum using harmonic descriptions of the wave functions, or a combination of these two factors.

The high eBE range of the spectrum is also particularly susceptible to the approximations inherent in employing the Franck-Condon approximation based on harmonic wave functions, as is implemented in PESCAL, including the lack of anharmonicity in the description of the wave

functions and couplings between the vibrational modes. As a consequence, the high variability in the calculated  $r_{\text{ON,c}}$  strongly affects the length of the Franck-Condon progression at this level of approximation.

Table 4.4: Comparison of HONO<sup>-</sup>, HONO (S<sub>0</sub>), and HONO (T<sub>1</sub>) harmonic frequencies for the *trans* isomer using different levels of theoretical treatment (CBS-QB3 composite method, MP2/aug-cc-pVTZ, CCSD/aug-cc-pVTZ and CCSD(T)/aug-cc-pVTZ). For the anion, ROMP2/aug-cc-pVTZ results are in parenthesis, while the values not in parentheses represent the results of UMP2 calculations.

	CBS-QB3	MP2/aug-cc-pVTZ	CCSD/aug-cc-pVTZ	CCSD(T)/aug-cc-pVTZ <sup>a</sup>
<b><i>trans</i>-HONO<sup>-</sup></b>				
O–H stretch	3776.1	3782.1 (3788.4)	3823.3	3762.6
N=O stretch	1568.1	2357.9 (1608.6)	1519.8	1687.6
HON bend	900.8	706.6 (815.6)	961.6	873.2
O–N stretch	283.1	249.1 (286.6)	224.4	234.1
ONO bend	533.2	424.5 (454.7)	525.3	478.6
Torsion	161.0	141.0 (127.2)	171.3	208.9
<b><i>trans</i>-HONO (S<sub>0</sub>)</b>				
O–H stretch	3775.9	3754.9	3817.6	3759.9
N=O stretch	1792.6	1659.9	1784.0	1715.2
HON bend	1297.7	1283.4	1352.4	1305.9
O–N stretch	834.0	805.3	878.3	816.4
ONO bend	618.7	602.5	675.4	616.7
Torsion	590.5	586.5	565.1	565.1
<b><i>trans</i>-HONO (T<sub>1</sub>)</b>				
O–H stretch	3784.2	3771.4	3825.7	-
N=O stretch	1493.5	2239.4	1458.3	-
HON bend	1287.3	1301.7	1316.8	-
O–N stretch	772.0	953.8	824.3	-
ONO bend	484.1	569.3	460.6	-
Torsion	145.0	278.8 <i>i</i>	167.2	-
<sup>a</sup> The anion geometry converged to a dihedral angle of 184°				

Table 4.5: Comparison of HONO<sup>-</sup>, HONO (S<sub>0</sub>), and HONO (T<sub>1</sub>) energies and geometries for the *trans* isomer using different levels of theoretical treatment. For the anion, ROMP2/aug-cc-pVTZ results are given in parenthesis, while the values not in parentheses represent the results of UMP2 calculations. Energies reported are relative to the energy of the *trans*-HONO<sup>-</sup> equilibrium geometry, where T<sub>0</sub> is the electronic adiabatic term energy and T<sub>v</sub> is the electronic vertical transition energy (from the anion equilibrium geometry).

	CBS-QB3	MP2/aug-cc-pVTZ	CCSD/aug-cc-pVTZ	CCSD(T)/aug-cc-pVTZ <sup>a</sup>
<b><i>trans</i>-HONO<sup>-</sup></b>				
r <sub>HO</sub> (Å)	0.964	0.968 (0.968)	0.962	0.967
r <sub>ON,c</sub> (Å)	1.811	1.936 (1.845)	1.721	1.808
r <sub>NO,t</sub> (Å)	1.219	1.193 (1.211)	1.220	1.215
∠HON (°)	92.0	96.0 (93.5)	97.2	97.3
∠ONO (°)	109.6	107.9 (107.9)	107.7	107.9
<b><i>trans</i>-HONO (S<sub>0</sub>)</b>				
r <sub>HO</sub> (Å)	0.968	0.970	0.965	0.969
r <sub>ON,c</sub> (Å)	1.433	1.428	1.405	1.432
r <sub>NO,t</sub> (Å)	1.166	1.177	1.168	1.174
∠HON (°)	102.3	101.6	102.8	102.0
∠ONO (°)	111.0	110.7	110.7	110.6
T <sub>0</sub> (eV)	0.245	0.150 (0.288)	0.211	0.194
T <sub>v</sub> (eV)	1.15	3.13 (1.05)	1.01	0.974
EA( <i>trans</i> -HONO) (eV)	0.349	0.214 (0.388)	0.233	0.289
<b><i>trans</i>-HONO (T<sub>1</sub>)</b>				
r <sub>HO</sub> (Å)	0.968	0.970	0.965	-
r <sub>ON,c</sub> (Å)	1.428	1.413	1.412	-
r <sub>NO,t</sub> (Å)	1.220	1.187	1.221	-
∠HON (°)	102.1	102.6	102.2	-
∠ONO (°)	119.2	127.4	117.9	-
T <sub>0</sub> (eV)	2.74	3.03	2.50	-
T <sub>v</sub> (eV)	3.00	5.55	2.77	-
<sup>a</sup> The anion geometry converged to a dihedral angle of 184°				

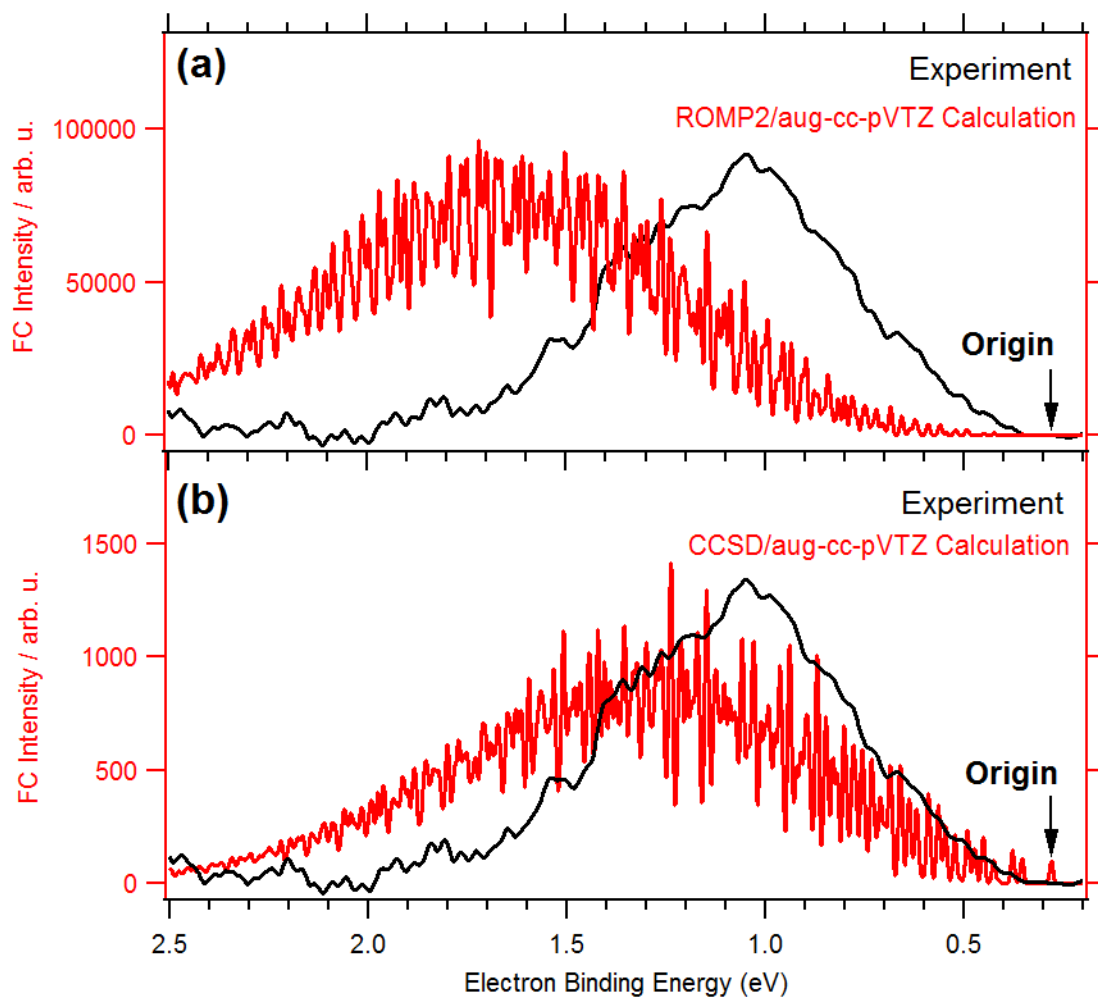


Figure 4.8: Calculated photoelectron spectrum of *trans*-HONO<sup>-</sup> (red trace) with (a) ROMP2/aug-cc-pVTZ, and (b) CCSD/aug-cc-pVTZ level of theory/basis-set. The experimental photoelectron spectrum using 3.49 eV photons (black, see Fig. 4.2) is shown for comparison. The arrow indicates the calculated origin of the progression, which was arbitrarily set to a FC intensity of 100.

Table 4.6: Comparison of HONO<sup>-</sup>, HONO (S<sub>0</sub>), and HONO (T<sub>1</sub>) energies and geometries for the *cis* isomer using different levels of theoretical treatment (CBS-QB3 composite method, MP2/aug-cc-pVTZ, CCSD/aug-cc-pVTZ, and CCSD(T)/aug-cc-pVTZ). For the anion, ROMP2/aug-cc-pVTZ results are given in parenthesis, while the values not in parentheses represent the results of UMP2 calculations. Energies reported are relative to the energy of the *cis*-HONO<sup>-</sup> equilibrium geometry, where T<sub>0</sub> is the electronic adiabatic term energy and T<sub>v</sub> is the electronic vertical transition energy (from the anion equilibrium geometry).

	CBS-QB3	MP2/aug-cc-pVTZ	CCSD/aug-cc-pVTZ	CCSD(T)/aug-cc-pVTZ
<b><i>cis</i>-HONO<sup>-</sup></b>				
r <sub>HO</sub> (Å)	0.966	0.971 (0.970)	0.966	0.969
r <sub>ON, c</sub> (Å)	1.696	1.657 (1.772)	1.558	1.663
r <sub>NO, t</sub> (Å)	1.245	1.238 (1.226)	1.264	1.252
∠HON (°)	93.9	95.5 (92.1)	97.0	94.9
∠ONO (°)	108.0	108.4 (108.0)	107.4	107.6
<b><i>cis</i>-HONO (S<sub>0</sub>)</b>				
r <sub>HO</sub> (Å)	0.980	0.980	0.979	0.978
r <sub>ON, c</sub> (Å)	1.388	1.387	1.391	1.396
r <sub>NO, t</sub> (Å)	1.180	1.192	1.190	1.187
∠HON (°)	105.9	104.6	105.2	104.6
∠ONO (°)	113.6	113.3	113.1	113.2
T <sub>0</sub> (eV)	0.296	0.180 (0.323)	0.230	0.264
T <sub>v</sub> (eV)	1.08	0.764 (1.19)	0.899	0.957
EA( <i>cis</i> -HONO) (eV)	0.384	0.247 (0.415)	0.315	0.352
<b><i>cis</i>-HONO (T<sub>1</sub>)</b>				
r <sub>HO</sub> (Å)	0.971	0.974	0.967	-
r <sub>ON, c</sub> (Å)	1.415	1.405	1.405	-
r <sub>NO, t</sub> (Å)	1.229	1.199	1.229	-
∠HON (°)	104.1	101.3	104.1	-
∠ONO (°)	121.7	129.7	120.3	-
T <sub>0</sub> (eV)	2.95	3.14	2.73	-
T <sub>v</sub> (eV)	3.19	3.97	2.97	-

Table 4.7: Comparison of HONO<sup>-</sup>, HONO (S<sub>0</sub>), and HONO (T<sub>1</sub>) harmonic frequencies for the *cis* isomer using different levels of theoretical treatment (CBS-QB3 composite method, MP2/aug-cc-pVTZ, CCSD/aug-cc-pVTZ, and CCSD(T)/aug-cc-pVTZ). For the anion, ROMP2/aug-cc-pVTZ results are given in parenthesis, while the values not in parentheses represent the results of UMP2 calculations.

	<b>CBS-QB3</b>	<b>MP2/aug-cc-pVTZ</b>	<b>CCSD/aug-cc-pVTZ</b>	<b>CCSD(T)/aug-cc-pVTZ</b>
<b><i>cis</i>-HONO<sup>-</sup></b>				
O–H stretch	3748.1	3714.3 (3733.8)	3762.8	3721.7
N=O stretch	1457.9	1533.4 (1559.7)	1404.6	1398.9
HON bend	1072.3	1133.3 (961.2)	1156.5	1069.9
O–N stretch	279.3	336.5 (269.1)	380.6	282.4
ONO bend	581.5	675.1 (529.1)	650.3	590.8
Torsion	305.6	274.8 (198.3)	337.6	289.5
<b><i>cis</i>-HONO (S<sub>0</sub>)</b>				
O–H stretch	3584.4	3591.2	3672.3	3609.3
N=O stretch	1720.6	1610.7	1732.2	1658.3
HON bend	1338.1	1320.2	1379.8	1336.7
O–N stretch	892.5	884.2	937.4	875.7
ONO bend	638.2	693.7	678.4	631.4
Torsion	718.2	634.0	670.0	667.1
<b><i>cis</i>-HONO (T<sub>1</sub>)</b>				
O–H stretch	3718.2	3700.1	3686.8	-
N=O stretch	1414.4	2154.4	1372.0	-
HON bend	1338.2	1369.9	1395.4	-
O–N stretch	771.5	910.6	826.5	-
ONO bend	452.9	558.0	441.7	-
Torsion	342.3 <i>i</i>	401.2 <i>i</i>	64.8 <i>i</i>	-

#### 4.3.f Thermochemistry of HONO

Using the experimentally measured EA(*cis*-HONO), we can also obtain the bond dissociation energy ( $D_0$ ) for  $\text{cis-HONO}^- \rightarrow \text{OH}^- + \text{NO}$ , referred to here as  $D_0(\text{HO}^--\text{NO})$ , via the thermodynamic cycle,

$$D_0(\text{HO}^--\text{NO}) = D_0(\text{HO}-\text{NO}) + \text{EA}(\text{cis-HONO}) - \text{EA}(\text{OH}) \quad (\text{Eq. 4.3})$$

where  $D_0(\text{HO}-\text{NO}) = 2.066(4) \text{ eV}^{17,23}$  and the  $\text{EA}(\text{OH}) = 1.828 \text{ eV}^{45}$ . This results in  $D_0(\text{HO}^--\text{NO}) = 0.594(9) \text{ eV}$ , significantly improving an earlier calculated value of  $0.49 \text{ eV}$  (Gaussian-2 composite method).<sup>18</sup> These results are summarized in Table 4.8. As previously noted, the extra electron in  $\text{cis-HONO}^-$  is added to a  $\pi^*$ -like anti-bonding molecular orbital, mainly localized along the central O–N bond. This results in a lengthening and weakening of the central bond upon the addition of an electron, consistent with the experimentally derived decrease in the O–N bond strength in  $\text{cis-HONO}^-$  compared to neutral *cis*-HONO.

The very weak central bond of  $\text{cis-HONO}^-$  and the small EA(*cis*-HONO) imply that it is unlikely that  $\text{cis-HONO}^-$  would be able to be formed via the reaction of  $\text{OH}^- + \text{NO}$  and collisionally stabilized in the troposphere before falling apart or undergoing electron autodetachment.<sup>18</sup> However, if  $\text{cis-HONO}^-$  is formed and stabilized, it would readily undergo photodetachment with any wavelength shorter than about 3000 nm. With a VDE of  $\sim 1.1 \text{ eV}$ , formation of neutral *cis*-HONO via photodetachment will preferentially be formed vibrationally hot, hence requiring less energy for dissociating and producing OH and NO radicals in the atmosphere.

Table 4.8: Summary of the Experimentally Determined Quantities: Electron Affinity and Term Energies of *cis*-HONO, and the Dissociation Energy of *cis*-HONO<sup>-</sup>.

<b>Parameter</b>	<b>Experimental</b>
Electron Affinity	0.356(8) eV
D <sub>0</sub> (HO <sup>-</sup> -NO)	0.594(9) eV
ΔE(T <sub>1</sub> - S <sub>0</sub> )	~ 2.3 eV

#### 4.3.g Triplet State: *cis*-HONO $\tilde{a}^3A''$

Fig. 4.9 shows the 301 nm (4.12 eV) photoelectron spectrum of *cis*-HONO<sup>-</sup>, spanning the T<sub>1</sub> excited state of *cis*-HONO. The excited state spectrum lies ~2.3 eV higher in energy than *cis*-HONO (S<sub>0</sub>) and consists of three peaks that are an order of magnitude broader (0.09 eV FMWH at 3.1 eV eBE) than the resolution of the photoelectron spectrometer in this electron kinetic energy range. This result means that the breadth of these three peaks is intrinsic to the electron photodetachment and not due to our experimental resolution. The peaks in the spectrum are spaced by roughly 0.195 eV, or 1570 cm<sup>-1</sup>. This energy is similar to the calculated frequency of the terminal N=O stretch in *cis*-HONO (T<sub>1</sub>) (1414 cm<sup>-1</sup>, CBS-QB3 composite method). A terminal N=O stretching vibration contribution to the photoelectron spectrum is also indicated based upon the calculated decrease in  $r_{\text{NO,t}}$ , from 1.25 Å to 1.23 Å from the anion to neutral (T<sub>1</sub>) equilibrium structures.

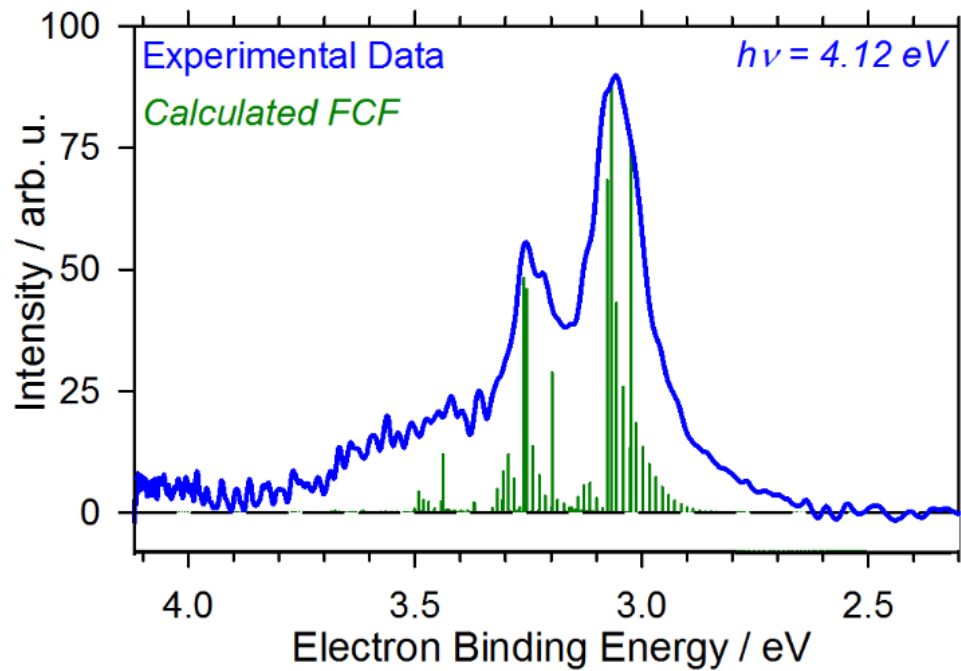


Figure 4.9: Detailed T1 excited state photoelectron spectrum of cis-HONO<sup>-</sup> using 301 nm (4.12 eV) photon energy. The green sticks are the calculated FCFs by the methods described in the text.

The potential energy curve for *cis*-HONO ( $T_1$ ) at the equilibrium geometry of *cis*-HONO<sup>-</sup> exhibits a transition state along the  $r_{\text{ON,c}}$  dissociation coordinate, as shown in Fig. 4.1. In order to model the experimentally observed photoelectron spectrum, we calculate the FCFs (green-sticks in Fig. 4.9) by approximating the transitions as bound to bound, as outlined in section 4.2.b. Essentially, an infinite potential wall is placed at large  $r_{\text{ON,c}}$  distances on the  $T_1$  potential energy curve, which allows for quantization of states along this HO–NO bond dissociation coordinate. While this is an approximation, the placement of an infinite wall only affects the density of states and not the overall shape of the envelope.

The overall shape of the calculated spectral envelope matches the experimental spectrum very well. The three main groups of peaks in the calculated spectrum reflect the active terminal N=O stretching vibration, as expected based on the experimental spacing of the peaks. Within each of these groups, there are two sets of peaks, which reflect the two regions of the  $T_1$  surface that can be accessed by the ground state wavefunction of the anion. The anion wavefunction has significant amplitude over a large range of  $r_{\text{ON,c}}$ . When this wavefunction is projected onto the triplet surface, it samples both scattering and bound states in the O–N bond dissociation coordinate. The relative intensities of these two types of transitions are sensitive to details of the triplet potential surface. In order to approximately reproduce the experimental peak contour, the triplet surface was shifted to larger  $r_{\text{ON,c}}$  distances by  $\sim 0.08$  Å relative to the anion surface. This shift is consistent with the variability of the calculated equilibrium  $r_{\text{ON,c}}$  bond length for the anion at several levels of electronic structure theory (see section 4.3.e). Due to the shallow anion potential energy surface along the central ON bond stretching coordinate, the  $r_{\text{ON,c}}$  in the anion optimized geometry spans a range of 0.2 Å. The potential shift results in an increase in the contribution of transitions to states that are localized in the well on the  $T_1$  state of *cis*-HONO to

the overall band contour. In addition, the energy scale of the calculated FCFs was shifted by ~30 meV to larger electron binding energy to more closely match the energetic position of the experimental spectrum. This shift roughly reflects the difference between the experimentally measured and calculated EA(*cis*-HONO).

The calculation indicates that the majority of the experimental peak breadth is due to the dissociation along  $r_{\text{ON,c}}$ , which would lead to the formation of OH and NO radicals. This analysis does not include other, smaller sources of peak broadening, such as rotational excitation of the separating OH and NO moieties, as well as activity in other *cis*-HONO ( $T_1$ ) vibrations. However, out of the possible active vibrations based on the geometry differences between the anion and *cis*-HONO ( $T_1$ ) equilibrium structures, only the N=O stretch remains bound following dissociation, and as such (unlike electron photodetachment to form the ground singlet state), only a progression in this vibration is expected to be reflected in the spectrum. Additional calculations show that including the torsion coordinate adds some further peak broadening, but does not change the overall contour. While the triplet potential energy surface is plotted only along one coordinate in Fig. 1, the local maximum in the blue curve is actually a second order saddle point, with the other imaginary frequency corresponding to the *cis*-HONO torsion. In other words, at the equilibrium geometry of *cis*-HONO<sup>-</sup>, *cis*-HONO ( $T_1$ ) is unstable with respect to isomerization to *trans*-HONO as well as to dissociation to OH + NO, and it is this feature of the  $T_1$  state potential that is responsible for the broadening.

There could also be a contribution to the photoelectron spectrum shown in Fig. 4.9 from photodetachment to *cis*-HONO ( $S_1$ ). Now that there is an experimental measurement of the EA of *cis*-HONO (0.356(8) eV), and a known  $S_0$ - $S_1$  term energy (3.26 eV),<sup>25</sup> the expected onset of the photoelectron spectrum corresponding to *cis*-HONO ( $S_1$ ) would be near 3.62 eV. The  $S_1$  state

of *cis*-HONO is known to be dissociative along the central HO-NO bond stretching coordinate<sup>8</sup> and so it might also exhibit broadened peaks. Any contribution of the S<sub>1</sub> state to the photoelectron spectrum assigned to detachment to *cis*-HONO (T<sub>1</sub>) is not conclusively identified, although there are photodetached electrons with very low kinetic energy seen in both the unprocessed photoelectron image (not shown) and the photoelectron spectrum (Fig. 4.9). Higher energy photons could be used to explore detachment to *cis*-HONO (S<sub>1</sub>), however, this state has been the focus of many past experimental studies<sup>24,25</sup> and current experimental details (particularly the large amount of background photoelectrons when using ultraviolet photon energies) inhibit this from being pursued further.

The major implication for the *cis*-HONO (T<sub>1</sub>) analysis stems from its potential atmospheric relevance as a source of OH radicals. For the photodissociation of *cis*-HONO (S<sub>0</sub>), producing OH radicals in the atmosphere, UV excitation accesses several higher lying singlet excited states. There is potential for intersystem crossing to play a role in the dissociation mechanism, as suggested by previous calculations.<sup>8,28</sup> The relative energies of the *cis*-HONO (T<sub>1</sub>) and *cis*-HONO (S<sub>0</sub>) electronic states (~2.3 eV), as well as the dissociation to form OH + NO from the triplet surface, is instructive to future theoretical investigations.

#### 4.4 Conclusions

We report the experimental photoelectron spectrum of *cis*-HONO<sup>-</sup>. In this experiment, *cis*-HONO<sup>-</sup> was formed in an association reaction of OH<sup>-</sup> and NO in a pulsed plasma-entrainment ion source. We observe the presence of only the *cis*-HONO<sup>-</sup> isomer, which is calculated to be the global minimum on the anion potential energy surface. The reported photoelectron spectra show photodetachment to both the singlet ground state ( $\tilde{X}^1A'$ ) and the triplet state ( $\tilde{a}^3A''$ ) of neutral *cis*-HONO. Based on the photoelectron spectrum, we obtain the

EA(*cis*-HONO) of 0.356(8) eV, with a VDE of approximately 1.1 eV. The large difference between the EA and the VDE is indicative of the significant geometry change upon electron photodetachment, which is consistent with the results of electronic structure calculations. In addition, detachment to form *cis*-HONO ( $S_0$ ) exhibits a photoelectron spectrum dominated by excitation of the central O–N stretching vibration ( $\nu_4$ ), further confirming the significant change in  $r_{\text{ON,c}}$  between the anion and neutral species. There are also significant contributions to the photoelectron spectrum from the ONO bending vibration ( $\nu_5$ ), particularly in combination bands with the central O–N stretching vibration. With the measurement of the EA, we also report the dissociation energy of the HO<sup>−</sup>–NO bond as 0.594(9) eV. Electronic structure calculations and photoelectron spectra simulations reported here show excellent agreement with the experimental data, providing confidence in our vibrational assignments. The previously unobserved *cis*-HONO ( $T_1$ ) state lies ~2.3 eV higher in energy than *cis*-HONO ( $S_0$ ). Vertical electron photodetachment from the anion onto the  $T_1$  state potential energy surface accesses a transition state which results in dissociation to OH + NO, as well as an active bound N=O vibration. Table 4.8 summarizes these experimentally determined quantities. With this study, we provide new experimental data on *cis*-HONO and its lowest lying excited electronic state, as well as information about its negative ion *cis*-HONO<sup>−</sup>. The information contained herein contributes to the knowledge of neutral *cis*-HONO as an important atmospheric species and precursor to OH radicals in the atmosphere.

## 4.5 Chapter 4 references

- <sup>1</sup> Y.-J. Lu, J.H. Lehman, and W.C. Lineberger, *J. Chem. Phys.* **142**, 44201 (2015).
- <sup>2</sup> A. Indarto, *Res. Chem. Intermed.* **38**, 1029 (2012).
- <sup>3</sup> R. Kurtenbach, K.H. Becker, J.A.G. Gomes, J. Kleffmann, J.C. Lorzer, M. Spittler, P. Wiesen, R. Ackermann, A. Geyer, and U. Platt, *Atmos. Environ.* **35**, 3385 (2001).
- <sup>4</sup> J. Kleffmann, T. Gavriloaiei, A. Hofzumahaus, F. Holland, R. Koppmann, L. Rupp, E. Schlosser, M. Siese, and A. Wahner, *Geophys. Res. Lett.* **32**, 5818 (2005).
- <sup>5</sup> D.G. Aubin and J.P.D. Abbatt, *J. Phys. Chem. A* **111**, 6263 (2007).
- <sup>6</sup> B.J. Finlayson-Pitts and J.N. Pitts, *Chemistry of the Upper and Lower Atmosphere : Theory, Experiments, and Applications* (Academic Press, San Diego, 2000).
- <sup>7</sup> R. Asatryan, J.W. Bozzelli, and J.M. Simmie, *Int. J. Chem. Kinet.* **39**, 378 (2007).
- <sup>8</sup> S.Y. Yu, C.G. Zhang, and M.B. Huang, *Chem. Phys. Lett.* **440**, 187 (2007).
- <sup>9</sup> D. Sengupta, R. Sumathi, and S.D. Peyerimhoff, *Chem. Phys.* **248**, 147 (1999).
- <sup>10</sup> F. Spataro and A. Ianniello, *J. Air Waste Manage. Assoc.* **64**, 1232 (2014).
- <sup>11</sup> T.C. VandenBoer, C.J. Young, R.K. Talukdar, M.Z. Markovic, S.S. Brown, J.M. Roberts, and J.G. Murphy, *Nat. Geosci.* **8**, 55 (2015).
- <sup>12</sup> B. Alicke, U. Platt, and J. Stutz, *J. Geophys. Res.* **107**, 9 (2002).
- <sup>13</sup> V. Bartolomei, M. Sorgel, S. Gligorovski, E.G. Alvarez, A. Gandolfo, R. Strekowski, E. Quivet, A. Held, C. Zetzsch, and H. Wortham, *Environ. Sci. Pollut. Res.* **21**, 9259 (2014).
- <sup>14</sup> J.M. Guilmot, M. Godefroid, and M. Herman, *J. Mol. Spectrosc.* **160**, 387 (1993).
- <sup>15</sup> J.M. Guilmot, F. Melen, and M. Herman, *J. Mol. Spectrosc.* **160**, 401 (1993).
- <sup>16</sup> F. Reiche, B. Abel, R.D. Beck, and T.R. Rizzo, *J. Chem. Phys.* **116**, 10267 (2002).
- <sup>17</sup> F. Reiche, B. Abel, R.D. Beck, and T.R. Rizzo, *J. Chem. Phys.* **112**, 8885 (2000).
- <sup>18</sup> J.M. Vandoren, A.A. Viggiano, R.A. Morris, A.E.S. Miller, T.M. Miller, J.F. Paulson, C.A. Deakyne, H.H. Michels, and J.A. Montgomery, *J. Chem. Phys.* **98**, 7940 (1993).
- <sup>19</sup> D.J. Finnigan, J.G. Smith, A.P. Cox, and A.H. Brittain, *J. Chem. Soc. Trans. II* **68**, 548 (1972).
- <sup>20</sup> R.T. Hall and G.C. Pimentel, *J. Chem. Phys.* **38**, 1889 (1963).
- <sup>21</sup> V. Botan and P. Hamm, *J. Chem. Phys.* **129**, 164506 (2008).
- <sup>22</sup> A.P. Cox, A.H. Brittain, and D.J. Finnigan, *Trans. Faraday Soc.* **67**, 2179 (1971).
- <sup>23</sup> V. Sironneau, J.M. Flaud, J. Orphal, I. Kleiner, and P. Chelin, *J. Mol. Spectrosc.* **259**, 100 (2010).
- <sup>24</sup> A. Bongartz, J. Kames, F. Welter, and U. Schurath, *J. Phys. Chem.* **95**, 1076 (1991).

- <sup>25</sup> G.W. King and D. Moule, *Can. J. Chem.* **40**, 2057 (1962).
- <sup>26</sup> R. Vasudev, R.N. Zare, and R.N. Dixon, *Chem. Phys. Lett.* **96**, 399 (1983).
- <sup>27</sup> G. Amaral, K.S. Xu, and J.S. Zhang, *J. Phys. Chem. A* **105**, 1465 (2001).
- <sup>28</sup> C. Larrieu, A. Dargelos, and M. Chaillet, *Chem. Phys. Lett.* **91**, 465 (1982).
- <sup>29</sup> N.S. Shuman, D.E. Hunton, and A.A. Viggiano, *Chem. Rev.* **115**, 4542 (2015).
- <sup>30</sup> K.M. Ervin, J. Ho, and W.C. Lineberger, *J. Phys. Chem.* **92**, 5405 (1988).
- <sup>31</sup> K.M. Ervin, W. Anusiewicz, P. Skurski, J. Simons, and W.C. Lineberger, *J. Phys. Chem. A* **107**, 8521 (2003).
- <sup>32</sup> D. Hanstorp and M. Gustafsson, *J. Phys. B At. Mol. Opt. Phys.* **25**, 1773 (1992).
- <sup>33</sup> K.M. Ervin, T.M. Ramond, G.E. Davico, R.L. Schwartz, S.M. Casey, and W.C. Lineberger, *J. Phys. Chem. A* **105**, 10822 (2001).
- <sup>34</sup> C.M. Deeley and I.M. Mills, *J. Mol. Struct.* **100**, 199 (1983).
- <sup>35</sup> L. Khriachtchev, J. Lundell, E. Isoniemi, and M. Rasanen, *J. Chem. Phys.* **113**, 4265 (2000).
- <sup>36</sup> M.J. Frisch, G.W. Trucks, H.B. Schlegel, G.E. Scuseria, M.A. Robb, J.R. Cheeseman, G. Scalmani, V. Barone, B. Mennucci, G.A. Petersson, H. Nakatsuji, M. Caricato, X. Li, H.P. Hratchian, A.F. Izmaylov, J. Bloino, G. Zheng, J.L. Sonnenberg, M. Hada, M. Ehara, K. Toyota, R. Fukuda, J. Hasegawa, M. Ishida, T. Nakajima, Y. Honda, O. Kitao, H. Nakai, T. Vreven, J.A. Montgomery Jr., J.E. Peralta, F. Ogliaro, M.J. Bearpark, J. Heyd, E.N. Brothers, K.N. Kudin, V.N. Staroverov, R. Kobayashi, J. Normand, K. Raghavachari, A.P. Rendell, J.C. Burant, S.S. Iyengar, J. Tomasi, M. Cossi, N. Rega, N.J. Millam, M. Klene, J.E. Knox, J.B. Cross, V. Bakken, C. Adamo, J. Jaramillo, R. Gomperts, R.E. Stratmann, O. Yazyev, A.J. Austin, R. Cammi, C. Pomelli, J.W. Ochterski, R.L. Martin, K. Morokuma, V.G. Zakrzewski, G.A. Voth, P. Salvador, J.J. Dannenberg, S. Dapprich, A.D. Daniels, Ö. Farkas, J.B. Foresman, J. V. Ortiz, J. Cioslowski, and D.J. Fox, *Gaussian 09 Revision B.01*, Gaussian Inc. Wallingford, CT (2009).
- <sup>37</sup> D.T. Colbert and W.H. Miller, *J. Chem. Phys.* **96**, 1982 (1992).
- <sup>38</sup> G.H. Gardenier, M.A. Johnson, and A.B. McCoy, *J. Phys. Chem. A* **113**, 4772 (2009).
- <sup>39</sup> G.H. Gardenier, M.A. Johnson, and A.B. McCoy, *J. Phys. Chem. A* **116**, 8797 (2012).
- <sup>40</sup> J.C. Bopp, J.R. Roscioli, M.A. Johnson, T.M. Miller, A.A. Viggiano, S.M. Villano, S.W. Wren, and W.C. Lineberger, *J. Phys. Chem. A* **111**, 1214 (2007).
- <sup>41</sup> D.L. Osborn, K.M. Vogelhuber, S.W. Wren, E.M. Miller, Y.J. Lu, A.S. Case, L. Sheps, R.J. McMahon, J.F. Stanton, L.B. Harding, B. Ruscic, and W.C. Lineberger, *J. Am. Chem. Soc.* **136**, 10361 (2014).
- <sup>42</sup> E.P. Wigner, *Phys. Rev.* **73**, 1002 (1948).
- <sup>43</sup> M.J. Travers, D.C. Cowles, E.P. Clifford, G.B. Ellison, and P.C. Engelking, *J. Chem. Phys.* **111**, 5349 (1999).
- <sup>44</sup> P.C. Engelking, *J. Phys. Chem.* **90**, 4544 (1986).

<sup>45</sup> J.R. Smith, J.B. Kim, and W.C. Lineberger, Phys. Rev. A **55**, 2036 (1997).

*this page is intentionally left blank*

## CHAPTER V

### PHOTOELECTRON SPECTROSCOPY OF THE HYDROXYMETHOXIDE ANION



This chapter is partially reproduced from: *Oliveira, A.M, Lehman, J.H., McCoy, A.B., Lineberger, W.C., The Journal of Chemical Physics, vol. 145, p. 124317 (2016)* with permission of the authors.

#### 5.1 Introduction

Alkoxy radicals are known to play an important role in tropospheric and combustion chemistry.<sup>1-7</sup> Many experimental and theoretical studies have focused on the effects of adding various substituents onto the methoxy radical, the simplest alkoxy radical, looking for trends in tropospheric reaction kinetics, unimolecular processes, and overall reactivity.<sup>1-5,8</sup> The hydroxymethoxy radical ( $\text{H}_2\text{C}(\text{OH})\text{O}^\bullet$ ) is an oxygenated alkoxy radical, proposed to be formed from the UV photofragmentation of hydroxymethyl hydroperoxide ( $\text{H}_2\text{C}(\text{OH})\text{OOH}$ ), a product from the tropospheric oxidation of alkenes.<sup>9-13</sup> In addition to the potential atmospheric importance of the  $\text{H}_2\text{C}(\text{OH})\text{O}^\bullet$  radical, its corresponding anion, hydroxymethoxide ( $\text{H}_2\text{C}(\text{OH})\text{O}^-$ ), is the conjugate base of methanediol ( $\text{H}_2\text{C}(\text{OH})_2$ ), considered to be a molecule of astrochemical and possible prebiotic relevance<sup>14-18</sup> as a building block of simple amino acids.<sup>19,20</sup> Despite the relevance of the hydroxymethoxy radical to combustion and planetary chemistry, very little is known about its spectroscopy. In fact,  $\text{H}_2\text{C}(\text{OH})\text{O}^\bullet$  has only recently been experimentally observed. Cao *et al.*<sup>21</sup> detected  $\text{H}_2\text{C}(\text{OH})\text{O}^\bullet$  as a product from the reaction of atomic hydrogen with formic acid in a krypton matrix isolation experiment. In this experiment,

the radical product was only stable for a few hours at the cryogenic matrix temperatures before isomerizing to  $\text{HC}'(\text{OH})_2$ . In general, the high reactivity of  $\text{H}_2\text{C}(\text{OH})\text{O}'$  makes a direct gas phase experimental observation very challenging.

The comparison of  $\text{H}_2\text{C}(\text{OH})\text{O}'$  with other alkoxy radicals is an interesting study on the effects of non-alkyl substituents on the electronic structure of the methoxy radical. Previous experimental and theoretical work studied the effect of methyl substitutions, forming ethoxy, isopropoxy, and *tert*-butoxy radicals.<sup>22-26</sup> The substitution of a methyl group for a hydrogen atom will change the electronic structure of the methoxy radical, breaking its  $C_{3v}$  symmetry. For the ethoxy radical, significant Jahn-Teller distortions were observed in the  $\text{CH}_3\text{CH}_2\text{O}'$  photoelectron spectrum, where the  $\text{CH}_3\text{CH}_2\text{O}' \tilde{A}$  state was found to be only  $355 \text{ cm}^{-1}$  higher in energy than the ground  $\tilde{X}$  state.<sup>22</sup> The inclusion of vibronic coupling was imperative in order to analyze its spectrum.<sup>24</sup> There was significantly less vibronic coupling observed for the isopropoxy and *tert*-butoxy radicals.<sup>22,26</sup>

While the work on interpreting the photoelectron spectra of the ethoxide anion yielded results that needed to be analyzed with the inclusion of Jahn-Teller distortions and vibronic coupling,<sup>22,24,25,27</sup> recent calculations suggest this will not be the case for hydroxymethoxy.<sup>28</sup> Einfeld and Francisco<sup>11</sup> studied low lying electronic states of  $\text{H}_2\text{C}(\text{OH})\text{O}'$ , focusing on calculating its electronic absorption spectra (CASSCF/CASPT2, CASSCF/MRCI+Q). Although they pointed out that nonadiabatic effects might exist between the low-lying electronic states of  $\text{H}_2\text{C}(\text{OH})\text{O}'$ , they were not explicitly included in the calculations.<sup>11</sup> Dillon and Yarkony,<sup>28</sup> on the other hand, explored the ground  $\tilde{X}^2A$  and first excited  $\tilde{A}^2A$  electronic states of  $\text{H}_2\text{C}(\text{OH})\text{O}'$  (SA-MCSCF/MR-SDCI), comparing its electronic structure with other substitutional isomers of the methoxy radical (ethoxy and isopropoxy radicals). This work showed that there are strong

nonadiabatic couplings between the ground ( $\tilde{X}^2A$ ) and the first excited ( $\tilde{A}^2A$ ) electronic states of  $\text{H}_2\text{C}(\text{OH})\text{O}^\bullet$ .

This chapter presents an anion photoelectron spectroscopic investigation of the hydroxymethoxy radical, as well as the measurement of its electron affinity (EA). Here, the ground  $\tilde{X}^2A$  and first excited  $\tilde{A}^2A$  states of  $\text{H}_2\text{C}(\text{OH})\text{O}^\bullet$  are observed through negative ion photoelectron spectroscopy of  $\text{H}_2\text{C}(\text{OH})\text{O}^-$ . The high reactivity of neutral  $\text{H}_2\text{C}(\text{OH})\text{O}^\bullet$  and its close relation to methanediol motivates its spectroscopic investigation through its negative ion,  $\text{H}_2\text{C}(\text{OH})\text{O}^-$ , which is predicted to be more stable by 2.232 eV.<sup>11</sup> A comparison with other small alkoxy radicals is drawn, together with an exploration of the H-OCO torsional motion. Quantum chemical calculations aid in the interpretation of the photoelectron spectra and provide accurate thermochemical quantities of the gas phase chemistry of methanediol.

## 5.2 Methods

### 5.2.a Experimental

The hydroxymethoxide anion is produced in the dual valve ion source described in Chapter 2 by the reaction between neutral formaldehyde ( $\text{H}_2\text{CO}$ ) and the hydroxide anion ( $\text{OH}^-$ ). In order to produce a mixture of pure formaldehyde in argon, a procedure similar to the one described by Ho *et al.* is followed.<sup>29</sup> Here, a solid sample of polyoxymethylene (formaldehyde polymer) is heated to 60(5) °C under a 40 psig flow of argon. The principal product from the decomposition of polyoxymethylene is gaseous monomeric formaldehyde, but water and other small oligomers, such as dimeric formaldehyde and trioxane, are also formed. This gaseous mixture flows through a glass trap equipped with a fritted glass disk and held at -80 °C (dry ice/methanol bath) in order to trap these undesired products and prevent repolymerization. The

vapor pressure of liquid formaldehyde at this temperature is enough to provide a ~0.8% mixture of formaldehyde in argon.<sup>30</sup>

### 5.2.b Theoretical Methods

In this work, all electronic structure calculations are performed using the Gaussian 09 software package.<sup>31</sup> In order to calculate the photoelectron spectra, geometry optimizations and harmonic frequencies are calculated at the CCSD(T)/aug-cc-pVTZ level of theory for  $\text{H}_2\text{C}(\text{OH})\text{O}^-$ , and ROCCSD(T)/aug-cc-pVTZ for the  $\text{H}_2\text{C}(\text{OH})\text{O}^{\cdot} \tilde{X}^2A$  state. For the excited  $\text{H}_2\text{C}(\text{OH})\text{O}^{\cdot} \tilde{A}^2A$  electronic state, geometry optimizations and frequencies are calculated using CIS/aug-cc-pVTZ, while single point energies were calculated at the EOMCCSD/aug-cc-pVTZ level of theory. The calculated normal modes and structural parameters are input into the PESCAL software package, which calculates Franck-Condon factors (FCF) based on the Sharp-Rosenstock-Chen method with Duschinsky rotations.<sup>32-34</sup> The resulting FCFs are used to generate calculated photoelectron spectra.

When the stationary points on the potential surface for the hydroxymethoxy radical are analyzed, it is found that the minimum energy structure is rotated about the H3-O2-C-O1 torsion angle (see the inset in Fig. 5.1 for atom labeling), labeled throughout this chapter as  $\phi_{\text{HOCO}}$ , by  $\pm 48^\circ$  relative to its value at the minimum on the hydroxymethoxide surface, which is at  $\phi_{\text{HOCO}} = 0^\circ$ . A dihedral angle of  $0^\circ$  is defined as a planar H-OCO moiety in the *cis*- conformation, as shown in the inset in Fig. 5.1. Based on this, the minimum for the ground  $\tilde{X}^2A$  state of hydroxymethoxy has  $C_1$  symmetry, while the minimum energy structure of the hydroxymethoxide anion has  $C_s$  symmetry. The lowest energy  $C_s$  symmetry structure on the hydroxymethoxy surface is  $160 \text{ cm}^{-1}$  above the minimum energy structure and corresponds to a

saddle point on the potential surface. By contrast, the harmonic frequency associated with the H-OCO torsion is  $240\text{ cm}^{-1}$ . Based on the above, it is not expected that this torsion vibration will be well-described by a harmonic treatment evaluated at the potential minimum, as is employed in the PESCAL simulation software. These attributes are also seen for the  $\text{H}_2\text{C}(\text{OH})\text{O}^{\bullet} \tilde{A}^2A$  state, although a larger energy difference between  $C_1$  and  $C_s$  minima is calculated ( $968\text{ cm}^{-1}$  energy difference,  $375\text{ cm}^{-1}$  harmonic frequency of the H-OCO torsion vibration). This is discussed in more detail in Section 5.5.A. To introduce this large amplitude motion into the Franck-Condon simulation, the harmonic wavefunctions for the torsion are replaced by the wavefunctions obtained by solving the one dimensional Schrödinger equation associated with the torsion, described below. The remaining vibrations are treated at the harmonic level, where the normal modes and harmonic frequencies are obtained at the  $C_s$  saddle point structure for hydroxymethoxy. These frequencies, rather than those obtained at the  $C_1$  minimum, are used because the torsion wavefunction for the electronic ground state of  $\text{H}_2\text{C}(\text{OH})\text{O}^{\bullet}$  has significant amplitude at this higher symmetry geometry, as is seen in Fig. 5.2.

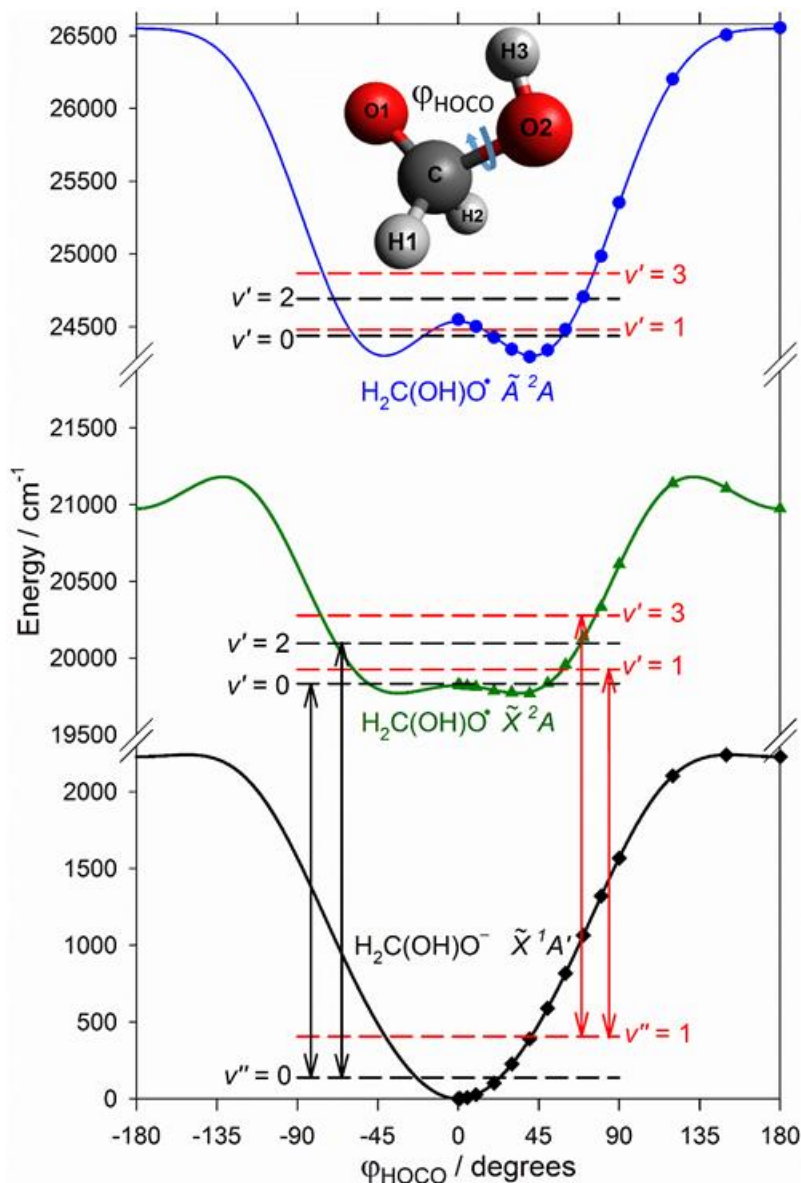


Figure 5.1: Calculated (CCSD(T)/aug-cc-pVTZ) 1D potential energy curves of the torsional coordinate for the electronic states of hydroxymethoxy accessed in the photodetachment process. The anion potential energy is as a relaxed scan. The neutral surfaces were constructed by calculating the energy of the neutral molecule at the optimized anion geometries. The dashed horizontal lines represent the eigenvalues of these potentials, while their colors, together with the double headed arrows between the anion and neutral ground states, represent the parity allowed transitions.

In addition, the higher symmetry of the  $C_s$  saddle point leads to improved separation of the torsion from the other vibrations in the construction of the normal modes due to the absence of coupling between vibrations of  $A'$  and  $A''$  symmetry in the development of the normal modes when the Hamiltonian is expressed in symmetry adapted linear combinations of internal coordinates. This approach is similar to that employed in our earlier study of the photoelectron spectra of  $\text{CHX}_2$ ,  $X = \text{Cl, Br and I}$ , which contained a similar large amplitude vibrational mode.<sup>35</sup> For a further discussion of the separability of the torsional coordinate, see section 5.4.a. To obtain the torsion wavefunctions, first a one-dimensional relaxed potential energy surface is evaluated for the hydroxymethoxide anion by varying the  $\varphi_{\text{HOCO}}$  dihedral angle while allowing all other coordinates to relax to their values at the minimum energy configuration. This scan (CCSD(T)/aug-cc-pVTZ) was performed from  $0^\circ$  to  $180^\circ$  with variable increments. Table 5.1 shows the calculated points and corresponding energies. In order to better represent the vertical transition region of the potential, which is sampled in the photodetachment experiment, the neutral surface was constructed by calculating the energies of hydroxymethoxy at the optimized anion geometries, as shown in Fig. 5.1. These energies were fit to:

$$V(\varphi_{\text{HOCO}}) = A + \sum_{n=1}^5 V_n (1 - \cos(n\varphi_{\text{HOCO}})) \quad (5.1)$$

where the value of  $A$  provides the energy of hydroxymethoxy at the minimum energy geometry of hydroxymethoxide, *e.g.* the vertical detachment energy. The optimized fit parameters are listed in Table 5.2.

The eigenvalues and eigenvectors of this potential were calculated by solving the one dimensional Schrödinger equation based on

$$H = \frac{1}{2} p_{\varphi_{\text{HOCO}}} G_{\varphi_{\text{HOCO}}, \varphi_{\text{HOCO}}}(\varphi_{\text{HOCO}}) p_{\varphi_{\text{HOCO}}} + V(\varphi_{\text{HOCO}}) \quad (5.2)$$

using a basis of Fourier functions,  $\psi(\varphi_{\text{HOCO}}) = \sqrt{\frac{1}{2\pi}} e^{-iJ\varphi_{\text{HOCO}}}$  with  $J=(-100,100)$ . The  $G_{\varphi_{\text{HOCO}}, \varphi_{\text{HOCO}}}$  term in Eq. (5.2) was evaluated using the expressions given by Frederick and Woywod,<sup>36</sup> and fit to an expansion in  $(1 - \cos(n\varphi_{\text{HOCO}}))$ , analogous to Eq. 5.1. Expanding the G-matrix element allows us to account for the effects of geometry changes in the relaxed scan on the effective mass associated with  $\varphi_{\text{HOCO}}$ . Operationally, the value of  $G_{\varphi_{\text{HOCO}}, \varphi_{\text{HOCO}}}$  changes by roughly 5% over the range of  $\varphi_{\text{HOCO}}$ . The expansion coefficients are also included in Table 5.2. The FCFs were then obtained by evaluating the overlap of the two lowest energy vibrational states on the hydroxymethoxide anion potential surface with vibrational states on the hydroxymethoxy neutral surface for the electronic state of interest. Because of the separate treatment of the H-OCO torsional mode and the remainder of the normal modes of the neutral hydroxymethoxy radical described above, the reported calculated spectrum was obtained by convolving each FCF of the remaining 3N-7 normal modes (obtained with PESCAL) with the spectrum obtained for the torsional transitions. The resulting FCFs were then convoluted with Gaussian functions of varying *fwhm* in order to match the experimental resolution, therefore providing a direct comparison between the calculated and experimental spectra. This procedure was repeated for the  $\text{H}_2\text{C}(\text{OH})\text{O}^* \tilde{A}^2A$  excited state calculations also performed here (CIS/aug-cc-pVTZ geometry optimization and vibrational frequencies, EOMCCSD/aug-cc-pVTZ single point energies). The calculations performed here for the optimized geometries and harmonic frequencies of the anion  $\tilde{X}^1A'$  and neutral  $\tilde{X}^2A$ ,  $\tilde{A}^2A$  states are in good agreement with the ones reported by Einfeld and Francisco<sup>11</sup> (anion: CCSD(T)/aug-cc-pVQZ, neutral: MRCI+Q/aug-cc-pVQZ) and Dillon and Yarkony (SA-MCSCF/MR-SDCI).<sup>28</sup>

Table 5.1: Calculated torsional potential energy surface scan (CCSD(T)/aug-cc-pVTZ) for  $\text{H}_2\text{C}(\text{OH})\text{O}^- \tilde{X}^1A'$  and  $\text{H}_2\text{C}(\text{OH})\text{O} \cdot \tilde{X}^2A$ , and EOM-CCSD/aug-cc-pVTZ for  $\text{H}_2\text{C}(\text{OH})\text{O} \cdot \tilde{A}^2A$ . The offset refers to the relative position of the calculated point to the energy of the anion  $\phi_{\text{HOCO}} = 0^\circ$  structure, *i.e.* summing the offset value to each column will result in the energy of these points relative to the anion minimum energy, which is plotted in Figs. 5.1 and 5.2.

$\phi_{\text{HOCO}} /$ degrees	$E_{\text{anion}} (\tilde{X}^1A')$ Relaxed / $\text{cm}^{-1}$	$E_{\text{neutral}} (\tilde{X}^2A)$ Relaxed / $\text{cm}^{-1}$	$E_{\text{neutral}} (\tilde{X}^2A)$ Vertical / $\text{cm}^{-1}$	$E_{\text{neutral}} (\tilde{A}^2A)$ Vertical / $\text{cm}^{-1}$
0	0	0	0	0
1	0.2	-0.2	-2.9	--
5	6.5	-4.5	-7.2	--
10	26.1	-17.5	-14.5	-47.4
20	102.7	-61.5	-39.2	-122.9
30	225.4	-112.5	-48.7	-204.3
40	389.4	-150.3	-56.8	-255.8
50	588.8	-159.5	9.8	-210
60	817.5	-131.2	129.5	-67.3
70	1065.9	-62.4	305.9	156.7
80	1321.4	43.3	507.4	435.7
90	1568	176.8	788.2	802.9
120	2104.5	587.5	1314.4	1652.2
150	2241.5	742.9	1280	1955.6
180	2229.1	730.1	1150.4	2004.9
Offset	0	17536.9	19768.4	24293

Table 5.2: Fit parameters of equation 5.1 for each of the potentials. The A parameter defines the absolute energy of the  $V(\varphi_{\text{HOCO}} = 0)$  point. All parameters have units of  $\text{cm}^{-1}$ . Also included are the expansion coefficients for the  $G_{\varphi_{\text{HOCO}},\varphi_{\text{HOCO}}}$  term in equation 5.2, which is an expansion in  $1 - \cos(n\varphi_{\text{HOCO}})$ , analogous to equation 5.1.

Fit Parameter	$E_{\text{anion}}(\tilde{X}^1A')$ Relaxed	$E_{\text{neutral}}(\tilde{X}^2A)$ Relaxed	$E_{\text{neutral}}(\tilde{X}^2A)$ Vertical	$E_{\text{neutral}}(\tilde{A}^2A)$ Vertical	$G_{\varphi_{\text{HOCO}},\varphi_{\text{HOCO}}}$
A (relative to anion min.)	0	17695	19821	24536	--
A (relative to potential min.)	0	158.13	52.606	243.43	22.519
$V_1$	1168	488.3	776.36	1248.2	-0.4662
$V_2$	227.05	-92.52	102.63	-98.568	0.5921
$V_3$	-57.421	-117.65	-205.24	-240.08	0.08515
$V_4$	3.7835	0.5374	-6.1282	-42.606	0.01402
$V_5$	3.8311	-5.7112	5.5903	-1.5042	--

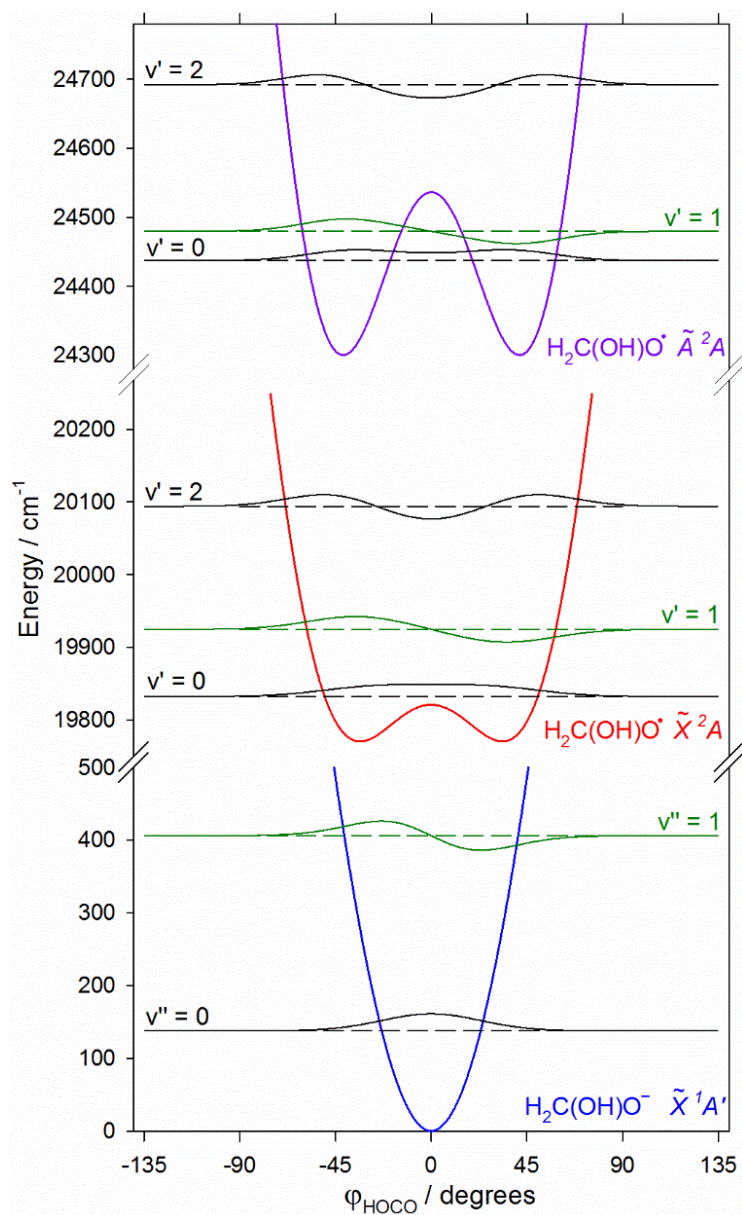


Figure 5.2: Calculated 1D potential energy curves as functions of the torsional coordinate for the  $\text{H}_2\text{C}(\text{OH})\text{O}^- \tilde{X}^1A'$  (blue),  $\text{H}_2\text{C}(\text{OH})\text{O}^\bullet \tilde{X}^2A$  (red), and  $\text{H}_2\text{C}(\text{OH})\text{O}^\bullet \tilde{A}^2A$  (purple) states. The vibrational wave functions are plotted in black (even functions) and green (odd functions). All potentials are the calculated at the optimized anion geometries and cover the same energy range. These potentials are the same as in Fig. 5.1, but with different angle and energy ranges in order to better view the wavefunctions.

### 5.3 Results

Following the ion generation procedure described in section 5.2.a, an anion with  $m/z = 47$  was successfully produced. Although  $\text{H}_2\text{C}(\text{OH})\text{O}^-$  is the most stable product with  $m/z = 47$  from the association reaction of  $\text{OH}^-$  with  $\text{H}_2\text{CO}$ ,<sup>37</sup> other structural isomers of  $\text{CH}_3\text{O}_2^-$  could exist in the ion beam. However, the use of photoelectron spectroscopy can unequivocally identify the presence or absence of these other isomers. The photoelectron spectrum of methyl hydroperoxide ( $\text{H}_3\text{COO}^-$ ) was reported previously by Blanksby *et al.*,<sup>38</sup> and does not match the reported spectrum here. The other possible isomers at  $m/z = 47$  are  $\text{H}_2\text{COOH}^-$  and  $\text{HC}(\text{OH})_2^-$ . Based on electronic structure calculations,  $\text{H}_2\text{COOH}^-$  is unstable with respect to isomerization to  $\text{H}_2\text{C}(\text{OH})\text{O}^-$  when calculated at B3LYP/aug-cc-pVTZ level of theory/basis. The other possible structural isomer,  $\text{HC}(\text{OH})_2^-$ , is also unlikely, due to the calculated electron affinity of  $\text{HC}(\text{OH})_2$  being negative (-0.011 eV, B3LYP/aug-cc-pVTZ).

#### 5.3.a Experimental Photoelectron Spectra and $EA(\text{H}_2\text{C}(\text{OH})\text{O}^*)$

The photoelectron spectrum taken with 3.49 eV photon energy is shown in the middle panel of Fig. 5.3. The spectrum shows two distinct regions: a structured, regularly spaced progression ranging from 2.2 to 2.7 eV; and a broader, partially resolved peak which spans from ~2.8 to 3.5 eV. The top panel of Fig. 5.3 shows the anisotropy parameter  $\beta$  as a function of eKE (top horizontal axis). The  $\beta$  parameter has a positive value ( $\beta = +0.3(2)$ ) for the broad, high eBE peak, while peaks A–D show increasingly negative  $\beta$  values, where peak A has  $\beta = -0.65(6)$ . Generally,<sup>39</sup> a positive  $\beta$  is associated with a photoelectron originating from an anion molecular orbital with more s-character, while a negative  $\beta$  is associated with photodetachment from an anion molecular orbital with more p-character. A quantitative determination of the fractional s or p character of these anion molecular orbitals is unable to be extracted from this experiment.

However, the difference between the photoelectron angular distributions indicates that the two regions of the spectrum can be associated with detachment to form two different electronic states of neutral hydroxymethoxy radical. Using a simple symmetry-based analysis, a transition from the anion HOMO ( $a''$  symmetry orbital) is associated with a negative  $\beta$ , while a transition from the anion HOMO-1 ( $a'$  symmetry) is associated with a positive  $\beta$ .<sup>40</sup> The ground and first excited states of  $\text{CH}_2(\text{OH})\text{O}^\bullet$ , using the  $C_s$  symmetry labels valid at  $\phi_{\text{HOCO}} = 0^\circ$ , are described by  $\tilde{X}^2A''$  and  $\tilde{A}^2A'$  state labels. The molecular orbitals associated with the two lowest energy electronic states of  $\text{H}_2\text{C}(\text{OH})\text{O}^\bullet$  have also already been calculated,<sup>11,28</sup> and are associated with a half-filled  $a''$  ( $a'$ ) symmetry  $p_y$  ( $p_x$ ) orbital at the O1 atom for the ground (excited) electronic state (note: in this representation, the heavy atoms are taken to lie in the  $xz$  plane). Thus, the electron angular anisotropy is consistent with electron detachment from  $\text{H}_2\text{C}(\text{OH})\text{O}^- \tilde{X}^1A'$  to form  $\text{H}_2\text{C}(\text{OH})\text{O}^\bullet \tilde{X}^2A''$  and  $\tilde{A}^2A'$  states (using  $C_s$  symmetry labels). In addition to the evidence provided by the sign of the angular anisotropy parameter, the calculated term energy ( $T_0$ ) of the lowest lying excited  $\text{H}_2\text{C}(\text{OH})\text{O}^\bullet \tilde{A}^2A$  state puts it approximately 0.38 eV higher in energy than the ground ( $\tilde{X}^2A$ ) state.<sup>11,28</sup> This value is in good agreement with the energy difference between the origins of the two features in Fig. 5.3 Higher lying excited states exist for  $\text{H}_2\text{C}(\text{OH})\text{O}^\bullet$ , but all are calculated to lie more than 3.5 eV above the ground  $\tilde{X}^2A$  state and should not be candidates for this progression.<sup>11</sup> Thus it is most likely that the higher energy electronic state that is observed is the excited  $\text{H}_2\text{C}(\text{OH})\text{O}^\bullet \tilde{A}^2A$  state.

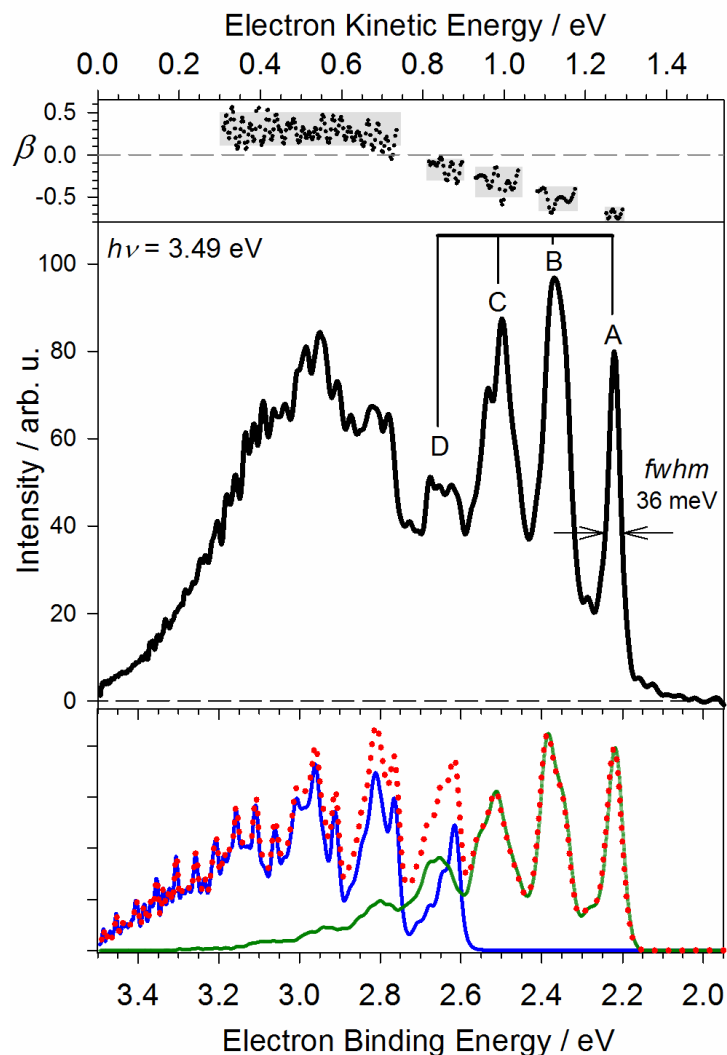


Figure 5.3: Upper panel: Experimental anisotropy parameters ( $\beta$ ) as a function of electron kinetic energy. The black circles are a series of  $\beta$  measured above the *fwhm* of each resolvable peak in the spectrum across each peak. The grey shaded regions indicate the average  $\beta$ , where the height shows the scatter of the  $\beta$  values across this width. Middle panel: Experimental photoelectron spectrum of  $\text{H}_2\text{C}(\text{OH})\text{O}^-$ , using 3.49 eV (355 nm) photon energy. Peaks A through D are discussed in the text. Lower panel: Convolved photoelectron simulations of detachment to the ground (green) and excited (blue) electronic states of  $\text{H}_2\text{C}(\text{OH})\text{O}^*$ , along with their sum (red dots).

The lowest eBE peak in the spectrum, peak A, has a *fwhm* of 0.036 eV, a value close to the experimental resolution, suggesting minimal rotational broadening (see Chapter 2). Surprisingly, all other peaks in the spectrum are considerably broader despite having lower eKE. This indicates that there are other contributions to the observed width. The  $\tilde{A}^2A$  excited state peak is located at the high eBE (low eKE) region, where an isolated peak at eKE  $\sim 0.5$  eV would be expected to have a width of  $\sim 15$  meV. The fact that no sharp peaks are observed in the  $\tilde{A}^2A$  state, particularly at the high binding energy edge of the spectrum, suggests that there is likely a large degree of spectral congestion in this region of the spectrum (discussed further in Section 5.3.c). The  $\tilde{X}^2A$  ground state progression, on the other hand, also exhibits increasingly broad peaks regularly spaced by  $\sim 0.14$  eV ( $1130\text{ cm}^{-1}$ ) as the eKE is decreased (eBE is increased). This suggests that peaks B through D consist of multiple vibrational transitions, which are not resolved at this eKE. Therefore, the use of a lower photon energy for photodetachment, yielding a lower eKE spectrum, should reduce the peak widths and provide a more structured spectrum of the  $\tilde{X}^2A$  state of hydroxymethoxy radical.

The photoelectron spectrum of hydroxymethoxide obtained with 2.737 eV photons (453 nm) is shown in the top panel of Fig. 5.4. The peak labels shown in Fig. 5.4 are the same as the ones shown in Fig. 5.3. This spectrum shows more resolved structure compared to the initial low resolution photoelectron spectrum from Fig. 5.3. Indeed, peaks B-D show additional resolved structure compared to those peaks in Fig. 5.3. Peak A now has a *fwhm* = 0.018 eV (*fwhm*/eKE = 3.5%); a factor of two improvement in absolute peak width when compared to the same peak in Fig. 2. In order to fully resolve the origin transition (peak A) and accurately determine the EA of  $\text{H}_2\text{C}(\text{OH})\text{O}^*$ , an even lower eKE (therefore higher resolution) photoelectron spectrum using 2.33 eV photon energy is obtained.

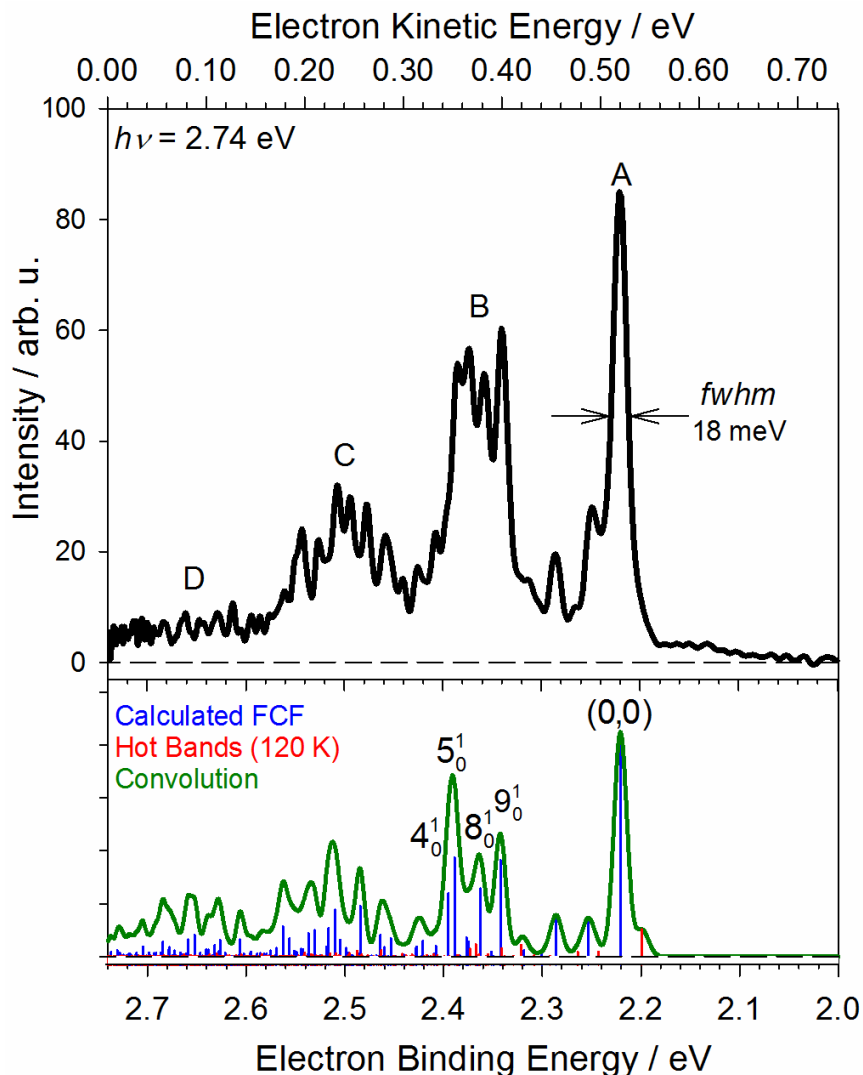


Figure 5.4. Upper panel: Experimental photoelectron spectrum of  $\text{H}_2\text{C}(\text{OH})\text{O}^-$  using 2.74 eV (453 nm) photon energy. The letters A through D are the same labels shown in Fig. 5.3. Lower panel: Calculated (CCSD(T)/aug-cc-pVTZ) Franck-Condon factors (sticks) and convoluted simulation (blue trace). The green sticks represent transitions from the vibrational ground state of the anion while the red sticks are vibrational hot bands, *i.e.* transitions from an excited vibrational state of the anion. The calculated stick spectrum was convoluted with Gaussian functions of varying *fwhm* in order to match the measured experimental resolution.

The high resolution photoelectron spectrum taken with 2.33 eV photons (532 nm) is shown in the top panel of Fig. 5.5 This spectrum shows peak A with  $fwhm = 0.008$  eV; another factor of two improvement in peak width when compared to the same peak in Fig. 3. Because the transitions that compose peak A are now clearly resolved, the peaks are relabeled with lowercase letters for individual assignments. Fig. 4 shows a clear origin of the vibrational progression centered at 2.2205 eV (peak a), which corresponds to the transition from the ground vibrational state of the  $\text{H}_2\text{C}(\text{OH})\text{O}^-$  anion to the ground vibrational state of the neutral  $\text{H}_2\text{C}(\text{OH})\text{O}^* \tilde{X}^2A$  radical. After a small shift to correct for an unresolved rotational envelope<sup>41</sup> (see Chapter 2), and inclusion of the uncertainties associated with the measurement, the EA of the hydroxymethoxy radical is assigned as 2.220(2) eV. This agrees very well with the calculated EA from this work (2.19 eV) and with that from a higher level (multireference) calculation (2.232 eV).<sup>13</sup> The uncertainty on the EA and the vibrational frequencies reported below come primarily from the energy scale calibration.

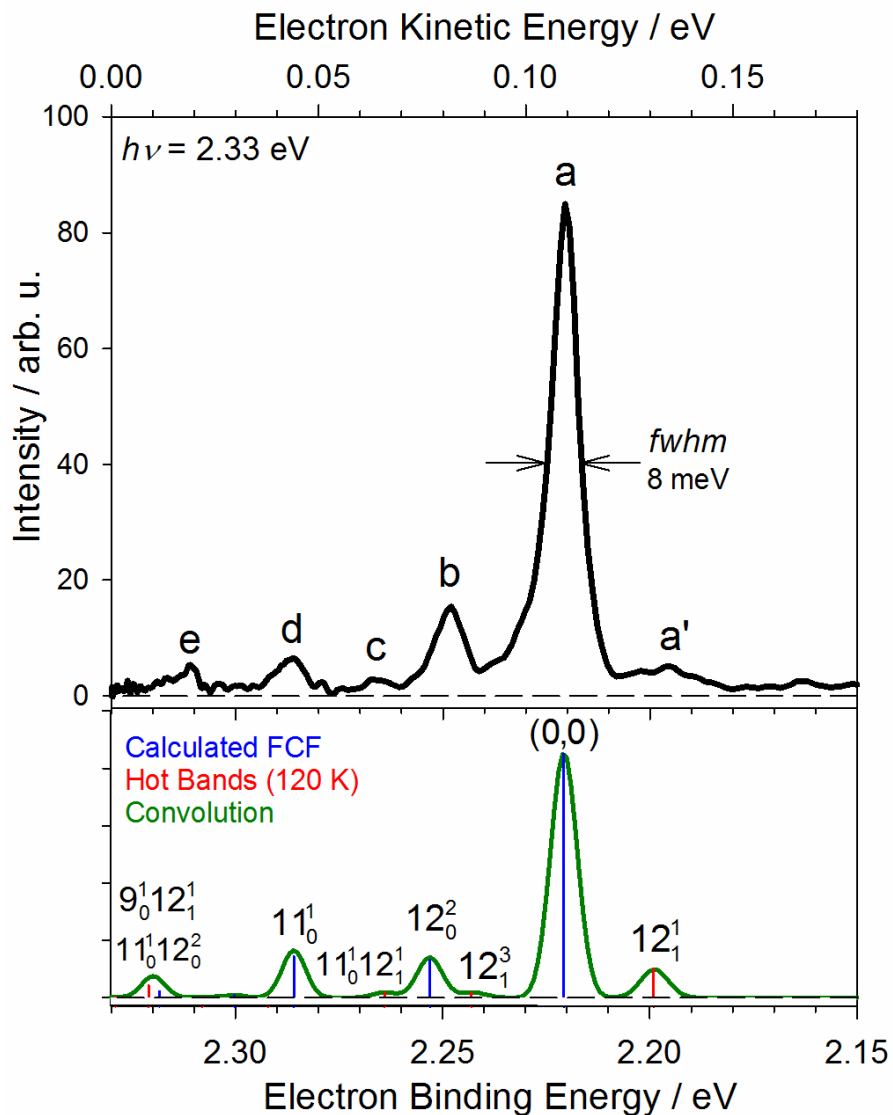


Figure 5.5: Upper panel: Photoelectron spectrum of  $\text{H}_2\text{C}(\text{OH})\text{O}^-$  using 2.33 eV (532 nm) photon energy. Peaks a–e are described in the text. Lower panel: Calculated (CCSD(T)/aug-cc-pVTZ) Franck-Condon factors (sticks) and convoluted simulation (blue trace) with assigned transitions. The green sticks correspond to transitions originating from the vibrational ground state of the anion, while the red sticks correspond to transitions with one quantum of excitation in a low frequency torsional ( $\nu_{12}$ ) mode of the anion.

### 5.3.b $\text{H}_2\text{C}(\text{OH})\text{O}^{\cdot-} \tilde{X}^2A$ Vibrational Assignments

The  $\text{H}_2\text{C}(\text{OH})\text{O}^{\cdot-} \tilde{X}^2A$  vibrational progression, depicted in Fig. 5.4, is characterized by an intense origin transition, followed by a progression of decreasing intensity and increasing congestion. Based on the changes in geometry between the anion and neutral equilibrium structures (see Table 5.6), which shows the largest changes occurring in the  $\angle_{\text{O}_1\text{CO}_2}$  and  $\angle_{\text{H}_3\text{O}_2\text{C}}$  angles and  $r_{\text{CO}_2}$  bond length, one might expect the most active vibrations to consist of OCO and HOC bends, symmetric and asymmetric OCO stretching vibrations, and combination bands involving these vibrations. The calculated photoelectron spectrum (lower panels of Figs. 5.3 – 5.5) indeed shows that the ground  $\tilde{X}^2A$  state progression (features A-D) is composed primarily of the vibrations  $\nu_{11}$  (OCO bend),  $\nu_9$  (OCO symmetric stretch),  $\nu_8$  (OCO asymmetric stretch),  $\nu_5$  (out of phase HOC bending/ $\text{CH}_2$  wagging), and  $\nu_4$  (HCH bend). See Tables 5.6 – 5.8 for the description of the molecular motion associated with all modes. In fact, the center of peaks A-D are separated (on average) by  $\sim 0.14$  eV ( $1130 \text{ cm}^{-1}$ ), which roughly corresponds to the OCO asymmetric stretching vibration ( $\nu_8$ ). The H-OCO torsion vibration ( $\nu_{12}$ ) is also active, and will be discussed in detail in section 5.4 below. Einfeld and Francisco<sup>11</sup> report extensive calculations on the hydroxymethoxy radical and include a simulated photoelectron spectrum of the anion accessing the ground  $\tilde{X}^2A$  state of the neutral, but not including the HOCO torsional mode. In spite of the fact that the reported geometries and frequencies of the anion and neutral ground  $\tilde{X}^2A$  state are very similar to the current work, the previous photoelectron spectrum simulation produces an extended vibrational progression, spanning close to 2 eV. The overall simulated photoelectron spectrum reported here is in excellent agreement with the experimentally observed spectrum and so it is used as an aid in order to assign the various vibrational transitions

responsible for the dominant peaks in the structured photoelectron spectrum shown in Figs. 5.4 and 5.5.

The spectral congestion apparent in peaks C and D in Figs. 5.3 and 5.4, and confirmed by the photoelectron spectrum simulation, makes individual transitions within these peaks impossible to assign. However, peak B appears to be much less congested, and based on the experimental spectrum, peak B in Fig. 5.4 appears to consist of four peaks. The calculated spectrum shows that five transitions are primarily responsible for the structure in peak B, namely transitions from the ground vibrational level of the anion to one quanta each of modes  $\nu_9$ ,  $\nu_8$ ,  $\nu_6$ ,  $\nu_5$  and  $\nu_4$  (labeled in Fig. 5.4). The transitions to the fundamentals in  $\nu_9$  and  $\nu_8$ , which correspond to the OCO symmetric and asymmetric stretches, respectively, are in a region where the spectral congestion is minimal and show very good agreement with experiment. Consequently, these transitions are unequivocally assigned, and the observed frequencies, calculated from the difference between the peak positions and the origin (EA) position, are presented in Table 5.4. The assignments of the  $\nu_6$ ,  $\nu_5$  and  $\nu_4$  fundamentals are not made due to the larger degree of spectral congestion.

Table 5.3: Calculated minimum energy structure of  $\text{H}_2\text{C}(\text{OH})\text{O}^- \tilde{X}^1A'$  (CCSD(T)/aug-cc-pVTZ),  $\text{H}_2\text{C}(\text{OH})\text{O} \cdot \tilde{X}^2A$  (ROCCSD(T)/aug-cc-pVTZ), and  $\text{H}_2\text{C}(\text{OH})\text{O} \cdot \tilde{A}^2A$  (CIS/aug-cc-pVTZ), as well as the difference between structural parameters of the anion and neutral structures ( $\Delta =$  anion structure – neutral structure). Fig. 5.1 shows the atom numbering used in this work. The values in boldface show the largest geometry changes. These calculated geometries agree well with the values in Refs. 11 and 28.

Parameter	$(\tilde{X}^1A')$	$(\tilde{X}^2A)$	$\Delta$	$(\tilde{A}^2A)$	$\Delta$
$r_{\text{CH}_1} / \text{\AA}$	1.121	1.111	0.01	1.084	0.037
$r_{\text{CH}_2} / \text{\AA}$	1.121	1.099	0.021	1.08	0.041
$r_{\text{CO}_1} / \text{\AA}$	1.317	1.349	-0.032	1.402	-0.085
$r_{\text{CO}_2} / \text{\AA}$	1.513	1.405	0.108	1.375	0.138
$r_{\text{OH}_3} / \text{\AA}$	0.967	0.964	0.003	0.941	0.026
$\angle_{\text{H}_1\text{CH}_2} / ^\circ$	107	107	0	110.5	-3.5
$\angle_{\text{O}_1\text{CO}_2} / ^\circ$	111.7	116.5	-4.8	107.5	4.2
$\angle_{\text{O}_2\text{CH}_3} / ^\circ$	96.8	107.7	-10.9	110.5	-13.7
$\varphi_{\text{H}_3\text{O}_2\text{CO}_1} / ^\circ$	0	47.6	-47.6	70.9	-70.9

The higher resolution spectrum presented in Fig. 5.5 has six labeled peaks, all of which are captured in the photoelectron simulation. From this spectrum, in addition to obtaining an accurate EA( $\text{H}_2\text{C}(\text{OH})\text{O}^\bullet$ ), transitions to the lowest frequency active modes are resolved, namely the OCO bending vibration ( $\nu_{11}$ ), the H-OCO torsion vibration ( $\nu_{12}$ ), and a few combination bands. Peak d can now be assigned as the transition from the ground vibrational level of the anion to the state on the neutral potential with one quantum of excitation in the OCO bend. Peaks b and a' are assigned to transitions involving the H-OCO torsion, namely  $\nu_{12}(\nu''=0 \rightarrow \nu'=2)$  and  $\nu_{12}(\nu''=1 \rightarrow \nu'=1)$ , which is further discussed in section 5.4.a. Throughout this chapter, primes (double primes) are used to denote vibrational levels in the neutral (anion) electronic state. The peak positions (absolute eBE and relative to the EA) for the peaks labeled in Figs. 5.4 and 5.5 are given in Table 5.4, together with the aforementioned assignments.

Table 5.4: Vibrational transition assignments for the peaks labeled a'–e (Fig. 5.5) and B (Fig. 5.4) in the photoelectron spectra reported in the main text. Both the absolute peak position (eBE, reported in eV) and the energy relative to the EA (reported in  $\text{cm}^{-1}$ ) are given. The  $\text{H}_2\text{C}(\text{OH})\text{O}^\bullet$  ( $\tilde{X}^2A$ ) ( $\nu_1'\nu_2' \dots$ )  $\leftarrow$   $\text{H}_2\text{C}(\text{OH})\text{O}^-$  ( $\tilde{X}^1A'$ ) ( $\nu_1''\nu_2'' \dots$ ) transitions are labeled using the standard shorthand notation ( $1_{\nu_1}^{\nu_1'} 2_{\nu_2}^{\nu_2'} \dots$ ) for vibrational transitions. The assignments are based on the results of the calculated photoelectron spectrum. The question marks indicate the peaks in this region where the assignment is ambiguous (see Figs. 5.4 and 5.5) due to spectral congestion.

Peak Label (Fig. 5.5)	Absolute Peak Center Position (eV)	Peak Position Relative to EA ( $\text{cm}^{-1}$ )	Assignment
a'	2.198	-181	$12_1^1$
a	2.220	0	$0_0^0$
b	2.248	224	$12_0^2$
c	2.266	364	? $11_0^1 12_1^1$
d	2.287	534	$11_0^1$
e	2.312	741	$9_0^1 12_1^1$ and/or $11_0^1 12_0^2$
B (Fig. 5.4)	2.339	963	$9_0^1$
	2.358	1110	$8_0^1$
	2.372	1225	? $6_0^1$
	2.384	1320	? $5_0^1$

### 5.3.c $\text{H}_2\text{C}(\text{OH})\text{O}^* \tilde{A}^2A$

Photoelectron detachment to form  $\text{H}_2\text{C}(\text{OH})\text{O}^* \tilde{A}^2A$  results in a relatively unstructured photoelectron spectrum (Fig. 5.3), peaked at  $\sim 3$  eV with a *fwhm* of  $\sim 0.5$  eV. As mentioned previously, since there is an approximately constant resolution (*fwhm*/eKE) of 3%, the narrowest peaks should be at low kinetic energy (large binding energy), meaning that detachment to the  $\tilde{A}^2A$  excited state should be the best resolved in this spectrum. This is not what is observed, which implies that photodetachment to the  $\tilde{A}^2A$  excited state could result in a large degree of spectral congestion.

In order to test this hypothesis, a photoelectron spectrum simulation based on excitation to the  $\tilde{A}^2A$  state of  $\text{H}_2\text{C}(\text{OH})\text{O}^*$  was calculated using the methods described above. Based on the measured EA( $\text{H}_2\text{C}(\text{OH})\text{O}^*$ ) and the calculated  $T_0$  of  $\text{H}_2\text{C}(\text{OH})\text{O}^* \tilde{A}^2A$  (0.377 eV<sup>28</sup> or 0.390 eV<sup>11</sup> with respect to  $\text{H}_2\text{C}(\text{OH})\text{O}^* \tilde{X}^2A$ ), the origin of the excited  $\tilde{A}^2A$  state was initially assumed to be approximately 2.6 eV. The resulting photoelectron spectrum simulation is shown in Fig. 2 (bottom panel). The spectrum shows a large degree of spectral congestion, primarily involving transitions to overtones and combination bands of the H-OCO torsion ( $\nu_{12}$ ), OCO asymmetric stretching ( $\nu_9$ ), and out-of-phase HOC bending/ $\text{CH}_2$  wagging ( $\nu_5$ ) vibrations. The simulated spectrum peaks  $\sim 0.3$  eV above the origin, and extends for at least another 1 eV. Since the experimental photon energy used is only 3.49 eV, the simulated spectrum shown in the lower panel of Fig. 2 is truncated at 3.49 eV. In addition, a threshold scaling factor<sup>42,43</sup> is introduced to help mimic the low eKE edge of the observed spectrum. Given that the experimentally observed positive anisotropy indicates this excited  $\tilde{A}^2A$  electronic state is a result of electron detachment from an orbital with relatively more s-like character than when the electron is detached to form the ground  $\tilde{X}^2A$  state of  $\text{H}_2\text{C}(\text{OH})\text{O}^*$ , the outgoing electron is approximated by a p-wave. Thus,

the photodetachment cross section scales as  $eKE^{l+0.5}$ , or  $eKE^{1.5}$ . This means that there is a much stronger threshold effect for the onset of the excited  $\tilde{A}^2A$  state compared to the ground  $\tilde{X}^2A$  state. This scaling factor for the detachment cross section is also consistent with why there are no observed peaks that can be unequivocally assigned to the origin of the excited  $\tilde{A}^2A$  state spectrum in the low  $eKE$  region of the 453 nm spectrum.

The overall photoelectron simulation matches the experimental spectrum very well, despite the harmonic treatment and assumption of separable vibrational modes, both of which likely results in undercounting the density of states on the  $\tilde{A}^2A$  potential surface. There is a repeating pattern of peaks in the simulation, spaced by  $\sim 1200\text{ cm}^{-1}$  (0.15 eV, or approximately one quanta of the neutral  $\nu_9$  vibration), which is a result of overtones in the OCO asymmetric stretching ( $\nu_9$ ) and HOC bending/ $\text{CH}_2$  wagging ( $\nu_5$ ) vibrations. Because the origin of the  $\text{H}_2\text{C}(\text{OH})\text{O}^{\bullet} \tilde{A}^2A$  state is obscured by transitions from the anion to high lying vibrations in the  $\text{H}_2\text{C}(\text{OH})\text{O}^{\bullet} \tilde{X}^2A$  state, there is some uncertainty in the spectrum's origin, shown in Fig. 2 as 2.615 eV to best match the experimental spectrum while still remaining close to the calculated origin. The calculated spectrum could just as easily shift by  $\pm 0.15$  eV, which is the spacing of the repeating pattern of peaks in the simulation, and still match the overall experimental spectrum. However, a shift this large seems unlikely, given the high level multireference calculations of the  $\text{H}_2\text{C}(\text{OH})\text{O}^{\bullet} \tilde{A} - \tilde{X}$  term energy.<sup>11,28</sup>

## 5.4 Discussion

### 5.4.a H-OCO Torsion

#### *i. Separability of the torsional coordinate*

The calculated FCFs of the H-OCO torsional mode were treated separately from the other normal modes. This separate 1D treatment is an approximation that is justified by comparing the structural parameters and vibrational frequencies of the minimum energy structure ( $C_1$  symmetry) and the transition state ( $C_s$  symmetry,  $\phi_{\text{HOCO}} = 0^\circ$ ). The corresponding calculated results are shown below in Tables 5.5 and 5.6, which show that there is a  $2\pm 2\%$  change in the structural parameters and vibrational frequencies between the equilibrium and transition state ( $\phi_{\text{HOCO}} = 0^\circ$ ) of  $\text{H}_2\text{C}(\text{OH})\text{O}^* \tilde{X}^2A$ . This implies that the torsional coordinate is indeed a coordinate which is separable from the remaining normal modes and hence it is well treated by the model discussed in the main text. Similar small changes are calculated between the  $\text{H}_2\text{C}(\text{OH})\text{O}^* \tilde{A}^2A$  equilibrium and transition state structures. The  $\text{H}_2\text{C}(\text{OH})\text{O}^* \tilde{A}^2A$  and  $\text{H}_2\text{C}(\text{OH})\text{O}^- \tilde{X}^1A$  vibrational frequencies are listed in Tables 5.7 and 5.8, respectively. Tables 5.5 through 5.7 are conveniently listed at the end of this chapter.

#### *ii. HOCO torsion discussion*

The relaxed H-OCO torsional potential energy surfaces for the anion and neutral ground  $\tilde{X}^2A$  and excited  $\tilde{A}^2A$  states can be found in Fig. 5.1 and 5.2 (also see Tables 5.1 and 5.2). As mentioned in section 5.2.b, the  $\tilde{X}^2A$  state of the anion has its minimum energy geometry at  $\phi_{\text{HOCO}} = 0^\circ$ . Although there is a higher energy minimum in the *trans* H-OCO configuration ( $\phi_{\text{HOCO}} = 180^\circ$ ,  $\sim 1200 \text{ cm}^{-1}$  relative to the global minimum), the barrier to conversion from the *trans* to *cis* configurations is too low (on the order of  $20 \text{ cm}^{-1}$ ) to support any bound vibrational

levels. For both the ground  $\tilde{X}^2A$  and excited  $\tilde{A}^2A$  states of  $\text{H}_2\text{C}(\text{OH})\text{O}^\bullet$ , the H-OCO torsional potential exhibits a double well, with the equilibrium structures corresponding to  $\varphi_{\text{HOCO}} = \pm 48^\circ$  and  $\pm 70.9^\circ$  for the  $\tilde{X}^2A$  and  $\tilde{A}^2A$  states, respectively. The multireference treatments of the  $\tilde{X}^2A$  state surface by both the Yarkony and Francisco groups results in an increase in the  $\varphi_{\text{HOCO}}$  angle for the equilibrium  $\text{H}_2\text{C}(\text{OH})\text{O}^\bullet \tilde{X}^2A$  structure ( $\pm 59.6^\circ$  and  $\pm 57^\circ$ , respectively). Depending on the level of theory used with single reference methods, this dihedral angle for the equilibrium structure can range from  $\varphi_{\text{HOCO}} = \pm 23^\circ$  (B3LYP/aug-cc-pVTZ) to  $\varphi_{\text{HOCO}} = \pm 56^\circ$  (MP2/aug-cc-pVTZ). Like the anion, the *trans* configuration ( $\varphi_{\text{HOCO}} \sim 180^\circ$ ) of the  $\tilde{X}^2A$  state of the neutral is much higher in energy than the *cis* configuration, and is separated from the global minimum by a very small barrier. In the neutral  $\tilde{A}^2A$  excited state, the *trans* configuration is higher in energy and unstable with respect to isomerization. In all cases, the relative stabilities of the *cis* and *trans* isomers arises from the stabilization of the *cis* isomer due to intramolecular interactions between the terminal oxygen (O1) and hydrogen (H3) atoms, as illustrated in the inset of Fig. 5.1. This interaction will be strongest in the anion, where the excess electron is localized on O1 leading to a stronger  $\text{O}^- \dots \text{HO}$  ionic hydrogen bond.

The two equivalent minimum energy structures have  $C_1$  symmetry with  $\varphi_{\text{HOCO}} = \pm 48^\circ$  or  $\pm 70.9^\circ$ , which are separated by a barrier in both the ground  $\tilde{X}^2A$  and excited  $\tilde{A}^2A$  state neutral electronic potential energy surfaces. A relaxed potential energy scan has a barrier to interconversion of  $158 \text{ cm}^{-1}$  for the ground  $\tilde{X}^2A$  state surface. For the relaxed scan, the energy of  $\text{H}_2\text{C}(\text{OH})\text{O}^\bullet$  was calculated at each  $\varphi_{\text{HOCO}}$  dihedral angle (stepped between  $0^\circ$  and  $180^\circ$ ) while allowing the remaining coordinates to be optimized. In order to provide a comparison between the neutral vertical and relaxed potentials energy curves (ROCCSD(T)/aug-cc-pVTZ), these potentials are shown in Fig. 5.6. As Fig. 5.6 shows, the main difference between these surfaces

are the location of the minima and the barrier heights, along with an energy offset relative to the anion minimum. The vertical surface is located *ca.* 2200 cm<sup>-1</sup> (0.27 eV) above the relaxed potential. This is lower than the multireference calculations from Dillon and Yarkony,<sup>28</sup> who report a barrier to interconversion of 361 cm<sup>-1</sup> for the ground  $\tilde{X}^2A$  state, and with Eisfeld and Francisco, who report a barrier of at most 550 cm<sup>-1</sup> for the  $\tilde{X}^2A$  state rotamer interconversion. The barrier to interconversion for the excited  $\tilde{A}^2A$  state is higher, at 968 cm<sup>-1</sup>, which agrees very well with the multireference calculations from Dillon and Yarkony (993 cm<sup>-1</sup>).<sup>28</sup> As mentioned previously, the vertical detachment region of the potential energy surface is what is accessed in the photoelectron detachment experiment performed here. In this region, the barrier lowers to only 50 cm<sup>-1</sup> for the ground  $\tilde{X}^2A$  state and 255 cm<sup>-1</sup> for the excited  $\tilde{A}^2A$  state. Based on the one-dimensional calculations of energies and wavefunctions for the H-OCO torsion performed using the potential cut shown in Fig. 5.1, we find that in the ground electronic state, the zero-point level lies 11 cm<sup>-1</sup> above the barrier to rotamer conversion, and the wavefunction has its largest amplitude at  $\angle_{\text{HOCO}} = 0^\circ$ . In the excited  $\tilde{A}^2A$  electronic state, there is still a barrier with respect to zero-point motion, and the ground vibrational state lies 99 cm<sup>-1</sup> below the barrier to free internal rotation. These conclusions agree well with those drawn by Dillon and Yarkony<sup>28</sup> based on their potential energy surfaces (which had all coordinates, besides  $\angle_{\text{HOCO}}$ , constrained to the equilibrium geometry of the anion)<sup>28</sup> and with Eisfeld and Francisco,<sup>11</sup> who excluded this coordinate from their work for this reason.

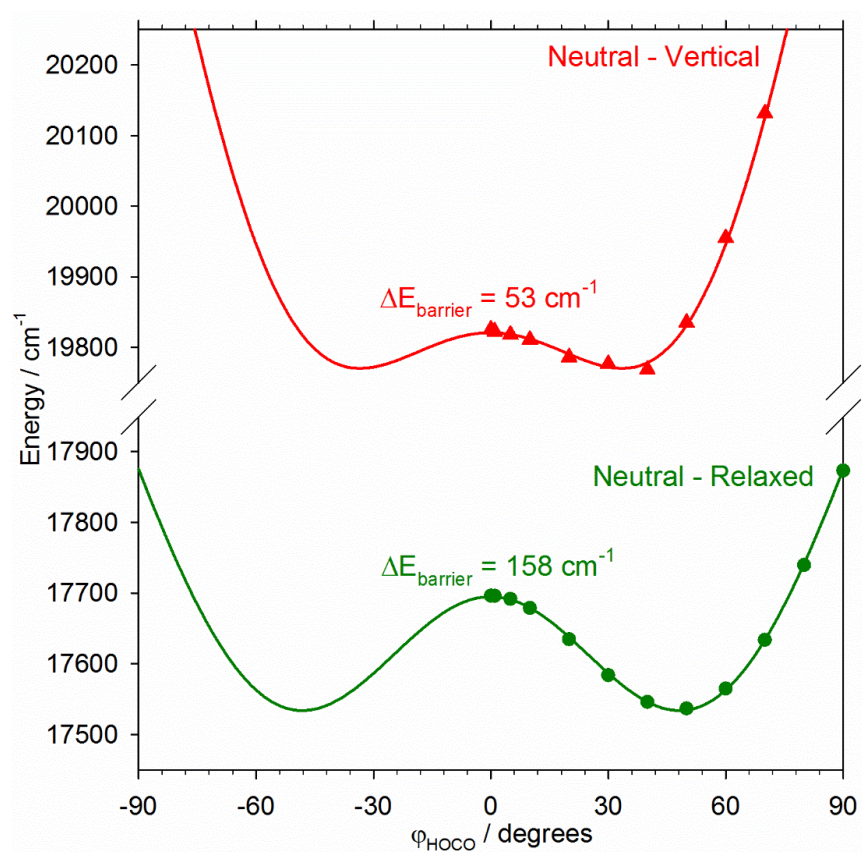


Figure 5.6:  $\text{H}_2\text{C}(\text{OH})\text{O}^{\bullet} \tilde{X}^2A$  H-OCO calculated (ROCCSD(T)/aug-cc-pVTZ) torsional potential comparison. The green circles and trace represent the relaxed potential energy surface, where all coordinates were optimized for each value of  $\phi_{\text{HOCO}}$ . The red triangles represent the vertical detachment surface, where the neutral surface was calculated at the optimized anion geometries for each value of  $\phi_{\text{HOCO}}$ .  $\Delta E_{\text{barrier}}$  represents the 1D barrier height with respect to the potential minima.

The consequences of the anion and the vibrationally averaged structure of neutral  $\text{H}_2\text{C}(\text{OH})\text{O}^*$  both having  $C_s$  symmetry leads to vibrational symmetry selection rules in the electronic spectra, resulting in vibrational modes  $\nu_{10}$  (in plane HCH rock),  $\nu_7$  (out of plane HCH rock), and  $\nu_2$  (HCH asymmetric stretch) not being active in the photoelectron spectrum (see Table 5.6). Moreover, the selection rules of the torsional transitions are determined by the parity enforced by the symmetry of the potential, as emphasized by the double-headed arrows shown in Fig. 5.1. Because of the parity selection rules in the torsional coordinate, peak b is assigned as  $\nu_{12}(\nu''=0 \rightarrow \nu'=2)$ , or  $12_0^2$ . Based on the difference in peak positions between peak b and the EA, the neutral  $2\nu_{12}$  has a frequency of  $220(10) \text{ cm}^{-1}$ . Peak a' is assigned as the anion-neutral sequence band  $\nu_{12}(\nu''=1 \rightarrow \nu'=1)$ , located  $180(60) \text{ cm}^{-1}$  from the origin transition (peak a). Because the  $\nu_{12}$  fundamental frequency for either the anion or neutral cannot be measured directly, and the neutral H-OCO potential is highly anharmonic, the anion and neutral  $\nu_{12}$  fundamental frequencies cannot be directly obtained from the measured  $2\nu_{12}$  overtone or the position of the  $\nu_{12}(\nu''=1 \rightarrow \nu'=1)$  sequence band.

We can, however, use a combination of the calculated anion fundamental frequency  $\nu_{12}(\nu''=0 \rightarrow \nu''=1) = 269 \text{ cm}^{-1}$  from the anion torsional potential energy surface (which is well-described as a harmonic oscillator near its equilibrium structure) in combination with the experiment to derive the  $\nu_{12}$  fundamental frequencies. Using the calculated  $\nu_{12}(\nu''=0 \rightarrow \nu''=1)$  and the position of the  $\nu_{12}(\nu''=1 \rightarrow \nu'=1)$  sequence band in relation to the EA, the neutral  $\nu_{12}$  fundamental frequency  $\nu_{12}(\nu' = 0 \rightarrow \nu' = 1) = 90(60) \text{ cm}^{-1}$ . By comparison, the calculated neutral  $\nu_{12}$  fundamental frequency ( $92.3 \text{ cm}^{-1}$ ) is very close to this value, which is calculated using the one-dimensional potential shown in Fig. 5.1 (based on the relaxed geometries of the anion). When a relaxed scan of the neutral  $\tilde{X}^2A$  torsional potential energy surface is used instead, this

frequency drops to 36.7 cm<sup>-1</sup> due to the larger barrier along this cut of the potential. This comparison further validates the approximations made in the treatment of the torsional mode. In addition, using this in combination with the measured neutral  $2\nu_{12}$ ,  $\nu_{12}(v' = 1 \rightarrow v' = 2) = 130(60)$  cm<sup>-1</sup> for H<sub>2</sub>C(OH)O<sup>•</sup>. The error bars on these frequencies are defined by the experimental error bars on the peak positions. This can be compared to the calculated values of 170 cm<sup>-1</sup> for the neutral  $\tilde{X}^2A$  potential energy curve calculated at the anion relaxed scan geometries (as shown in Fig. 5.1) and 155 cm<sup>-1</sup> for the neutral  $\tilde{X}^2A$  relaxed surface. Unfortunately, this type of analysis and comparison of experiment with theory for the H<sub>2</sub>C(OH)O<sup>•</sup>  $\tilde{A}^2A$  torsional frequency is not possible. The torsional frequency for H<sub>2</sub>C(OH)O<sup>•</sup>  $\tilde{A}^2A$  could not be measured due to the highly spectrally congested spectrum (including spectral overlap with detachment to the ground  $\tilde{X}^2A$  state) and the relatively low-resolution of the spectrum shown in Fig. 5.3.

#### 5.4.b Methanediol Thermochemistry

The measurement of the EAs of molecules can provide information about the gas phase chemistry of their protonated counterpart with the use of a thermochemical cycle. The thermochemical cycle for methanediol is described by Eq. 3:

$$D_0(\text{H}_2\text{C}(\text{OH})\text{O}-\text{H}) = \Delta_{\text{acid}}\text{H}_{0\text{K}}^\circ(\text{H}_2\text{C}(\text{OH})_2) - \text{IE}(\text{H}) + \text{EA}(\text{H}_2\text{C}(\text{OH})\text{O}) \quad (5.3)$$

Here, the EA of H<sub>2</sub>C(OH)O<sup>•</sup> is experimentally determined as 2.220(2) eV or 51.19(5) kcal mol<sup>-1</sup>.

The ionization energy of atomic hydrogen (IE(H)=313.59 kcal mol<sup>-1</sup>) is known.<sup>44</sup> With this equation, either the O–H bond dissociation energy,  $D_0(\text{H}_2\text{C}(\text{OH})\text{O}-\text{H})$ , or the gas phase deprotonation enthalpy,  $\Delta_{\text{acid}}\text{H}_{0\text{K}}^\circ(\text{H}_2\text{C}(\text{OH})_2)$ , of methanediol can be obtained. Since there is no experimental measurement of either of these quantities, quantum chemical calculations must be relied upon to obtain one of these values. In this instance, the  $\Delta_{\text{acid}}\text{H}_{0\text{K}}^\circ(\text{H}_2\text{C}(\text{OH})_2)$  was chosen

since this quantity only depends on calculating formation enthalpies of closed shell species, namely  $\text{H}_2\text{C}(\text{OH})\text{O}^-$ ,  $\text{H}_2\text{C}(\text{OH})_2$ , and  $\text{H}^+$ . Here, the G4 composite method was used yielding  $\Delta_{\text{acid}}\text{H}^{\circ}_{0\text{K}}(\text{H}_2\text{C}(\text{OH})_2) = 366 \text{ kcal mol}^{-1}$ . Other composite methods were also used and verified this result, specifically CBS-APNO ( $366.4 \text{ kcal mol}^{-1}$ ) and CBS-QB3 ( $365.7 \text{ kcal mol}^{-1}$ ). Since the predicted uncertainty in these calculations is on the order of  $0.8$  to  $1.5 \text{ kcal mol}^{-1}$ , this results in  $D_0(\text{H}_2\text{C}(\text{OH})\text{O}-\text{H}) = 104(2) \text{ kcal mol}^{-1}$ , using a conservative estimate of the uncertainty. A previously calculated O–H bond dissociation energy<sup>45</sup> of  $102.7 \text{ kcal mol}^{-1}$  is in excellent agreement with our semi-empirical value.

#### *5.4.c Photodetachment Producing $\text{H}_2\text{C}(\text{OH})\text{O}^{\bullet} \tilde{X}^2A$ and $\tilde{A}^2A$ Electronic States*

While it is tempting to compare the photoelectron spectrum of  $\text{H}_2\text{C}(\text{OH})\text{O}^-$  with those of other alkoxy anions, such as methoxide ( $\text{CH}_3\text{O}^-$ ) and ethoxide ( $\text{H}_2\text{C}(\text{CH}_3)\text{O}^-$ ), this would not be a fair comparison, especially with respect to the Jahn-Teller coupling that was essential for a proper interpretation of the methoxide and ethoxide photoelectron spectra. There, the substitution of a methyl group from methoxy to ethoxy was seen as a perturbation of the Jahn-Teller distortion, and an accordingly strong coupling and small energy difference between the neutral radical ground and first excited electronic states. However, the substitution of a hydroxyl group drastically changes the electronic structure and any neutral ground/excited electronic state coupling, as described by Dillon and Yarkony.<sup>28</sup> Experimentally, there is at least an order of magnitude larger energy difference between the ground and first excited electronic states in hydroxymethoxy compared to ethoxy. While there is still significant coupling between the ground and first excited electronic states in hydroxymethoxy, exemplified by a low-lying seam of conical intersection, there are substantial differences in the topology of the electronic state surfaces of hydroxymethoxy compared to the classic Jahn-Teller topology found in the electronic

structure of methoxy radical (or even in the pseudo Jahn-Teller ethoxy radical). See Reference 28 for a thorough discussion on the topic.

The photoelectron simulation of detachment forming  $\text{H}_2\text{C}(\text{OH})\text{O}^* \tilde{A}^2A$  captures the experimental data very well (Fig. 5.3). The differences between the experiment and simulation likely differ mostly due to the separable harmonic treatment employed here. However, it would be interesting if there is any additional broadening or spectral congestion in the high eBE portion of the photoelectron spectrum that could be due to any nonadiabatic coupling between the two electronic states of the neutral. Interestingly, Dillon and Yarkony found that there is a significant dependence on the  $\phi_{\text{HOCO}}$  torsion coordinate for the energy of the seam of conical intersection between the two states, ranging from  $\sim 0.38$  eV to  $\sim 0.53$  eV above the ground electronic state minimum. This is energetically accessible in the experiments performed here. However, whether or not photodetachment accesses these regions of strong coupling on the neutral potential energy surfaces is unknown. While the calculation used here certainly matches the experimental spectrum qualitatively, a more detailed calculation including the possible effects of nonadiabatic coupling would be interesting.

## 5.5 Conclusions

Photodetachment of the hydroxymethoxide anion,  $\text{H}_2\text{C}(\text{OH})\text{O}^-$ , with 355 nm photons forms the ground ( $\tilde{X}^2A$ ) and first excited ( $\tilde{A}^2A$ ) states of  $\text{H}_2\text{C}(\text{OH})\text{O}^*$ . The photoelectron spectrum provides the electron affinity of  $\text{H}_2\text{C}(\text{OH})\text{O}^*$  (EA = 2.220(2) eV), together with the measurement of several vibrational frequencies of the hydroxymethoxy radical in its  $\tilde{X}^2A$  electronic state. These major experimental results are presented in Table X below. The  $\tilde{A}^2A$  excited state spectrum is characterized by a long vibrational progression which results in a

mostly unstructured photoelectron spectrum with an  $\tilde{X} \rightarrow \tilde{A}$  excitation term energy of  $\sim 0.4$  eV. Franck-Condon activity in specific vibrational modes is indicative of a change in the equilibrium structures between the anion and neutral states. The H-OCO torsion is one of the main active vibrations in the spectra, along with overtones and combination bands of the OCO stretching and HOC bending/CH<sub>2</sub> wagging vibrations. Motion along the neutral H-OCO torsional double-well potentials is not well described by the harmonic oscillator approximation and hence requires explicit treatment to calculate the associated Franck-Condon factors, unlike the other vibrational modes. The resulting calculated photoelectron spectra for detachment to both ground  $\tilde{X}^2A$  and excited  $\tilde{A}^2A$  states show good agreement with the experimental data, supporting the interpretation of the spectra. Because of the agreement between calculation and experiment, the inclusion of nonadiabatic vibronic coupling between the electronic states of hydroxymethoxy does not appear to be necessary to reproduce accurately the experimental photoelectron spectrum. This observation further separates hydroxymethoxy from other small substituted alkoxy radicals, such as ethoxy (H<sub>2</sub>C(CH<sub>3</sub>)O<sup>•</sup>), in which the inclusion of vibronic coupling was crucial to simulating the experimental photoelectron spectrum.

Table 5.9: Summary of the major results. The calculated results are based on the CCSD(T)/aug-cc-pVTZ (EA and vibrational frequencies) and the G4 composite method (gas phase acidity).

	Experiment	Calculation <sup>b</sup>
Electron Affinity / eV	2.220(2)	2.19
$\Delta_{\text{acid}}H_{0\text{K}}^{\circ}(\text{H}_2\text{C}(\text{OH})_2)$ / kcal mol <sup>-1</sup>	-	366(2)
$\Delta_{\text{acid}}H_{298\text{K}}^{\circ}(\text{H}_2\text{C}(\text{OH})_2)$ / kcal mol <sup>-1</sup>	-	367(2)
$D_0(\text{H}_2\text{C}(\text{OH})\text{O}-\text{H})$ / kcal mol <sup>-1</sup>	104(2) <sup>a</sup>	
$\text{H}_2\text{C}(\text{OH})\text{O}^{\cdot} \tilde{X}^2A'$ Vibrational Frequencies / cm <sup>-1</sup>		
$2\nu_{12}$	220(10)	261
$\nu_{11}$	530(10)	526
$\nu_9$	960(50)	982
$\nu_8$	1110(50)	1146
<sup>a</sup> Determined based on experimental and calculated quantities through the thermochemical cycle shown in Eq. 5.3		
<sup>b</sup> Calculated values are based on harmonic vibrational frequencies, except for $\nu_{12}$ , as discussed in the text		

## 5.6 Geometry optimization and frequencies of hydroxymethoxide and hydroxymethoxy

Table 5.5: Calculated (ROCCSD(T)/aug-cc-pVTZ) optimized geometries of  $\text{H}_2\text{C}(\text{OH})\text{O}^{\cdot-} \tilde{X}^2A$  at its equilibrium ( $\varphi_{\text{HOCO}} = \pm 48^\circ$ ) and transition state ( $\varphi_{\text{HOCO}} = 0^\circ$ ) structures. Bond distances ( $r$ ) are given in Angstroms while bond angles ( $\angle$ ) and dihedral angles ( $\varphi$ ) are given in degrees. The atom numbering is based on Fig. 5.1.

Parameter	Equilibrium	Transition State	$\Delta$ (TS-Eq) (%)
$r_{\text{CO1}}$	1.35	1.34	0.65
$r_{\text{CO2}}$	1.41	1.41	0.32
$r_{\text{CH1}}$	1.11	1.11	0.28
$r_{\text{CH2}}$	1.10	1.11	0.71
$r_{\text{OH3}}$	0.96	0.96	0.04
$\angle_{\text{O1CO2}}$	116.5	116.3	0.18
$\angle_{\text{H1CO1}}$	104.6	107.7	2.95
$\angle_{\text{H2CO1}}$	110.2	107.7	2.28
$\angle_{\text{H3O2C}}$	107.7	106.4	1.25
$\varphi_{\text{H1CO1O2}}$	123.8	122.9	0.71
$\varphi_{\text{H2CO1O2}}$	-121.6	-122.9	1.12
$\varphi_{\text{H3O2CO1}}$ ( $\equiv \varphi_{\text{HOCO}}$ )	47.6	0.0	-

Table 5.6: Calculated (ROCCSD(T)/aug-cc-pVTZ) harmonic vibrational frequencies of  $\text{H}_2\text{C}(\text{OH})\text{O}^* \tilde{X}^2A$ , for both the equilibrium structure ( $\phi_{\text{HOCO}} = \pm 48^\circ$ ) and transition state ( $\phi_{\text{HOCO}} = 0^\circ$ ), together with the approximate mode description. All values are reported in  $\text{cm}^{-1}$ .

$\omega_i$	Mode description	$\tilde{X}^2A$ Equilibrium Structure	$\tilde{X}^2A$ Transition State	$\Delta$ (TS-Eq) (%)
12	O-H torsion	239	198 <i>i</i>	-
11	OCO bend	547	526	3.8
10	In plane HCH rock	767	747	2.6
9	OCO Sym. Stretch	1002	982	2.0
8	OCO Asym. Stretch	1113	1146	2.9
7	Out of plane HCH rock	1137	1185	4.3
6	In phase HOC bending/ $\text{CH}_2$ wagging	1310	1258	4.0
5	Out of phase HOC bending/ $\text{CH}_2$ wagging	1370	1353	1.2
4	HCH bend	1413	1406	0.5
3	HCH Sym. Stretch	2868	2893	0.9
2	HCH Asym. Stretch	2996	2909	2.9
1	OH Stretch	3815	3817	0.0

Table 5.7: Calculated (CIS/aug-cc-pVTZ) harmonic vibrational frequencies of  $\text{H}_2\text{C}(\text{OH})\text{O} \cdot \tilde{A}^2A$  for both the equilibrium structure ( $\phi_{\text{HOCO}} = \pm 70.9^\circ$ ) and transition state ( $\phi_{\text{HOCO}} = 0^\circ$ ), together with the approximate mode description. All values are reported in  $\text{cm}^{-1}$ .

$\omega_i$	Mode description	$\tilde{A}^2A$ Equilibrium Structure	$\tilde{A}^2A$ Transition State	$\Delta$ (TS-Eq) (%)
12	O–H torsion	375	419 <i>i</i>	-
11	OCO bend	523	504	3.6
10	OCO Sym. Stretch	1137	1116	1.8
9	OCO Asym. Stretch	1167	1202	2.9
8	In plane HCH rock	1216	1283	5.2
7	In phase HOC bending/ $\text{CH}_2$ wagging	1440	1373	4.8
6	Out of plane HCH rock	1514	1422	6.5
5	Out of phase HOC bending/ $\text{CH}_2$ wagging	1557	1583	1.6
4	HCH bend	1688	1709	1.3
3	HCH Sym. Stretch	3178	3185	0.2
2	HCH Asym. Stretch	3250	3230	0.6
1	OH Stretch	4147	4150	0.1

Table 5.8: Calculated (CCSD(T)/aug-cc-pVTZ) harmonic vibrational frequencies of  $\text{H}_2\text{C}(\text{OH})\text{O}^- \tilde{X}^1A$ . Note the difference in mode descriptions between the anion and neutral structures. The convention used in this paper is to refer to modes based on the *neutral*  $\text{H}_2\text{C}(\text{OH})\text{O} \tilde{X}^2A$  mode numbering/descriptor. All values are reported in  $\text{cm}^{-1}$ .

$\omega_i$	Mode description	$\text{H}_2\text{C}(\text{OH})\text{O}^- \tilde{X}^1A$
12	O–H torsion	273
11	OCO bend	468
10	OCO Sym. Stretch	771
9	OCO Asym. Stretch	1121
8	In plane HCH rock	1131
7	Out of plane HCH rock	1208
6	In phase HOC bending/ $\text{CH}_2$ wagging	1310
5	HCH bend	1389
4	Out of phase HOC bending/ $\text{CH}_2$ wagging	1535
3	HCH Asym. Stretch	2269
2	HCH Sym. Stretch	2722
1	OH Stretch	3757

## 5.7 Chapter 5 references

- <sup>1</sup> J.J. Orlando, G.S. Tyndall, and T.J. Wallington, *Chem. Rev.* **103**, 4657 (2003).
- <sup>2</sup> P. Devolder, *J. Photochem. Photobiol. a-Chemistry* **157**, 137 (2003).
- <sup>3</sup> R. Atkinson, *Atmos. Environ.* **41**, 8468 (2007).
- <sup>4</sup> C.C. Carter, J.R. Atwell, S. Gopalakrishnan, and T.A. Miller, *J. Phys. Chem. A* **104**, 9165 (2000).
- <sup>5</sup> H.J. Curran, *Int. J. Chem. Kinet.* **38**, 250 (2006).
- <sup>6</sup> H.J. Curran, P. Gaffuri, W.J. Pitz, and C.K. Westbrook, *Combust. Flame* **114**, 149 (1998).
- <sup>7</sup> A.C. Davis and J.S. Francisco, *J. Phys. Chem. A* **118**, 10982 (2014).
- <sup>8</sup> M.L. Weichman, J.B. Kim, and D.M. Neumark, *J. Phys. Chem. A* **119**, 6140 (2015).
- <sup>9</sup> P. Neeb, F. Sauer, O. Horie, and G.K. Moortgat, *Atmos. Environ.* **31**, 1417 (1997).
- <sup>10</sup> L. Vereecken and J.S. Francisco, *Chem. Soc. Rev.* **41**, 6259 (2012).
- <sup>11</sup> W. Eisfeld and J.S. Francisco, *J. Chem. Phys.* **131**, 134313 (2009).
- <sup>12</sup> S. Bauerle and G.K. Moortgat, *Chem. Phys. Lett.* **309**, 43 (1999).
- <sup>13</sup> J.S. Francisco and W. Eisfeld, *J. Phys. Chem. A* **113**, 7593 (2009).
- <sup>14</sup> C. Barrientos, P. Redondo, H. Martinez, and A. Largo, *Astrophys. J.* **784**, 132 (2014).
- <sup>15</sup> F. Duvernay, G. Danger, P. Theule, T. Chiavassa, and A. Rimola, *Astrophys. J.* **791**, 75 (2014).
- <sup>16</sup> F. Duvernay, A. Rimola, P. Theule, G. Danger, T. Sanchez, and T. Chiavassa, *Phys. Chem. Chem. Phys.* **16**, 24200 (2014).
- <sup>17</sup> B.M. Hays and S.L. Widicus-Weaver, *J. Phys. Chem. A* **117**, 7142 (2013).
- <sup>18</sup> D.R. Kent, S.L. Widicus, G.A. Blake, and W.A. Goddard, *J. Chem. Phys.* **119**, 5117 (2003).
- <sup>19</sup> M. Baker and W. Gabryelski, *Int. J. Mass Spectrom.* **262**, 128 (2007).
- <sup>20</sup> A. Simakov, G.B.S. Miller, A.J.C. Bunkan, M.R. Hoffmann, and E. Uggerud, *Phys. Chem. Chem. Phys.* **15**, 16615 (2013).
- <sup>21</sup> Q. Cao, S. Berski, Z. Latajka, M. Rasanen, and L. Khriachtchev, *Phys. Chem. Chem. Phys.* **16**, 5993 (2014).
- <sup>22</sup> T.M. Ramond, G.E. Davico, R.L. Schwartz, and W.C. Lineberger, *J. Chem. Phys.* **112**, 1158 (2000).
- <sup>23</sup> J.J. Dillon and D.R. Yarkony, *J. Chem. Phys.* **130**, 154312 (2009).
- <sup>24</sup> J.J. Dillon and D.R. Yarkony, *J. Chem. Phys.* **131**, 134303 (2009).
- <sup>25</sup> D.M. Neumark, *J. Phys. Chem. A* **112**, 13287 (2008).
- <sup>26</sup> J. Jin, I. Sioutis, G. Tarczay, S. Gopalakrishnan, A. Bezant, and T.A. Miller, *J. Chem. Phys.* **121**, 11780 (2004).

- <sup>27</sup> G.B. Ellison, P.C. Engelking, and W.C. Lineberger, *J. Phys. Chem.* **86**, 4873 (1982).
- <sup>28</sup> J.J. Dillon and D.R. Yarkony, *J. Chem. Phys.* **137**, 154315 (2012).
- <sup>29</sup> P. Ho, D.J. Bamford, R.J. Buss, Y.T. Lee, and C.B. Moore, *J. Chem. Phys.* **76**, 3630 (1982).
- <sup>30</sup> R. Spence and W. Wild, *J. Chem. Soc.* **1**, 506 (1935).
- <sup>31</sup> M.J. Frisch, G.W. Trucks, H.B. Schlegel, G.E. Scuseria, M.A. Robb, J.R. Cheeseman, G. Scalmani, V. Barone, B. Mennucci, G.A. Petersson, H. Nakatsuji, M. Caricato, X. Li, H.P. Hratchian, A.F. Izmaylov, J. Bloino, G. Zheng, J.L. Sonnenberg, M. Hada, M. Ehara, K. Toyota, R. Fukuda, J. Hasegawa, M. Ishida, T. Nakajima, Y. Honda, O. Kitao, H. Nakai, T. Vreven, J.A. Montgomery Jr., J.E. Peralta, F. Ogliaro, M.J. Bearpark, J. Heyd, E.N. Brothers, K.N. Kudin, V.N. Staroverov, R. Kobayashi, J. Normand, K. Raghavachari, A.P. Rendell, J.C. Burant, S.S. Iyengar, J. Tomasi, M. Cossi, N. Rega, N.J. Millam, M. Klene, J.E. Knox, J.B. Cross, V. Bakken, C. Adamo, J. Jaramillo, R. Gomperts, R.E. Stratmann, O. Yazyev, A.J. Austin, R. Cammi, C. Pomelli, J.W. Ochterski, R.L. Martin, K. Morokuma, V.G. Zakrzewski, G.A. Voth, P. Salvador, J.J. Dannenberg, S. Dapprich, A.D. Daniels, Ö. Farkas, J.B. Foresman, J. V. Ortiz, J. Cioslowski, and D.J. Fox, *Gaussian 09 Revision B.01*, Gaussian Inc. Wallingford, CT (2009).
- <sup>32</sup> K.M. Ervin, T.M. Ramond, G.E. Davico, R.L. Schwartz, S.M. Casey, and W.C. Lineberger, *J. Phys. Chem. A* **105**, 10822 (2001).
- <sup>33</sup> K.M. Ervin, J. Ho, and W.C. Lineberger, *J. Phys. Chem.* **92**, 5405 (1988).
- <sup>34</sup> T.E. Sharp and H.M. Rosenstock, *J. Chem. Phys.* **41**, 3453 (1964).
- <sup>35</sup> K.M. Vogelhuber, S.W. Wren, A.B. McCoy, K.M. Ervin, and W.C. Lineberger, *J. Chem. Phys.* **134**, 184306 (2011).
- <sup>36</sup> J.H. Frederick and C. Woywod, *J. Chem. Phys.* **111**, 7255 (1999).
- <sup>37</sup> Y.C. Zhao, B.X. Wang, H.Y. Li, and L. Wang, *J. Mol. Struct. Theochem* **818**, 155 (2007).
- <sup>38</sup> S.J. Blanksby, T.M. Ramond, G.E. Davico, M.R. Nimlos, S. Kato, V.M. Bierbaum, W.C. Lineberger, G.B. Ellison, and M. Okumura, *J. Am. Chem. Soc.* **123**, 9585 (2001).
- <sup>39</sup> A. Sanov, *Annu. Rev. Phys. Chem.* **65**, 341 (2014).
- <sup>40</sup> D.J. Goebbert, K. Pichugin, and A. Sanov, *J. Chem. Phys.* **131**, 164308 (2009).
- <sup>41</sup> P.C. Engelking, *J. Phys. Chem.* **90**, 4544 (1986).
- <sup>42</sup> E.P. Wigner, *Phys. Rev.* **73**, 1002 (1948).
- <sup>43</sup> W.C. Lineberger and B.W. Woodward, *Phys. Rev. Lett.* **25**, 424 (1970).
- <sup>44</sup> U.D. Jentschura, S. Kotochigova, E.O. LeBigot, P.J. Mohr, and B.N. Taylor, *The Energy Levels of Hydrogen and Deuterium (Version 2.1)*, National Institute of Standards and Technology, Gaithersburg, MD, available online at [physics.nist.gov/PhysRefData/HDEL/energies.html](http://physics.nist.gov/PhysRefData/HDEL/energies.html), 2017.
- <sup>45</sup> C.K. Huang, Z.F. Xu, M. Nakajima, H.M.T. Nguyen, M.C. Lin, S. Tsuchiya, and Y.P. Lee, *J. Chem. Phys.* **137**, (2012).

*this page is intentionally left blank*

## CHAPTER VI

### PHOTOELECTRON SPECTROSCOPY OF THE AMINOMETHOXIDE ANION, $\text{H}_2\text{C}(\text{NH}_2)\text{O}^-$

This chapter is partially reproduced from: *Oliveira, A.M, Lehman, J.H., Lineberger, W.C., The Journal of Chemical Physics, to be submitted Dec. 2017.*

#### 6.1 Introduction

Alkoxy radicals are an important class of molecules in atmospheric<sup>1-5</sup> and combustion processes,<sup>6-12</sup> where they often act as highly reactive intermediates. As an open-shelled species with the radical center located on the oxygen, complicated further by some radicals possessing high symmetry, alkoxy radicals often have complex electronic structure making it difficult to fully characterize these molecules spectroscopically. Both their high reactivity and challenging electronic structure have motivated the investigation of alkoxy radicals using a variety of experimental and theoretical methods.<sup>13-19</sup> Experimentally, alkoxy radicals have been studied in the gas phase mainly via spectroscopic techniques.<sup>14,20-27</sup> Theoretically, the electronic structure of small alkoxy radicals have been investigated,<sup>28-31</sup> particularly with regard to Jahn-Teller interactions, spin-orbit splittings, and vibronic couplings.<sup>14,30,32-36</sup>

Several investigations, including extensive work by Miller and coworkers,<sup>32-35</sup> have focused on building from the simplest alkoxy radical (methoxy) to larger alkyl substituted radicals, studying how the vibrational and electronic structure are altered upon the addition of different functional groups.<sup>14,32-34,36</sup> For example, the study by Ramond *et al.*<sup>14</sup> investigated the ethoxy ( $\text{H}_2\text{C}(\text{CH}_3)\text{O}^\bullet$ ), isopropoxy ( $\text{HC}(\text{CH}_3)_2\text{O}^\bullet$ ) and *tert*-butoxy ( $\text{C}(\text{CH}_3)_3\text{O}^\bullet$ ) radicals via photoelectron spectroscopy of the corresponding anions and measures their electron affinities

(EA) and term energies ( $T_0(\tilde{A} \leftarrow \tilde{X})$ ). In ethoxy, the term energy was measured as  $355(10) \text{ cm}^{-1}$  by Ramond *et al.*<sup>14</sup> via anion photoelectron spectroscopy, agreeing well with the term energy of  $364(1) \text{ cm}^{-1}$  measured by Jin *et al.*<sup>35</sup> via dispersed fluorescence spectroscopy. Upon further substitution, forming isopropoxy, the term energy lowers to  $68(10) \text{ cm}^{-1}$ .<sup>35</sup> In addition to these examples, the hydroxymethoxy radical ( $\text{H}_2\text{C}(\text{OH})\text{O}^\bullet$ ) was investigated via anion photoelectron spectroscopy to study the effect of non-alkyl substitution.<sup>37</sup> The hydroxymethoxy term energy was found to be  $T_0(\tilde{A} \leftarrow \tilde{X}) \sim 3300 \text{ cm}^{-1}$ , close to an order of magnitude larger than ethoxy.<sup>37</sup> In the present work, we extend this study by investigating the aminomethoxy radical ( $\text{H}_2\text{C}(\text{NH}_2)\text{O}^\bullet$ ) via anion photoelectron spectroscopy of aminomethoxide ( $\text{H}_2\text{C}(\text{NH}_2)\text{O}^-$ ). A comparison of the  $T_0(\tilde{A} \leftarrow \tilde{X})$  provides a useful insight on how the substituent group affects the electronic structure of substituted alkoxy radicals.

However, the motivation to study the aminomethoxy radical and its corresponding anion extends beyond a fundamental chemical and electronic structure investigation. The aminomethoxide anion is the conjugate base of aminomethanol ( $\text{H}_2\text{C}(\text{NH}_2)(\text{OH})$ ), an important prebiotic molecule as a precursor to simple amino acids.<sup>38,39</sup> Spectroscopic studies of aminomethanol are non-existent, due to its inherent instability in the gas phase.<sup>40,41</sup> Approaching the spectroscopy of aminomethoxy via its anion is an attractive strategy as it provides a measurement of the EA of aminomethoxy. The O–H bond dissociation energy in aminomethanol can then be obtained in a thermochemical cycle from a measurement of the EA of aminomethoxy in conjunction with the gas phase acidity of aminomethanol.<sup>42</sup>

This work investigates the aminomethoxy radical via photoelectron spectroscopy of the aminomethoxide anion ( $\text{H}_2\text{C}(\text{NH}_2)\text{O}^-$ ), with the aid of quantum chemical calculations. The photoelectron spectrum acquired here using velocity map imaging (VMI) provides the first

spectroscopic investigation of aminomethoxy, and includes a measurement of the EA, vibrational frequencies, and  $T_0(\tilde{A} \leftarrow \tilde{X})$ . The measurement of the EA results in a determination of the O–H bond dissociation energy of aminomethanol via a thermochemical cycle. Finally, a comparison between the measured EAs and  $T_0(\tilde{A} \leftarrow \tilde{X})$  of singly substituted alkoxy radicals ( $\text{H}_2\text{C}(\text{R})\text{O}^\bullet$ , R =  $\text{CH}_3$ ,  $\text{NH}_2$  or  $\text{OH}$ ) is performed, establishing a link between identities of functional groups and the electronic structure of singly substituted alkoxy radicals.

## 6.2 Methods

### 6.2.a Experimental

In this experiment, we make use of the instrument described in detail in Chapter 2. The procedures which are specific to this chapter, in particular regarding the production of the anions of interest, are described here. The aminomethoxide anion ( $\text{H}_2\text{C}(\text{NH}_2)\text{O}^-$ ,  $m/z=46$ ) is produced *via* the reaction between neutral formaldehyde ( $\text{H}_2\text{CO}$ ) and the amide anion ( $\text{NH}_2^-$ ). The ions are produced using a dual pulsed valve plasma entrainment source, which is described in detail in Chapter 2 and Ref. 43. Here the main supersonic expansion consists of ~1%  $\text{H}_2\text{CO}$  in argon gas (40 psig) as described in Chapter 5, and the secondary expansion, of a mixture of 10%  $\text{NH}_3$  (35 psig, 99.999% purity) in argon, wherein the anions are formed *via* an electrical discharge ( $\Delta V = -2$  kV,  $\Delta t \sim 130$   $\mu\text{s}$ ). The primary anion formed in such discharge is  $\text{NH}_2^-$ , which is able to react with neutral  $\text{H}_2\text{CO}$  upon crossing of the main and side expansions, forming the desired anionic products. The products of this process, specifically anions with  $m/z = 46$ , will be described in section 6.3.b.

For photodetaching electrons from aminomethoxide, we use the second and third harmonics of a pulsed Nd:YAG laser:  $h\nu = 2.329$  eV (532.3 nm) and 3.494 eV (354.8 nm),

respectively. In addition, photons with energies of 2.172 eV (570.8 nm) and 2.038 eV (608.4 nm) are also employed, and are generated by a 354.8 nm pumped optical parametric oscillator (OPO). The limits of our instrument resolution are determined from the photoelectron spectrum of a reference atomic anion, which is  $S^-$  for this experiment,<sup>44,45</sup> using the above photon energies. Since our experimental resolution does not allow for separation of the rotational structure, the peak center does not necessarily correspond to the band origin of a transition. In order to address this, the procedure described by Engelking<sup>46,47</sup> for rotational band shifts is employed (see Chapter 2 in conjunction with Table 6.5).

### 6.2.b Theoretical

Quantum chemical calculations that did not require the use of high level methods were performed in the Gaussian 09<sup>48</sup> program suite. These concern the neutral and anionic ground electronic states of aminomethoxy and its structural isomers. The enthalpies for the reaction ( $\Delta_{\text{rxn}}H_{0\text{K}}^{\circ}$ ) between  $\text{NH}_2^-$  and  $\text{H}_2\text{CO}$  forming various structural isomers of  $\text{H}_4\text{CNO}^-$  ( $m/z=46$ ) together with the EAs of the neutral products (see supplementary material) were calculated using B3LYP/aug-cc-pVTZ. The energy of excited states of the aminomethoxide anion were calculated with the EOM-CCSD method with the aug-cc-pVTZ basis set.

The electronic structure calculations utilized for the generation of simulated photoelectron spectra were performed by the Molpro program (version 2012.1)<sup>49</sup> Specifically, geometry optimization and harmonic vibrational normal mode calculations regarding aminomethoxide and aminomethoxy were performed using the CCSD(T)/aug-cc-pVTZ (ROCCSD(T) for the neutral radical) level of theory. The excited electronic state of aminomethoxy ( $\tilde{A}^2A''$ ) was calculated using multiconfigurational self-consistent-field (MCSCF)

methods with the aug-cc-pVTZ basis set. Specifically, the complete active space method (CASSCF) was used for geometry optimization and calculation of the harmonic vibrational normal modes. The resulting optimizations are displayed in Tables 6.1 through 6.5, which are listed at the end of this chapter for convenience. For the MCSCF calculations active space consisting of five active electrons in four active orbitals (CAS(5,4)) was employed. The orbitals in the active space nominally correspond to the  $\sigma(\text{CO})$ , oxygen  $2p_y$  and  $2p_x$ , and  $\sigma^*(\text{CO})$  orbitals. This is the same active space (number of electrons, and number and type of orbitals) as the one used by Dillon and Yarkony for ethoxy<sup>50</sup> and hydroxymethoxy<sup>51</sup> (also see Appendix II). This method for the excited state was chosen, instead of a couple-cluster based approach as in the neutral ground state, due to the inability of the EOM-CCSD method to handle open-shelled radicals in the Molpro 2012.1 suite and also based on the successful calculations reported in previous work by Dillon and Yarkony when calculating excited states of substituted alkoxy radicals.<sup>50-52</sup> For simulating the photoelectron spectrum we found that utilizing the higher level, CCSD(T)/aug-cc-pVTZ calculation for the ground state calculations in combination with the CASSCF approach for the excited state showed a significantly better agreement with experiment when compared with a full CASSCF approach for all the electronic states. Finally, we calculate the  $T_0(\tilde{A} \leftarrow \tilde{X})$  using the state averaged multireference configuration interaction with explicitly correlated energies (SA MRCI-F12), where the geometries and zero-point energies (ZPE) are obtained from the CAS optimization for the neutral  $\tilde{X}$  and  $\tilde{A}$  states. Molpro was utilized instead of Gaussian for these cases due to its considerably faster computation times for coupled-cluster calculations, and due to its significantly larger degree of control over the parameters for performing calculations with multiconfigurational methods.

The photoelectron spectra are calculated using the ezSpectrum<sup>53</sup> program, by the methods described in section 2.2.b. These calculations were carried out assuming a vibrational temperature of 150 K, based on previous experiments.<sup>37,54</sup> This procedure generates a discrete spectrum of sticks, where the intensities correspond to the calculated FC factor and the positions correspond to the calculated vibrational frequency relative to the transition between the ground vibrational and electronic level in the anion to ground vibrational level in the neutral electronic states. In order to provide a direct comparison between calculation and experiment, the stick spectrum is convolved with Gaussian functions where the integral is equal to the calculated transition intensity and the *fwhm* is consistent with the eKE-dependent instrumental resolution of the VMI spectrometer.

## 6.3 Results

### 6.3.a Initial remarks

Given that the EA of NH<sub>2</sub> (0.771 eV)<sup>55</sup> is sufficiently less than that of O (1.461 eV),<sup>56</sup> the negative charge on aminomethoxide is largely localized on the oxygen atom, as with the other alkoxide anions.<sup>14,37,57,58</sup> Thus, the EA of the aminomethoxy radical should be similar to the other alkoxy radicals,<sup>14,37,57,58</sup> *i.e.* near 2 eV. In addition, this formal negative charge on the oxygen causes a strong intramolecular electrostatic interaction between the oxygen and the amino group. Upon electron photodetachment, it is expected that the strength of the intramolecular interaction will be significantly lessened, causing major geometry changes associated with the weakening of this interaction. For example, the OCN angle and the distance between the oxygen atom and the amino group hydrogen atoms would be larger for the neutral radical compared to the anion. The calculated equilibrium geometries of aminomethoxide and aminomethoxy are detailed in Table 6.1 and support this physical interpretation. These changes in structural parameters will lead to

vibrational transitions involving excitation of the HNH wag, OCN bend, and OC or CN stretches. If there is a sufficiently large degree of structural change, this could result in a photoelectron spectrum showing an extended vibrational progression. It is also likely that transitions involving a low-lying excited electronic state would be observed, as is the case with other substituted alkoxide photoelectron spectra. Given that the  $T_0(\tilde{X} \leftarrow \tilde{A})$  for other alkoxy radicals range from approximately  $70 \text{ cm}^{-1}$  to  $3300 \text{ cm}^{-1}$ , it might be expected that the  $T_0(\tilde{X} \leftarrow \tilde{A})$  for aminomethoxy would lie somewhere within this range. In the following sections, results from the experiment are presented, where the anion produced in our ion source with  $m/z = 46$  is identified as aminomethoxide and its photoelectron electron spectrum is measured with several photon energies. The EA and  $T_0(\tilde{X} \leftarrow \tilde{A})$  of aminomethoxy are determined, along with several vibrational frequencies.

### *6.3.b Identification of anion with $m/z=46$*

Following the procedure described in section 6.2.a, the mass spectra confirmed the production of an anion with  $m/z=46$ . The identity of  $m/z=46$  was confirmed by the following series of tests. This mass was only formed when both  $\text{H}_2\text{CO}$  was in the main expansion and  $\text{NH}_3$  was discharged in the side expansion. If only argon is present in the main expansion, the discharge of  $\text{NH}_3$  in the side expansion generates a large amount of  $\text{NH}_2^-$ , along with several other N, H containing anions and their clusters with argon.  $\text{NH}_2^-$  is a strong base capable of deprotonating  $\text{H}_2\text{CO}$ <sup>59</sup> whereas other anions generated in the  $\text{NH}_3$  discharge are not thermodynamically capable of doing so. When  $\text{H}_2\text{CO}$  is added to the main expansion, the reaction of  $\text{NH}_2^-$  with  $\text{H}_2\text{CO}$  is confirmed by the appearance of  $m/z=29$  ( $\text{HCO}^-$ ).<sup>60</sup> In addition to deprotonating formaldehyde,  $\text{NH}_2^-$  can also react with formaldehyde in an association reaction,

forming  $m/z=46$ . This reaction product can be collisionally cooled and stabilized by the argon present in abundance in the main expansion.

In the association reaction between  $\text{NH}_2^-$  and  $\text{H}_2\text{CO}$ , the formation of a C–N bond is the most likely to occur, resulting in the aminomethoxide anion being formed (inset graphic of Fig. 1). The calculations performed here (CCSD(T)/aug-cc-pVTZ) predict the EA of aminomethoxy as 1.89 eV, in agreement with the observed EA of 1.944 eV (see section 6.2.b). Other structural isomers of  $\text{H}_4\text{CNO}$  that could arise from photodetachment from other association reaction products between  $\text{NH}_2^-$  and  $\text{H}_2\text{CO}$  possess EAs at least 0.6 eV lower than what is predicted for aminomethoxy, as discussed below. However, no photoelectron signal was observed below an electron binding energy of approximately 1.9 eV, suggesting that it is highly unlikely that these other isomers are being formed in any significant abundance. Calculations performed here and by Rosenberg,<sup>61</sup> suggest that the formation of aminomethoxide from  $\text{NH}_2^-$  and  $\text{H}_2\text{CO}$  is exothermic by  $\sim -40 \text{ kcal mol}^{-1}$ . In the gas phase, unless the heat of formation in this reaction is efficiently dissipated, other structural isomers of aminomethoxide could in principle be formed as well. In our experiment, the energy is removed by collisions with the argon atoms present in abundance in the primary supersonic expansion. The presence of multiple isomers of  $\text{H}_4\text{CNO}^-$  could potentially pose difficulty to the interpretation of the photoelectron spectra. In order to investigate the likelihood that our photoelectron spectra would show signatures of these other isomers of aminomethoxide, we calculated (B3LYP/aug-cc-pVTZ) the reaction enthalpies ( $\Delta_{\text{rxn}} H_{0\text{K}}^0$ ) between  $\text{NH}_2^-$  and  $\text{H}_2\text{CO}$  forming the anionic products shown in Fig. 6.1, together with the EAs of the neutral counterparts (Table 6.6). The relative energies between isomers show that the only expected products would be aminomethoxide (isomer I) and III, but the considerably different EAs show that the identification of these isomers in the photoelectron

spectra should be straightforward. Based on the experimental spectra, aminomethoxide is the dominant anion with  $m/z=46$  formed in this experiment.

### 6.3.c Overview and Electron Affinity of Aminomethoxy

The lower panel of Fig. 6.2 displays the photoelectron spectrum of aminomethoxide acquired with a photon energy of 3.494 eV, which covers the complete range of eBE wherein photoelectron signal was observed. This figure displays a spectrum which originates at approximately 1.94 eV (peak labeled A) and has peaks extending to an eBE of approximately 3.0 eV. Even though peak A is located at the highest eKE in this spectrum, it is apparently the narrowest peak, with a *fwhm* of 48 meV. This goes counter to the eKE dependence of the VMI resolution as described above in section 2.a. Also, the fact that this peak is close to resolution limited, which is 43 meV, indicates that here is likely a large degree of spectral congestion in this region of the spectrum. A higher resolution spectrum, obtained with a lower photon energy will indeed prove this statement in the subsequent analysis. The labels B through D represent the peaks that are displayed in higher resolution in Fig. 6.3. The upper panel of Fig. 6.2 shows the anisotropy parameter ( $\beta$ ) of the spectrum (black circles). The anisotropy parameter is generally positive for the progression, becoming more positive with higher eBE. The negative values of  $\beta$  correspond to the peaks labeled A and C. When this is compared to the overall positive  $\beta$  of the rest of the progression, it suggests that two distinct electronic states of aminomethoxy are accessed using this photon energy. In order to analyze this further, a photoelectron spectrum with higher resolution is required, and hence we obtain a spectrum using a lower photon energy,<sup>58</sup> which is presented in Fig. 6.3.

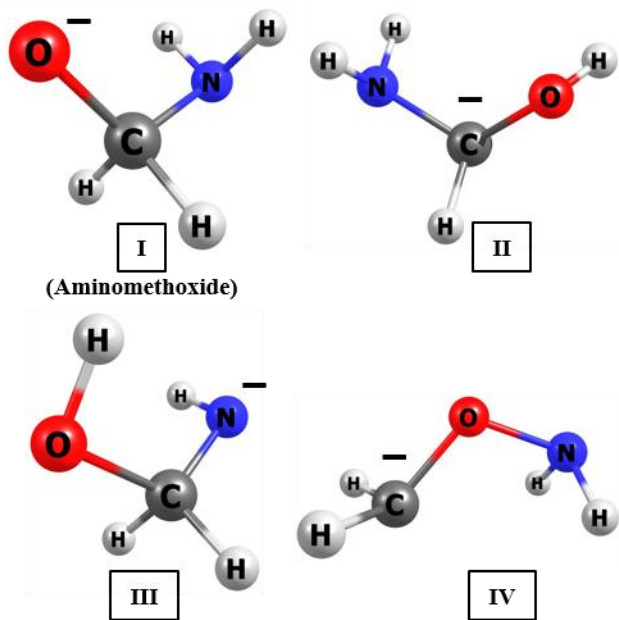


Figure 6.1: Structural isomers of aminomethoxide discussed in the text. The optimized structures were calculated at the B3LYP/aug-cc-pVTZ level of theory/basis set. See Table 6.6 for relative energies and calculated electron affinities of the corresponding neutral radicals.

Table 6.6: Calculated (B3LYP/aug-cc-pVTZ) addition reaction enthalpies ( $\Delta_{\text{rxn}}H_{0\text{K}}^{\circ}$ ) between amide anion ( $\text{NH}_2^-$ ) and formaldehyde ( $\text{H}_2\text{CO}$ ) forming the anionic products shown in Fig. 6.1 and electron affinities of the corresponding neutral species. All values include zero-point energy.

<b>Product<sup>a</sup></b>	<b><math>\Delta_{\text{rxn}}H_{0\text{K}}^{\circ}</math><sup>b</sup></b> <b>/ kcal mol<sup>-1</sup></b>	<b>Neutral EA</b> <b>/ eV</b>
I	-35.4	1.92
II	2.2	-0.11
III	-23.9	1.32
IV	34.1	0.28

<sup>a</sup> See Fig.1 for structure  
<sup>b</sup> Relative to the reactants  $\text{NH}_2^- + \text{H}_2\text{CO}$

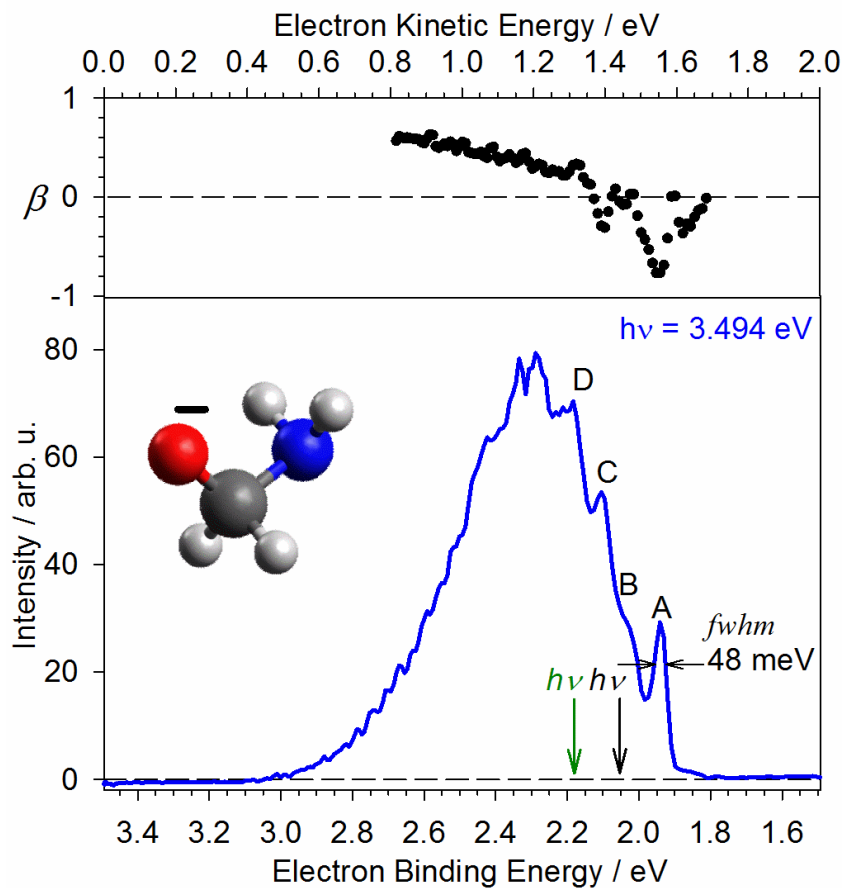


Figure 6.2: Upper panel: Photoelectron anisotropy parameter ( $\beta$ ) of aminomethoxide (black dots) as a function of electron kinetic energy (eKE). The  $\beta$  values are only displayed where a significant photoelectron signal was observed. Lower panel: VMI photoelectron spectrum of aminomethoxide obtained with a photon energy of 3.494 eV. The structure of aminomethoxide is depicted. The green and black arrows indicate the other photon energies (2.172 and 2.038 eV, respectively) used to obtain the higher resolution spectra shown in Figs. 6.3 and 6.4.

The photoelectron spectrum acquired with a photon energy of 2.172 eV (570.8 nm) is presented in Fig. 6.3. This results in a higher resolution photoelectron spectrum and reveals a number of resolved peaks between 1.94 and 2.17 eV eBE, in contrast to the spectrum shown in Fig. 6.2. The peaks labeled with letters in Fig. 6.2 are indicated in Fig. 6.3 as groups of peaks under brackets with the same labels. This shows that the proximity between peaks undermined our ability to resolve the transitions under these brackets when employing the 3.494 eV photon energy (Fig. 6.2), a problem which is solved by the higher resolution attainable with a lower photon energy. In this spectrum, the *fwhm* of peak 1 is 13 meV, significantly narrower than peak A in Fig. 6.2 (48 meV) and also reasonable close to being resolution limited (9 meV). Fig. 6.3 also displays the calculated photoelectron spectrum in the lower panel. The red sticks represent transitions from the ground vibrational and electronic state of aminomethoxide to the ground electronic state of neutral aminomethoxy ( $\tilde{X}$ ) and the blue sticks represent transitions to the neutral excited electronic state ( $\tilde{A}$ ). From this point onward in this work, the  $\tilde{X}$  and  $\tilde{A}$  states will always refer to the electronic states of the neutral aminomethoxy. The simulation displayed in the lower panel of Fig. 6.3 was built by shifting and scaling the stick spectra so that the origin transitions of the  $\tilde{X}$  and  $\tilde{A}$  states of aminomethoxy matched the position and ratio of the areas of peaks 1 and 3, respectively. With the improved resolution, a thorough analysis of the spectrum can be performed, providing the assignments of the EA,  $T_0(\tilde{X} \leftarrow \tilde{A})$ , and vibrational frequencies.

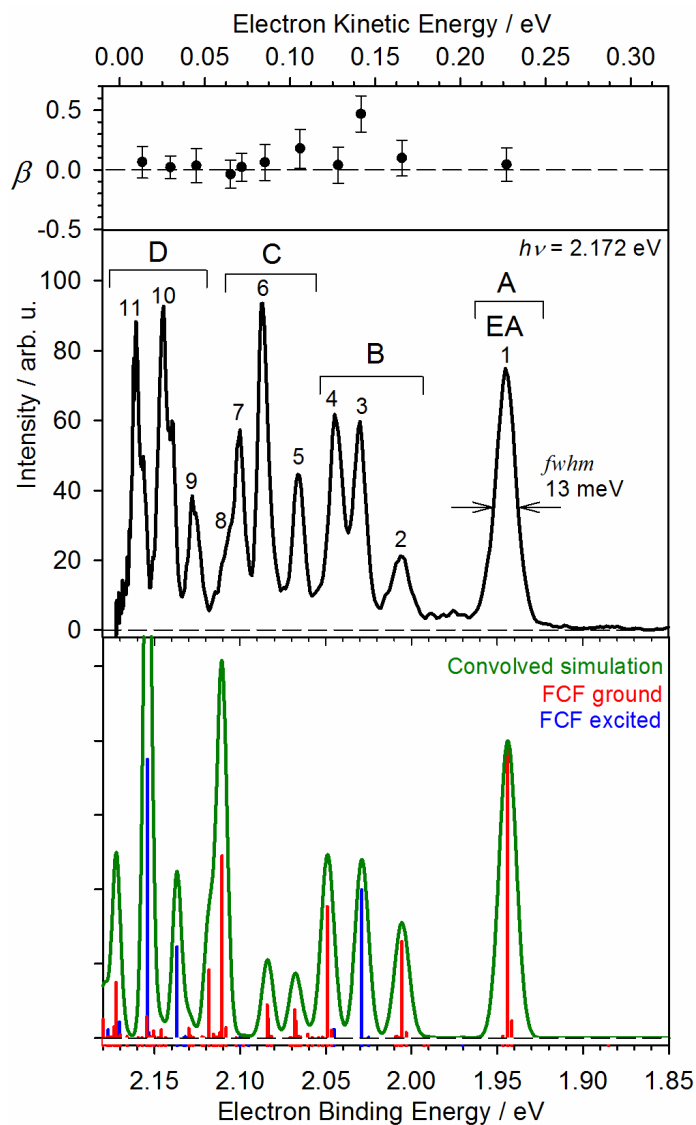


Figure 6.3: Upper panel: Measured anisotropy parameter  $\beta$  associated with the experimental photoelectron spectrum found in the middle panel. The  $\beta$  values shown correspond to average values across the top  $\frac{1}{4}$  of each peak in order to minimize the contribution from neighboring peaks to the measured anisotropy of individual peaks. The error bars correspond to the standard deviation of the mean  $\beta$  values across the points averaged for each peak. Middle panel: Photoelectron spectrum obtained using a photon energy of 2.172 eV. Lower panel: Calculated photoelectron spectrum for transitions from the ground electronic state of the aminomethoxy (150 K), to vibrational levels of the neutral ground (red sticks) and neutral excited (blue sticks) electronic states of aminomethoxy, convolved to the expected experimental resolution.

For the assignment of the EA of aminomethoxy, we focus on peak 1 of Fig. 6.3 (peak A in Fig. 6.2), which is the apparent origin of the overall vibrational progression. As mentioned previously, the CCSD(T)/aug-cc-pVTZ calculations predict the EA of aminomethoxy as 1.89 eV, in close agreement with the corresponding eBE of the center of peak 1. A comparison between calculation and experiment suggests that peak 1 arises primarily from the origin of the  $\tilde{X}$  state vibrational progression. In order to establish our best assignment of the EA of aminomethoxy, we obtain a photoelectron spectrum with a photon energy of 2.038 eV, displayed in Fig. 6.4. Using this lower photon energy, peak 1 has a *fwhm* of 9 meV. From the center position of peak 1 (1.944(2) eV) and the consideration of the uncertainties and shifts discussed in sections 6.2.a and 2.3.b, the EA of aminomethoxy is assigned as 1.944(5) eV. Other important assignments are based on Fig. 6.4, such as the determination of  $T_0(\tilde{X} \leftarrow \tilde{A})$ . Such assignment is described in the following section.

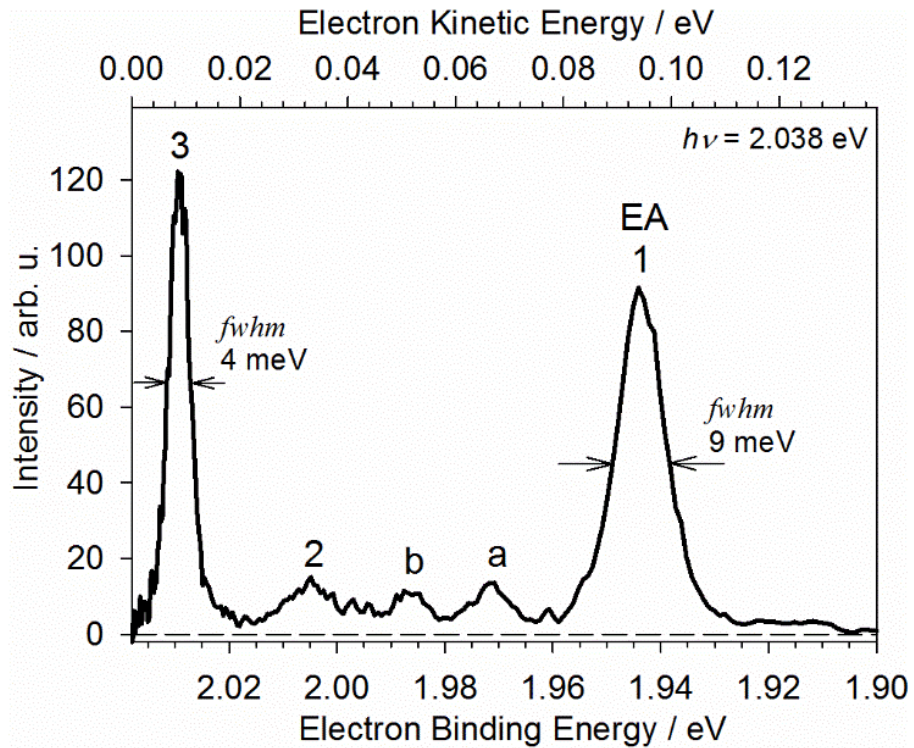


Figure 6.4: Photoelectron spectrum obtained using a photon energy of 2.038 eV. Peak labels are discussed in the text.

#### 6.3.d Determination of Aminomethoxy Term Energy, $T_0(\tilde{A} \leftarrow \tilde{X})$

The experimental assignment of the origin of the  $\tilde{A}$  state vibrational progression is determined from two factors: experimental peak-specific anisotropy parameters and comparison with the theoretically predicted photoelectron spectra. In the spectrum obtained with a photon energy of 3.494 eV (Fig. 6.2), the  $\tilde{X}$  state origin peak (peak A) has a  $\beta < 0$ , while the high eBE region (above  $\sim 2.2$  eV) has  $\beta$  values that are greater than 0. As previously mentioned, this changing anisotropy parameter across the spectrum suggests the presence of transitions to at least two different electronic states. The high eBE region is likely dominated by transitions to the higher-lying  $\tilde{A}$  state, which is confirmed by the calculated spectrum over the full range of eBEs (Fig. 6.6). However, because of the reduced resolution, the origin of the  $\tilde{A}$  state vibrational progression cannot be determined from the spectrum in Fig. 6.3. From the higher resolution photoelectron spectrum (Fig. 6.3), an analysis of the  $\beta$  parameter shows that most of the observed peaks have a near isotropic photoelectron angular distribution ( $\beta \approx 0$ ), apart from peak 3 with  $\beta \approx +0.5$ . A photoelectron spectrum obtained with a slightly higher photon energy of 2.329 eV (Fig. 6.5) further corroborates this observation of the positive anisotropy of peak 3 compared to neighboring peaks. The photoelectron spectrum obtained using 2.329 eV photon energy (532 nm) is shown in Figure S1. As mentioned above, this photoelectron spectrum confirms the distinct positive anisotropy parameter of peak 3. This suggests that peak 3 is dominated by a transition from the anion to the excited  $\tilde{A}$  state of the neutral radical. Although other peaks seem to have positive anisotropies as well, and therefore could be associated with the excited electronic state, the large degree of congestion makes a definite assignment very challenging.

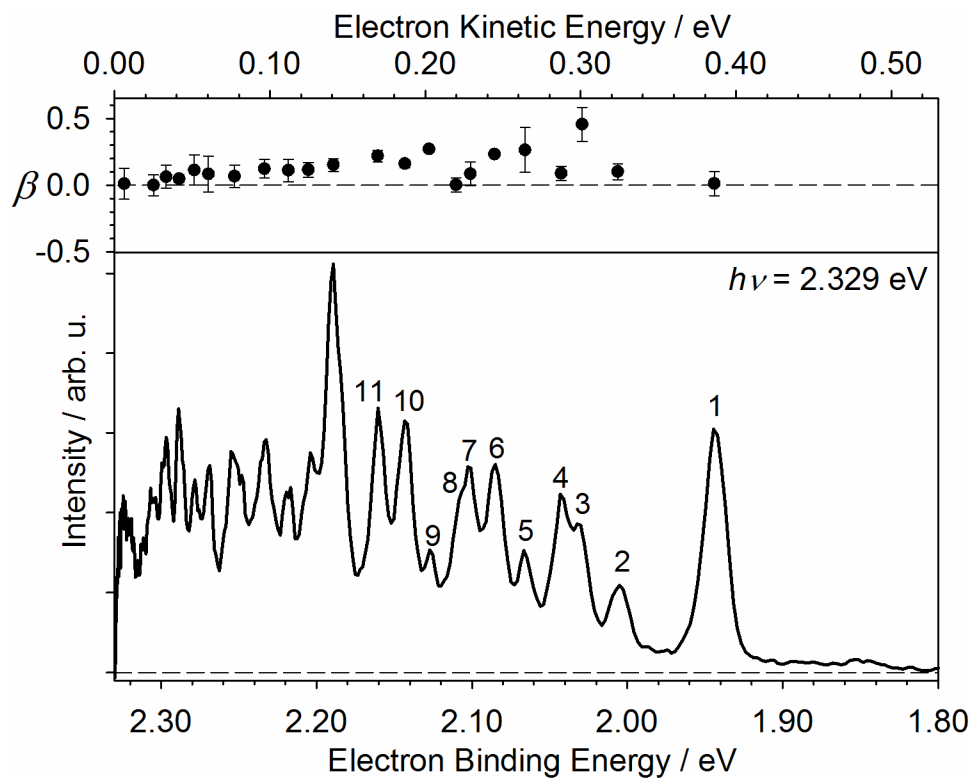


Figure 6.5: Lower panel: Photoelectron spectrum obtained using 2.329 eV photon energy (532 nm) as a function of decreasing eBE. The peak labels are the same as the ones in Fig. 3 of the main text. Upper panel: Anisotropy parameter  $\beta$  as a function of eKE. The  $\beta$  values shown correspond to average values across the top  $\frac{1}{4}$  of each peak to minimize the contribution to the anisotropy from neighboring peaks. The error bars correspond to scatter of  $\beta$  values across the points averaged for each peak.

Peak 3 is the lowest eBE peak that does not have an assignment corresponding to a transition from the anion to the ground  $\tilde{X}$  state of the neutral radical. Peak 3 is centered at 2.029(1) eV (Fig. 3), which is 689(16)  $\text{cm}^{-1}$  relative to the  $\tilde{X}$  state origin. While this peak spacing is similar to the HCH torsional frequency of the  $\tilde{X}$  state (see Table 6.3), transitions involving this symmetry breaking vibrational mode are not allowed. There are no other predicted transitions to the ground  $\tilde{X}$  state with significant FCFs that could be assigned to peak 3. Given this and the observed photoelectron angular anisotropy, this peak is assigned to the  $\tilde{A}$  state origin transition. This assignment is further confirmed by the overall satisfactory agreement between the calculated and experimental spectra over the full range of eBEs (Fig. 6.6) once the calculated photoelectron spectrum accessing the excited state is set to originate at peak 3. This agreement is particularly good with regard to the overall width of the vibrational envelope and the position of its maximum, located at approximately 2.28 eV eBE. Thus, the  $T_0(\tilde{A} \leftarrow \tilde{X})$  term energy is obtained from the highest resolution spectrum (Fig. 6.4) and is determined as 0.085(5) eV. The calculations performed here (CAS(5,4)//MRCI-F12/aug-cc-pVTZ) to provide the term energy of aminomethoxy as  $T_0(\tilde{A} \leftarrow \tilde{X}) = 0.201$  eV. Although the agreement with the experimental measurement is not completely satisfactory, the experimental evidence of the origin of the ground and first excited electronic states is clear.

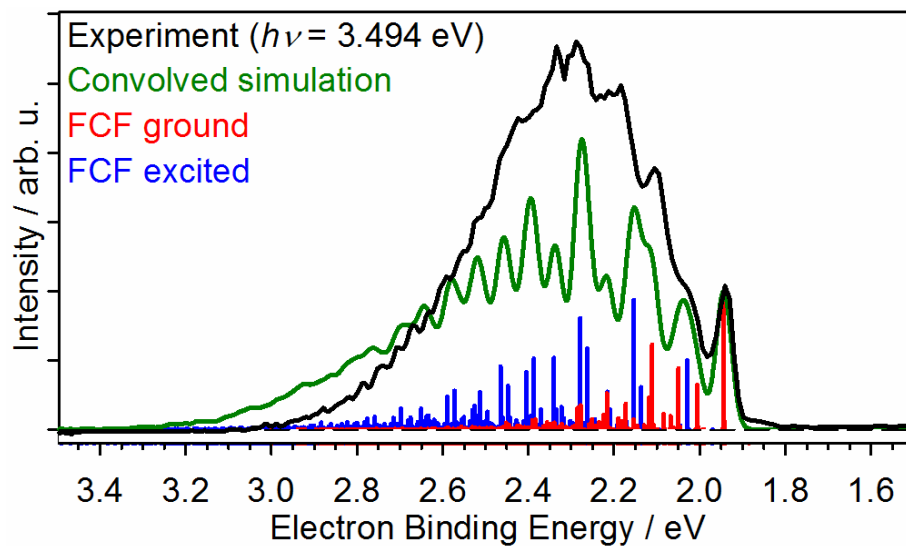


Figure 6.6: Experimental photoelectron spectrum obtained with 3.494 eV photon energy (black trace), calculated FCFs for transitions from the ground state of the anion ( $\tilde{X}^1A'(v=0)$ ) to neutral ground (red sticks) and neutral excited (blue sticks) electronic states of aminomethoxy. The green trace represents the convolved calculated spectrum using the experimental resolution.

### 6.3.e Vibrational analysis

In order to conduct a vibrational analysis, we perform simulations of the photoelectron spectrum by the methods described in section 2.b, with results displayed in the lower panel of Fig. 6.3. For convenience, the transition energies are given relative to the specified electronic state's vibrational origin ( $\tilde{X}$  or  $\tilde{A}$ ) and reported in wavenumbers and therefore represent the vibrational frequencies of the final, neutral state. The calculated spectrum provides vibrational assignments by comparison of the positions of the experimental and calculated peaks (see Tables 6.2 through 6.4). Our calculations predict that the most active vibrations in the photoelectron spectrum will be the HNH wag, OCN bend, C–N and O–C stretches, based on the geometry change between the anion and neutral  $\tilde{X}$  and  $\tilde{A}$  states. From a chemical intuition point of view, the loss of a formal charge in the oxygen atom of aminomethoxide upon photodetachment, forming aminomethoxy, would result in the decrease of the strength of the intramolecular electrostatic interaction between the oxygen and NH<sub>2</sub> moieties. This would result in an increase in the OCN angle, a distancing of the NH<sub>2</sub> hydrogens from the oxygen atom, leading to a similar prediction on the vibrational activity. As the subsequent analysis shows, our experimental observations indeed confirm our predictions, providing further confidence to the assignments made here.

Peak 2 is spaced from peak 1 by 496(10) cm<sup>-1</sup>, a value that agrees well with the calculated OCN bend harmonic frequency (498 cm<sup>-1</sup>) of the neutral  $\tilde{X}$  state. This provides a measurement of the OCN bending frequency  $\nu_{14}(\tilde{X}) = 500(40)$  cm<sup>-1</sup>. The transition which is predicted to dominate peak 4 can be assigned as  $\nu_{12}(\tilde{X}) = 790(30)$  cm<sup>-1</sup>, as it agrees well with the calculated harmonic frequency of the HNH wag (847 cm<sup>-1</sup>). The assignments of peaks 5 through 11 are more complicated due to the presence of transitions whose proximity would make them

impossible to experimentally separate due to the resolution of the instrument. As an example, peak 5 is spaced from the  $\tilde{X}$  state origin by  $985(13) \text{ cm}^{-1}$ , which can correspond to either the first overtone of the OCN bend in the ground electronic state,  $2\nu_{14}(\tilde{X})$ , calculated as  $996 \text{ cm}^{-1}$ , or the C–O stretch  $\nu_{11}(\tilde{X})$ , calculated as  $1002 \text{ cm}^{-1}$ . The ambiguity of the assignments cannot be eliminated with our experimental resolution which limits our capability of accurately assigning these transitions. Nevertheless, tentative assignments were made and are reported below in Table 6.7. Other transitions which were not assigned in this section, namely the peaks labeled *a* and *b* are discussed in the following section (6.3.b).

Table 6.7: Vibrational transition assignments for the peaks in the photoelectron spectra (Figs. 6.3, 6.4 and 6.5). The absolute peak position (eBE, reported in eV) and the energy relative to the origin of the neutral ground and excited state progressions (reported in  $\text{cm}^{-1}$ ) are given. The  $\text{H}_2\text{C}(\text{NH}_2)\text{O}^- (\tilde{X}^1A') (v_1'v_2' \dots) \rightarrow \text{H}_2\text{C}(\text{NH}_2)\text{O}^* (\tilde{X}^2A' \text{ or } \tilde{A}^2A'') (v_1v_2 \dots) + e^-$  (eKE) transitions (second column) are labeled using the standard shorthand notation ( $1_{v_1'}^{v_1'} 2_{v_2'}^{v_2'} \dots$ ).

Peak label	eBE position / eV	Spacing from Peak 1 / $\text{cm}^{-1}$	Spacing from Peak 3 / $\text{cm}^{-1}$	Possible assignments of transitions <sup>a</sup> (2 <sup>nd</sup> column)
<b>1</b>	1.944(3)	0	-	$\tilde{X}^1A'(v=0) \rightarrow \tilde{X}^2A'(v=0)$
<b>a</b>	1.971(3)	222	-	?
<b>b</b>	1.987(9)	344	-	?
<b>2</b>	2.005(4)	494	-	$14_0^1$
<b>3</b>	2.029(1)	689	0	$\tilde{X}^1A'(v=0) \rightarrow \tilde{A}^2A''(v=0)$
<b>4</b>	2.042(3)	803	114	$12_0^1$
<b>5</b>	2.066(1)	986	296	$14_0^2, 11_0^1$
<b>6</b>	2.087(1)	1151	461	$9_0^1, 14_0^1$
<b>7</b>	2.101(1)	1265	576	$8_0^1$
<b>8</b>	2.107(3)	1306	616	$7_0^1$
<b>9</b>	2.127(2)	1477	787	$13_0^1$
<b>10</b>	2.145(1)	1620	930	$12_0^1$
<b>11</b>	2.161(1)	1748	1059	$8_0^1 14_0^1$

<sup>a</sup> Assignments are tentative with the exception of the vibrational origin transitions (peaks 1 and 3) and are based on the calculated spectrum shown in Fig. 6.3.

### 6.3.f Unassigned transitions

The high resolution photoelectron spectrum in Fig. 6.4 reveals two additional peaks, labeled *a* and *b*, which are not accounted for in the calculated spectrum. The spacings from peak 1 to peaks *a* and *b* are 220(30) cm<sup>-1</sup> and 350(40) cm<sup>-1</sup>, respectively. The lowest calculated frequency mode of the  $\tilde{X}$  state of aminomethoxy is the HNH torsion, calculated to be 252 cm<sup>-1</sup>. While this vibrational frequency matches the peak spacing fairly well, this is a symmetry-forbidden transition. These peaks are also not observed when using a higher photon energy (such as in the spectra reported in Figs. 6.3 and 6.5), but otherwise using the same experimental conditions. In anion photoelectron spectroscopy, peak intensities can change as a function of photon energy simply as a threshold effect, but such effect decreases peak intensities due to decreasing photodetachment cross section with lower eKE.<sup>62</sup> The observation that the integrated areas of peaks *a* and *b* increase in the lower eKE spectrum with respect to other peaks in the spectrum cannot be explained by threshold effects. These observations suggest that peaks *a* and *b* result from electron autodetachment, which is the most likely explanation of this behavior, as described in previous investigations.<sup>63-70</sup> It is possible that the normally forbidden torsional mode gains intensity via the autodetachment process. Vibrational activity of Franck-Condon forbidden modes has previously been attributed to autodetachment in the photoelectron spectrum of small molecular anions, such as H<sub>2</sub>CCN<sup>-</sup>.<sup>65,71</sup>

## 6.4 Discussion

### 6.4.a Thermochemistry of aminomethanol

Some basic thermochemical properties of aminomethanol can be obtained from a thermochemical cycle<sup>42</sup> using the experimentally measured EA of aminomethoxy:

$$D_0(\text{H}_2\text{C}(\text{NH}_2)\text{O}-\text{H}) = \Delta_{\text{acid}}H_{0\text{K}}^0(\text{H}_2\text{C}(\text{NH}_2)\text{OH}) - \text{IE}(\text{H}) + \text{EA}(\text{H}_2\text{C}(\text{NH}_2)\text{O}^\bullet) \quad (6.1)$$

There is no experimental measurement of the O–H bond dissociation energy,  $D_0(\text{H}_2\text{C}(\text{NH}_2)\text{O}-\text{H})$ , or the gas phase acidity,  $\Delta_{\text{acid}}H_{0\text{K}}^0(\text{H}_2\text{C}(\text{NH}_2)\text{OH})$ , of aminomethanol. Thus, quantum chemical calculations must be employed to obtain either one of these values. In this work,  $\Delta_{\text{acid}}H_{0\text{K}}^0(\text{H}_2\text{C}(\text{NH}_2)\text{OH})$  was selected since this quantity only depends on calculating the formation enthalpies of the closed shell species  $\text{H}_2\text{C}(\text{NH}_2)\text{O}^-$ ,  $\text{H}_2\text{C}(\text{NH}_2)\text{OH}$ , and  $\text{H}^+$ . The G4 composite method was applied yielding  $\Delta_{\text{acid}}H_{0\text{K}}^0(\text{H}_2\text{C}(\text{NH}_2)\text{OH}) = 374.0 \text{ kcal mol}^{-1}$ , where the predicted uncertainty in these calculations is predicted to be on the order of 1 to 2  $\text{kcal mol}^{-1}$ .<sup>72</sup> Using the experimentally determined  $\text{EA}(\text{H}_2\text{C}(\text{NH}_2)\text{O}^\bullet) = 1.944(5) \text{ eV}$  and the well-known ionization energy of atomic hydrogen,<sup>73</sup>  $D_0(\text{H}_2\text{C}(\text{NH}_2)\text{O}-\text{H})$  is determined to be  $106.3 \pm 2.0 \text{ kcal mol}^{-1}$ , using a conservative estimate of the uncertainty. Our value derived from a combination of experiment and calculation compares nicely to the calculate (G4 composite method) value of  $D_0(\text{H}_2\text{C}(\text{NH}_2)\text{O}-\text{H}) = 107.7 \text{ kcal mol}^{-1}$ . Table 6.8 summarized this result, together with other major experimental results reported in this chapter.

Table 6.8: Summary of major results.

Summary of major results	Experiment	Calculation
$EA(\text{H}_2\text{C}(\text{NH}_2)\text{O}^\bullet) / \text{eV}$	1.944(5)	1.89 eV <sup>a</sup>
$T_0(\tilde{A} \leftarrow \tilde{X})(\text{H}_2\text{C}(\text{NH}_2)\text{O}^\bullet) / \text{eV}$	0.085(5)	0.201 eV <sup>b</sup>
$\Delta_{\text{acid}}H_{0\text{K}}^\circ(\text{H}_2\text{C}(\text{NH}_2)\text{OH}) / \text{kcal mol}^{-1}$	-	374.0 <sup>c</sup>
$D_0(\text{H}_2\text{C}(\text{NH}_2)\text{O}-\text{H}) / \text{kcal mol}^{-1}$	106(2) <sup>d</sup>	107.7 <sup>c</sup>
<sup>a</sup> CCSD(T)/aug-cc-pVTZ (RO method used for neutral)		
<sup>b</sup> CAS(5,4)//MRCI-F12/aug-cc-pVTZ, see section 6.2.b		
<sup>c</sup> G4 composite method, see section 6.4.a		
<sup>d</sup> Value based on the thermochemical cycle (Eq. 1) using the calculated $\Delta_{\text{acid}}H_{0\text{K}}^\circ(\text{H}_2\text{C}(\text{NH}_2)\text{OH})$		

#### 6.4.b Comparison of aminomethoxy with other singly substituted alkoxy radicals

It is instructive to compare of the EAs of ethoxy, aminomethoxy, and hydroxymethoxy, since they have similar atom connectivity, are isoelectronic radicals, but have different functional groups attached to the central carbon atom. Comparing the experimentally measured EAs of  $\text{H}_2\text{C}(\text{R})\text{O}^\bullet$  we see a trend of increasing values: 1.712(4), 1.944(5) and 2.220(2) eV for  $\text{R} = \text{CH}_3$ ,  $\text{NH}_2$  and  $\text{OH}$ , respectively. This trend correlates with the increasing electronegativity of the R group.

The photoelectron spectra of aminomethoxide and hydroxymethoxide<sup>37</sup> (see Chapter 5) are quite similar to each other, as shown in Fig. 6.7. The analysis of the hydroxymethoxide photoelectron spectrum presented in Chapter 5 showed significant excitation in OCO stretches and bends for the transition from the anion to the neutral  $\tilde{X}$  state. The activity of these vibrational modes is associated with the weakening of the electrostatic intramolecular interaction between the hydroxyl group and the oxygen atom. This observation is analogous to the one reported here for aminomethoxy. While the photoelectron spectra of aminomethoxy and hydroxymethoxy appear very similar, there is a significant difference between the term energies of these radicals:  $T_0(\tilde{A} \leftarrow \tilde{X}) = 0.085(5)$  eV for aminomethoxy and  $T_0(\tilde{A} \leftarrow \tilde{X}) \sim 0.4$  eV for hydroxymethoxy.<sup>37</sup> This five-fold difference between the  $T_0(\tilde{A} \leftarrow \tilde{X})$  suggests that exchanging the amino group for a hydroxyl group has a significant effect on the electronic structure of these singly substituted alkoxy radicals. In addition to their work on ethoxy,<sup>50</sup> Dillon and Yarkony performed a theoretical study of hydroxymethoxy<sup>51</sup> focusing on its distinct electronic structure. In that study, they argue that the electronic structure and the topography of the  $\tilde{X}$  and  $\tilde{A}$  states of hydroxymethoxy are drastically different from the typical Jahn-Teller influenced topography of ethoxy. This difference is mainly attributed to the strength of the intramolecular interaction

between the hydroxyl group and the oxygen atom. In aminomethoxy, the amino group is also able to form a strong electrostatic intramolecular interaction with the O moiety, but the nitrogen atom is less electron-withdrawing than oxygen and, therefore, polarizes the hydrogen atoms to a lesser extent. Aminomethoxy also exhibits an equilibrium geometry in which the hydrogen atoms are not as close to the O moiety when compared to hydroxymethoxy. This is because of the average geometry of hydroxymethoxy forms a four-membered planar O-C-O-H ring, while in aminomethoxy, the oxygen bisects the HNH angle, causing both hydrogens of the amino group to be out of the O-C-N plane. Thus, the interatomic distances between the hydrogen and the opposite oxygen atom are 2.68 Å in aminomethoxy *versus* 2.29 Å in hydroxymethoxy, which can make the interaction between these moieties considerably weaker for aminomethoxy than hydroxymethoxy.

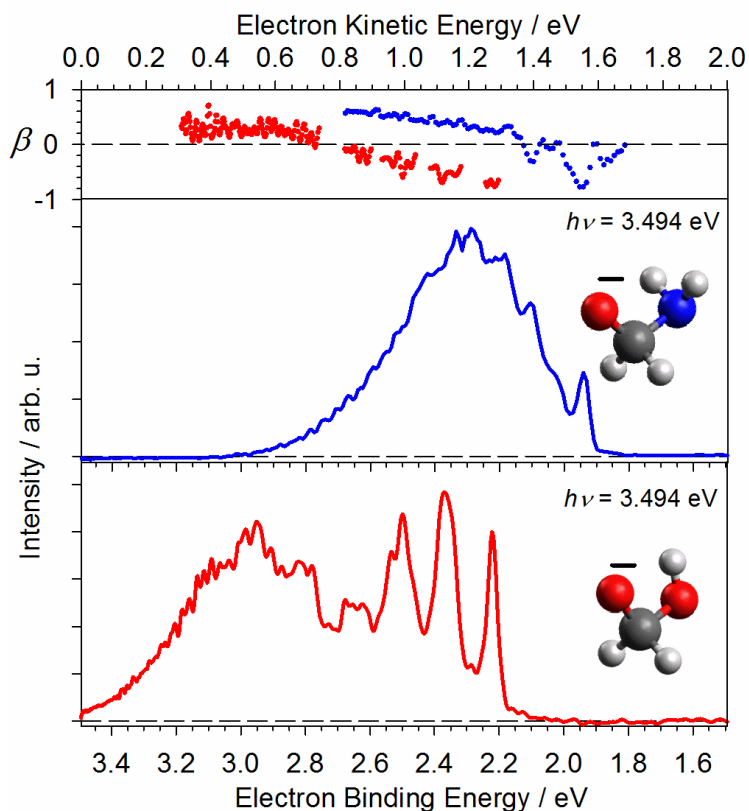


Figure 6.7: Upper panel: Photoelectron anisotropy parameter ( $\beta$ ) as a function of electron kinetic energy (eKE) for aminomethoxy (blue dots) and hydroxymethoxy (red dots). The  $\beta$  values were truncated to exclude points where no significant photoelectron signal was observed. The spectrum of hydroxymethoxide is reproduced from Ref. <sup>37</sup>. Lower panels: Photoelectron spectrum of hydroxymethoxide (red) and aminomethoxide anions (blue) obtained with a photon energy of 3.49 eV (355 nm) as a function of decreasing electron binding energy (eBE). The inset graphic depicts the optimized structures of the anions.

A comparison between aminomethoxy and other small substituted alkoxy radicals provides a possible explanation of why the calculated and experimental photoelectron spectrum presented in Fig. 6.3 have a less than perfect agreement, particularly for peaks above 2.06 eV. It has been shown previously that for other small alkoxy radicals, the inclusion of vibronic coupling, *i.e.* coupling of electronic and vibrational degrees of freedom, was the primary contributor to generating accurate calculated photoelectron spectra.<sup>37,50-52</sup> Similar to aminomethoxide, the photoelectron spectrum of ethoxide reported by Ramond *et al.*<sup>14</sup> displayed numerous prominent disagreements between harmonic calculations and the experiment, particularly regarding peak intensities. This photoelectron spectrum was later investigated by Dillon and Yarkony,<sup>50</sup> who, by including vibronic coupling between the ethoxy  $\tilde{X}$  and  $\tilde{A}$  states in the calculation, significantly increased the level of agreement between theory and experiment while also shedding light on why there was disagreement to begin with. Thus, it is likely that vibronic coupling between the  $\tilde{X}$  and  $\tilde{A}$  states in aminomethoxy is also a dominant contributor to the disagreement between calculation and experiment for the photoelectron spectrum of aminomethoxide. However, it is beyond the scope of this work to attempt this level of theory for aminomethoxy.

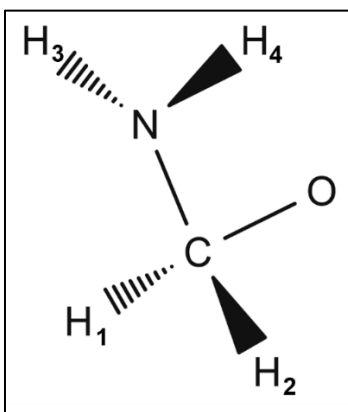
## 6.5 Conclusions

In this work, the aminomethoxide ( $\text{H}_2\text{C}(\text{NH}_2)\text{O}^-$ ) anion was successfully produced in the gas phase from the reaction between the amide anion ( $\text{NH}_2^-$ ) and neutral formaldehyde ( $\text{H}_2\text{CO}$ ). The photoelectron spectrum of  $\text{H}_2\text{C}(\text{NH}_2)\text{O}^-$  obtained with a photon energy of 3.494 eV accesses the ground ( $\tilde{X}^2A'$ ) and first excited ( $\tilde{A}^2A''$ ) electronic states of the neutral aminomethoxy radical ( $\text{H}_2\text{C}(\text{NH}_2)\text{O}^\bullet$ ). The photoelectron spectrum accessing these two electronic states of  $\text{H}_2\text{C}(\text{NH}_2)\text{O}^-$  is broad, extending for approximately 1 eV. The extent of the progression indicates that there is a

large degree of geometry change between anion and neutral electronic states upon photodetachment. Higher resolution photoelectron spectra obtained using photon energies of 2.172 or 2.038 eV resolve vibrational transitions between anion ground state and neutral ground ( $\tilde{X}^2A'$ ) and excited ( $\tilde{A}^2A''$ ) electronic states. The high resolution photoelectron spectrum provides an experimental measurement of the electron affinity of aminomethoxy to be 1.944(5) eV) and the term energy to be 0.085(5) eV. Several vibrational assignments were made by a comparison between experimental and calculated spectrum, which exhibits strong Franck-Condon activity mainly in the OCN bending and HNH wagging vibrations of aminomethoxy. Some significant discrepancies between calculated and experimental peak intensity ratios were observed. Because of the small energy separation between the  $\tilde{X}^2A'$  and  $\tilde{A}^2A''$  states of aminomethoxy, and following a comparison with the ethoxy radical, it is suggested that not including vibronic coupling between these electronic states likely results in the observed disagreement between experiment and theory. A comparison between the term energies and photoelectron spectra of aminomethoxy and other singly substituted alkoxy radicals  $H_2C(R)O\cdot$ , ethoxy ( $R=CH_3$ ) and hydroxymethoxy ( $R=OH$ ) shows that aminomethoxy likely has more resemblance to ethoxy than with hydroxymethoxy, particularly with regard to their electronic structure. This difference is in part due to the strength of the electrostatic intramolecular interaction between the R group and oxygen atom, with  $CH_3$  being the weakest and OH strongest.

## 6.6 General Optimization Results

Table 6.1: Optimized structural parameters of  $\text{H}_2\text{C}(\text{NH}_2)\text{O}^-$  (CCSD(T)/aug-cc-pVTZ) and  $\text{H}_2\text{C}(\text{NH}_2)\text{O}$  in its ground (ROCCSD(T)/aug-cc-pVTZ) and excited (CAS(5,4)/aug-cc-pVTZ) states, together with the relative change in structural parameters with respect to the anion structure. The figure shows the atom connectivity and numbering in aminomethoxy.



Description of parameter	Anion ( $\tilde{X}^1A'$ )	Neutral ( $\tilde{X}^2A'$ )	% Change (Anion – Neutral $\tilde{X}$ )	Neutral ( $\tilde{A}^2A''$ )	% Change (Anion – Neutral $\tilde{A}$ )
$r_{\text{C-O}}$	1.332	1.377	3.38	1.439	8.03
$r_{\text{C-N}}$	1.528	1.444	-5.50	1.424	-6.81
$r_{\text{C-H1}}$	1.124	1.102	-1.96	1.081	-3.83
$r_{\text{C-H2}}$	1.124	1.102	-1.96	1.081	-3.83
$r_{\text{N-H3}}$	1.022	1.014	-0.78	0.997	-2.45
$r_{\text{N-H4}}$	1.022	1.014	-0.78	0.997	-2.45
$\angle_{\text{OCN}}$	115.15	118.406	2.83	109.292	-5.09
$\angle_{\text{OCH1}}$	114.808	106.501	-7.24	108.79	-5.24
$\angle_{\text{OCH2}}$	114.811	106.474	-7.26	108.828	-5.21
$\angle_{\text{NCH1}}$	102.794	110.154	7.16	112.243	9.19
$\angle_{\text{NCH2}}$	102.798	110.162	7.16	112.243	9.19
$\phi_{\text{H1CON}}$	118.764	123.757	4.20	120.063	1.09
$\phi_{\text{H2CON}}$	-118.765	-123.757	4.20	-120.082	1.11
$\phi_{\text{H3NCO}}$	52.796	58.969	11.69	61.743	16.95
$\phi_{\text{H4NCO}}$	-52.902	-59.016	11.56	-61.785	16.79

Table 6.2: Calculated (CCSD(T)/aug-cc-pVTZ) harmonic vibrational frequencies ( $\omega_i$ ) of  $\text{H}_2\text{C}(\text{NH}_2)\text{O}^- \tilde{X}^1A'$  and approximate description of the molecular motions associated with the normal modes. All values are given in wavenumbers ( $\text{cm}^{-1}$ ).

<b>Vibrational mode <math>\omega_i</math></b>	<b>Calculated frequencies (Anion, <math>\tilde{X}^1A'</math>)</b>	<b>Approximate description</b>	<b>Symmetry (<math>C_s</math> point group)</b>
15	276	HNH torsion	$A''$
14	475	OCN bend	$A'$
13	818	C–N stretch	$A'$
12	901	out of phase HNH + HCH twist	$A''$
11	1041	HNH wag (umbrella)	$A'$
10	1211	C–O stretch	$A'$
9	1221	HCH torsion	$A''$
8	1332	in phase HNH + HCH twist	$A''$
7	1361	HCH wag	$A'$
6	1464	HCH bend	$A'$
5	1631	HNH bend	$A'$
4	2657	HCH asym. stretch	$A''$
3	2699	HCH sym. stretch	$A''$
2	3396	HNH sym. stretch	$A'$
1	3463	HNH asym. stretch	$A''$

Table 6.3: Harmonic vibrational frequencies ( $\omega_i$ ) of  $\text{H}_2\text{C}(\text{NH}_2)\text{O}^*$ ,  $\tilde{X}^2A'$  (ROCCSD(T)/aug-cc-pVTZ) and approximate description of the molecular motions associated with the normal modes.

All values are given in wavenumbers ( $\text{cm}^{-1}$ ).

<b>Vibrational mode <math>\omega_i</math></b>	<b>Calculated frequencies (Neutral, <math>\tilde{X}^2A'</math>)</b>	<b>Approximate description</b>	<b>Symmetry (<math>C_s</math> point group)</b>
15	252	HNH torsion	$A''$
14	498	OCN bend	$A'$
13	666	HCH torsion	$A''$
12	847	HNH wag (umbrella)	$A'$
11	1002	C–O stretch	$A'$
10	1010	out of phase HNH + HCH twist	$A''$
9	1132	C–N stretch	$A'$
8	1344	HCH wag	$A'$
7	1350	in phase HNH + HCH twist	$A''$
6	1398	HCH bend	$A'$
5	1606	HNH bend	$A'$
4	2958	HCH sym. stretch	$A''$
3	2987	HCH asym. stretch	$A''$
2	3502	HNH sym. stretch	$A'$
1	3587	HNH asym. stretch	$A''$

Table 6.4: Harmonic vibrational frequencies ( $\omega_i$ ) of  $\text{H}_2\text{C}(\text{NH}_2)\text{O}^*$ ,  $\tilde{A}^2A''$  (CAS(5,4)/aug-cc-pVTZ) and approximate description of the molecular motions associated with the normal modes.

All values are given in wavenumbers ( $\text{cm}^{-1}$ ).

<b>Vibrational mode <math>\omega_i</math></b>	<b>Calculated frequencies</b> (Neutral, $\tilde{A}^2A''$ )	<b>Approximate description</b>	<b>Symmetry</b> ( $C_s$ point group)
15	416	HNH torsion	$A''$
14	442	OCN bend	$A'$
13	871	HNH wag (umbrella)	$A'$
12	1009	C–O stretch	$A'$
11	1020	out of phase HNH + HCH twist	$A''$
10	1195	C–N stretch	$A'$
9	1455	in phase HNH + HCH twist	$A''$
8	1497	HCH wag	$A'$
7	1654	HCH bend	$A'$
6	1801	HNH bend	$A'$
5	1930	HCH torsion	$A''$
4	3195	HCH sym. stretch	$A''$
3	3247	HCH asym. stretch	$A''$
2	3740	HNH sym. stretch	$A'$
1	3826	HNH asym. stretch	$A''$

Table 6.5: Calculated rotational constants for aminomethoxy: Anion  $\tilde{X}^1A'$  and neutral ground  $\tilde{X}^2A'$  (RCCSD(T)/aug-cc-pVTZ, RO for neutral) and neutral excited  $\tilde{A}^2A''$  (CAS(5,4)/aug-cc-pVTZ) .

All values are given in  $\text{cm}^{-1}$ .

Rotational Constants / $\text{cm}^{-1}$	Anion ( $\tilde{X}^1A'$ )	Neutral ( $\tilde{X}^2A'$ )	Neutral ( $\tilde{A}^2A''$ )
A	1.384	1.484	1.296
B	0.342	0.335	0.360
C	0.302	0.302	0.312

## 6.7 Chapter 6 references

- <sup>1</sup> J.J. Orlando, G.S. Tyndall, and T.J. Wallington, *Chem. Rev.* **103**, 4657 (2003).
- <sup>2</sup> R. Atkinson and W.P.L. Carter, *J. Atmos. Chem.* **13**, 195 (1991).
- <sup>3</sup> R. Atkinson, *Int. J. Chem. Kinet.* **29**, 99 (1997).
- <sup>4</sup> T.P.W. Jungkamp, J.N. Smith, and J.H. Seinfeld, *J. Phys. Chem. A* **101**, 4392 (1997).
- <sup>5</sup> A.C. Davis and J.S. Francisco, *J. Phys. Chem. A* **118**, 10982 (2014).
- <sup>6</sup> J.M. Simmie, G. Black, H.J. Curran, and J.P. Hinde, *J. Phys. Chem. A* **112**, 5010 (2008).
- <sup>7</sup> C. Fittschen, H. Hippler, and B. Viskolcz, *Phys. Chem. Chem. Phys.* **2**, 1677 (2000).
- <sup>8</sup> J.K. Kochi, *J. Am. Chem. Soc.* **84**, 1193 (1962).
- <sup>9</sup> A.C. Davis and J.S. Francisco, *J. Am. Chem. Soc.* **133**, 18208 (2011).
- <sup>10</sup> G. Vourliotakis, G. Skevis, and M.A. Founti, *Proc. Combust. Inst.* **35**, 437 (2015).
- <sup>11</sup> R. Grana, A. Frassoldati, T. Faravelli, U. Niemann, E. Ranzi, R. Seiser, R. Cattolica, and K. Seshadri, *Combust. Flame* **157**, 2137 (2010).
- <sup>12</sup> K.Y. Choo and S.W. Benson, *Int. J. Chem. Kinet.* **13**, 833 (1981).
- <sup>13</sup> A. Gao, Z. Jiao, and A. Li, *J. Mol. Struct. Theochem* **848**, 40 (2008).
- <sup>14</sup> T.M. Ramond, G.E. Davico, R.L. Schwartz, and W.C. Lineberger, *J. Chem. Phys.* **112**, 1158 (2000).
- <sup>15</sup> S.C. Foster, Y.C. Hsu, C.P. Damo, X. Liu, C.Y. Kung, and T.A. Miller, *J. Phys. Chem.* **90**, 6766 (1986).
- <sup>16</sup> B.B. Shen, B.L.J. Poad, and R.E. Continetti, *J. Phys. Chem. A* **118**, 10223 (2014).
- <sup>17</sup> D.R. Yarkony, *Chem. Rev.* **112**, 481 (2012).
- <sup>18</sup> M. Dupuis, J.J. Wendoloski, and W.A. Lester, *J. Chem. Phys.* **76**, 488 (1982).
- <sup>19</sup> G. Tarczay, S. Gopalakrishnan, and T.A. Miller, *J. Mol. Spectrosc.* **220**, 276 (2003).
- <sup>20</sup> C.C. Carter, J.R. Atwell, S. Gopalakrishnan, and T.A. Miller, *J. Phys. Chem. A* **104**, 9165 (2000).
- <sup>21</sup> S.D. Brossard, P.G. Carrick, E.L. Chappell, S.C. Hulegaard, and P.C. Engelking, *J. Chem. Phys.* **84**, 2459 (1986).
- <sup>22</sup> Y. Endo, S. Saito, and E. Hirota, *J. Chem. Phys.* **81**, 122 (1984).
- <sup>23</sup> G.B. Ellison, P.C. Engelking, and W.C. Lineberger, *J. Phys. Chem.* **86**, 4873 (1982).
- <sup>24</sup> S.C. Foster, P. Misra, T.Y.D. Lin, C.P. Damo, C.C. Carter, and T.A. Miller, *J. Phys. Chem.* **92**, 5914 (1988).

- <sup>25</sup> G. Inoue, H. Akimoto, and M. Okuda, *Chem. Phys. Lett.* **63**, 213 (1979).
- <sup>26</sup> G. Inoue, M. Okuda, and H. Akimoto, *J. Chem. Phys.* **75**, 2060 (1981).
- <sup>27</sup> S. Gopalakrishnan, L. Zu, and T.A. Miller, *Chem. Phys. Lett.* **380**, 749 (2003).
- <sup>28</sup> C.L. Malbon, D.R. Yarkony, and X.L. Zhu, *J. Mol. Spectrosc.* **311**, 36 (2015).
- <sup>29</sup> W. Domcke and D.R. Yarkony, *Annu. Rev. Phys. Chem.* **63**, 325 (2012).
- <sup>30</sup> U. Höper, P. Botschwina, and H. Köppel, *J. Chem. Phys.* **112**, 4132 (2000).
- <sup>31</sup> G.D. Bent, G.F. Adams, R.H. Bartram, G.D. Purvis, and R.J. Bartlett, *J. Chem. Phys.* **76**, 4144 (1982).
- <sup>32</sup> T.A. Barckholtz and T.A. Miller, *Int. Rev. Phys. Chem.* **17**, 435 (1998).
- <sup>33</sup> J.J. Liu, N.J. Reilly, A. Mason, and T.A. Miller, *J. Phys. Chem. A* **119**, 11804 (2015).
- <sup>34</sup> J.J. Liu, D. Melnik, and T.A. Miller, *J. Chem. Phys.* **139**, 94308 (2013).
- <sup>35</sup> J. Jin, I. Sioutis, G. Tarczay, S. Gopalakrishnan, A. Bezant, and T.A. Miller, *J. Chem. Phys.* **121**, 11780 (2004).
- <sup>36</sup> J. Alam, M.A. Reza, A. Mason, N.J. Reilly, and J.J. Liu, *J. Phys. Chem. A* **119**, 6257 (2015).
- <sup>37</sup> A.M. Oliveira, J.H. Lehman, A.B. McCoy, and W.C. Lineberger, *J. Chem. Phys.* **145**, 124317 (2016).
- <sup>38</sup> G. Danger, F. Duvernay, P. Theule, F. Borget, and T. Chiavassa, *Astrophys. J.* **756**, 11 (2012).
- <sup>39</sup> F. Duvernay, G. Danger, P. Theule, T. Chiavassa, and A. Rimola, *Astrophys. J.* **791**, 75 (2014).
- <sup>40</sup> M.T. Feldmann, S.L. Widicus, G.A. Blake, D.R. Kent IV, and W.A. Goddard III, *J. Chem. Phys.* **123**, 34304 (2005).
- <sup>41</sup> B.M. Hays and S.L. Widicus-Weaver, *J. Phys. Chem. A* **117**, 7142 (2013).
- <sup>42</sup> S.J. Blanksby and G.B. Ellison, *Acc. Chem. Res.* **36**, 255 (2003).
- <sup>43</sup> Y.-J. Lu, J.H. Lehman, and W.C. Lineberger, *J. Chem. Phys.* **142**, 44201 (2015).
- <sup>44</sup> H. Hotop and W.C. Lineberger, *J. Phys. Chem. Ref. Data* **14**, 731 (1985).
- <sup>45</sup> C. Blondel, W. Chaibi, C. Delsart, C. Drag, F. Goldfarb, and S. Kröger, *Eur. Phys. J. D - At. Mol. Opt. Plasma Phys.* **33**, 335 (2005).
- <sup>46</sup> G.B. Ellison, P.C. Engelking, and W.C. Lineberger, *J. Am. Chem. Soc.* **100**, 2556 (1978).
- <sup>47</sup> M.J. Travers, D.C. Cowles, E.P. Clifford, G.B. Ellison, and P.C. Engelking, *J. Chem. Phys.* **111**, 5349 (1999).
- <sup>48</sup> M.J. Frisch, G.W. Trucks, H.B. Schlegel, G.E. Scuseria, M.A. Robb, J.R. Cheeseman, G. Scalmani, V. Barone, B. Mennucci, G.A. Petersson, H. Nakatsuji, M. Caricato, X. Li, H.P. Hratchian, A.F. Izmaylov, J. Bloino, G. Zheng, J.L. Sonnenberg, M. Hada, M. Ehara, K. Toyota,

R. Fukuda, J. Hasegawa, M. Ishida, T. Nakajima, Y. Honda, O. Kitao, H. Nakai, T. Vreven, J.A. Montgomery Jr., J.E. Peralta, F. Ogliaro, M.J. Bearpark, J. Heyd, E.N. Brothers, K.N. Kudin, V.N. Staroverov, R. Kobayashi, J. Normand, K. Raghavachari, A.P. Rendell, J.C. Burant, S.S. Iyengar, J. Tomasi, M. Cossi, N. Rega, N.J. Millam, M. Klene, J.E. Knox, J.B. Cross, V. Bakken, C. Adamo, J. Jaramillo, R. Gomperts, R.E. Stratmann, O. Yazyev, A.J. Austin, R. Cammi, C. Pomelli, J.W. Ochterski, R.L. Martin, K. Morokuma, V.G. Zakrzewski, G.A. Voth, P. Salvador, J.J. Dannenberg, S. Dapprich, A.D. Daniels, Ö. Farkas, J.B. Foresman, J. V. Ortiz, J. Cioslowski, and D.J. Fox, Gaussian 09 Revision B.01, Gaussian Inc. Wallingford, CT (2009).

<sup>49</sup> H.J. Werner, P.J. Knowles, G. Knizia, F.R. Manby, and M. Schutz, *WIREs Comput. Mol. Sci.* **2**, 242 (2012).

<sup>50</sup> J.J. Dillon and D.R. Yarkony, *J. Chem. Phys.* **131**, 134303 (2009).

<sup>51</sup> J. Dillon and D.R. Yarkony, *J. Chem. Phys.* **137**, 154315 (2012).

<sup>52</sup> J.J. Dillon and D.R. Yarkony, *J. Chem. Phys.* **130**, 154312 (2009).

<sup>53</sup> V.A. Mozhayskiy and A.I. Krylov, ezSpectrum, available online at [iopshell.usc.edu/downloads/](http://iopshell.usc.edu/downloads/) (2016).

<sup>54</sup> A.M. Oliveira, J.H. Lehman, A.B. McCoy, and W.C. Lineberger, *J. Phys. Chem. A* **120**, 1652 (2016).

<sup>55</sup> C.T. Wickhamjones, K.M. Ervin, G.B. Ellison, and W.C. Lineberger, *J. Chem. Phys.* **91**, 2762 (1989).

<sup>56</sup> D.M. Neumark, K.R. Lykke, T. Andersen, and W.C. Lineberger, *Phys. Rev. A* **32**, 1890 (1985).

<sup>57</sup> M.L. Weichman, L. Cheng, J.B. Kim, J.F. Stanton, and D.M. Neumark, *J. Chem. Phys.* **146**, 224309 (2017).

<sup>58</sup> D.M. Neumark, *J. Phys. Chem. A* **112**, 13287 (2008).

<sup>59</sup> K.M. Ervin and V.F. DeTuro, *J. Phys. Chem. A* **106**, 9947 (2002).

<sup>60</sup> T. Su, E.C.F. Su, M.T. Bowers, S.D. Tanner, G.I. Mackay, and D.K. Bohme, *J. Chem. Phys.* **69**, 407 (1978).

<sup>61</sup> R.E. Rosenberg, *J. Org. Chem.* **73**, 6636 (2008).

<sup>62</sup> E.P. Wigner, *Phys. Rev.* **73**, 1002 (1948).

<sup>63</sup> D.J. Nelson, W.K. Gichuhi, E.M. Miller, J.H. Lehman, and W.C. Lineberger, *J. Chem. Phys.* **146**, 74302 (2017).

<sup>64</sup> D.M. Neumark, K.R. Lykke, T. Andersen, and W.C. Lineberger, *J. Chem. Phys.* **83**, 4364 (1985).

<sup>65</sup> M.L. Weichman, J.B. Kim, and D.M. Neumark, *J. Chem. Phys.* **140**, 104305 (2014).

<sup>66</sup> J.M. Weber, W.H. Robertson, and M.A. Johnson, *J. Chem. Phys.* **115**, 10718 (2001).

- <sup>67</sup> C.L. Adams, H. Schneider, and J.M. Weber, *J. Phys. Chem. A* **114**, 4017 (2010).
- <sup>68</sup> R.D. Mead, K.R. Lykke, W.C. Lineberger, J. Marks, and J.I. Brauman, *J. Chem. Phys.* **81**, 4883 (1984).
- <sup>69</sup> K.R. Lykke, R.D. Mead, and W.C. Lineberger, *Phys. Rev. Lett.* **52**, 2221 (1984).
- <sup>70</sup> L.S. Wang, *J. Chem. Phys.* **143**, 40901 (2015).
- <sup>71</sup> K.R. Lykke, D.M. Neumark, T. Andersen, V.J. Trapa, and W.C. Lineberger, *J. Chem. Phys.* **87**, 6842 (1987).
- <sup>72</sup> K.A. Peterson, D. Feller, and D.A. Dixon, *Theor. Chem. Acc.* **131**, 1079 (2012).
- <sup>73</sup> U.D. Jentschura, S. Kotochigova, E.O. LeBigot, P.J. Mohr, and B.N. Taylor, *The Energy Levels of Hydrogen and Deuterium (Version 2.1)*, National Institute of Standards and Technology, Gaithersburg, MD, available online at [physics.nist.gov/PhysRefData/HDEL/energies.html](http://physics.nist.gov/PhysRefData/HDEL/energies.html), 2017.

## CHAPTER VII

### PHOTOELECTRON SPECTROSCOPY OF 7-AZAINDOLIDE AND 7-AZAINDOLE DIMER ANIONS

#### 7.1 Introduction

Indoles and related species are ubiquitous molecules in biological processes. The photoelectron spectrum of indolide, or deprotonated indole, was recently investigated by our group.<sup>1</sup> A summary of such experiments, showing the overview low resolution spectrum obtained with a photon energy of 3.494 eV, and a high resolution magnification of the peak attributed to the EA of the associated indolyl radical, obtained with a photon energy of 2.4500 eV, are displayed in Fig. 7.1. The overview low resolution photoelectron spectrum showed an extended progression that is well captured by calculation. The use of the SEVI technique (see Chapter 2), where only slow electrons are detected, significantly narrows the lowest eBE peak (gray shaded area) which is dominated by the origin transition (bold stick in the calculate spectrum). This results in a high precision measurement ( $\pm 1.7$  meV) of the EA of the indolyl radical, as discussed in Ref. 1. In this chapter, we investigate the analogous 7-azaindolidide, which differs from indolide by a single substitution of a C-H group for an N atom, as depicted in Scheme 7.1 below. In this chapter we conduct similar experiments the ones reported in Ref.1 for the analogous species 7-azaindolidide.

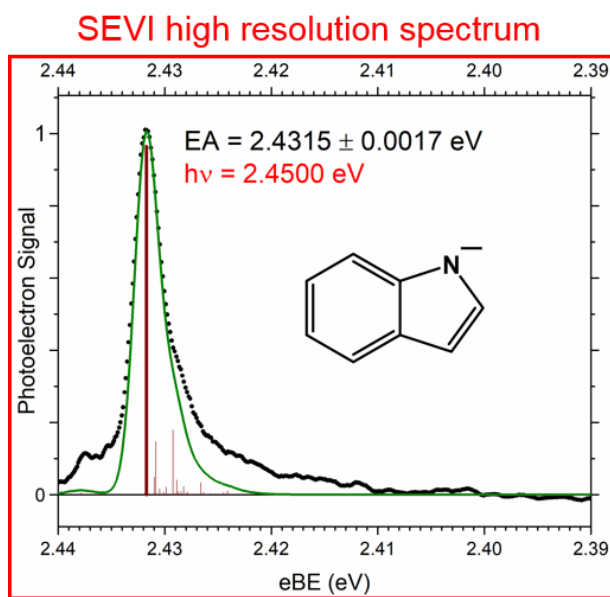
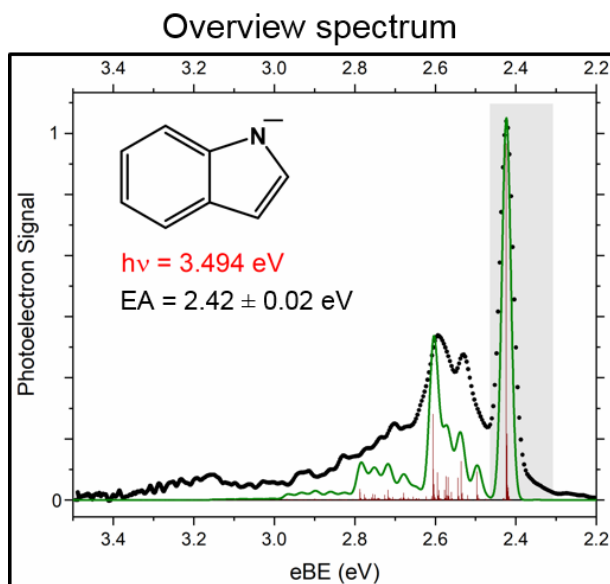
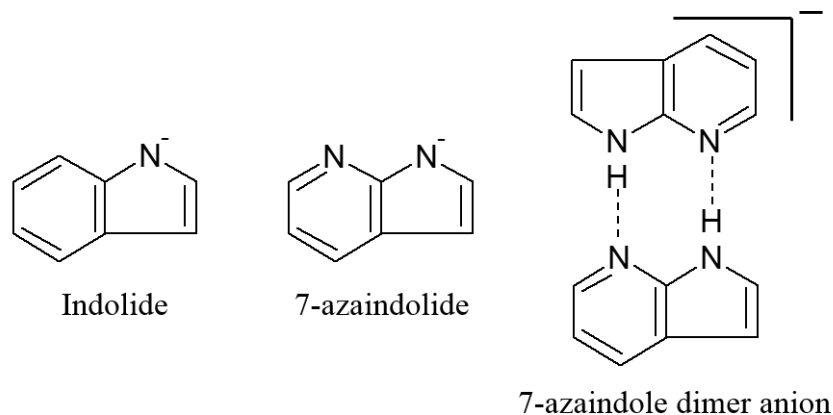


Figure 7.1: Photoelectron spectrum of indolide reproduced from Nelson *et al.*<sup>1</sup> with some modifications. The calculated transitions and their associated intensities are represented by red sticks, while the convolution of these sticks with Gaussian functions whose *fwhm* is commensurate with the instrument resolution is shown in green. This simulation assumed a temperature of 200 K. The shaded region was also obtained in high resolution, as shown in the lower panel.



Scheme 7.1: Chemical structures of indolide, 7-azaindolide and the 7-azaindole dimer anion.

7-azaindole is a heterocyclic aromatic molecule which has attracted attention from the scientific community due to its analogous structure to nucleobases.<sup>2-9</sup> The interest in studying 7-azaindole arise primarily from its ability to form a stable dimer via hydrogen bonding (see Scheme 7.1).<sup>2-6,10-13</sup> Thus, over the past 40 years,<sup>8,14-16</sup> 7-azaindole has been utilized as a model system for Watson-Crick nucleobases due to its similar pairing mechanism.<sup>3,4,7,14,16-20</sup>

Similarly to a DNA base pair, 7-azaindole is involved in excited state double proton transfer within the dimer.<sup>3,4,10,14,21-24</sup> Therefore, understanding the double proton transfer mechanism has been the target of many spectroscopic studies in both condensed<sup>3,8,10,16,17,25-29</sup> and gas phases.<sup>12,21,30-34</sup> In the studies by the groups of Zewail<sup>2-4</sup> and Castleman,<sup>35,36</sup> the proton transfer was described by a stepwise mechanism, with a zwitterionic pair as an intermediate. Other groups claim the double proton transfer is concerted, happening in one single step.<sup>21,37,38</sup> Although the dimer has been thoroughly studied, there is still a debate on the proton transfer mechanism.<sup>5,38-42</sup> This ongoing debate motivates a continued investigation of the fundamental properties of this molecule.

Because of the importance of this molecule and, in particular, the coordinates wherein the proton transfer takes place, a study of isolated 7-azaindole should be illuminating. To achieve this study, anion photoelectron spectroscopy is an attractive technique, since it can determine the electron affinity (EA) of the corresponding 7-azaindoyl radical. From this measurement, the gas phase acidity,  $\Delta_{\text{acid}}\text{H}^0(\text{N-H})$ , or the N-H bond dissociation energy,  $D_0(\text{N-H})$ , of 7-azaindole can be obtained *via* a thermochemical cycle.<sup>43</sup> While there has been a previous anion photoelectron study by Nakajima *et al.*,<sup>30</sup> only low resolution anion photoelectron spectra of clusters of 7-azaindole anion with 7-azaindole were investigated and, thus, the aforementioned properties could not be deduced.

This chapter presents the first photoelectron spectroscopic investigation of 7-azaindolidide, with interpretation aided by quantum chemical calculations. This study provides a measurement of the EA of 7-azaindoyl together with some unexpected results on the electronic structure of this species and its corresponding anion. An analysis of the structure and properties of 7-azaindoyl is presented and is based on a comparison with the analogous indoyl, recently investigated by our group.<sup>1</sup> The EA of the 7-azaindole dimer was measured previously, but in low resolution.<sup>30</sup> This presents an opportunity for improving the accuracy of this measurement, as our instrument allows for *i*) formation of ions that are internally colder and *ii*) higher resolution when employing the measurement of slow electrons, when compared to the previous study. Thus, we also revisit the photoelectron spectroscopy of the 7-azaindole dimer anion.

## 7.2 Methods

### 7.2.a Experimental

The photoelectron spectra of 7-azaindolidide and  $(7\text{-azaindole})_2^-$  are acquired in the instrument described in detail in Chapter 2. In this chapter we will solely describe the procedures which are specific to the generation of 7-azaindolidide and  $(7\text{-azaindole})_2^-$ , as well as describing the wavelengths utilized for the acquisition of the photoelectron spectra reported here.

The production of 7-azaindolidide and  $(7\text{-azaindole})_2^-$  is achieved by using a mixture of 15 psi-gauge, ~1% 7-azaindole, balance argon, in the main expansion (see section 2.1.b) and the frequently used mixture (35 psi-gauge, 1% O<sub>2</sub>, 30% H<sub>2</sub>, balance Ar) for the generation of OH<sup>-</sup> anions, *via* a pulsed discharge (-2000 V, ~150 μs). The 7-azaindole sample (98%, Sigma-Aldrich), utilized without further purification, is introduced in the main expansion by flowing 15 psi-gauge of argon gas over the 7-azaindole sample. Due to the low vapor pressure of 7-azaindole at room temperature, the sample is heated to approximately 116 °C in order to attain the desired 7-azaindole partial pressure in the main expansion. In order to minimize condensation of 7-azaindole in the main valve, we heat the valve body to ~70 °C by way of an aluminum block equipped with a resistive heater, which is thermally insulated from the chamber and surrounds the main valve body with low clearance, as described in section 2.1.b. This discharge successfully generates the hydroxide anion (OH<sup>-</sup>), and with appropriate timing of the gas pulses of the main and side valves, the two expansions are overlapped and the anions in the side expansion are allowed to react with the neutral reagents in the main expansion. The 7-azaindolidide anion is generated from the deprotonation of 7-azaindole by OH<sup>-</sup>. The resulting mass spectrum from this ion generation procedure is displayed below in Fig. 7.2.

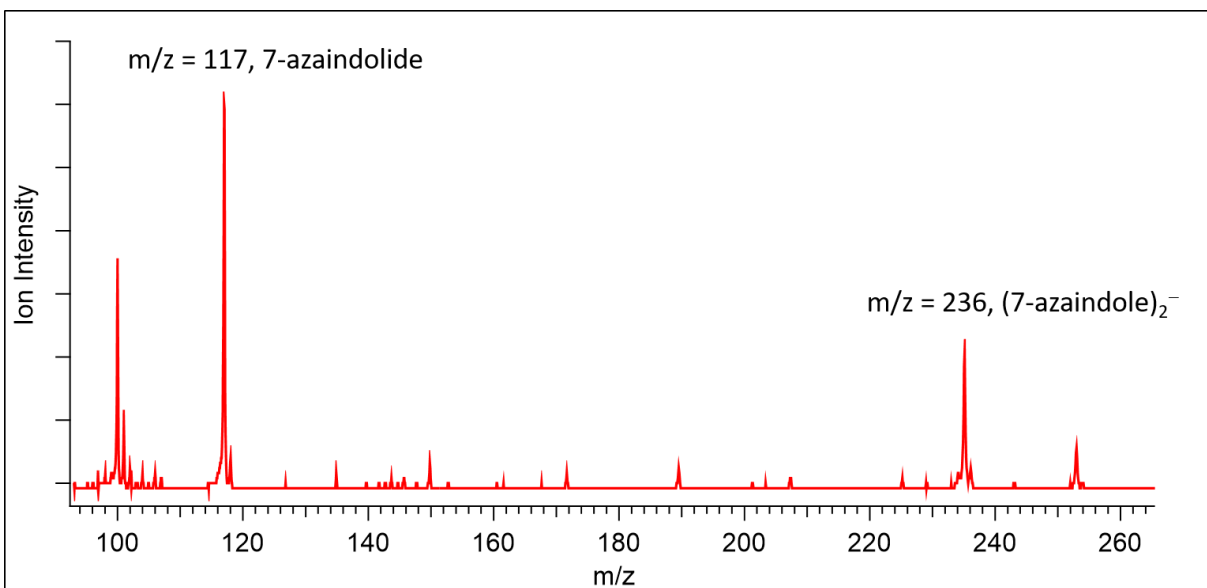


Figure 7.2: Resulting mass spectrum from ion generation procedure described in section 7.2.a.

The displayed range of mass units shows the production of 7-azaindolide and (7-azaindole)<sub>2</sub><sup>-</sup>.

The other major peak in this spectrum, at m/z = 100, represents the CrO<sub>3</sub><sup>-</sup> anion, which is always produced in this ion source when discharging an oxidizing mixture through stainless steel electrodes.

In order to take advantage of the eKE-dependent resolution of the VMI (see section 2.1.e.), we utilize a collection of wavelengths to obtain photoelectron spectra. Generally, our laser source is based on a seeded Nd:YAG laser, which outputs 1064 nm light, utilized for acquiring the high-resolution spectrum of 7-azaindole dimer. For the overview spectrum presented in Fig. 7.3, we utilize the third harmonic of the Nd:YAG laser (355.4 nm). For the higher resolution spectra of 7-azaindole, we employ a 355.4 nm pumped dye laser (Quanta-Ray, PDL 1) equipped with either Coumarin 440 or Coumarin 460 dyes. The laser is focused into the interaction region with the ions with a 0.5 m focal length lens.

For the overview spectra presented in this work, the eKE scale is calibrated utilizing the known photoelectron spectrum of sulfur anion ( $S^-$ ), which provides the magnification factor (correspondence between pixel on the CCD and electron speed) of the VMI at a particular operational setting. The spectra obtained with the dye laser are calibrated based on the magnification obtained observing the shift of an individual peak in the spectrum of 7-azaindole when employing different photon energies, which in turn are measured with a wavemeter (ATOS  $\lambda$ -meter, LRL-005).

The uncertainties in the measurements in this experiment result from a combination of the uncertainties in the energy scale calibration, an unresolved rotational contour<sup>44,45</sup> and the statistical error in the peak centering from the fitting of a Gaussian function to each peak. In addition, due to unresolved vibrational hot bands and sequence bands, it is possible that a peak's maximum position does not correspond to the actual individual transition that would be observed in a cold spectrum where only the vibronic ground state of the anion is populated. The accuracy of the assignment thus depends on calculated spectrum. Depending on the number of predicted transitions under an observed peak, the uncertainty of the measurement can take different values.

For example, if the calculation predicts the origin transition as dominant, as happens to be the case in Fig. 7.2, the uncertainty in finding the eBE of the center of the peak is essentially the statistical error in fitting the peak to a line shape function. The total uncertainty of the measurement is almost completely due to the uncertainty in the energy scale calibration (see Chapter 2). In the case that many transitions of similar magnitude are responsible for a peak's intensity, the true cold transition can, therefore, be located somewhere within a peak's *fwhm*. In this particular work, for reasons that will become clear in section 7.3, we report our measurements as a peak's center position  $\pm fwhm/2$  from a Gaussian fit to the line shape of each peak.

### 7.2.b Theoretical

The assignments in the photoelectron spectra reported here rely in part on a comparison with calculations of simulated spectra, which are described in this section. Electronic structure calculations are performed primarily using the Gaussian 09 suite of programs.<sup>46</sup> These calculations consist of geometry optimization and normal mode calculations of the 7-azaindolidine anion and 7-azaindolyl radical, utilizing the B3LYP/aug-cc-pVTZ method/basis set,<sup>47,48</sup> and calculation of excitation energies with TD-B3LYP, also in the Gaussian 09 suite. With the normal-mode displacement vectors and vibrational frequency outputs of the *ab-initio* calculations as inputs, we utilize the PESCAL program<sup>49,50</sup> to generate simulated photoelectron spectra. By employing the Sharp-Rosenstock-Chen method with Duschinsky rotations, PESCAL generates a spectrum of Franck-Condon (FC) factors which represent transitions from the anion electronic and vibrational ground state to vibrational states of the neutral state. PESCAL also includes the calculation of vibrational hot-bands and sequence bands, transitions that originate from excited vibrational states of the anionic electronic ground state, by obtaining the pertinent

FC factor and scaling the transitions by the appropriate Boltzmann factor at a set vibrational temperature. Here, we calculate hot-band populations at a temperature of 300 K, a temperature which is 100 K higher than our previous choice with this anion source,<sup>51,52</sup> but reasonable when we consider that our sample, gas lines and main valve body are on average heated to approximately 100 °C (or 373 K). While this is a conservative estimate of how cold the expansion is, as a comparison between experiment and calculation will show, we are not able to quantify the vibrational temperature of the ions, and 300 K is a reasonable upper limit, based on peak widths and intensities of hot and sequence band transitions. In order to provide a direct comparison between calculated and experimental spectra, the individual FC factors are then convolved with Gaussian functions whose *fwhm* is set to the eKE-dependent instrumental resolution and whose areas are equal to that of the calculated FC factor.

## 7.3 Results and Discussion

### 7.3.a Overview spectrum of 7-azaindolidide

The preliminary analysis of the overview spectrum of 7-azaindolidide begins with a comparison with the previously studied indolidide.<sup>1</sup> The photoelectron spectrum of indolidide, presents a convenient predictive model for 7-azaindole, since the only difference between the structure of 7-azaindolidide and indolidide is an isoelectronic substitution of an N atom for a C–H group. In the photoelectron spectrum of indolidide (upper panel, Fig. 7.1), most of the observed vibrational activity is in ring distortion modes, a consequence of the geometry change between the indolidide anion and indolyl neutral radical equilibrium structures. The EA of indolyl was found to be 2.4315(17) eV, measured in high resolution (see lower panel of Fig 7.1). Based on the relation between 7-azaindolidide and indolidide, we expect that 7-azaindolidide will behave in a very similar manner. Therefore, it is reasonable to expect that ring distortion vibrations would be

responsible for the vibrational activity in the photoelectron spectrum of 7-azaindole and that the EA of 7-azaindolyl would be of a similar magnitude, with a vibrational origin transition located at  $\sim 2.5$  eV. The analysis of the spectrum in the subsequent paragraphs will confirm the aforementioned expectations. In addition, the calculation of the simulated overview photoelectron spectrum of 7-azaindole provides quantitative agreement with the experimental data accessing the ground electronic state of 7-azaindolyl.

The overview photoelectron spectrum of 7-azaindole obtained with a photon energy of 3.494 eV is displayed in Fig. 7.3. Upon first analysis, we see that the photoelectron spectrum has an intense origin transition, located approximately around an eBE of 2.7 eV and a first group of peaks, spanning from 2.75 to 2.90 eV eBE. The spectrum becomes increasingly more congested above this eBE showing a second broad progression which spans all the way to 3.494 eV eBE. Upon comparing the spectra of indole (Fig. 7.2) to that of 7-azaindole (Fig. 7.3) one sees remarkable similarity. The photoelectron spectra span approximately the same range of eBEs and have a very similar overall shape. The 7-azaindole spectrum is more congested than the spectrum of indole in the high eBE range (above 2.9 eV), but not at the origin. This seems to indicate that there is a greater extent of geometry change upon photodetachment in 7-azaindole. However, the overall similarity between spectra suggests that our expectations described above are reasonably correct.

In order to analyze the photoelectron spectrum in Fig. 7.3, and assign the EA of 7-azaindolyl we bring attention to the calculated spectrum, also shown in this figure as the red sticks and the blue trace. This calculated spectrum was shifted so that its origin transition matched the position of the lowest eBE peak, the EA of 7-azaindolyl. The calculation has acceptable agreement with the experiment, which allows us to assign the peaks corresponding to

the EA of the ground state and some of the observed peaks with reasonable confidence. By a comparison between experiment and calculation, we observe the lowest eBE transition at  $\sim 2.68$  eV. The EA of 7-azaindoyl can thus be assigned as the eBE value of the center of the origin peak, which is obtained by fitting the observed peak with a Gaussian function. From the quality of the fit of the origin peak using a Gaussian function, we can infer that it is likely dominated by a single vibrational transition, namely the transition from the ground vibrational state of the anion to the ground vibrational state of the neutral. However, the *fwhm* of this peak of 38 meV is larger than expected (24 meV at 0.804 eV eKE, see Chapter 2), which indicates that more transitions are responsible for its intensity and width. The calculation corroborates the observations, as it shows the vibrational origin as the dominant transition under the peak and other hot and sequence band transitions which are a factor of at least five smaller than the origin. Consequently, we can assign the eBE of the center of this peak as the EA of 7-azaindoyl, which is 2.69(1) eV, using a conservative uncertainty based on the *fwhm* of the peak.

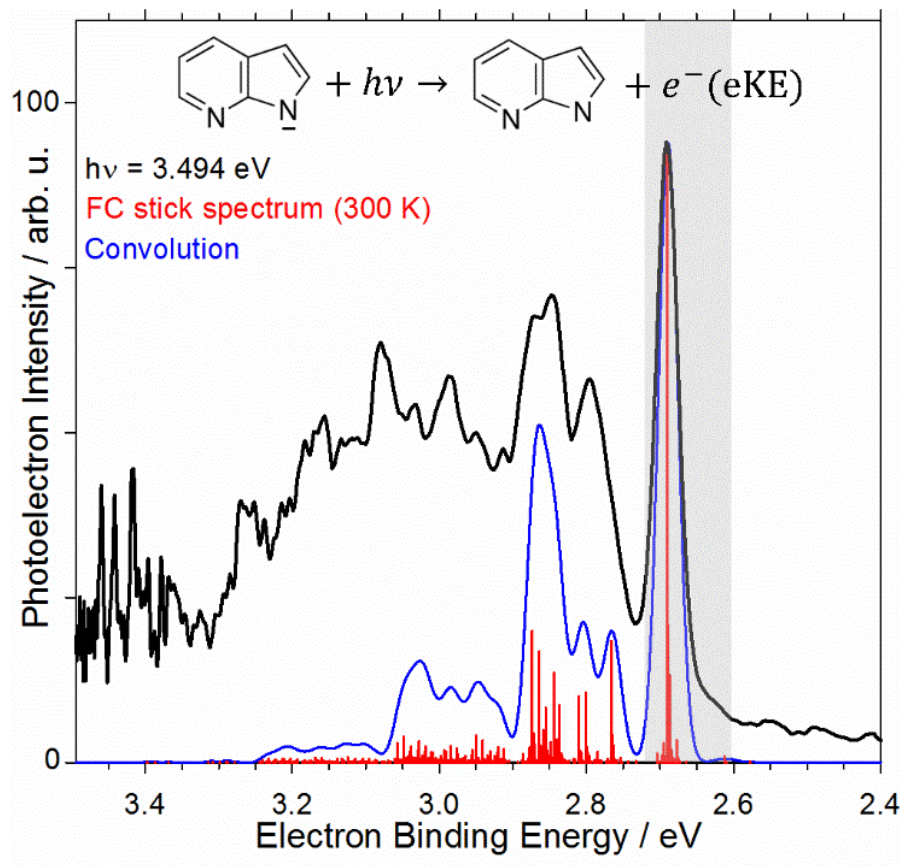


Figure 7.3: Overview photoelectron spectrum of the 7-azaindole anion obtained with a photon energy 3.494 eV (black trace) accessing the ground electronic state of 7-azaindoly. The calculated photoelectron spectrum is presented as red sticks (FC factors), while the blue trace is the convolution of these sticks as described in the text. The gray shaded region represents the region of the spectrum that will be investigated in higher resolution, which is shown in Figs. 7.4 and 7.5.

A preliminary vibrational analysis of the spectrum can also be extracted from the comparison between experiment and theory. The calculation confirms that the observed peaks are due to vibrational activity in ring distortion modes, consistent with our expectations from the photoelectron spectrum of indolide. The reasonable agreement between experiment and calculation quickly ceases to be true, when we move above 2.9 eV eBE. More prominent disagreements between theory and experiment appear in the region above 2.9 eV eBE, and the agreement gets progressively worse when we move to higher eBEs. Some degree of disagreement between calculation and experiment is expected at higher eBE (relative to the origin transition) due to the increasing contribution of anharmonic effects and number of active combination bands, leading to a high degree of spectral congestion. As mentioned in section 7.2, the calculation of the photoelectron spectrum employs the harmonic oscillator approximation. Therefore, it is not surprising that it fails when trying to reproduce features far from the vibrational origin transition. A further vibrational analysis with proper assignments is not possible with this experimental resolution, and thus the application of a lower photon energy is necessary. Such experiments would require the use of a wavelength of  $\sim 430$  nm, which is unfortunately out of the range of tunable wavelengths that we have available. For this reason, and reasons that will become clear later in the chapter, we will not provide a detailed vibrational analysis beyond the qualitative description done in this paragraph.

### *7.3.b High resolution photoelectron spectra of 7-azaindolide*

To obtain a more accurate measurement of the EA of 7-azaindolyl, we take advantage of the eKE-dependent resolution of the VMI by employing a photon energy close to the photodetachment threshold. This approach is the same as that followed for indolide, as depicted in the lower panel of Fig 7.2, where the origin transition is observed and the EA transition

measured to an accuracy of  $\pm 1.7$  meV. We expect to attain a similar precision with this procedure for 7-azaindole, based upon the simulation presented in Fig. 7.3, which shows that the peak is dominated by the origin transition. Specifically, we employ a photon energy of 2.719 eV and detect electrons whose eBEs correspond to the range depicted as the gray shaded area of Fig. 7.3 (0.119 eV). Based on previous experience with this instrument, we can expect a roughly constant resolution over this energy range, which is, conservatively,  $\leq 4$  meV. In order to form our expectations about the appearance of the resulting spectrum, we magnified the gray shaded area of Fig. 7.3 and displayed it in Fig. 7.4. We thus infer that, with a 4 meV resolution, we would observe a strong peak corresponding primarily to the EA of 7-azaindolyl, and a couple of low intensity side bands, corresponding to hot and sequence bands. Thus, a high resolution spectrum should be able to provide an accurate measurement of the EA of 7-azaindolyl. Note that the widths of the simulation also preclude additional peaks outside of the shaded region

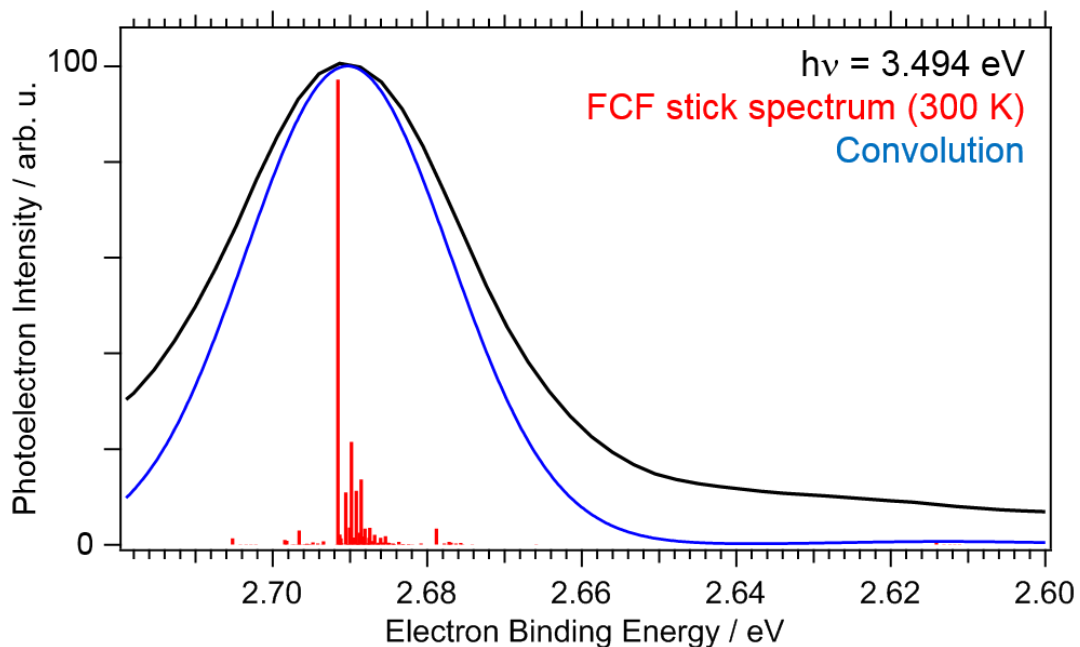


Figure 7.4: Comparison between the experimental low resolution overview spectrum of 7-azaindolidide (black trace) and calculated spectrum (red sticks). The calculated sticks and shifted are convolved with Gaussian functions (blue trace) whose *fwhm* are equivalent to the expected resolution. The spectrum is displayed over the range of eBE which corresponds to the gray shaded area in Fig. 7.3.

For a precise determination of the EA of 7-azaindolyl we obtain a photoelectron spectrum employing the SEVI technique.<sup>53</sup> With a photon energy of 2.719 eV, which is slightly above the expected detachment threshold (2.69(1) eV, based on Figs. 7.3 and 7.4), we collect the spectrum presented in Fig. 7.5 (green trace). In Fig. 7.5, the eBE axis spans a range of 0.119 eV (from 2.719 eV to 2.600 eV), and corresponds to the same magnified region as shown in Fig. 7.4. The first striking observation we draw from Fig. 7.5 is that five peaks of roughly the same intensity are observed in the spectrum, which is very different from our expectation of one major peak with possible small side bands (Fig. 7.4). This observation suggests that this could be a result of the much higher resolution we attain at this eKE. However, if we contrast the observed spectrum with the FCF calculation we see essentially no equivalence. More importantly, when comparing the spectra in Fig. 7.4 with that in Fig. 7.5, we see that the peaks in the high resolution spectrum span a considerably broader range of widths than what is expected based on the low resolution spectrum. As the blue circle and double headed arrow indicate, the measured EA, obtained from the lowest eBE peak in Fig. 7.3, can be attributed to peaks “A” or  $\gamma$ , but there are three other peaks that are considerably outside the range of expected transitions based on both the calculation and the low resolution experiment (Fig. 7.3). From this figure, it is evident that the spectrum resulting from photodetachment with 2.719 eV photons is not equivalent to the overview spectrum acquired with 3.494 eV photon energy, even though they were acquired under the same experimental conditions. Thus, it is not possible to precisely assign the EA of 7-azaindolyl at this stage.

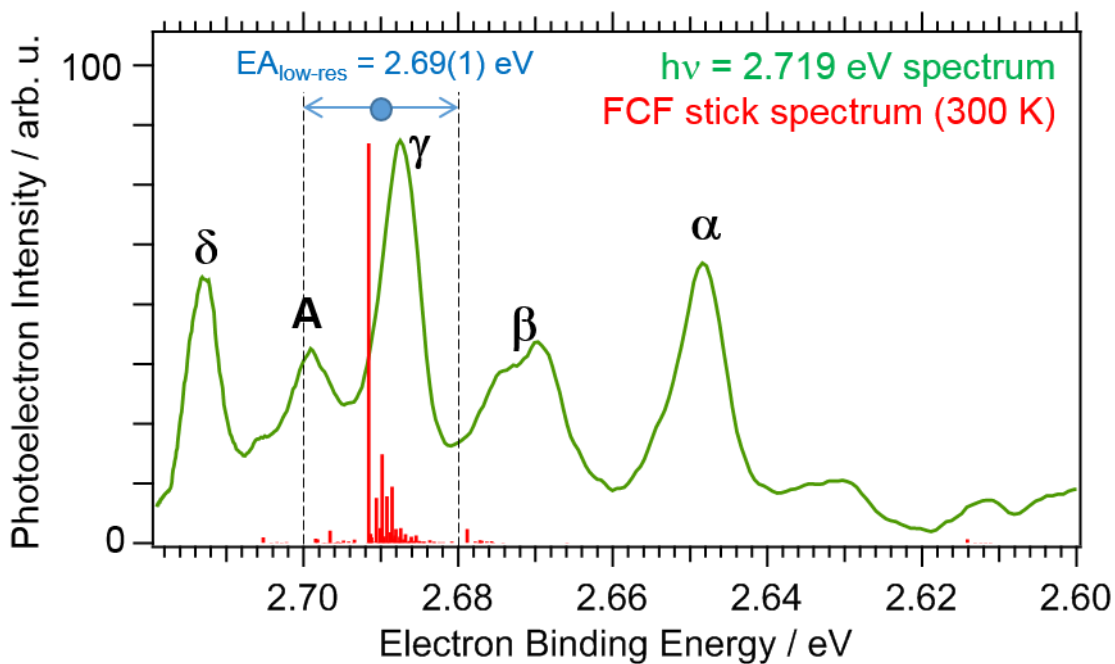


Figure 7.5: Photoelectron spectrum of 7-azaindole acquired with a photon energy of 2.719 eV and calculated FCF stick spectrum (red sticks). The eBE axis spans a range of 0.119 eV, and corresponds to the same magnified region as shown in Figs. 7.3 and 7.4. The peak letter labels are discussed in the text. The double headed blue arrow represents the low-resolution measurement of the EA of 7-azaindoly and the corresponding uncertainty.

There are several possibilities that could explain the difference between the spectra presented in Figs. 7.4 and 7.5. The most obvious explanation for this is that the two spectra are different simply due to different experimental conditions, leading to the production of a different molecule of the same  $m/z$ , such as an isomer of 7-azaindolid. This possibility must be discarded since, upon this observation, we acquired spectra with these two wavelengths (3.494 eV and 2.719 eV) consecutively, employing the same experimental conditions. We also followed this procedure on at least three different days and the same result was recovered. The second option to explain this phenomenon is that in the 3.494 eV spectrum, due to the larger photon flux attainable and employed at this wavelength, a sequential photon absorption could lead to the observed discrepancy. This possibility must also be discarded, since lower light intensities were used (not shown here) and the same result is again recovered. Finally, an explanation could derive from a photon energy dependent effect, where the photodetachment cross section is changing with photon energy. The photodetachment cross sections can vary due to the threshold effect, especially when close to threshold, as described by the Wigner threshold law (see section 1.2). As the subsequent analysis will show, none of the aforementioned phenomena are able to explain the photon energy dependence observed for 7-azaindolid. This leaves one plausible explanation, which is that of electron autodetachment and, as the following analysis will show, is likely the cause for the observations here.

Electron autodetachment is a phenomenon different than direct photodetachment as it occurs through an initial photon absorption by the anion, raising it to an anion excited state which is close in energy to a neutral state. The excited anionic state then couples to the neutral state's electronic manifold with subsequent release of the electron. The detachment probability in this case is a function of the photon energy, since the different anion states that are initially

accessed each have a distinct absorption cross section. Therefore, instead of the transition intensity being well described by the FC factor between anion and neutral vibrational wavefunctions, now the transition intensity derives from the overlap between the anion ground state wavefunction and the anion excited state wavefunction. The nature of the electron autodetaching state can be diverse, depending on the strength of the coupling of the anion state to the electron continuum. Electron autodetachment can occur if the anion is first raised to an electronic excited state, where the vibrations of this state are well defined. The initial transition thus takes place in a similar way to that of absorption spectroscopy, a bound to bound transition, following the appropriate selection rules. This state, when nearly degenerate with the neutral electronic state, can couple to this surface and the free electron continuum. This process was rigorously described for atoms in Refs. 54–56. Another form of electron autodetachment is that of vibrational autodetachment, where an excited vibrational state of the anion is close to or above the detachment energy. By way of intramolecular energy redistribution, this above threshold state can live for some period of time with subsequent detachment forming the lower energy neutral molecule. This scenario normally happens when the EA of the neutral is on the order of a few vibrational energy spacings ( $\sim 10^3 \text{ cm}^{-1}$ ). For examples such as this one see Ref. 57 and references within. Electron autodetachment can also be due to a dipole bound state,<sup>58–61</sup> wherein the electron is first excited to a very large orbit of the anion and, at that point, is essentially only bound to the neutral molecule *via* the long range dipole interaction ( $V(r) \sim 1/r^2$ ). That is, the electron is bound to the permanent dipole of the neutral. This type of electron autodetachment is possible when the permanent dipole of the neutral molecule is  $\sim 2$  Debye or larger.<sup>55,62,63</sup> Regardless of the form, the autodetachment cross section should be very sensitive to photon energy. Examples of the photon energy dependence of the autodetachment features can be seen

in the photoelectron spectrum of methylphenoxide<sup>51</sup> and indolide,<sup>1</sup> recently published by our group, in addition to numerous other references.<sup>57–60,62,64,65</sup> An investigation of the photon energy dependence of the photoelectron spectrum will reveal whether or not electron autodetachment is a probable explanation and provide insight on the nature of the autodetaching state.

In order to further investigate the photon energy dependence of the spectrum, we obtain spectra with a collection of photon energies, which are specified in Fig. 7.6. We expect that the peaks that are due to autodetachment will have their intensities significantly altered. Presumably, a change in peak intensities will occur for all peaks with the exception of those which are due to direct photodetachment. By using a slightly lower photon energy of 2.699 eV (panel (b)), we observe four peaks. Upon closer inspection we notice that these four peaks seem to be the same peaks as the ones in panel (c), with the exception of the peak centered at 2.699 eV eBE (peak A). If we use a slightly higher photon energy of 2.739 eV, similar peaks are recovered, with an apparent new peak, also centered at 2.699 eV eBE, now in a different position relative to the other peaks. This observation indicates that there is one transition which remains centered at 2.699 eV eBE, while the other four peaks (labeled with Greek letters) are shifting in eBE by an amount that is equal to the photon energy difference between spectra. Panels (e) and (f) continue to show similar four peaks that are shifting in eBE while also displaying a new broad peak that also shifts in eBE but whose intensity and shape changes. The peak centered at 2.699 eV, however, still remains in the same position and with similar intensity. To more clearly illustrate the invariance with respect to photon energy of certain peaks in the spectrum, we have plotted a selected number of these spectra as a function of eKE in Fig. 7.7. The vertical dashed blue lines correspond to the center of each of the peaks. One can notice that four peaks labeled with Greek letters are invariant regardless of the photon energy utilized, *i.e.* their centers remain in the same

position and their intensities and widths are roughly identical. We shall describe these peaks as “eKE-invariant peaks” from this point forward in the chapter. In order to comprehend what is occurring in this experiment we should go back to the conservation law described in equation 1.2 in Chapter 1:  $eKE = h\nu - eBE$ , which is true for a photodetachment event. Given that the vibrational eigenvalues of the anion and neutral states are immutable, a change in photon energy must accompany a change in eKE in order to preserve energy conservation if these peaks are in fact due to direct photodetachment. The experimental observations, however, show that this is simply not the case, and thus transitions must indeed be due to electron autodetachment. It should be noted that another method for identifying autodetaching features is by analyzing the anisotropy parameters of the peaks, but unfortunately, an analysis of the anisotropy of the peaks in Figs. 7.5 and 7.6 showed all features with  $\beta \sim 0$ , which is expected for detachment close to threshold. This prevents us from distinguishing between peaks that are due to direct photodetachment and electron autodetachment. The unexpected result from this experiment requires further analysis, but for continuing the discussion of the photon energy dependence of the photoelectron spectrum, we must first proceed with the assignment of the EA of 7-azaindoyl.

The EA of 7-azaindoyl can be obtained accurately and some tentative vibrational assignments may be made, in spite of the complication of interpreting the spectrum. By definition, the EA of an atom or molecule is the energy difference between the generalized ground state of the anion to the generalized ground state of the neutral. Therefore, the lowest eBE peak that is observed due to direct photodetachment can be assigned as the EA of 7-azaindoyl. Such peak is labeled “A” marked with the vertical blue dashed line in Fig. 7.6 and as the downward pointing green arrow in Fig. 7.7. From the center position of this peak (A) and its measured *fwhm* we determine the EA of 7-azaindoyl as 2.699(2) eV. This measured value is in

close agreement with our calculation (2.642 eV, B3LYP/aug-cc-pVTZ) and certainly within the uncertainty preliminary assignment of the EA in the overview spectrum (2.69(1) eV). In addition, the four eKE-invariant peaks must be due to an active vibration of neutral 7-azaindoly. From comparison between the spacing between the peaks of  $\sim 0.02$  eV ( $\sim 160$  cm<sup>-1</sup>) and our harmonic vibrational calculation, there are four normal modes that could be attributed to peaks  $\alpha$  through  $\gamma$ , all of which are out-of-plane ring bending vibrations. These vibrations should normally be symmetry forbidden. However, the autodetachment selection rules are different than those of direct photodetachment,<sup>59,66</sup> so normally FC forbidden transitions might be observed if they are due to autodetachment. From the attribution of the eKE-invariant peaks to autodetachment, it is possible that they represent the symmetry forbidden, out-of-plane ring bending vibrations.

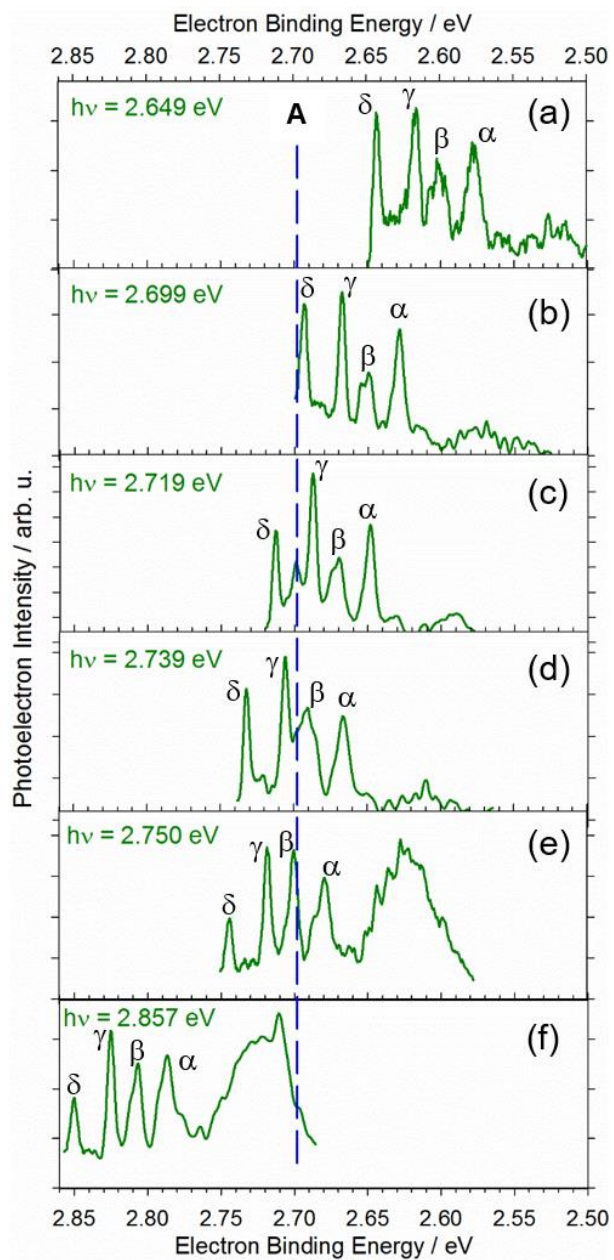


Figure 7.6: Compiled photoelectron spectra of 7-azaindole acquired with various photon energies plotted as a function of electron Binding Energy (eBE). The dashed blue line indicates the origin transition that originates from direct photodetachment (EA of 7-azaindoly), which is centered at a constant eBE value (2.699 eV) and corresponds to the EA of 7-azaindoly. The photon energies utilized in the acquisition of each spectrum are displayed in the top left corner of each panel.

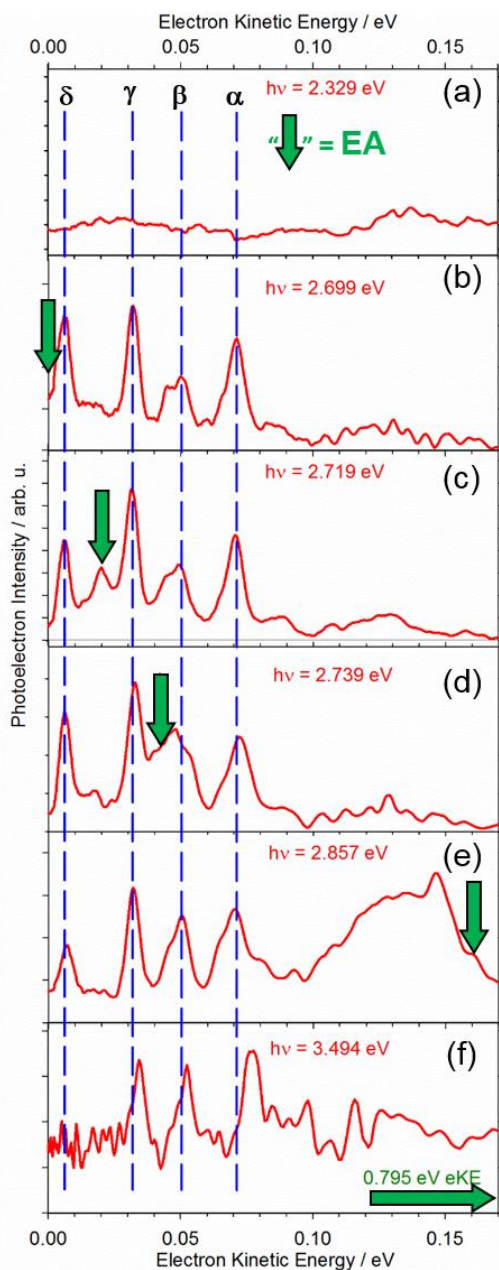


Figure 7.7: Compiled photoelectron spectra of 7-azaindole acquired with various photon energies and plotted as a function of eKE. The photon energies utilized in the acquisition of each spectrum are displayed on each panel. The vertical blue lines indicate peaks that are observed at constant eKE as a function of photon energy (see text) referred to as “eKE-invariant peaks” and labeled with Greek letters. The green downward pointing arrow represents the only feature in these spectra that is due to direct photodetachment (EA of 7-azaindoly).

A further analysis of the photon energy experiment described above can offer an explanation for the autodetaching nature of the photoelectron spectrum of 7-azaindolid. First, we note panel (a) in Fig. 7.6. The spectrum displayed in this panel was acquired with a photon energy of 2.649 eV. Now that we have assigned the EA of 7-azaindolyl we can see that the same eKE-invariant peaks are still present, even when we utilize a photon energy below detachment threshold. These peaks disappear when we acquire the spectrum with 2.329 eV photons, well below the EA. We also observe the eKE-invariant peaks when utilizing a photon energy of 2.857 eV, which also shows the appearance of a very broad peak at the low eBE side. This experiment shows that the eKE-invariant peaks are observed over a range of at least 0.208 eV. In the overview spectrum, if we expand the low kinetic energy region (Fig. 7.7, panel (f)), we see the presence of similar peaks. Although there is the exclusion of peak  $\delta$  and a small shift in the position of the remaining peaks ( $\alpha$ ,  $\beta$ , and  $\gamma$ ), this suggests that the autodetaching state is being accessed even with this photon energy (3.494 eV). This results indicates that the autodetaching states are accessible over the range of at least 0.845 eV! With this information, we can infer that there must be a very large number of accessible anion excited states over this range of photon energies for autodetachment behavior to be observed. In addition, the density of states must be large enough so that changes in the photon energy do not significantly alter the peak intensities. Finally, there must be a mechanism by which the remaining energy difference which is not converted to eKE is dissipated, and the energy conservation relation,  $eKE = h\nu - eBE$ , is obeyed. To explain the first and second points, a plausible explanation is that these excited states of the anion are dipole bound states. We base this assumption on the fact that the observation of eKE-invariant peaks is not unique to this work, as has been observed previously by Wang and coworkers in the photoelectron spectrum of the phenoxide anion.<sup>65,67</sup> In that work, they found a

collection of three resonant dipole bound transitions, which were observed at constant eKE when changing the photon energy. This observation is similar to those reported here. Dipole bound states, which are the anion analogs to Rydberg states of neutral molecules, are essentially highly excited hydrogenic states whose energy spacing is very small, almost approaching a continuum. Therefore, it allows for the very high density of states that are required for the autodetaching peak intensities to be insensitive to photon energy. We now offer an explanation for our second point, the eKE-invariant peaks: 7-azaindole initially absorbs a photon, taking the electron to one of the many resonant dipole bound states. The highly excited anion can then relax to a specific state which has significant overlap with the neutral electronic ground state and the electron continuum, with the concomitant production of neutral 7-azaindole plus the free electron which is detected. The remaining energy that is not detected as eKE is thus dissipated through a sink of available states, and the measured eKE is equivalent to the energy difference between an anion excited state and the final neutral state. In this manner, regardless of the photon energy utilized, the same peak (or collection of peaks) will be observed at a constant value of eKE.

The existence of such a high density of dipole bound states, however, requires a number of conditions to be true. It is known that for a molecule to support a dipole bound state, its permanent dipole moment has to be  $\sim 2$  Debye or greater.<sup>58-60,62,63,65,68</sup> In the same experiment by Wang and coworkers, eKE-invariant features were observed in the photoelectron spectrum of phenoxide. Those eKE-invariant peaks were attributed to autodetachment *via* dipole bound states. The phenoxyl radical has a permanent dipole moment of 4.0 Debye, as predicted by electronic structure calculations, and thus supports dipole bound states.<sup>65,67</sup> Thus, for our conjecture on the autodetachment *via* a high density of dipole bound states to be valid, the predicted dipole

moment of 7-azaindolyl must be high. Indeed, this is the case, as the calculated permanent dipole moment of 7-azaindolyl is even larger than that of phenoxyl, with a value of 4.6 Debye. This finding corroborates our hypothesis. However, while in the photoelectron spectrum of phenoxide the eKE-invariant peaks were observed to significantly change in intensity when different photon energies were utilized, the eKE-invariant peaks here ( $\alpha$  through  $\delta$ ) do not change in intensity. This suggests that, while it is reasonable to attribute the eKE-invariant peaks to autodetachment *via* dipole bound states, based on a comparison with a previous study,<sup>65,67</sup> some observations still require explanation.

Many questions associated with the intriguing features of the photoelectron spectrum of 7-azaindolide still remain. For instance, one question is related to the wavelength that photoelectron signal ceases to be observed, *i.e.* what the autodetachment threshold is. Another pertinent question is to know at which value of photon energy we recover the agreement with calculation observed in the overview spectrum obtained with 3.494 eV photons, as presented in Fig. 7.3. Since the B3LYP calculation done here, which does not account for electron autodetachment, has acceptable agreement with calculation, we postulate that there must be a value of photon energy at which the experiment and calculation recover the level of agreement observed in Fig. 7.3, that was simply a photon energy independent calculation. The use of a larger collection of photon energies should allow for the investigation of how much of the total photoelectron signal is due to direct photodetachment as opposed to autodetachment. From the spectrum shown in Fig. 7.6, we can conclude that most of the photoelectron signal is due to autodetachment, with a sole peak, the origin transition, being attributed to direct photodetachment. In the overview spectrum shown in Fig. 7.3, the spectrum seems to be primarily composed of direct photodetachment transitions, which can be inferred from the

reasonable agreement between experiment and calculation. However, some of the eKE-invariant transitions seem to be present and there seems to be a broad continuum of states under the entirety of the spectrum. To illustrate this, we fit this apparent continuum with a Gaussian function and artificially subtract this Gaussian envelope from the spectrum, as exhibited in Fig. 7.8. The result of this procedure is encouraging, as the relative intensities of the peaks predicted by the calculation are in much better agreement with the experiment. However, this procedure is not rigorous, and experiments employing a wider range of photon energies, above and especially below 3.494 eV, which are unavailable in our experimental setup, must be accomplished to answer these remaining questions.

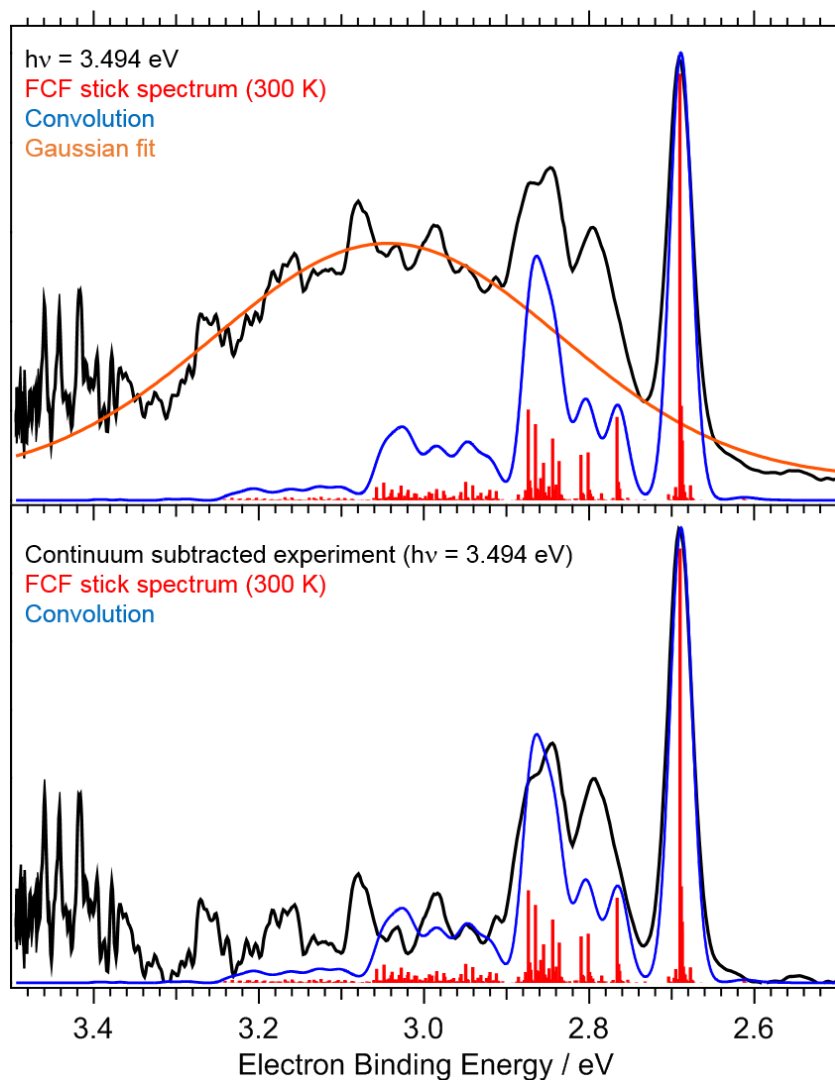


Figure 7.8: Upper panel: Overview photoelectron spectrum of 7-azaindole (black trace) and the Gaussian fit (orange trace) to the apparent underlying baseline (see text for details). Lower panel: Photoelectron spectrum of 7-azaindole with a Gaussian continuum (orange trace in the upper panel) subtracted. Both panels display the calculated FC stick spectrum, together with the convolution of such sticks with Gaussian functions whose widths correspond to the instrumental resolution.

The results described in the paragraphs above are unexpected, and verifying the validity of our conjectures requires further experiments and calculations. A possible experiment is currently being planned in collaboration with Prof. Lai-Sheng Wang. Such experiment will have two major goals: *i*) employ a cryogenic ion-trap to cool the 7-azaindolid ions and; *ii*) employ a variety of photon energies that cover the range between our highest energy dye-laser wavelength (2.857 eV) and the UV wavelength utilized for acquiring the overview spectrum of Fig. 7.3 (3.494 eV). The former will investigate whether or not the eKE-invariant features are temperature dependent, in an experiment similar to the one described in Refs. 65 and 67 for phenoxide. The latter will investigate at which point in photon energy the overview photoelectron spectrum, with reasonable agreement with calculation (Fig. 7.3), is recovered. In addition, we have initiated a collaboration with theorist Prof. John Stanton, to accurately calculate the possible autodetachment states of 7-azaindolid and dipole bound states of 7-azaindolyl. Currently, our explanation of the unexpected eKE-invariant peaks in the photoelectron spectrum of 7-azaindolid is qualitative and derives from comparison with similar species, such as phenoxide, and the analogous indolid, as described in the following section.

### *7.3.c Comparison between indolyl and 7-azaindolyl*

A comparison between the experimentally determined and calculated properties of indolyl and 7-azaindolyl can offer some interesting conclusions. Indolyl is a convenient comparison for a number of reasons. First, its chemical structures are remarkably similar, with the sole difference being an isoelectronic substitution of an N atom for a C–H group in the 7-position. Second, the photoelectron spectrum of indolid also presented signatures of electron autodetachment. There, some peaks displayed a drastic change in intensity when small changes in photon energy are made and these results were attributed to electron autodetachment.

However, the photon energy dependence is not nearly as dramatic as those observed for 7-azaindole. As Fig. 7.2 shows, the acquisition of the photoelectron spectrum with a photon energy close to detachment threshold met our expectations, as a photon energy close to threshold essentially just narrows the observed origin peak, when compared to the overview low resolution spectrum. The spectrum of 7-azaindole, on the other hand, presents a very different scenario, where the spectrum not only shows peaks of changing intensity, but also displays the same four peaks over a wide range of photon energies, as described in the previous section.

As mentioned in section 7.3.b, for electron autodetachment to be a viable route, some anion excited state must exist with an excitation energy comparable to the energy of a neutral state. In aromatic molecules, it is common that many optically accessible anion excited electronic states exist in an energy range equivalent to the EA of the neutral state. For example, in indole<sup>1</sup> and methylphenoxide<sup>51</sup> we calculated that there are as many as nine optically accessible anion excited states within the energy range between anion and neutral electronic ground states. This is also the case for 7-azaindole, where we predict five accessible anion excited states within the same range of photon energies (TD-B3LYP/aug-cc-pVTZ). In order to interpret the dramatic difference between the photoelectron spectra of indole and 7-azaindole, we shall rely on electronic structure calculations. The calculations performed for both molecules with the same level of theory show mostly similar properties with one main exception: the calculated dipole moment. While indole has a rather large dipole moment of 2.6 Debye (B3LYP/aug-cc-pVTZ), which deems it capable of sustaining dipole bound states, the calculated dipole moment of 7-azaindole is 4.6 Debye. The consequence of this is that 7-azaindole should be capable of supporting more dipole bound states, which indeed seems to be the case. While the larger permanent dipole moment of 7-azaindole corroborates the larger contribution of electron

autodetachment to the overall photoelectron signal, the reason for a qualitatively different autodetaching behavior remains unexplained. The comparison between the photoelectron spectra of 7-azaindole and indole, and the properties of 7-azaindolyl *versus* indolyl shows that a seemingly small change in molecular structure can result in a qualitatively different electronic structure and lead to a drastically distinct photoelectron spectrum.

#### 7.4.d Photoelectron spectrum of $(7\text{-azaindole})_2^-$

The photoelectron spectra of the  $(7\text{-azaindole})_2^-$  were previously obtained by Nakajima *et al.* in a magnetic bottle photoelectron spectrometer<sup>30</sup> Here, we revisit the experiment with the much higher resolution attainable with the VMI. In addition, the employment of the dual-valve ion source likely produces anions that are considerably colder than the previously employed single valve discharge. In Nakajima's experiment, the photoelectron spectrum of  $(7\text{-azaindole})_2^-$  was observed to be very broad and unstructured. Although there is a disappointing lack of insight on why the spectrum is so broad, we can infer that it is due to either a large degree of geometry change between anion and neutral equilibrium structures, a large degree of fluxionality of the neutral dimer (*i.e.* many low frequency vibrations), or both of these effects in conjunction. It is reasonable to assume that the neutral dimer would have very low frequency vibrational modes since the two monomers are bound by hydrogen bonds. It is also reasonable that the geometry change between anion and neutral structures is large, with the addition of an electron to the neutral dimer. The ongoing calculations will reveal if these assumptions are valid.

The overview spectrum of  $(7\text{-azaindole})_2^-$  is shown in Fig. 7.9. This spectrum is similar to that obtained by Nakajima, but with a considerably larger signal-to-noise ratio. As expected based on the Nakajima study, the spectrum is broad and unstructured. We observe photodetachment to both ground and first excited states of  $(7\text{-azaindole})_2$ . To better investigate

the low eBE region of detachment for each of these electronic states of (7-azaindole)<sub>2</sub>, we acquire spectra employing the SEVI technique. The regions of the spectrum obtained in high resolution are shown as shaded areas in Fig. 7.9.

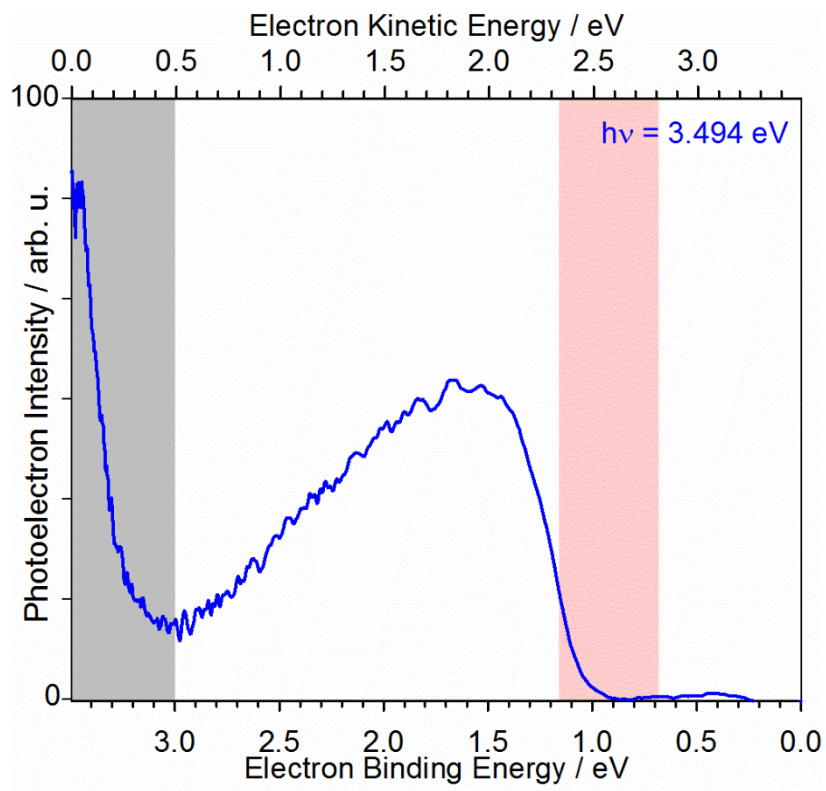


Figure 7.9: Overview photoelectron spectrum of  $(7\text{-azaindole})_2^-$ , accessing the ground and first excited states of  $(7\text{-azaindole})_2$ . This spectrum is obtained with a photon energy of 3.494 eV. The shaded regions represent the magnified eBE ranges that are acquired in high resolution with 1.165 eV (red) and 3.494 eV (gray) photon energies and are displayed in Figs. 7.10 and 7.11, respectively.

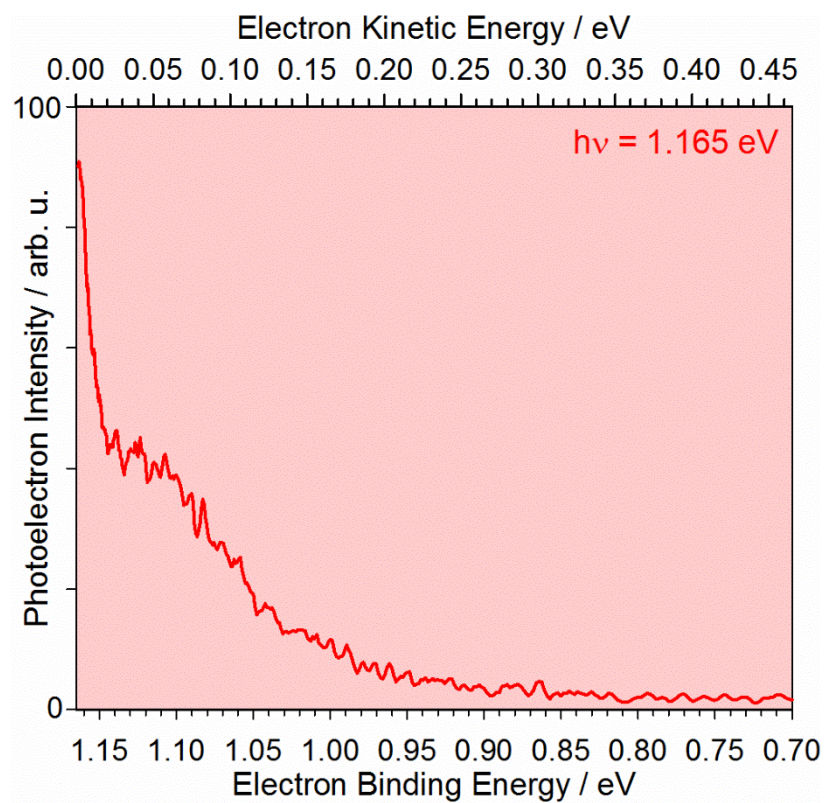


Figure 7.10: Photoelectron spectrum of  $(7\text{-azaindole})_2^-$  acquired with a photon energy of 1.165 eV. The resolution ranges from  $\sim 3$  meV to  $\sim 18$  meV as the eKE ranges from 0.0 to 0.5 eV (see Chapter 2).

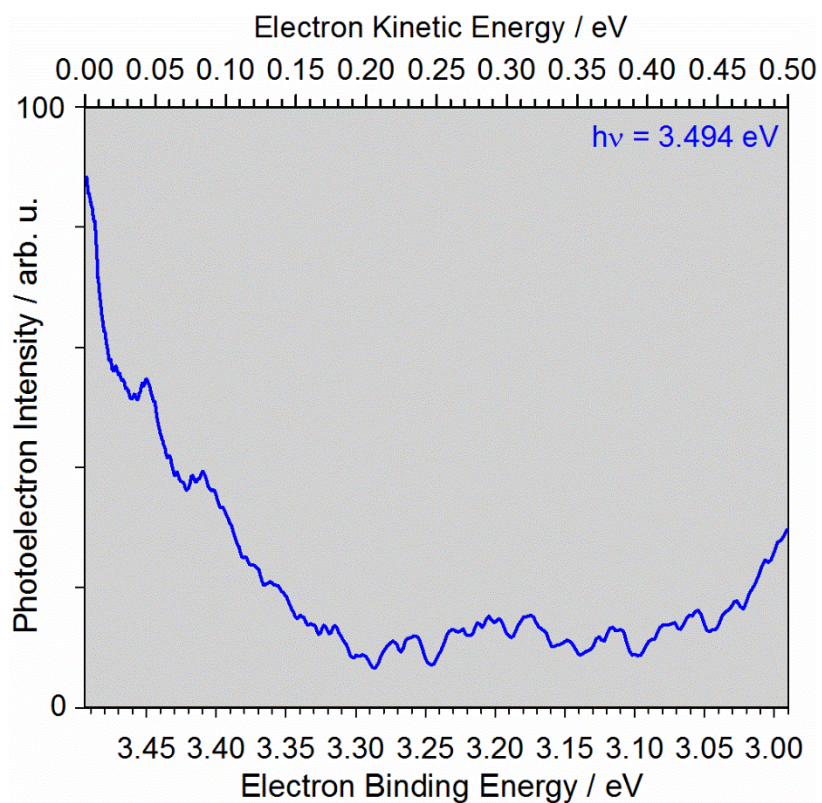


Figure 7.11: High resolution view of a portion of the photoelectron spectrum of  $(7\text{-azaindole})_2^-$  acquired with a photon energy of 3.494 eV. The resolution ranges from  $\sim 3$  meV to  $\sim 18$  meV as the eKE ranges from 0.0 to 0.5 eV (see Chapter 2).

The high resolution photoelectron spectra can provide more accurate measurements of the EA of (7-azaindole)<sub>2</sub> and insight on the vibrational activity upon photodetachment. We will first focus on the high resolution photoelectron spectrum accessing the ground state of (7-azaindole)<sub>2</sub> acquired with a photon energy of 1.165 eV (Fig. 7.10). This result shows that, even close to threshold, when detecting slow electrons, the spectrum is essentially without structure. Since there are no well-defined peaks, a precise assignment of the EA of (7-azaindole)<sub>2</sub> is not possible. This results require a modification of the conclusion of previous work by Nakajima *et al.* In their study, where they report EA (7-azaindole)<sub>2</sub> = 0.88(12) eV. This precision seems optimistic, since the large spectral congestion prevents a precise assignment and we believe it is more appropriate to determine the EA as an upper bound, as is done here. From the spectrum showed in Fig. 7.10, considering the noise level of ~ 1.4, we can affirm that true photoelectron signal is detected at an eBE as low as 0.985 eV, with a 3 $\sigma$  confidence level (~99.7%). We thus report EA (7-azaindole)<sub>2</sub> < 1.0 eV. This value is within the upper limit as measured by Nakajima *et al.* The excited state high resolution scan leads to similar conclusions, with the establishment of the term energy as T<sub>0</sub> ~ 2.4(1) eV in agreement with the Nakajima *et al.* measurement. However, the excited state vibrational progression does seem more structured when compared to the ground state progression. From the spectrum in Fig.7.11 we observe a progression of three peaks, spaced by ~0.04 eV, or ~320 cm<sup>-1</sup>, which were not observed by Nakajima *et al.* These peaks can potentially be attributed to a vibration of the excited state of (7-azaindole)<sub>2</sub>, which will likely be revealed by the ongoing calculations. Overall, the fact that the spectrum reveals itself to be highly congested even when investigated in high resolution prevents us from extracting quantitative information and little more insight than that given by Nakajima *et al.* study. Thus, further analysis will not be attempted here.

## 7.5 Conclusions

In this chapter the photoelectron spectrum of 7-azaindolidine and 7-azaindole dimer anion are investigated. The photoelectron spectrum of 7-azaindolidine, when acquired in low resolution with a photon energy far from detachment threshold (3.494 eV), showed reasonable agreement with calculation, which allowed for a preliminary assignment of the EA of 7-azaindolyl, together with revealing vibrational activity in ring distortion modes. Upon inspection of the origin transition in high resolution, the spectrum provided unexpected results. Instead of the expected narrowing of the origin peak, which would have allowed for an accurate measurement of the EA of 7-azaindolyl, a qualitatively different spectrum was obtained. In the high resolution spectrum instead of the observation of a strong origin transition, as predicted by calculation, a collection of five essentially equally intense peaks, spanning a much wider energy range, were observed. In addition, other high resolution spectra obtained with a range of photon energies spanning ~0.2 eV showed that four of these peaks were always observed at the same eKE, regardless of the photon energy employed, an apparent violation of energy conservation. The unexpected eKE-invariant peaks are attributed to electron autodetachment *via* a high density of dipole bound states, which explains the apparent shift in electron binding energies in the photoelectron spectrum. The high resolution spectra allows for a precise determination of the EA of 7-azaindolyl as 2.699(2) eV. A comparison between 7-azaindolyl and the previously investigated indolyl<sup>1</sup> shows how two very similar molecules, where the sole difference is an isoelectronic substitution of an N atom for a C-H group, can have qualitatively different properties. Of all the properties, the permanent dipole moment is highlighted, as it is calculated to be 2.6 Debye in indolyl and 4.6 Debye in 7-azaindolyl, a change that could explain the much more prevalent autodetachment signatures in the photoelectron spectrum of 7-azaindolidine when compared to

indolide. Finally, the photoelectron spectrum of 7-azaindole dimer anion, previously investigated by Nakajima,<sup>30</sup> is revisited in higher resolution. The photoelectron spectrum of the dimer showed an unstructured broad spectrum, regardless of the increase in resolution. These results indicate a large degree of fluxionality of the neutral dimer vibrational structure and very little information can be obtained from the spectrum. However, we do offer a measurement of the EA of the neutral dimer, establishing the bound of EA < 1.0 eV.

## 7.6. Chapter 7 references

- <sup>1</sup> D.J. Nelson, A.M. Oliveira, and W.C. Lineberger, *J. Chem. Phys.* **submitted**, (2017).
- <sup>2</sup> A. Douhal, S.K. Kim, and A.H. Zewail, *Nature* **378**, 260 (1995).
- <sup>3</sup> O.-H. Kwon and A.H. Zewail, *Proc. Natl. Acad. Sci.* **104**, 8703 (2007).
- <sup>4</sup> T. Fiebig, M. Chachisvilis, M. Manger, A.H. Zewail, A. Douhal, I. Garcia-Ochoa, and A. de La Hoz Ayuso, *J. Phys. Chem. A* **103**, 7419 (1999).
- <sup>5</sup> H. Sekiya and K. Sakota, *J. Photochem. Photobiol. C Photochem. Rev.* **9**, 81 (2008).
- <sup>6</sup> K. Fuke and H. Ishikawa, *Chem. Phys. Lett.* **623**, 117 (2015).
- <sup>7</sup> D.B. Bucher, A. Schlueter, T. Carell, and W. Zinth, *Angew. Chemie - Int. Ed.* **53**, 11366 (2014).
- <sup>8</sup> C. Al Taylor, M. Ashraf El-Bayoumit, and M. Kasha, *Proc. Natl. Acad. Sci.* **63**, 253 (1969).
- <sup>9</sup> J.D. Watson and F.H.C. Crick, *Nature* **171**, 737 (1953).
- <sup>10</sup> X. Yu, S. Yamazaki, and T. Taketsugu, *Phys. Chem. Chem. Phys.* **19**, 23289 (2017).
- <sup>11</sup> P.T. Chou, W.S. Yu, Y.C. Chen, C.Y. Wei, and S.S. Martinez, *J. Am. Chem. Soc.* **120**, 12927 (1998).
- <sup>12</sup> K. Fuke, H. Yoshiuchi, and K. Kaya, *J. Phys. Chem.* **88**, 5840 (1984).
- <sup>13</sup> M.S. Gordon, *J. Phys. Chem.* **100**, 3974 (1996).
- <sup>14</sup> C. Li, Y. Yang, D. Li, and Y. Liu, *Phys. Chem. Chem. Phys.* **19**, 4802 (2017).
- <sup>15</sup> J. Yi and H. Fang, *J. Mol. Model.* **23**, 312 (2017).
- <sup>16</sup> M.S. Mehata, A.K. Singh, and R.K. Sinha, *J. Mol. Liq.* **231**, 39 (2017).

- <sup>17</sup> A. Rosspeintner, B. Lang, and E. Vauthey, *Annu. Rev. Phys. Chem.* **64**, 247 (2013).
- <sup>18</sup> D.R. Weinberg, C.J. Gagliardi, J.F. Hull, C.F. Murphy, C.A. Kent, B.C. Westlake, A. Paul, D.H. Ess, D.G. McCafferty, and T.J. Meyer, *Chem. Rev.* **112**, 4016 (2012).
- <sup>19</sup> S. Arulmozhiraja and M.L. Coote, *J. Chem. Theory Comput.* **8**, 575 (2012).
- <sup>20</sup> S. Arulmozhiraja, M.L. Coote, and J.Y. Hasegawa, *J. Chem. Phys.* **143**, 204304 (2015).
- <sup>21</sup> K. Sakota and H. Sekiya, *J. Phys. Chem. A* **109**, 2722 (2005).
- <sup>22</sup> J. Yi and H. Fang, *Photochem. Photobiol.* **in press**, doi:10.1111/php.12839 (2017).
- <sup>23</sup> C. Carmona, E. García-Fernández, J. Hidalgo, A. Sánchez-Coronilla, and M. Balón, *J. Fluoresc.* **24**, 45 (2014).
- <sup>24</sup> O.H. Kwon and D.J. Jang, *J. Phys. Chem. B* **109**, 20479 (2005).
- <sup>25</sup> S. Takeuchi and T. Tahara, *J. Phys. Chem. A* **102**, 7740 (1998).
- <sup>26</sup> H. Sekiya, K. Sakota, N. Komure, and W. Ishikawa, *J. Chem. Phys.* **130**, 224307 (2009).
- <sup>27</sup> T. Kato and H. Shirota, *J. Chem. Phys.* **134**, 164504 (2011).
- <sup>28</sup> M. Mukherjee, B. Bandyopadhyay, and T. Chakraborty, *Chem. Phys. Lett.* **546**, 74 (2012).
- <sup>29</sup> H. Shirota, T. Fukuda, and T. Kato, *J. Phys. Chem. B* **117**, 16196 (2013).
- <sup>30</sup> A. Nakajima, Y. Negishi, R. Hasumi, and K. Kaya, *Eur. Phys. J. D* **9**, 303 (1999).
- <sup>31</sup> H. Sekiya and K. Sakota, *Bull. Chem. Soc. Jpn.* **79**, 373 (2006).
- <sup>32</sup> C. Kang, J.T. Yi, and D.W. Pratt, *Chem. Phys. Lett.* **423**, 7 (2006).
- <sup>33</sup> K. Sakota, C. Jouvét, C. Dedonder, M. Fujii, and H. Sekiya, *J. Phys. Chem. A* **114**, 11161 (2010).
- <sup>34</sup> H. Ishikawa, T. Nakano, T. Takashima, H. Yabuguchi, and K. Fuke, *Chem. Phys.* **419**, 101 (2013).
- <sup>35</sup> D.E. Folmer, E.S. Wisniewski, J.R. Stairs, and A.W. Castleman, *J. Phys. Chem. A* **104**, 10545 (2000).
- <sup>36</sup> D.E. Folmer, E.S. Wisniewski, and A.W. Castleman, *Chem. Phys. Lett.* **318**, 637 (2000).
- <sup>37</sup> S. Takeuchi and T. Tahara, *Chem. Phys. Lett.* **347**, 108 (2001).
- <sup>38</sup> J. Catalan, *Proc. Natl. Acad. Sci.* **105**, E78 (2008).
- <sup>39</sup> O.-H. Kwon and A.H. Zewail, *Proc. Natl. Acad. Sci.* **105**, E79 (2008).
- <sup>40</sup> S. Takeuchi and T. Tahara, *Proc. Natl. Acad. Sci.* **104**, 5285 (2007).
- <sup>41</sup> R. Crespo-Otero, N. Kungwan, and M. Barbatti, *Chem. Sci.* **6**, 5762 (2015).
- <sup>42</sup> X.F. Yu, S. Yamazaki, and T. Taketsugu, *J. Chem. Theory Comput.* **7**, 1006 (2011).

- <sup>43</sup> S.J. Blanksby and G.B. Ellison, *Acc. Chem. Res.* **36**, 255 (2003).
- <sup>44</sup> A.M. Oliveira, Y.J. Lu, J.H. Lehman, P.B. Changala, J.H. Baraban, J.F. Stanton, and W.C. Lineberger, *J. Am. Chem. Soc.* **137**, 12939 (2015).
- <sup>45</sup> P.C. Engelking, *J. Phys. Chem.* **90**, 4544 (1986).
- <sup>46</sup> M.J. Frisch, G.W. Trucks, H.B. Schlegel, G.E. Scuseria, M.A. Robb, J.R. Cheeseman, G. Scalmani, V. Barone, B. Mennucci, G.A. Petersson, H. Nakatsuji, M. Caricato, X. Li, H.P. Hratchian, A.F. Izmaylov, J. Bloino, G. Zheng, J.L. Sonnenberg, M. Hada, M. Ehara, K. Toyota, R. Fukuda, J. Hasegawa, M. Ishida, T. Nakajima, Y. Honda, O. Kitao, H. Nakai, T. Vreven, J.A. Montgomery Jr., J.E. Peralta, F. Ogliaro, M.J. Bearpark, J. Heyd, E.N. Brothers, K.N. Kudin, V.N. Staroverov, R. Kobayashi, J. Normand, K. Raghavachari, A.P. Rendell, J.C. Burant, S.S. Iyengar, J. Tomasi, M. Cossi, N. Rega, N.J. Millam, M. Klene, J.E. Knox, J.B. Cross, V. Bakken, C. Adamo, J. Jaramillo, R. Gomperts, R.E. Stratmann, O. Yazyev, A.J. Austin, R. Cammi, C. Pomelli, J.W. Ochterski, R.L. Martin, K. Morokuma, V.G. Zakrzewski, G.A. Voth, P. Salvador, J.J. Dannenberg, S. Dapprich, A.D. Daniels, Ö. Farkas, J.B. Foresman, J. V. Ortiz, J. Cioslowski, and D.J. Fox, *Gaussian 09 Revision B.01*, Gaussian Inc. Wallingford, CT (2009).
- <sup>47</sup> A.D. Becke, *J. Chem. Phys.* **98**, 5648 (1993).
- <sup>48</sup> T.H. Dunning, *J. Chem. Phys.* **90**, 1007 (1989).
- <sup>49</sup> K.M. Ervin, J. Ho, and W.C. Lineberger, *J. Phys. Chem.* **92**, 5405 (1988).
- <sup>50</sup> K.M. Ervin, PESCAL, available online at [wolfweb.unr.edu/~ervin/pes/](http://wolfweb.unr.edu/~ervin/pes/) (2010).
- <sup>51</sup> D.J. Nelson, W.K. Gichuhi, E.M. Miller, J.H. Lehman, and W.C. Lineberger, *J. Chem. Phys.* **146**, 74302 (2017).
- <sup>52</sup> A.M. Oliveira, J.H. Lehman, A.B. McCoy, and W.C. Lineberger, *J. Chem. Phys.* **145**, 124317 (2016).
- <sup>53</sup> D.M. Neumark, *J. Phys. Chem. A* **112**, 13287 (2008).
- <sup>54</sup> W.R. Garrett, *Phys. Rev. A* **3**, 961 (1971).
- <sup>55</sup> W.R. Garrett, *Chem. Phys. Lett.* **5**, 393 (1970).
- <sup>56</sup> E. Fermi and E. Teller, *Phys. Rev.* **72**, 399 (1947).
- <sup>57</sup> C.L. Adams, H. Schneider, and J.M. Weber, *J. Phys. Chem. A* **114**, 4017 (2010).
- <sup>58</sup> K.R. Lykke, R.D. Mead, and W.C. Lineberger, *Phys. Rev. Lett.* **52**, 2221 (1984).
- <sup>59</sup> K.R. Lykke, D.M. Neumark, T. Andersen, V.J. Trapa, and W.C. Lineberger, *J. Chem. Phys.* **87**, 6842 (1987).
- <sup>60</sup> M.L. Weichman, J.B. Kim, and D.M. Neumark, *J. Chem. Phys.* **140**, 104305 (2014).
- <sup>61</sup> C.L. Adams, H. Schneider, K.M. Ervin, and J.M. Weber, *J. Chem. Phys.* **130**, 74307 (2009).
- <sup>62</sup> J. Marks, J.I. Brauman, R.D. Mead, K.R. Lykke, and W.C. Lineberger, *J. Chem. Phys.* **88**, 6785 (1988).

<sup>63</sup> R.D. Mead, K.R. Lykke, W.C. Lineberger, J. Marks, and J.I. Brauman, *J. Chem. Phys.* **81**, 4883 (1984).

<sup>64</sup> D.M. Neumark, K.R. Lykke, T. Andersen, and W.C. Lineberger, *J. Chem. Phys.* **83**, 4364 (1985).

<sup>65</sup> L.S. Wang, *J. Chem. Phys.* **143**, 40901 (2015).

<sup>66</sup> R.S. Berry, *J. Chem. Phys.* **45**, 1228 (1966).

<sup>67</sup> H.T. Liu, C.G. Ning, D.L. Huang, P.D. Dau, and L.S. Wang, *Angew. Chemie - Int. Ed.* **52**, 8976 (2013).

<sup>68</sup> D.J. Goebbert, K. Pichugin, and A. Sanov, *J. Chem. Phys.* **131**, 164308 (2009).

## BIBLIOGRAPHY

1. Adams, C.L., et al., Low-energy photoelectron imaging spectroscopy of nitromethane anions: Electron affinity, vibrational features, anisotropies, and the dipole-bound state. *The Journal of Chemical Physics*, 2009. 130(7): p. 074307.
2. Adams, C.L., H. Schneider, and J.M. Weber, Vibrational Autodetachment - Intramolecular Vibrational Relaxation Translated into Electronic Motion. *Journal of Physical Chemistry A*, 2010. 114(12): p. 4017.
3. Alam, J., et al., Dispersed Fluorescence Spectroscopy of Jet-Cooled 2-, 3-, and 4-Methylcyclohexoxy Radicals. *Journal of Physical Chemistry A*, 2015. 119(24): p. 6257.
4. Aliche, B., U. Platt, and J. Stutz, Impact of Nitrous Acid Photolysis on the Total Hydroxyl Radical Budget During the Limitation of Oxidant Production. *Journal of Geophysical Research: Atmospheres*, 2002. 107(D22): p. 9.
5. Amaral, G., K.S. Xu, and J.S. Zhang,  $\text{H}^+\text{NO}_2$  Channels in the Photodissociation of HONO at 193.3 nm. *Journal of Physical Chemistry A*, 2001. 105(9): p. 1465.
6. Araki, M., H. Ozeki, and S. Saito, Experimental determination of the ground-state inversion splitting in  $\text{D}_3\text{O}^+$  by microwave spectroscopy. *The Journal of Chemical Physics*, 1998. 109(14): p. 5707.
7. Arulmozhiraja, S. and M.L. Coote,  $^1\text{L}_a$  and  $^1\text{L}_b$  states of indole and azaindole: Is density functional theory inadequate? *Journal of Chemical Theory and Computation*, 2012. 8(2): p. 575.
8. Arulmozhiraja, S., M.L. Coote, and J.Y. Hasegawa, Electronic spectra of azaindole and its excited state mixing: A symmetry-adapted cluster configuration interaction study. *The Journal of Chemical Physics*, 2015. 143(20): p. 204304.
9. Asatryan, R., J.W. Bozzelli, and J.M. Simmie, Thermochemistry for Enthalpies and Reaction Paths of Nitrous Acid Isomers. *International Journal of Chemical Kinetics*, 2007. 39(7): p. 378.
10. Atkinson, R., Atmospheric reactions of alkoxy and beta-hydroxyalkoxy radicals. *International Journal of Chemical Kinetics*, 1997. 29(2): p. 99.
11. Atkinson, R., Rate constants for the atmospheric reactions of alkoxy radicals: An updated estimation method. *Atmospheric Environment*, 2007. 41(38): p. 8468.
12. Atkinson, R. and W.P.L. Carter, Reactions of Alkoxy Radicals under Atmospheric Conditions - the Relative Importance of Decomposition Versus Reaction with  $\text{O}_2$ . *Journal of Atmospheric Chemistry*, 1991. 13(2): p. 195.
13. Aubin, D.G. and J.P.D. Abbatt, Interaction of  $\text{NO}_2$  with Hydrocarbon Soot: Focus on HONO Yield, Surface Modification, and Mechanism. *Journal of Physical Chemistry A*, 2007. 111(28): p. 6263.
14. Baker, M. and W. Gabryelski, Collision induced dissociation of deprotonated glycolic acid. *International Journal of Mass Spectrometry*, 2007. 262(1-2): p. 128.

15. Barckholtz, T.A. and T.A. Miller, Quantitative insights about molecules exhibiting Jahn-Teller and related effects. *International Reviews in Physical Chemistry*, 1998. 17(4): p. 435.
16. Barrientos, C., et al., Computational Prediction of the Spectroscopic Parameters of Methanediol, an Elusive Molecule for Interstellar Detection. *Astrophysical Journal*, 2014. 784(2): p. 132.
17. Bartlett, R.J., et al., Non-iterative fifth-order triple and quadruple excitation energy corrections in correlated methods. *Chemical Physics Letters*, 1990. 165(6): p. 513.
18. Bartolomei, V., et al., Formation of Indoor Nitrous Acid (HONO) by Light-Induced NO<sub>2</sub> Heterogeneous Reactions with White Wall Paint. *Environmental Science and Pollution Research*, 2014. 21(15): p. 9259.
19. Bauerle, S. and G.K. Moortgat, Absorption cross-sections of HOCH<sub>2</sub>OOH vapor between 205 and 360 nm at 298 K. *Chemical Physics Letters*, 1999. 309(1-2): p. 43.
20. Becke, A.D., Density functional thermochemistry. III. The role of exact exchange. *The Journal of Chemical Physics*, 1993. 98(7): p. 5648.
21. Bent, G.D., et al., Many-body perturbation theory electronic structure calculations for the methoxy radical. I. Determination of Jahn-Teller energy surfaces, spin-orbit splitting, and Zeeman effect. *The Journal of Chemical Physics*, 1982. 76(8): p. 4144.
22. Berry, R.S., Ionization of Molecules at Low Energies. *The Journal of Chemical Physics*, 1966. 45(4): p. 1228.
23. Bierbaum, V.M., Go with the flow: Fifty years of innovation and ion chemistry using the flowing afterglow. *International Journal of Mass Spectrometry*, 2015. 377(1): p. 456.
24. Blanksby, S.J. and G.B. Ellison, Bond dissociation energies of organic molecules. *Accounts of Chemical Research*, 2003. 36(4): p. 255.
25. Blanksby, S.J., et al., Negative-ion photoelectron spectroscopy, gas-phase acidity, and thermochemistry of the peroxy radicals CH<sub>3</sub>OO and CH<sub>3</sub>CH<sub>2</sub>OO. *Journal of the American Chemical Society*, 2001. 123(39): p. 9585.
26. Blondel, C., et al., The electron affinities of O, Si, and S revisited with the photodetachment microscope. *The European Physical Journal D - Atomic, Molecular, Optical and Plasma Physics*, 2005. 33(3): p. 335.
27. Bongartz, A., et al., Near-UV Absorption Cross-sections and trans-cis Equilibrium of Nitrous-Acid. *Journal of Physical Chemistry*, 1991. 95(3): p. 1076.
28. Boo, D.W., et al., Femtosecond Dynamics of Linear Ag<sub>3</sub><sup>-</sup>. *Journal of Physical Chemistry*, 1997. 101(97): p. 6688.
29. Bopp, J.C., et al., Spectroscopic Characterization of the Isolated SF<sub>6</sub><sup>-</sup> And C<sub>4</sub>F<sub>8</sub><sup>-</sup> Anions: Observation of Very Long Harmonic Progressions in Symmetric Deformation Modes Upon Photodetachment. *Journal of Physical Chemistry A*, 2007. 111(7): p. 1214.
30. Borin, A.C. and A.V.S. de Araujo, Tips on active space construction in multiconfigurational calculations: A case study. *Quimica Nova*, 2015. 38(5): p. 738.

31. Borucki, W.J., et al., Predictions of the Electrical-Conductivity and Charging of the Aerosols in Titan's Atmosphere. *Icarus*, 1987. 72(3): p. 604.
32. Botan, V. and P. Hamm, Intramolecular Vibrational Energy Relaxation in Nitrous Acid (HONO). *Journal of Chemical Physics*, 2008. 129(16): p. 164506.
33. Brossard, S.D., et al., The  $^2A_1$   $^2E$  electronic spectrum of methoxy,  $CH_3O$ : Vibrational progressions, and spin-orbit and Jahn-Teller couplings. *The Journal of Chemical Physics*, 1986. 84(5): p. 2459.
34. Bucher, D.B., et al., Watson-Crick Base Pairing Controls Excited - State Decay in Natural DNA. *Angewandte Chemie - International Edition*, 2014. 53(42): p. 11366.
35. Campargue, R., Progress in overexpanded supersonic jets and skimmed molecular beams in free-jet zones of silence. *The Journal of Physical Chemistry*, 1984. 88(20): p. 4466.
36. Cao, Q., et al., Reaction of atomic hydrogen with formic acid. *Physical Chemistry Chemical Physics*, 2014. 16(13): p. 5993.
37. Capone, L.A., et al., Lower Ionosphere of Titan. *Icarus*, 1976. 28(3): p. 367.
38. Carmona, C., et al., New insights on the 7-Azaindole photophysics: The overlooked role of its non phototautomerizable hydrogen bonded complexes. *Journal of Fluorescence*, 2014. 24(1): p. 45.
39. Carter, C.C., et al., Jet-cooled laser-induced fluorescence spectroscopy of some alkoxy radicals. *Journal of Physical Chemistry A*, 2000. 104(40): p. 9165.
40. Catalan, J., On the concerted mechanism of photo-induced biprotonic transfer in  $C_{2h}$  7-azaindole dimer. *Proceedings of the National Academy of Sciences*, 2008. 105(45): p. E78.
41. Celotta, R.J., et al., Molecular photodetachment spectrometry. II. The electron affinity of  $O_2$  and the structure of  $O_2^-$ . *Physical Review A*, 1972. 6(2): p. 631.
42. Changala, P.B., NITROGEN Numerical and Iterative Techniques for Rovibronic Energies with General Internal Coordinates, 2015.
43. Chen, F.F., *Introduction to Plasma Physics*, 1995: Springer US.
44. Choo, K.Y. and S.W. Benson, Arrhenius Parameters for the Alkoxy Radical Decomposition Reactions. *International Journal of Chemical Kinetics*, 1981. 13(9): p. 833.
45. Chou, P.T., et al., Ground-state reverse double proton transfer of 7-azaindole. *Journal of the American Chemical Society*, 1998. 120(49): p. 12927.
46. Cleeton, C.E. and N.H. Williams, Electromagnetic Waves of 1.1 cm Wave-Length and the Absorption Spectrum of Ammonia. *Physical Review*, 1934. 45: p. 234.
47. Coates, A.J., et al., Discovery of heavy negative ions in Titan's ionosphere. *Geophysical Research Letters*, 2007. 34(22): p. L22103.
48. Colbert, D.T. and W.H. Miller, A Novel Discrete Variable Representation for Quantum-Mechanical Reactive Scattering via the S-Matrix Kohn Method. *The Journal of Chemical Physics*, 1992. 96(3): p. 1982.

49. Cooper, J. and R.N. Zare, Angular Distribution of Photoelectrons. *The Journal of Chemical Physics*, 1968. 48(2): p. 942.
50. Cox, A.P., A.H. Brittain, and D.J. Finnigan, Microwave Spectrum, Structure, Dipole Moment and Quadrupole Coupling Constants of cis and trans Nitrous Acids. *Transactions of the Faraday Society*, 1971. 67(584): p. 2179.
51. Cramer, C.J., *Essentials of computational chemistry: theories and models*, 2004: Wiley. 596.
52. Crespo-Otero, R., N. Kungwan, and M. Barbatti, Stepwise double excited-state proton transfer is not possible in 7-azaindole dimer. *Chemical Science*, 2015. 6(10): p. 5762.
53. Curran, H.J., Rate constant estimation for C-1 to C-4 alkyl and alkoxy radical decomposition. *International Journal of Chemical Kinetics*, 2006. 38(4): p. 250.
54. Curran, H.J., et al., A comprehensive modeling study of n-heptane oxidation. *Combustion and Flame*, 1998. 114(1-2): p. 149.
55. Danger, G., et al., Hydroxyacetonitrile (HOCH<sub>2</sub>CN) Formation in Astrophysical Conditions. Competition with the Aminomethanol, a Glycine Precursor. *Astrophysical Journal*, 2012. 756(1): p. 11.
56. Davis, A.C. and J.S. Francisco, Reactivity Trends within Alkoxy Radical Reactions Responsible for Chain Branching. *Journal of the American Chemical Society*, 2011. 133(45): p. 18208.
57. Davis, A.C. and J.S. Francisco, Hydroxyalkoxy Radicals: Importance of Intramolecular Hydrogen Bonding on Chain Branching Reactions in the Combustion and Atmospheric Decomposition of Hydrocarbons. *Journal of Physical Chemistry A*, 2014. 118(46): p. 10982.
58. Davis, S., et al., Jet-cooled molecular radicals in slit supersonic discharges: Sub-Doppler infrared studies of methyl radical. *The Journal of Chemical Physics*, 1997. 107(15): p. 5661.
59. Deeley, C.M. and I.M. Mills, The Infrared Vibration-Rotation Spectrum of trans-Nitrous and cis-Nitrous Acid. *Journal of Molecular Structure*, 1983. 100: p. 199.
60. Demchenko, A.P., K.-C. Tang, and P.-T. Chou, Excited-state proton coupled charge transfer modulated by molecular structure and media polarization. *Chemical Society Reviews*, 2013. 42(3): p. 1379.
61. DePuy, C.H. and V.M. Bierbaum, Gas-Phase Reactions of Organic Anions As Studied by the Flowing Afterglow Technique. *Accounts of Chemical Research*, 1981. 14(5): p. 146.
62. DePuy, C.H., J.J. Grabowski, and V.M. Bierbaum, Chemical reactions of anions in the gas phase. *Science*, 1982. 218(4576): p. 955.
63. DePuy, C.H., et al., The gas-phase acidities of the alkanes. *Journal of the American Chemical Society*, 1989. 111: p. 1968.
64. Devolder, P., Atmospheric fate of small alkoxy radicals: recent experimental and theoretical advances. *Journal of Photochemistry and Photobiology A - Chemistry*, 2003. 157(2-3): p. 137.

65. Dick, B., Inverting ion images without Abel inversion: maximum entropy reconstruction of velocity maps. *Physical Chemistry Chemical Physics*, 2014. 16(2): p. 570.
66. Dillon, J. and D.R. Yarkony, Nonadiabatic effects in substitutional isomers of Jahn-Teller molecules: The strange case of hydroxymethoxy. *The Journal of Chemical Physics*, 2012. 137(15): p. 154315.
67. Dillon, J.J. and D.R. Yarkony, The photoelectron spectrum of the ethoxide anion: Conical intersections, the spin-orbit interaction, and sequence bands. *The Journal of Chemical Physics*, 2009. 131(13): p. 134303.
68. Dillon, J.J. and D.R. Yarkony, The photoelectron spectrum of the isopropoxide anion: Nonadiabatic effects due to conical intersections and the spin-orbit interaction. *The Journal of Chemical Physics*, 2009. 130(15): p. 154312.
69. Dixon, D.A., D. Feller, and K.A. Peterson, Accurate Calculations of the Electron Affinity and Ionization Potential of the Methyl Radical. *Journal of Physical Chemistry A*, 1997. 101: p. 9405.
70. Domcke, W. and D.R. Yarkony, Role of Conical Intersections in Molecular Spectroscopy and Photoinduced Chemical Dynamics. *Annual Review of Physical Chemistry*, 2012. 63: p. 325.
71. Douhal, A., S.K. Kim, and A.H. Zewail, Femtosecond molecular dynamics of tautomerization in model base pairs. *Nature*, 1995. 378(6554): p. 260.
72. Dribinski, V., et al., Reconstruction of Abel-transformable images: The Gaussian basis-set expansion Abel transform method. *Review of Scientific Instruments*, 2002. 73(7): p. 2634.
73. Droege, A.T. and P.C. Engelking, Supersonic expansion cooling of electronically excited OH radicals. *Chemical Physics Letters*, 1983. 96(3): p. 316.
74. Dunning, T.H., Gaussian basis sets for use in correlated molecular calculations. I. The atoms boron through neon and hydrogen. *The Journal of Chemical Physics*, 1989. 90(2): p. 1007.
75. Dupuis, M., J.J. Wendoloski, and W.A. Lester, Electronic structure of vinoxy radical CH<sub>2</sub>CHO. *The Journal of Chemical Physics*, 1982. 76(1): p. 488.
76. Duvernay, F., et al., Formaldehyde Chemistry in Cometary Ices: On the Prospective Detection of NH<sub>2</sub>CH<sub>2</sub>OH, HOCH<sub>2</sub>OH, and Pom by the on-Board Rosina Instrument of the Rosetta Mission. *Astrophysical Journal*, 2014. 791(2): p. 75.
77. Duvernay, F., et al., Formaldehyde chemistry in cometary ices: the case of HOCH<sub>2</sub>OH formation. *Physical Chemistry Chemical Physics*, 2014. 16(44): p. 24200.
78. Dyke, J., E. Lee, and A. Morris, Vacuum Ultraviolet Photoelectron-Spectroscopy of Transient Species .7. Methyl Radical. *Journal of the Chemical Society-Faraday Transactions II*, 1976. 72: p. 1385.
79. Einstein, A., "for his services to Theoretical Physics, and especially for his discovery of the law of the photoelectric effect", Nobel Prize in Physics, 1921.
80. Einfeld, W. and J.S. Francisco, Structure, spectroscopic properties, and photochemistry of the hydroxymethoxy radical. *The Journal of Chemical Physics*, 2009. 131(13): p. 134313.

81. Ellison, G.B., P.C. Engelking, and W.C. Lineberger, An experimental determination of the geometry and electron affinity of methyl radical. *Journal of the American Chemical Society*, 1978. 100: p. 2556.
82. Ellison, G.B., P.C. Engelking, and W.C. Lineberger, Photoelectron-Spectroscopy of Alkoxide and Enolate Negative-Ions. *Journal of Physical Chemistry*, 1982. 86(25): p. 4873.
83. Endo, Y., S. Saito, and E. Hirota, The microwave spectrum of the methoxy radical CH<sub>3</sub>O. *The Journal of Chemical Physics*, 1984. 81(1): p. 122.
84. Engelking, P.C., Approximate Rotational Band Shifts. *Journal of Physical Chemistry*, 1986. 90(19): p. 4544.
85. Eppink, A.T.J.B. and D.H. Parker, Velocity map imaging of ions and electrons using electrostatic lenses: Application in photoelectron and photofragment ion imaging of molecular oxygen. *Review of Scientific Instruments*, 1997. 68(9): p. 3477.
86. Ervin, K.M., PESCAL, available online at [wolfweb.unr.edu/~ervin/pes/2010](http://wolfweb.unr.edu/~ervin/pes/2010).
87. Ervin, K.M., et al., The Only Stable State of O<sub>2</sub><sup>-</sup> is the X <sup>2</sup>P Ground State and it (Still!) has an Adiabatic Electron Detachment Energy of 0.45 eV. *Journal of Physical Chemistry A*, 2003. 107(41): p. 8521.
88. Ervin, K.M. and V.F. DeTuro, Anchoring the gas-phase acidity scale. *Journal of Physical Chemistry A*, 2002. 106(42): p. 9947.
89. Ervin, K.M., J. Ho, and W.C. Lineberger, Ultraviolet Photoelectron-Spectrum of NO<sub>2</sub>. *Journal of Physical Chemistry*, 1988. 92(19): p. 5405.
90. Ervin, K.M., et al., Naphthyl Radical: Negative Ion Photoelectron Spectroscopy, Franck-Condon Simulation, and Thermochemistry. *Journal of Physical Chemistry A*, 2001. 105(48): p. 10822.
91. Fawzy, W.M., T.J. Sears, and P.B. Davies, Infrared Diode-Laser Spectroscopy of the Nu-3 Fundamental of the CD<sub>3</sub> Radical. *The Journal of Chemical Physics*, 1990. 92(12): p. 7021.
92. Fehsenfeld, F.C. and A.L. Schmeltekopf, Ion-Molecule Reaction Rates Measured in a Discharge Afterglow. *Advances in Chemistry*, 1969. 80: p. 83.
93. Feldmann, M.T., et al., Aminomethanol water elimination: Theoretical examination. *The Journal of Chemical Physics*, 2005. 123(3): p. 34304.
94. Ferguson, E.E., A Personal history of the early development of the flowing afterglow technique for ion-molecule reaction studies. *Journal of the American Society for Mass Spectrometry*, 1992. 3(5): p. 479.
95. Fermi, E. and E. Teller, The capture of negative mesotrons in matter. *Physical Review*, 1947. 72(5): p. 399.
96. Fiebig, T., et al., Femtosecond Dynamics of Double Proton Transfer in a Model DNA Base Pair: 7-Azaindole Dimers in the Condensed Phase. *The Journal of Physical Chemistry A*, 1999. 103(37): p. 7419.

97. Finlayson-Pitts, B.J. and J.N. Pitts, *Chemistry of the Upper and Lower Atmosphere: Theory, Experiments, and Applications* 2000, San Diego: Academic Press.
98. Finnigan, D.J., et al., Centrifugal Distortion in Microwave-Spectra of cis-Nitrous and trans-Nitrous Acids - Determination of Quadratic Potential Functions and Average Structures. *Journal of the Chemical Society-Faraday Transactions II*, 1972. 68: p. 548.
99. Fittschen, C., H. Hippler, and B. Viskolcz, The beta C-C bond scission in alkoxy radicals: thermal unimolecular decomposition of t-butoxy radicals. *Physical Chemistry Chemical Physics*, 2000. 2(8): p. 1677.
100. Folmer, D.E., E.S. Wisniewski, and A.W. Castleman, Excited state double proton transfer in the 7-azaindole dimer revisited. *Chemical Physics Letters*, 2000. 318(6): p. 637.
101. Folmer, D.E., et al., Water-Assisted Proton Transfer in the Monomer of 7-Azaindole. *The Journal of Physical Chemistry A*, 2000. 104(45): p. 10545.
102. Foster, S.C., et al., Implications of the rotationally resolved spectra of the alkoxy radicals for their electronic structure. *The Journal of Physical Chemistry*, 1986. 90(26): p. 6766.
103. Foster, S.C., et al., Free jet-cooled laser-induced fluorescence spectrum of methoxy. 1. Vibronic analysis of the A and X states. *The Journal of Physical Chemistry*, 1988. 92(21): p. 5914.
104. Francisco, J.S. and W. Eisfeld, Atmospheric Oxidation Mechanism of Hydroxymethyl Hydroperoxide. *Journal of Physical Chemistry A*, 2009. 113(26): p. 7593.
105. Frederick, J.H. and C. Woywod, General formulation of the vibrational kinetic energy operator in internal bond-angle coordinates. *The Journal of Chemical Physics*, 1999. 111(16): p. 7255.
106. Frisch, M.J., et al., *Gaussian 09 Revision B.01*, 2009, Gaussian, Inc.: Wallingford, CT, USA.
107. Frye, J.M., T.J. Sears, and D. Leitner, Diode laser spectroscopy of the  $\nu_2$  band of  $\text{CD}_3$ . *The Journal of Chemical Physics*, 1988. 88: p. 5300.
108. Fuke, K. and H. Ishikawa, Dynamics of proton transfer reactions of model base pairs in the ground and excited states: Revisited. *Chemical Physics Letters*, 2015. 623: p. 117.
109. Fuke, K., H. Yoshiuchi, and K. Kaya, Electronic spectra and tautomerism of hydrogen-bonded complexes of 7-azaindole in a supersonic jet. *The Journal of Physical Chemistry*, 1984. 88(24): p. 5840.
110. Gao, A., Z. Jiao, and A. Li, The alkoxy radicals and their anions: Structures and electron affinities. *Journal of Molecular Structure: Theochem*, 2008. 848(13): p. 40.
111. Garand, E., T.I. Yacovitch, and D.M. Neumark, Slow photoelectron velocity-map imaging spectroscopy of  $\text{C}_2\text{N}^-$ ,  $\text{C}_4\text{N}^-$ , and  $\text{C}_6\text{N}^-$ . *The Journal of Chemical Physics*, 2009. 130(6): p. 064304.
112. Gardenier, G.H., M.A. Johnson, and A.B. McCoy, Spectroscopic Study of the Ion-Radical H-Bond in  $\text{H}_4\text{O}_2^+$ . *Journal of Physical Chemistry A*, 2009. 113(16): p. 4772.

113. Gardenier, G.H., M.A. Johnson, and A.B. McCoy, Correction to "Spectroscopic Study of the Ion-Radical H-Bond in  $\text{H}_4\text{O}_2^+$ ". *Journal of Physical Chemistry A*, 2012. 116(34): p. 8797.
114. Garrett, W.R., Critical binding of an electron to a non-stationary electric dipole. *Chemical Physics Letters*, 1970. 5(7): p. 393.
115. Garrett, W.R., Critical binding of an electron to a rotationally excited dipolar system. *Physical Review A*, 1971. 3(3): p. 961.
116. Gauss, J., M.E. Harding, and P.G. Szalay, CFOUR Coupled-Cluster techniques for Computational Chemistry, 2015.
117. Goebbert, D.J., K. Pichugin, and A. Sanov, Low-lying electronic states of  $\text{CH}_3\text{NO}_2$  via photoelectron imaging of the nitromethane anion. *The Journal of Chemical Physics*, 2009. 131(16): p. 164308.
118. Gopalakrishnan, S., L. Zu, and T.A. Miller, Radiative and non-radiative decay of selected vibronic levels of the (B)over-tilde state of alkoxy radicals. *Chemical Physics Letters*, 2003. 380(5-6): p. 749.
119. Gordon, J.P., et al., Molecular Microwave Oscillator and High-Resolution Spectrometer. *Science*, 1954. 120(3124): p. 780.
120. Gordon, J.P., H.J. Zeiger, and C.H. Townes, Molecular Microwave Oscillator and New Hyperfine Structure in the Microwave Spectrum of  $\text{NH}_3$ . *Physical Review*, 1954. 95(1): p. 282.
121. Gordon, M.S., Hydrogen Transfer in 7-Azaindole. *The Journal of Physical Chemistry*, 1996. 100(10): p. 3974.
122. Grana, R., et al., An experimental and kinetic modeling study of combustion of isomers of butanol. *Combustion and Flame*, 2010. 157(11): p. 2137.
123. Graul, S.T. and R.R. Squires, Gas-phase reactions of the methyl anion. *Journal of the American Chemical Society*, 1989. 111: p. 892.
124. Grumbling, E.R. and A. Sanov, Photoelectron angular distributions in negative-ion photodetachment from mixed sp states. *The Journal of Chemical Physics*, 2011. 135(16): p. 164302.
125. Guilmot, J.M., M. Godefroid, and M. Herman, Rovibrational Parameters for trans-Nitrous Acid. *Journal of Molecular Spectroscopy*, 1993. 160(2): p. 387.
126. Guilmot, J.M., F. Melen, and M. Herman, Rovibrational Parameters for cis-Nitrous Acid. *Journal of Molecular Spectroscopy*, 1993. 160(2): p. 401.
127. Hagen, O.F. and W. Obert, Cluster Formation in Expanding Supersonic Jets: Effect of Pressure, Temperature, Nozzle Size, and Test Gas. *The Journal of Chemical Physics*, 1972. 56(5): p. 1793.
128. Hall, R.T. and G.C. Pimentel, Isomerization of Nitrous Acid - an Infrared Photochemical Reaction. *The Journal of Chemical Physics*, 1963. 38(8): p. 1889.

129. Handschuh, H., G. Gantefoer, and W. Eberhardt, Vibrational spectroscopy of clusters using a "magnetic bottle" electron spectrometer. *Review of Scientific Instruments*, 1995. 66(7): p. 3838.
130. Hanstorp, D. and M. Gustafsson, Determination of the Electron-Affinity of Iodine. *Journal of Physics B: Atomic, Molecular and Optical Physics*, 1992. 25(8): p. 1773.
131. Harris, D.C. and M.D. Bertolucci, *Symmetry and spectroscopy: an introduction to vibrational and electronic spectroscopy*. 1989: Dover Publications.
132. Hays, B.M. and S.L. Widicus-Weaver, Theoretical Examination of O(<sup>1</sup>D) Insertion Reactions to Form Methanediol, Methoxymethanol, and Aminomethanol. *Journal of Physical Chemistry A*, 2013. 117(32): p. 7142.
133. Hermann, H.W. and S.R. Leone, Photofragment infrared emission spectroscopy: Vibrational progression and potential parameters of the CH<sub>3</sub> (ν<sub>2</sub>) umbrella mode. *The Journal of Chemical Physics*, 1982. 76: p. 4759.
134. Herschbach, D.R., Y.T. Lee, and J.C. Polanyi, "for their contributions concerning the dynamics of chemical elementary processes", Nobel Prize in Chemistry, 1986.
135. Hertz, H., Ueber einen Einfluss des ultravioletten Lichtes auf die elektrische Entladung. *Annalen der Physik*, 1887. 267(8): p. 983.
136. Herzberg, G., Bakerian Lecture - Spectra and Structures of Free Methyl and Free Methylene. *Proceedings of the Royal Society of London Series A - Mathematical and Physical Sciences*, 1961. 262(1310): p. 291.
137. Herzberg, G. and J. Shoosmith, Absorption Spectrum of Free CH<sub>3</sub> and CD<sub>3</sub> Radicals. *Canadian Journal of Physics*, 1956. 34(5): p. 523.
138. Ho, P., et al., Photo-Dissociation of Formaldehyde in a Molecular-Beam. *The Journal of Chemical Physics*, 1982. 76(7): p. 3630.
139. Hock, C., et al., Slow photoelectron velocity-map imaging spectroscopy of cold negative ions Slow photoelectron velocity-map imaging spectroscopy of cold negative ions. *The Journal of Chemical Physics*, 2012. 137: p. 244201.
140. Hooker, S. and C.E. Webb, *Laser physics 2010*: Oxford University Press. 586.
141. Hoeper, U., P. Botschwina, and H. Kaepfel, Theoretical study of the Jahn-Teller effect in X<sup>2</sup>E CH<sub>3</sub>O. *The Journal of Chemical Physics*, 2000. 112(9): p. 4132.
142. Hotop, H. and W.C. Lineberger, Binding energies in atomic negative ions. *Journal of Physical and Chemical Reference Data*, 1975. 4(3): p. 539.
143. Hotop, H. and W.C. Lineberger, Binding Energies in Atomic Negative Ions: II. *Journal of Physical and Chemical Reference Data*, 1985. 14(3): p. 731.
144. Huang, C.K., et al., Dynamics of the reactions of O(<sup>1</sup>D) with CD<sub>3</sub>OH and CH<sub>3</sub>OD studied with time-resolved Fourier-transform IR spectroscopy. *The Journal of Chemical Physics*, 2012. 137(16): p. 164307.

145. Indarto, A., Heterogeneous Reactions of HONO Formation From NO<sub>2</sub> and HNO<sub>3</sub>: A Review. *Research on Chemical Intermediates*, 2012. 38(3-5): p. 1029.
146. Inoue, G., H. Akimoto, and M. Okuda, Laser-Induced Fluorescence-Spectra of CH<sub>3</sub>O. *Chemical Physics Letters*, 1979. 63(2): p. 213.
147. Inoue, G., M. Okuda, and H. Akimoto, Laser-induced fluorescence of the C<sub>2</sub>H<sub>5</sub>O radical. *The Journal of Chemical Physics*, 1981. 75(5): p. 2060.
148. Ishikawa, H., et al., Deuteration effect on the NH/ND stretch band of the jet-cooled 7-azaindole and its tautomeric dimers: Relation between the vibrational relaxation and the ground-state double proton-transfer reaction. *Chemical Physics*, 2013. 419: p. 101.
149. Jacox, M.E., Matrix-Isolation Study of IR-Spectrum and Structure of CH<sub>3</sub> Free-Radical. *Journal of Molecular Spectroscopy*, 1977. 66(2): p. 272.
150. Jentschura, U.D., et al., *The Energy Levels of Hydrogen and Deuterium (version 2.1)*, 2017: Gaithersburg, MD.
151. Jin, J., et al., Dispersed fluorescence spectroscopy of primary and secondary alkoxy radicals. *The Journal of Chemical Physics*, 2004. 121(23): p. 11780.
152. Johnson, C.J., et al., Electron Affinities, Well Depths, and Vibrational Spectroscopy of cis- and trans-HOCO. *Journal of the American Chemical Society*, 2011. 133(49): p. 19606.
153. Jones, L.H., Measurement and analysis of the  $\nu_2$  bands of <sup>14</sup>ND<sub>3</sub> and <sup>15</sup>ND<sub>3</sub>. *Journal of Molecular Spectroscopy*, 1979. 74: p. 409.
154. Jungkamp, T.P.W., J.N. Smith, and J.H. Seinfeld, Atmospheric Oxidation Mechanism of n-Butane: The Fate of Alkoxy Radicals. *The Journal of Physical Chemistry A*, 1997. 101(24): p. 4392.
155. Kang, C., J.T. Yi, and D.W. Pratt, Stark effects in the gas phase: Dipole moment of 7-azaindole in its ground and electronically excited states. *Chemical Physics Letters*, 2006. 423(1-3): p. 7.
156. Kasdan, A. and W.C. Lineberger, Alkali-metal negative ions. II. Laser photoelectron spectrometry. *Physical Review A*, 1974. 10(5): p. 1658.
157. Kato, T. and H. Shirota, Intermolecular vibrational modes and orientational dynamics of cooperative hydrogen-bonding dimer of 7-azaindole in solution. *The Journal of Chemical Physics*, 2011. 134(16): p. 164504.
158. Kebarle, P. and S. Chowdhury, Electron Affinities and Electron-Transfer Reactions. *Chemical Reviews*, 1987. 87(3): p. 513.
159. Kendall, R.A., T.H. Dunning, and R.J. Harrison, Electron affinities of the first-row atoms revisited. Systematic basis sets and wave functions. *The Journal of Chemical Physics*, 1992. 96(9): p. 6796.
160. Kent, D.R., et al., A theoretical study of the conversion of gas phase methanediol to formaldehyde. *The Journal of Chemical Physics*, 2003. 119(10): p. 5117.

161. Khriachtchev, L., et al., HONO in Solid Kr: Site-Selective trans  $\leftrightarrow$  cis Isomerization with Narrow-Band Infrared Radiation. *The Journal of Chemical Physics*, 2000. 113(10): p. 4265.
162. Kim, J.B., et al., Spectroscopic observation of resonances in the F + H<sub>2</sub> reaction. *Science*, 2015. 349(6247): p. 510.
163. King, G.W. and D. Moule, Ultraviolet Absorption Spectrum of Nitrous Acid in the Vapor State. *Canadian Journal of Chemistry*, 1962. 40(11): p. 2057.
164. Kleffmann, J., et al., Daytime Formation of Nitrous Acid: A Major Source of OH Radicals in a Forest. *Geophysical Research Letters*, 2005. 32(5): p. 5818.
165. Kochi, J.K., Chemistry of Alkoxy Radicals - Cleavage Reactions. *Journal of the American Chemical Society*, 1962. 84(7): p. 1193.
166. Kraemer, W.P., et al., Inversion-vibration energies of CH<sub>3</sub><sup>-</sup> and adiabatic electron affinity of CH<sub>3</sub>. *Journal of Molecular Spectroscopy*, 1991. 147: p. 526.
167. Kurtenbach, R., et al., Investigations of Emissions and Heterogeneous Formation of HONO in a Road Traffic Tunnel. *Atmospheric Environment*, 2001. 35(20): p. 3385.
168. Kuyatt, C.E. and J.A. Simpson, Electron monochromator design. *Review of Scientific Instruments*, 1967. 38(1): p. 103.
169. Kwon, O.H. and D.J. Jang, Excited-state double proton transfer of 7-azaindole in water nanopools. *Journal of Physical Chemistry B*, 2005. 109(43): p. 20479.
170. Kwon, O.H. and A.H. Zewail, Reply to Catalan: Double-proton-transfer dynamics of photo-excited 7-azaindole dimers. *Proceedings of the National Academy of Sciences*, 2008. 105(45): p. E79.
171. Kwon, O.-H. and A.H. Zewail, Double proton transfer dynamics of model DNA base pairs in the condensed phase. *Proceedings of the National Academy of Sciences*, 2007. 104(21): p. 8703.
172. Laidler, K.J. and M.C. King, Development of transition-state theory. *The Journal of Physical Chemistry*, 1983. 87(15): p. 2657.
173. Larrieu, C., A. Dargelos, and M. Chaillet, Theoretical-Study of Nitrous-Acid Electronic-Spectrum and Photofragmentation. *Chemical Physics Letters*, 1982. 91(6): p. 465.
174. Lehman, J.H. and W.C. Lineberger, Photoelectron spectroscopy of the thiazate (NSO<sup>-</sup>) and thionitrite (SNO<sup>-</sup>) isomer anions. *The Journal of Chemical Physics*, 2017. 147(1): p. 013943.
175. Levine, I.N., *Quantum Chemistry 2009*: Pearson Prentice Hall: p. 750.
176. Li, C., et al., A theoretical study of the potential energy surfaces for the double proton transfer reaction of model DNA base pairs. *Phys. Chem. Chem. Phys.*, 2017. 19(6): p. 4802.
177. Li, X., et al., Unexpected Stability of Al<sub>4</sub>H<sub>6</sub>: A Borane Analog? *Science*, 2007. 315(5810): p. 356.
178. Lineberger, W.C. and B.W. Woodward, High Resolution Photodetachment of S<sup>-</sup> near Threshold. *Physical Review Letters*, 1970. 25(7): p. 424.

179. Liu, D.J. and T. Oka, Experimental Determination of the Ground-State Inversion Splitting in  $\text{H}_3\text{O}^+$ . *Physical Review Letters*, 1985. 54: p. 1787.
180. Liu, H.T., et al., Observation of mode-specific vibrational autodetachment from dipole-bound states of cold anions. *Angewandte Chemie - International Edition*, 2013. 52(34): p. 8976.
181. Liu, J.J., D. Melnik, and T.A. Miller, Rotationally resolved  $\text{B} \leftarrow \text{X}$  electronic spectra of the isopropoxy radical: A comparative study. *The Journal of Chemical Physics*, 2013. 139(9): p. 094308.
182. Liu, J.J., et al., Laser-Induced Fluorescence Spectroscopy of Jet-Cooled t-Butoxy. *Journal of Physical Chemistry A*, 2015. 119(49): p. 11804.
183. Lu, Y.-J., Photoelectron Spectroscopy of Small Organic Anions Prepared Using a Novel Cold Ion Source Employing Entrainment of Charged Particles, University of Colorado, 2014.
184. Lu, Y.-J., J.H. Lehman, and W.C. Lineberger, A versatile, pulsed anion source utilizing plasma-entrainment: Characterization and applications. *The Journal of Chemical Physics*, 2015. 142(4): p. 44201.
185. Lykke, K.R., R.D. Mead, and W.C. Lineberger, Observation of Dipole-Bound States of Negative Ions. *Physical Review Letters*, 1984. 52(25): p. 2221.
186. Lykke, K.R., K.K. Murray, and W.C. Lineberger, Threshold photodetachment of  $\text{H}^-$ . *Physical Review A*, 1991. 43(11): p. 6104.
187. Lykke, K.R., et al., Autodetachment spectroscopy and dynamics of  $\text{CH}_2\text{CN}^-$  and  $\text{CD}_2\text{CN}^-$ . *The Journal of Chemical Physics*, 1987. 87(12): p. 6842.
188. Mabbs, R., et al., Photoelectron imaging: an experimental window into electronic structure. *Chemical Society Reviews*, 2009. 38(8): p. 2169.
189. Malbon, C.L., D.R. Yarkony, and X.L. Zhu, On the electronic structure of the ground state of cyclopentoxy. The case for a two coupled state description. *Journal of Molecular Spectroscopy*, 2015. 311: p. 36.
190. Marks, J., et al., Spectroscopy and dynamics of the dipole-supported state of acetyl fluoride enolate anion. *The Journal of Chemical Physics*, 1988. 88(11): p. 6785.
191. Mead, R.D., et al., Spectroscopy and dynamics of the dipole-bound state of acetaldehyde enolate. *The Journal of Chemical Physics*, 1984. 81(11): p. 4883.
192. Mehata, M.S., A.K. Singh, and R.K. Sinha, Investigation of charge-separation/change in dipole moment of 7-azaindole: Quantitative measurement using solvatochromic shifts and computational approaches. *Journal of Molecular Liquids*, 2017. 231: p. 39.
193. Miller, J.T., et al., CARS Spectroscopy of Gas-Phase  $\text{CD}_3$ . *Chemical Physics Letters*, 1989. 158(3-4): p. 179.
194. Mitchell, S.E., P.M. Conklin, and J.W. Farley, First observation of autodetachment lifetimes of methide,  $\text{CH}_3^-$ . *The Journal of Chemical Physics*, 2003. 118: p. 11017.

195. Mozhayskiy, V.A. and A.I. Krylov, ezSpectrum 3.0, available online at <http://iopshell.usc.edu/downloads/>, 2016.
196. Mukherjee, M., B. Bandyopadhyay, and T. Chakraborty, Ultraviolet and infrared spectroscopy of matrix-isolated 7-azaindole dimer: Matrix effect on excited state tautomerization. *Chemical Physics Letters*, 2012. 546: p. 74.
197. Murzin, S.N. and O.N. Stepanov, Inversion Spectra of  $^{14}\text{ND}_3$  and  $^{15}\text{ND}_3$  in the 1.29-2.56 GHz Frequency-Range. *Optika i Spektroskopiya*, 1990. 69(3): p. 497.
198. Nakajima, A., et al., Photoelectron spectroscopy of 7-azaindole-water cluster anions. *The European Physical Journal D*, 1999. 9(1): p. 303.
199. Neeb, P., et al., Formation of hydroxymethyl hydroperoxide and formic acid in alkene ozonolysis in the presence of water vapour. *Atmospheric Environment*, 1997. 31(10): p. 1417.
200. Nelson, D.J., et al., Anion photoelectron spectroscopy of deprotonated ortho-, meta-, and para-methylphenol. *The Journal of Chemical Physics*, 2017. 146(7): p. 074302.
201. Nelson, D.J., A.M. Oliveira, and W.C. Lineberger, Anion Photoelectron Spectroscopy of Deprotonated Indole and Indoline. *The Journal of Chemical Physics*, 2017. submitted.
202. Neumark, D.M., Transition-State Spectroscopy via Negative Ion Photodetachment. *Accounts of Chemical Research*, 1993. 26(2): p. 33.
203. Neumark, D.M., Slow Electron Velocity-Map Imaging of Negative Ions: Applications to Spectroscopy and Dynamics. *Journal of Physical Chemistry A*, 2008. 112(51): p. 13287.
204. Neumark, D.M., et al., Infrared-Spectrum and Autodetachment Dynamics of  $\text{NH}^-$ . *The Journal of Chemical Physics*, 1985. 83(9): p. 4364.
205. Neumark, D.M., et al., Laser photodetachment measurement of the electron affinity of atomic oxygen. *Physical Review A*, 1985. 32(3): p. 1890.
206. Oliveira, A.M., et al., Photoelectron Spectroscopy of cis-Nitrous Acid Anion ( $\text{cis-HONO}^-$ ). *Journal of Physical Chemistry A*, 2016. 120(10): p. 1652.
207. Oliveira, A.M., et al., Photoelectron spectroscopy of the hydroxymethoxide anion,  $\text{H}_2\text{C}(\text{OH})\text{O}^-$ . *The Journal of Chemical Physics*, 2016. 145(12): p. 124317.
208. Oliveira, A.M., et al., Photoelectron spectroscopy of the methide anion: Electron affinities of  $\text{CH}_3^-$  and  $\text{CD}_3^-$  and inversion splittings of  $\text{CH}_3^-$  and  $\text{CD}_3^-$ . *Journal of the American Chemical Society*, 2015. 137(40): p. 12939.
209. Orlando, J.J., G.S. Tyndall, and T.J. Wallington, The atmospheric chemistry of alkoxy radicals. *Chemical Reviews*, 2003. 103(12): p. 4657.
210. Osborn, D.L., et al., Photodissociation spectroscopy and dynamics of the  $\text{N}_2\text{O}_2^-$  anion. *The Journal of Chemical Physics*, 1996. 104(13): p. 5026.
211. Osborn, D.L., et al., Electronic States of the Quasilinear Molecule Propargylene ( $\text{HCCCH}$ ) from Negative Ion Photoelectron Spectroscopy. *Journal of the American Chemical Society*, 2014. 136(29): p. 10361.

212. Pamidimukkala, K.M., D. Rogers, and G.B. Skinner, Ideal-Gas Thermodynamic Properties of CH<sub>3</sub>, CD<sub>3</sub>, CD<sub>4</sub>, C<sub>2</sub>D<sub>2</sub>, C<sub>2</sub>D<sub>4</sub>, C<sub>2</sub>D<sub>6</sub>, C<sub>2</sub>H<sub>6</sub>, CH<sub>3</sub>N<sub>2</sub>CH<sub>3</sub>, and CD<sub>3</sub>N<sub>2</sub>CD<sub>3</sub>. *Journal of Physical and Chemical Reference Data*, 1982. 11(1): p. 83.
213. Parsons, A.F., *An introduction to free-radical chemistry*, 2000: Blackwell Science.
214. Patterson, T.A., et al., Resonances in alkali negative-ion photodetachment and electron affinities of the corresponding neutrals. *Physical Review Letters*, 1974. 32(5): p. 189.
215. Peoples, P.R. and J.B. Grutzner, Structure of the 7-Phenylbornyl Carbanion - a Pyramidal Organo-Lithium and Planar Organopotassium. *Journal of the American Chemical Society*, 1980. 102(14): p. 4709.
216. Peterson, K.A., D. Feller, and D.A. Dixon, Chemical accuracy in ab initio thermochemistry and spectroscopy: current strategies and future challenges. *Theoretical Chemistry Accounts*, 2012. 131(1): p. 1079.
217. Poularikas, A.D., *The Transforms and Applications Handbook*. 2000: CRC Press.
218. Rajamaki, T., A. Miani, and L. Halonen, Vibrational energy levels for symmetric and asymmetric isotopomers of ammonia with an exact kinetic energy operator and new potential energy surfaces. *The Journal of Chemical Physics*, 2003. 118(14): p. 6358.
219. Rajamaki, T., A. Miani, and L. Halonen, Six-dimensional ab initio potential energy surfaces for H<sub>3</sub>O<sup>+</sup> and NH<sub>3</sub>: Approaching the subwave number accuracy for the inversion splittings. *The Journal of Chemical Physics*, 2003. 118(24): p. 10929.
220. Ramond, T.M., et al., Vibronic structure of alkoxy radicals via photoelectron spectroscopy. *The Journal of Chemical Physics*, 2000. 112(3): p. 1158.
221. Reiche, F., et al., Double-Resonance Overtone Photofragment Spectroscopy of trans-HONO. I. Spectroscopy and Intramolecular Dynamics. *The Journal of Chemical Physics*, 2000. 112(20): p. 8885.
222. Reiche, F., et al., Double-Resonance Overtone Photofragment Spectroscopy of trans-HONO. II. State- And Time-Resolved Dissociation and OH-Product State Distributions. *The Journal of Chemical Physics*, 2002. 116(23): p. 10267.
223. Rosenberg, R.E., Addition of anions to carbonyl compounds: An ab initio study. *Journal of Organic Chemistry*, 2008. 73(17): p. 6636.
224. Rosspeintner, A., B. Lang, and E. Vauthey, Ultrafast Photochemistry in Liquids. *Annual Review of Physical Chemistry*, 2013. 64(1): p. 247.
225. Ruscic, B., Active Thermochemical Tables: Sequential Bond Dissociation Enthalpies of Methane, Ethane, and Methanol and the Related Thermochemistry. *Journal of Physical Chemistry A*, 2015. 119(28): p. 7810.
226. Sakota, K., et al., Excited-State Triple-Proton Transfer in 7-Azaindole(H<sub>2</sub>O)<sub>2</sub> and Reaction Path Studied by Electronic Spectroscopy in the Gas Phase and Quantum Chemical Calculations. *The Journal of Physical Chemistry A*, 2010. 114(42): p. 11161.

227. Sakota, K. and H. Sekiya, Excited-state double-proton transfer in the 7-azaindole dimer in the gas phase. 2. Cooperative nature of double-proton transfer revealed by H/D kinetic isotopic effects. *Journal of Physical Chemistry A*, 2005. 109(12): p. 2722.
228. Sanov, A., Laboratory-Frame Photoelectron Angular Distributions in Anion Photodetachment: Insight into Electronic Structure and Intermolecular Interactions. *Annual Review of Physical Chemistry*, 2014. 65: p. 341.
229. Sanov, A., et al., Photodetachment anisotropy for mixed s-p states: 8/3 and other fractions. *The Journal of Chemical Physics*, 2013. 138: p. 054311.
230. Schmidt, M.W. and M.S. Gordon, The construction and interpretation of MCSCF wavefunctions. *Annual Review of Physical Chemistry*, 1998. 49(1): p. 233.
231. Schwenke, D.W., A theoretical study of the re-vibrational spectrum of the X state of CH<sub>3</sub>. *Spectrochimica Acta Part A - Molecular and Biomolecular Spectroscopy*, 1999. 55(3): p. 731.
232. Sears, T.J., et al., Diode laser absorption spectroscopy of D<sub>3</sub>O<sup>+</sup>: Determination of the equilibrium structure and potential function of the oxonium ion. *The Journal of Chemical Physics*, 1985. 83: p. 2676.
233. Sears, T.J., et al., Extended measurements of the  $\nu_2$  band of CD<sub>3</sub> and the determination of the vibrational potential function for methyl radical. *The Journal of Chemical Physics*, 1989. 90: p. 2125.
234. Sekiya, H. and K. Sakota, Excited-state double-proton transfer in the 7-azaindole dimer in the gas phase. Resolution of the stepwise versus concerted mechanism controversy and a new paradigm. *Bulletin of the Chemical Society of Japan*, 2006. 79(3): p. 373.
235. Sekiya, H. and K. Sakota, Excited-state double-proton transfer in a model DNA base pair: Resolution for stepwise and concerted mechanism controversy in the 7-azaindole dimer revealed by frequency- and time-resolved spectroscopy, 2008, Elsevier. p. 81.
236. Sekiya, H., et al., Spectroscopic study on the structural isomers of 7-azaindole (ethanol)<sub>n</sub> (n=1-3) and multiple-proton transfer reactions in the gas phase. *The Journal of Chemical Physics*, 2009. 130(22): p. 224307.
237. Sengupta, D., R. Sumathi, and S.D. Peyerimhoff, Unimolecular Decomposition of the Isomers of [HNO<sub>2</sub>]<sup>+</sup> and [HNO<sub>2</sub>]<sup>-</sup> Systems: A DFT Study. *Chemical Physics*, 1999. 248(2-3): p. 147.
238. Serrano-Andres, L., et al. Theoretical studies on the spectroscopy of the 7-azaindole monomer and dimer. John Wiley & Sons, Inc.
239. Sharp, T.E. and H.M. Rosenstock, Franck-Condon Factors for Polyatomic Molecules. *The Journal of Chemical Physics*, 1964. 41(11): p. 3453.
240. Shen, B.B., B.L.J. Poad, and R.E. Continetti, Photoelectron-Photofragment Coincidence Studies of the tert-Butoxide Anion (CH<sub>3</sub>)<sub>3</sub>CO<sup>-</sup>, the Carbanion Isomer (CH<sub>3</sub>)<sub>2</sub>CH<sub>2</sub>COH<sup>-</sup>, and Corresponding Radicals. *The Journal of Physical Chemistry A*, 2014. 118(44): p. 10223.

241. Shirota, H., T. Fukuda, and T. Kato, Solvent dependence of 7-azaindole dimerization. *Journal of Physical Chemistry B*, 2013. 117(50): p. 16196.
242. Shuman, N.S., D.E. Hunton, and A.A. Viggiano, Ambient and Modified Atmospheric Ion Chemistry: From Top to Bottom. *Chemical Reviews*, 2015. 115(10): p. 4542.
243. Simakov, A., et al., The dissociation of glycolate-astrochemical and prebiotic relevance. *Physical Chemistry Chemical Physics*, 2013. 15(39): p. 16615.
244. Simmie, J.M., et al., Enthalpies of Formation and Bond Dissociation Energies of Lower Alkyl Hydroperoxides and Related Hydroperoxy and Alkoxy Radicals. *The Journal of Physical Chemistry A*, 2008. 112(22): p. 5010.
245. Sironneau, V., et al., Absolute Line Intensities of HONO and DONO in the Far-Infrared and Re-Determination of the Energy Difference Between the trans- and cis- Species of Nitrous Acid. *Journal of Molecular Spectroscopy*, 2010. 259(2): p. 100.
246. Smalley, R.E., L. Wharton, and D.H. Levy, Molecular Optical Spectroscopy with Supersonic Beams and Jets. *Accounts of Chemical Research*, 1977. 10(4): p. 139.
247. Smith, J.R., J.B. Kim, and W.C. Lineberger, High-Resolution Threshold Photodetachment Spectroscopy of OH. *Physical Review A*, 1997. 55(3): p. 2036.
248. Song, Y., et al., A pulsed field ionization study of the dissociative photoionization reaction  $CD_4+h\nu \rightarrow CD_3^+ + D + e^-$ . *Chemical Physics Letters*, 2001. 347(1-3): p. 51.
249. Spataro, F. and A. Ianniello, Sources of Atmospheric Nitrous Acid: State of the Science, Current Research Needs, and Future Prospects. *Journal of the Air & Waste Management Association*, 2014. 64(11): p. 1232.
250. Spence, R. and W. Wild, The vapour pressure curve of formaldehyde, and some related data. *Journal of the Chemical Society*, 1935. 1(1): p. 506.
251. Stanton, J.F., Why CCSD(T) works: a different perspective. *Chemical Physics Letters*, 1997. 281(1): p. 130.
252. Su, T., et al., An experimental study of nucleophilic addition to formaldehyde in the gas phase. *J. Chem. Phys.*, 1978. 69: p. 407.
253. Takeuchi, S. and T. Tahara, Femtosecond Ultraviolet-Visible Fluorescence Study of the Excited-State Proton-Transfer Reaction of 7-Azaindole Dimer. *The Journal of Physical Chemistry A*, 1998. 102(40): p. 7740.
254. Takeuchi, S. and T. Tahara, Excitation-wavelength dependence of the femtosecond fluorescence dynamics of 7-azaindole dimer: Further evidence for the concerted double proton transfer in solution. *Chemical Physics Letters*, 2001. 347(1-3): p. 108.
255. Takeuchi, S. and T. Tahara, The answer to concerted versus step-wise controversy for the double proton transfer mechanism of 7-azaindole dimer in solution. *Proceedings of the National Academy of Sciences*, 2007. 104(13): p. 5285.
256. Tarczay, G., S. Gopalakrishnan, and T.A. Miller, Theoretical prediction of spectroscopic constants of 1-alkoxy radicals. *Journal of Molecular Spectroscopy*, 2003. 220(2): p. 276.

257. Taylor, C.A., M. Ashraf El-Bayoumit, and M. Kasha, Excited-state two-proton tautomerism in hydrogen bonded N-heterocyclic base pairs. *Proceedings of the National Academy of Sciences*, 1969. 63(2): p. 253.
258. Tian, Z.X., et al., Lithium monoxide anion: A ground-state triplet with the strongest base to date. *Proceedings of the National Academy of Sciences of the United States of America*, 2008. 105(22): p. 7647.
259. Travers, M.J., et al., Photoelectron Spectroscopy of the  $\text{CH}_3\text{N}^-$  ion. *The Journal of Chemical Physics*, 1999. 111(12): p. 5349.
260. Trucks, G.W., J.A. Pople, and M. Head-Gordon, A fifth-order perturbation comparison of electron correlation theories. *Chemical Physics Letters*, 1989. 157(6): p. 479.
261. Truhlar, D.G., Current Status of Transition-State Theory. *The Journal of Physical Chemistry*, 1983. 87(15): p. 2664.
262. Truhlar, D.G., B.C. Garrett, and S.J. Klippenstein, Current Status of Transition-State Theory. *The Journal of Physical Chemistry*, 1996. 100(31): p. 12771.
263. Tyminska, N., M. Wloch, and A.T. Royappa, Mind the Correct Basis Set: A Case Study for Predicting Gas Phase Acidities of Small Compounds Using Calculations from First Principles. *International Journal of Quantum Chemistry*, 2015. 115(1): p. 42.
264. VandenBoer, T.C., et al., Nocturnal Loss and Daytime Source of Nitrous Acid Through Reactive Uptake and Displacement. *Nature Geoscience*, 2015. 8(1): p. 55.
265. Van Doren, J.M., et al., Experimental and Theoretical-Study of the Reaction of  $\text{HO}^-$  with NO. *The Journal of Chemical Physics*, 1993. 98(10): p. 7940.
266. Vasudev, R., R.N. Zare, and R.N. Dixon, Dynamics of Photo-Dissociation of HONO at 369 nm - Motional Anisotropy and Internal State Distribution of the OH Fragment. *Chemical Physics Letters*, 1983. 96(4): p. 399.
267. Vereecken, L. and J.S. Francisco, Theoretical studies of atmospheric reaction mechanisms in the troposphere. *Chemical Society Reviews*, 2012. 41(19): p. 6259.
268. Vogelhuber, K.M., et al., Photoelectron spectra of dihalomethyl anions: Testing the limits of normal mode analysis. *The Journal of Chemical Physics*, 2011. 134(18): p. 184306.
269. Vourliotakis, G., G. Skevis, and M.A. Founti, Some aspects of combustion chemistry of C1-C2 oxygenated fuels in low pressure premixed flames. *Proceedings of the Combustion Institute*, 2015. 35: p. 437.
270. Vuitton, V., et al., Negative ion chemistry in Titan's upper atmosphere. *Planetary and Space Science*, 2009. 57(13): p. 1558.
271. Wang, L.S., Perspective: Electrospray photoelectron spectroscopy: From multiply-charged anions to ultracold anions. *The Journal of Chemical Physics*, 2015. 143(4): p. 040901.
272. Watson, J.D. and F.H.C. Crick, Molecular Structure of Nucleic Acids: A Structure for Deoxyribose Nucleic Acid. *Nature*, 1953. 171(4356): p. 737.

273. Weber, J.M., W.H. Robertson, and M.A. Johnson, Argon predissociation and electron autodetachment spectroscopy of size-selected  $\text{CH}_3\text{NO}_2 \bullet \text{Ar}_n^-$  clusters. *The Journal of Chemical Physics*, 2001. 115(23): p. 10718.
274. Weichman, M.L., et al., Feshbach resonances in the exit channel of the  $\text{F} + \text{CH}_3\text{OH} \rightarrow \text{HF} + \text{CH}_3\text{O}$  reaction observed using transition-state spectroscopy. *Nature Chemistry*, 2017. 9: p. 950.
275. Weichman, M.L., et al., Isomer-specific vibronic structure of the 9-, 1-, and 2-anthracenyl radicals via slow photoelectron velocity-map imaging. *Proceedings of the National Academy of Sciences*, 2016. 113(7): p. 1698.
276. Weichman, M.L., J.B. Kim, and D.M. Neumark, Rovibronic structure in slow photoelectron velocity-map imaging spectroscopy of  $\text{CH}_2\text{CN}^-$  and  $\text{CD}_2\text{CN}^-$ . *The Journal of Chemical Physics*, 2014. 140(10): p. 104305.
277. Weichman, M.L., J.B. Kim, and D.M. Neumark, Slow Photoelectron Velocity-Map Imaging Spectroscopy of the ortho-Hydroxyphenoxide Anion. *Journal of Physical Chemistry A*, 2015. 119(23): p. 6140.
278. Weinberg, D.R., et al., Proton-coupled electron transfer, *Chemical Reviews*, 2012. 112(7): p. 4016.
279. Werner, H.J., et al., Molpro: a general-purpose quantum chemistry program package. *WIREs Comput. Mol. Sci.*, 2012. 2(2): p. 242.
280. Whitaker, B.J., *Imaging in molecular dynamics: technology and applications: a user's guide*. 2004: Cambridge University Press. 249.
281. Wickhamjones, C.T., et al.,  $\text{NH}_2$  Electron-Affinity. *The Journal of Chemical Physics*, 1989. 91(1989): p. 2762.
282. Wigner, E.P., On the Behavior of Cross Sections Near Thresholds. *Physical Review*, 1948. 73(9): p. 1002.
283. Wiley, W.C. and I.H. McLaren, Time-of-flight mass spectrometer with improved resolution. *Review of Scientific Instruments*, 1955. 26(12): p. 1150.
284. Wilson, E.B., J.C. Decius, and P.C. Cross, *Molecular vibrations: the theory of infrared and Raman vibrational spectra*. 1980: Dover Publications.
285. Yamada, C., E. Hirota, and K. Kawaguchi, Diode laser study of the  $\nu_2$  band of the methyl radical. *The Journal of Chemical Physics*, 1981. 75: p. 5256.
286. Yarkony, D.R., *Nonadiabatic Quantum Chemistry: Past, Present, and Future*. *Chemical Reviews*, 2012. 112(1): p. 481.
287. Yi, J. and H. Fang, Theoretical investigation on the water-assisted excited-state proton transfer of 7-azaindole derivatives: substituent effect. *Journal of Molecular Modeling*, 2017. 23(11): p. 312.

288. Yi, J. and H. Fang, Theoretical Study on the Substituent Effect on the Excited-State Proton Transfer in the 7-Azaindole-Water Derivatives. *Photochemistry and Photobiology*, 2017. in press: doi:10.1111/php.12839.
289. Young, R.A. and D.R. Yarkony, Towards a highly efficient theoretical treatment of Jahn-Teller effects in molecular spectra: The  $1^2A$  and  $2^2A$  electronic states of the ethoxy radical. *The Journal of Chemical Physics*, 2006. 125(23): p. 234301.
290. Yu, S.Y., C.G. Zhang, and M.B. Huang, A CAS Study of the  $S_0$ ,  $T_1$ ,  $S_1$ ,  $T_2$ , and  $S_2$  States of the trans-HONO Molecule. *Chemical Physics Letters*, 2007. 440(4-6): p. 187.
291. Yu, X.F., S. Yamazaki, and T. Taketsugu, Concerted or stepwise mechanism? CASPT2 and LC-TDDFT study of the excited-state double proton transfer in the 7-azaindole dimer. *Journal of Chemical Theory and Computation*, 2011. 7(4): p. 1006.
292. Yu, X.-f., S. Yamazaki, and T. Taketsugu, Solvent effects on the excited-state double proton transfer mechanism in the 7-azaindole dimer: a TDDFT study with the polarizable continuum model. *Phys. Chem. Chem. Phys.*, 2017. 19(34): p. 23289.
293. Zahedi, M., J.A. Harrison, and J.W. Nibler, 266 nm  $CH_3I$  Photodissociation -  $CH_3$  Spectra and Population-Distributions by Coherent Raman-Spectroscopy. *The Journal of Chemical Physics*, 1994. 100(6): p. 4043.
294. Zhao, Y.C., et al., Theoretical studies on the reactions of formaldehyde with OH and OH. *Journal of Molecular Structure: Theochem*, 2007. 818(1-3): p. 155.
295. Zhou, S., et al., An ab initio global potential-energy surface for and vibrational spectrum of the Renner-Teller system An ab initio global potential-energy surface for  $NH_2$ . *The Journal of Chemical Physics*, 2009. 130: p. 184307.

## APPENDICES

### Appendix I

**Wolfram Mathematica (.nb extension) program to calculate the approximate times-of-flight of ions in our instrument, based on the originating position in the initial stage of the mass spectrometer.**

Defining constants and equations in this experiment

```
ev:=1.6 10^-19 (*electron charge in Coulomb*)
amu := 1.66 10^-27 (*atomic mass unit in kg*)
x1:=0.084 (*m*) (*distance from extraction plate to ground plate*)
x2:=0.051(*m*) (*distance from the ground plate to the enf of the
acceleration stack*)
x3:=2.03(*m*) (*remainder of the flight tube length*)
t0[x_,m_,v_,d1_]:= (d1-x)*Sqrt[2 (m*amu)/(ev*v(1-x/d1))] (*Initial
extraction segment*)
v0[x_,m_,v_]:=Sqrt[2 (ev*v(1-x/0.084))/(m*amu)] (*velocity after
first stage*)
t1[d2_,m_,d1_,x_,v_]:= (-
m*amu*v0[x,m,v]*d2+Sqrt[(d2^2*m^2*amu^2+2*d2^2*2300*ev*m*amu)])/(2300*
ev) (*acceleration stack*)
t3[d3_,m_,v_,x_]:=d3*Sqrt[(2*m*amu)/(ev*(2300+v(1-
x/0.084)))] (*free flight path*)
f[d2_,m_]:=Sqrt[d2^2*m^2*amu^2+2*d2^2*2300*ev*m*amu] (*for
debugging*)
```

Flight time from extraction to ground plate

```
Manipulate[t0[x,16,v,x1],{x,0,0.08399},{v,500,1000}]
```

Velocity after first acceleration stage

```
Manipulate[v0[x,16,v],{x,0,0.083999},{v,500,1000}]
```

Time from ground plate to end of acceleration stack

```
Manipulate[t1[x2,16,x1,x,v],{x,0.0001,0.08399},{v,500,1000}]
```

Approximate total TOF in microseconds for m/z=16

```
Manipulate[(t0[x,16,v,x1]+t1[x2,16,x1,x,v])*10^6+15,{x,0.000001,0.0839999},{v,100,1500}]
```

## Appendix II

### The choice of active space in CAS SCF calculations: A case study applied to aminomethoxy $\text{H}_2\text{C}(\text{NH}_2)\text{O}$

In this appendix, I will briefly summarize the procedure taken in order to choose the active space in the CAS calculations performed for aminomethoxy,  $\text{H}_2\text{C}(\text{NH}_2)\text{O}^\bullet$ .

I ran single point energy calculations (ground and excited, SA-MCSCF) for a collection of active spaces. The geometry chosen was the neutral ground state optimized structure at the CCSD(T)/aug-cc-pVTZ level of theory. The aminomethoxy radical has a total of 25 electrons. These electrons would be distributed in the first 13 orbitals of the molecule. The qualitative description of the orbitals is, in increasing energetic ordering (quantities in parenthesis are the orbital occupancy):

1. O 1s (2)
  2. N 1s (2)
  3. C 1s (2)
  4.  $\sigma$  C-H (2)
  5.  $\sigma$  O-C-N (2)
  6.  $\sigma(\text{p}_z)$  C-O (2)
  7.  $\pi$  C-O (2)
  8. N  $\text{sp}^3$  (2)
  9.  $\sigma$  C-N (2)
  10.  $\sigma$  C-N (2) +  $\sigma$  N-H (2)
  11.  $\sigma$  C-O (2)
  12. O  $\text{p}_y$  (1.5)
  13. O  $\text{p}_x$  (1.5)  $\rightarrow$  HOMO, (has fractional occ. because of State Averaging (SA))
- 
14.  $\sigma^*$  C-O (0)  $\rightarrow$  LUMO
  15. N 2 $\text{p}_y$  (0)
  16.  $\sigma^*$  O-C-N (0)
  17. etc...

The order and the “looks” of the orbitals might change a little with different active spaces, but are generally qualitatively similar. One thing to keep in mind is that the most important thing to look for are the actual wavefunctions (linear combinations of the molecular orbitals) and not the orbitals.

The predicted ground and first electronic excited states for this molecule are the orbital configurations which have the unpaired electron in either the O px or the O py orbitals, respectively. A logical first choice for the active space is, therefore, only to include the HOMO and the HOMO-1, namely the O px and O py orbitals, since they are the ones to participate in the excitations. This means that all doubly occupied orbitals are not part of the active space. Keep in mind that in the way this was done, these closed orbitals are still optimized, even though they are not part of the active space.

The table below shows the active spaces used, with the corresponding ground and excited states energies. The notation is the following: cX\_oY, meaning X orbitals are closed (but optimized), and Y orbitals are allowed to have occupancy (this doesn't mean that they will have occupancy!). Number of orbitals in the active space (AS) is therefore  $AS=(Y-X)$ . So on to the table:

closed	occupied	active space	Elec. in active space	Ground (Hartree)	Excited (Hartree)	Delta E (eV)
3	13	10	19	-169.51949610	-169.51048853	0.2451084
3	14	11	19	-169.53821803	-169.52963943	0.2334355
3	16	13	19	-169.59472127	-169.58663664	0.2199939
3	17	14	19	-169.61482451	-169.60664608	0.2225465
6	14	8	13	-169.53845983	-169.52988445	0.2333479
6	16	10	13	-169.59382497	-169.58563398	0.2228881
6	19	13	13	-169.66677021	-169.65479687	0.3258111
9	13	4	7	-169.51949610	-169.51048854	0.2451081
9	14	5	7	-169.54433355	-169.53262498	0.3186063
9	19	10	7	-169.61343695	-169.60380722	0.2620382
10	13	3	5	-169.51949610	-169.51048854	0.2451081
10	14	4	5	-169.54164901	-169.53258556	0.2466290
11	13	2	3	-169.51949610	-169.51048854	0.2451081

We can see here that, with the exception of a few outliers, the energy difference is pretty invariant with the choice of the active space. In order to understand what's going on in each of these calculations we have to look not only at the energies, but what is the active space doing to the actual wavefunctions that result in the eigenvalues for each of the states. In order to do this we look at the Configuration Interaction (CI) vector coefficients given by Molpro for each of the calculations.

Starting from the top, with our smallest active space, o11\_c13, the wavefunctions are represented by

	a2	2a
State 1	a2 1.00000	2a -0.0000268
State 2	2a 0.0000268	a2 1.00000

This reads, State 1 is defined by almost exclusively (CI coefficient of 1) the a2 configuration, which means the unpaired electron (a) is located in the first active orbital (O px) and the second active orbital (O py) is doubly occupied. The story is analogous for State 2, which now has the unpaired electron in the (O py) orbital, with a doubly occupied (O px).

If we then expand the active space to include all bonding orbitals, leaving only the O, C and N 1s orbitals closed, we obtain the following CI vector.

State 1	22222222a2	1.0000000	0.0000000
State 2	22222222a	-0.0000000	1.0000000

This shows that the inclusion of more of the occupied orbitals did not change the character of the states, and they are still represented by exactly the same configurations. The orbitals that were allowed to be excited just remained doubly occupied and the energy is the same. The wavefunction representing these states therefore, is also the same as in the case that we had 11 closed orbitals, resulting in basically the same eigenvalues.

Now we move on to including virtual orbitals in the active space, i.e. the LUMO and orbitals above. If I just include the LUMO in the active space the CI vectors I get are the following:

State 1	22222222a0	0.9951042	-0.0204313
State 2	22222222a20	0.0204170	0.9949922
State 3	22222220a2	-0.0955207	0.0019397
State 4	22222220a22	-0.0019761	-0.0953048

Again, the ground and excited states have the same representation, where the unpaired electron is in either non-bonding O p-orbitals, hence the energy difference between State 1 and State 2 is very similar to the one where we don't include the LUMO. The difference here is that now we have contributions from excitations from the doubly occupied inner orbitals to the LUMO, therefore, changing the active space has a bigger effect on the energy when the LUMO is included. Regardless, the contribution of these other configurations is minor so it seems that this molecule does not have a strong multireference character. Therefore, for a QUALITATIVE description of the molecule (does not guarantee that the energetics will be quantitative) even the smallest active space tested should be sufficient.

After a lot of exploration, we decided to go with the CAS(5,4) active space, namely the c10\_o14, which closes (but still optimizes) the first 10 core orbitals and includes 1 unoccupied orbital in the active space. This active space is the same as the one utilized by Dillon and Yarkony for hydroxymethoxy, ethoxy and isopropoxy. Again the configuration of the first 2 states is essentially the same as the previous active spaces, hence, the energy is again very similar. This shows that the aminomethoxy radical does not have a strong multireference character. Thus, the difficulty in calculating the photoelectron spectrum is likely due to the vibronic coupling between the ground and first excited neutral electronic states, as discussed in Chapter 6.

## Appendix III

### **Finding image centers for a proper reconstruction: A case study of the $\text{CH}_3^-$ VMI photoelectron spectrum.**

In the 1064 nm  $\text{CD}_3^-$  images, the signal-to-noise is worse than in  $\text{CH}_3^-$ ; therefore, the ability to find the center by just our eyes is not accurate to a pixel. To verify what effect this has on our spectra and analysis, the center was initially chosen by eye to be {692,592} and then we varied the x and y center positions for a total of 8 different centers. A full analysis was carried out for each image center, paying close attention to three things: (1) agreement between energy scales ( $\text{O}_2$  and internal  $\text{CD}_3$  calibration); (2) variation of EAs between determinations (e.g. EA from  $v = 4$  minus known vibrational frequencies or the EA from the position of  $v=0$  peak); and (3) any observed systematic shift in the determination of the EA. The initial analysis was carried out with full image reconstructions, and then we replaced one of the quadrants that had poor resolution and carried out the analysis again with the quadrant replaced image for the best centers we found. Choosing the correct image center is essentially asking how well we know where our zero-kinetic energy spot is located in the image. This will greatly affect the absolute energy scaling (and obviously the resolution following reconstruction), but not the relative energy scaling (so the vibrational frequencies and inversion splitting is not affected by this, but the EA determination is).

Below are three tables showing analysis of three different image centers, specifically focused on the EA determination. These are illustrative of the process we went through to validate our chosen image center and our new understanding of the error associated with choosing an image center. The three image centers described below are pixels located:

	Table A1 {692,592}	
Table A3 {691,591}	Table A2 {692,591}	

Table A1: EA determinations for a wrong image center {692,592}; the initial center, picked by eye, and resulted in what appeared to be a very nice reconstruction.

Center: {692,592}	Calibration Species	
	O <sub>2</sub> calibration	CD <sub>3</sub> calibration
from $v = 0$	0.0858	0.0721
from $v = 1$	0.0849	0.0719
from $v = 2$	0.0843	0.0720
from $v = 3$	0.0838	0.0725
from $v = 4$	0.0833	0.0724
Average EA	0.0841	0.0722
Standard Deviation	0.0007	0.0003

Note that there is no agreement between the different energy scales and there is a clear systematic shift in the EA determination using the external calibration species. This shows that the center is not properly chosen. Since the best CH<sub>3</sub>, O<sub>2</sub>, and CD<sub>3</sub> data were all taken on the same day, and we've already rigorously tested the CH<sub>3</sub> data, we know that the O<sub>2</sub> energy scale is good. In addition, the O<sub>2</sub> energy scale calibration is based on peak spacing, but is also consistent with the reported PES peak positions.

Table A2. Example with 1 pixel away {692,593}.

Center: Symm. {692,593}	Calibration Species	
	O <sub>2</sub> calibration	CD <sub>3</sub> calibration
EA determination		
from $v = 0$	0.0835	0.0767
from $v = 1$	0.0843	0.0767
from $v = 2$	0.0836	0.0765
from $v = 3$	0.0836	0.0771
from $v = 4$	0.0825	0.0764
Average EA	0.0835	0.0766
Standard Deviation	0.0008	0.0003

There are no large systematic shifts in the EA determinations, but the energy scales still do not agree with each other. Other centers had agreement in energy scales but showed systematic shifts and poor resolution following reconstruction.

Table A3: Best center {691,593}, after symmetrization (data used in the paper).

Symm. {691,593}	Calibration Species		
	O <sub>2</sub>	CD <sub>3</sub>	CH <sub>3</sub>
EA determination			
from v = 0	0.0834	0.0838	0.0825
from v = 1	0.0836	0.0832	0.0820
from v = 2	0.0841	0.0838	0.0826
from v = 3	0.0832	0.0829	0.0816
from v = 4	0.0838	0.0834	0.0822
Average EA	0.0836	0.0834	0.0822
Standard Deviation	0.0003	0.0004	0.0004
Total Average	0.0831		
Total St dev	0.0007		

Here, the energy scales agree with each other to about 0.001 eV. We also show the results from using CH<sub>3</sub> as the calibration species for additional verification. The agreement of the energy scales and the absence of a systematic shift in the energy scale shows that our zero-kinetic energy release point, i.e. the image center, is the most accurate we can possibly be, since a 1 pixel change results in a disagreement. Moreover, this center also results in a reconstruction of acceptable resolution, as seen in Figure 2 in the manuscript and shown below.

Note that the numbers in the tables are averages, without any statistical weighting. The weighted analysis results in an EA of 0.0833 eV, with an uncertainty of 0.0007 eV. However, we can potentially still have a wrong center, by an amount smaller than 1 pixel. Since each pixel at this kinetic energy range corresponds roughly to 0.005 eV, we can have an error bar of  $\pm\frac{1}{2}$  pixel, or  $\pm 0.0025$  eV. Adding the uncertainties in quadrature, we get EA(CD<sub>3</sub>) = 0.083(3) eV.